Mesoscale Modelling of Concrete Materials under Complex Loadings

QINGCHEN LIU

BSc, ME

Supervisor: A/Prof. Yixiang Gan

A thesis submitted in fulfilment of
the requirements for the degree of
Doctor of Philosophy

School of Civil Engineering
Faculty of Engineering
The University of Sydney
Australia

2026

Statement of Originality

This is to certify that to the best of my knowledge, the content of this thesis is my own work. This thesis has not been submitted for any degree or other purposes.

I certify that the intellectual content of this thesis is the product of my own work and that all the assistance received in preparing this thesis and sources have been acknowledged. No content produced by generative AI tools was used in the preparation of this thesis.

Abstract

As a typical construction material, concrete is widely used in various engineering fields, such as infrastructure, buildings, and transportation. Marine resource exploration has become an international priority and coastal infrastructure plays a critical role in supporting this development. In marine environment, the durability and mechanical performance of concrete have received significant attention from the scientific community. Among the various behaviours of concrete, ionic diffusion leading to chloride-induced corrosion and the structural durability under complex stress conditions are of primary concern, particularly with regard to the influence of material constituents across different length scales, from the nano- to macroscale. The mesoscale is the focus of this work, as it provides greater relevance and accessibility to practice compared to other scales. At this scale, concrete (or mortar) can be treated as a three-phase composite consisting of cement paste or mortar, aggregates (fine or coarse), and the interfacial transition zone (ITZ) in between them. As the impermeable and strongest phase of concrete, aggregates have received considerable attention in experimental and numerical studies due to their significant influence on concrete performance. Many numerical studies still simplify aggregates using regular shapes, and experimental control over aggregate shape irregularity is often difficult to achieve. As a result, the effects of aggregate shape on concrete diffusivity and fracture remain insufficiently addressed, failing to reflect the realistic macro and micro response of concrete.

This thesis focuses on the transport and mechanical behaviours of concrete, with particular emphasis on the influence of aggregate shape. It begins by introducing the research background and objectives, followed by a literature review on the current state of research related to marine challenges. The remainder of the thesis is organised into three chapters, in which realistic aggregate shapes are used to construct the mesoscale structure of concrete, highlighting the effects of aggregate morphology. Based on these models, various numerical simulations of concrete behaviours are conducted, including ion diffusion, triaxial static fracture, and dynamic fracture. Finally, the thesis concludes with key research findings and potential directions for future work.

In Chapter 3, addressing durability concerns related to corrosion, the diffusion behaviour of cement-based composites is investigated using mesoscale modelling. The influence of aggregate shape on effective diffusivity is then highlighted at the same solid fraction and

aggregate size. Rougher aggregates result in a smaller effective diffusivity due to more tortuous diffusion paths, as evidenced by a broader throat size distribution. An empirical equation is developed to predict the effective diffusivity as a function of multiscale geometric indices characterising realistic aggregate shape, which are the fractal dimension and relative roughness.

In Chapter 4, considering multiaxial stress condition in marine environment, fracture behaviour of concrete with realistically shaped aggregates under triaxial loading is investigated to emphasise the effects of grain morphology on macroscopic failure strength under varying confining pressures. Similar to the uniaxial stress state, rougher aggregates result in higher concrete strength under triaxial stress conditions. Although this effect becomes more pronounced with increasing confining pressure, a universal scaling relationship between normalised concrete strength and confining pressure is observed across different aggregate shapes. When the stress–strain response reaches the peak, the heterogeneous stress distribution across different aggregate shapes tends to converge. Moreover, with increasing aggregate roughness, a competitive mechanism between the interfacial transition zone (ITZ) and aggregates exists in both the peak and post-peak regions.

In Chapter 5, to account for the concrete response to rapid loading from occasional natural hazards in marine environments, *e.g.*, rogue waves, ship impacts, mesoscale modelling of Split Hopkinson Pressure Bar (SHPB) tests on concrete is conducted to investigate the dynamic response of concrete. We highlight the role of internal strain rate and damage on dynamic increase factor (DIF) from different aspects including loading ramp rate, internal friction and confining pressure. As key results, only a higher loading ramp rate induces more significant strain rate effects on the DIF, as evidenced by pronounced increases in both internal strain rate and damage in the mortar and aggregate phases. In contrast, higher internal friction and confining pressure weakens the strain rate effect on the DIF, primarily due to the mortar phase, as effectively reflected by local damage rather than internal strain rate.

In summary, our mesoscale modelling provides new macro- and microscopic insights into the influence of aggregate shape on various single-physical behaviours of concrete related to marine challenges. It offers valuable understanding for concrete mix design, where the shape irregularity of aggregates and their association with transport and mechanical properties, *e.g.*, diffusivity and strength, should be carefully considered. This thesis establishes a foundation for future research on enhancing the overall concrete performance, *e.g.*, coupled behaviours, in complex loading environments.

List of Publications

Published:

- Liu, Q., Wei, D., Zhang, H., Zhai, C., Gan, Y., 2022. A numerical investigation on effective diffusion in cement-based composites: the role of aggregate shape. *Transport in Porous Media* 143(3), 681-702.
- Liu, Q., Wei, D., Gan, Y., 2025. Mesoscale Modelling of Triaxial Concrete Fracture: The Role of Aggregate Shapes. *International Journal of Mechanical Sciences*, 110570.
- Liu, Q. and Gan, Y., 2026. Mesoscale modelling of confined split-Hopkinson pressure bar tests on concrete: effects of internal damage and strain rates, *Engineering Fracture Mechanics*, 339, p.112079.

Authorship Attribution Statement

Chapter 3 of this thesis is published as:

Liu, Q., Wei, D., Zhang, H., Zhai, C., Gan, Y., 2022. A numerical investigation on effective diffusion in cement-based composites: the role of aggregate shape. *Transport in Porous Media* 143(3), 681-702.

Author Contributions: Qingchen Liu: Writing – original draft, Visualization, Validation, Methodology, Investigation, Formal analysis, Data curation, Conceptualization**. Deheng Wei:** Writing – review & editing, Supervision, Software, Resources, Methodology, Investigation, Formal analysis, Data curation, Conceptualization. **Hongzhi Zhang:** Writing – review & editing. **Chongpu Zhai:** Writing – review & editing. **Yixiang Gan:** Writing – review & editing, Visualization, Supervision, Resources, Methodology, Investigation, Funding acquisition, Formal analysis, Conceptualization.

Chapter 4 of this thesis is published as:

Liu, Q., Wei, D., Gan, Y., 2025. Mesoscale Modelling of Triaxial Concrete Fracture: The Role of Aggregate Shapes. *International Journal of Mechanical Sciences*, 110570.

Author Contributions: Qingchen Liu: Writing – original draft, Visualization, Validation, Methodology, Investigation, Formal analysis, Data curation, Conceptualization**. Deheng Wei:** Writing – review & editing, Supervision, Software, Resources, Methodology, Investigation, Formal analysis, Data curation, Conceptualization. **Yixiang Gan:** Writing – review & editing, Visualization, Supervision, Resources, Methodology, Investigation, Funding acquisition, Formal analysis, Conceptualization.

Chapter 5 of this thesis is published as:

Liu, Q. and Gan, Y., 2026. Mesoscale modelling of confined split-Hopkinson pressure bar tests on concrete: effects of internal damage and strain rates, *Engineering Fracture Mechanics*, 339, p.112079.

Author Contributions: Qingchen Liu: Writing – original draft, Visualization, Validation, Methodology, Investigation, Formal analysis, Data curation, Conceptualization**. Yixiang Gan:** Writing – review & editing, Visualization, Supervision, Resources, Methodology, Investigation, Funding acquisition, Formal analysis, Conceptualization.

For the aforementioned publications, I conducted the numerical simulations, analysed the data, and drafted the manuscripts. The co-authors reviewed the drafts and offered valuable feedback.

In addition to the statements above, in cases where I am not the corresponding author of a published item, permission to include the published material has been granted by the corresponding author.

Student name: Qingchen Liu

As supervisor for the candidature upon which this thesis is based and the corresponding author of above publications, I can confirm that the authorship attribution statements above are correct.

Supervisor name: Yixiang Gan

Acknowledgements

Firstly, I would like to express my deep gratitude to my supervisor, A/Prof. Yixiang Gan, for his support throughout this journey. Discussions with him have not only inspired my research through his suggestions and ideas, but have also broadened my understanding of scientific inquiry. He has continually encouraged me to move forward and has gradually helped me develop the ability to tackle more complex problems. I would like to thank Dr. Deheng Wei for his helpful comments and valuable ideas on my research work, which have motivated me to gain deeper insights into my research questions and improve the quality of my work. I would also like to thank another collaborator, Dr. Chongpu Zhai, for his support with research resources.

I am grateful to my PEM panel members, A/Prof. Daniel Dias-Da-Costa and Prof. Abbas El-Zein, for their constructive suggestions and feedback on my PEM sessions. I would also like to thank Ms Daniela Entenmann from the HDR office for her timely assistance in the purchase of essential computing devices. In addition, I am deeply appreciative of the companionship and insightful discussions with group members, including Dr Mingrui Dong, Dr Shi Zhang, Dr Zhongzheng Wang, Dr Yu Chen, Mr Dongsheng Chen, Mr Yuyao Zhang, Mr Jike Li, Mr Xiaoqian Bi, Mr Yingjie Gu, Mr Dong Geng, Ms Haiyi Zhong, and Ms Jiayin Zhao.

Finally, I would like to thank my family for their unconditional support throughout my PhD, their care in everyday life, and their constant encouragement.

Table of Contents

Statement of Originality ..... **ii**
Abstract ..... **iii**
List of Publications ..... **v**
Authorship Attribution Statement ..... **vi**
Acknowledgements ..... **viii**
Table of Contents ..... **ix**
CHAPTER 1 Introduction **1**
1.1 Background 1
1.2 Research objectives 3
1.3 Thesis outlines 3
CHAPTER 2 Literature Review **6**
2.1 Concrete materials 6
2.1.1 Concrete materials across length scales 7
2.1.2 Challenges to coastal concrete infrastructure 8
2.2 Transport behaviours 9
2.2.1 Mechanisms of ionic transport 10
2.2.1.1 Ionic diffusion 10
2.2.1.2 Absorption 10
2.2.1.3 Permeation 11
2.2.2 Correlation of ionic transports with corrosion 11
2.2.3 Ionic transport under varying exposure conditions 12
2.2.4 Influence of microstructure across length scales 16
2.3 Mechanical behaviours 19
2.3.1 Mechanical mechanisms 19
2.3.1.1 Fracture or cracking 19
2.3.1.2 Fatigue 21
2.3.1.3 Time-dependent behaviour 21
2.3.1.4 Dynamic behaviour 22
2.3.2 Mechanical properties under varying exposure conditions 23
2.3.3 Influence of microstructure on mechanical properties 26
2.4 Managements of concrete performance 30
2.4.1 Monitoring 30
2.4.2 Protection 31

2.4.3 Maintenance 32
2.5 Research methods 33
2.5.1 Analytical approaches 33
2.5.2 Experimental approaches 34
2.5.3 Numerical modelling 36
2.5.3.1 Modelling framework 36
2.5.3.2 Representative elementary volume of concrete microstructure 37
2.5.3.3 Image-based generation of concrete microstructure 37
2.5.3.4 Non-image-based generation of concrete microstructure 38
2.6 Summary 39
Chapter 3 Mesoscale Modelling of Diffusion in Concrete 42
3.1 Introduction 43
3.2 Methods 45
3.2.1 Packing structure of aggregates 46
3.2.1.1 Ordered packing 46
3.2.1.2 Disordered packing 46
3.2.2 Generation of aggregate shapes with multi-scale morphology features 47
3.2.3. FEM Modelling effective diffusivity 49
3.3. Results and discussion 51
3.3.1. Spatial distribution of aggregates 51
3.3.2. Aggregate elongation 53
3.3.3. Global aggregate morphology features 55
3.3.4. Correlating shape indices to effective diffusivity 57
3.4. Summary 61
Chapter 4 Mesoscale Modelling of Triaxial Concrete Fracture 63
4.1. Introduction 64
4.2. Methodology 69
4.2.1. Mesoscale structure of concrete 71
4.2.1.1 Voronoi tessellation 71
4.2.1.2 Packing for irregular aggregate shapes 72
4.2.1.3 Generation of material components for the mesoscale model 73
4.2.2 Constitutive laws for mesoscale model of concrete 75
4.2.2.1 CDP model for mortar and aggregate 77
4.2.2.2 Cohesive interface element method for ITZ 79
4.2.3 Triaxial loading conditions 81
4.3. Results and discussion 82
4.3.1 Stress-strain responses 83

4.3.2 Local stress distributions....86
4.3.3 Damage evolutions....90
4.3.4 Crack patterns....93
4.4. Summary....98
Chapter 5 Mesoscale Modelling of Dynamic Fracture of Concrete....100
5.1. Introduction....101
5.2. Methods....106
5.2.1. Mesoscale sample generation....107
5.2.2 Constitutive models for dynamic fracture....109
5.2.2.1 Concrete damage plasticity (CDP) model....110
5.2.2.2 Cohesive element method for ITZ....111
5.2.2.3 Strain rate effects....111
5.2.3 Loading conditions and wave signal processing....113
5.2.3.1 Loading conditions....113
5.2.3.2 Wave signal processing....114
5.2.4 Validation....116
5.3. Results and Discussion....119
5.3.1. Loading ramp rate....119
5.3.2. Internal friction....124
5.3.3. Confining pressure....126
5.3.4. Discussion....128
5.4. Conclusion....129
Chapter 6 Conclusion and Future Work....131
6.1 Conclusion....131
6.2 Future work....132
Appendix A: Derivation of Relative Roughness....134
Appendix B: Derivation of Hashin-Shrinkman....135
Appendix C: Modelling of Static Fracture of Concrete....136
Appendix D: Strain Wave and Stress-Strain Curve....137
Appendix E: Distributions of Internal Strain Rate....139
Bibliography....141

CHAPTER 1 Introduction

1.1 Background

With advances in science and technology, the exploration of marine resources has become a major international priority. Coastal infrastructure, such as civil and military terminals, offshore airports, wind power stations, and submarine tunnels, plays an essential role in this development (Manzur et al., 2019; MH et al., 2020), and has been built with various construction materials, such as steel (Nassar, 2022), concrete (Seleem et al., 2010) and timber (Treu et al., 2019). Due to its high versatility in meeting specific building designs and cost-effectiveness compared with other construction materials, concrete has become the most extensively used and preferred choice for coastal infrastructure (Alexander and Nganga, 2016). During their service life, offshore concrete structures face challenges to durability and structural stability in marine environments, such as chloride-rich corrosion (Nassar, 2022) and complex stress conditions, *e.g.*, uniaxial, multiaxial, static, dynamic, and sustained stresses, caused by deep-water pressure, rogue waves or tsunamis, and ship impacts (Gerwick Jr, 1970; Alexander and Nganga, 2016). These issues are related to both the transport behaviours, *e.g.*, diffusion, sorption and permeation, and mechanical, *e.g.*, fracture, fatigue, creep and shrinkage, behaviours of concrete, some related properties, *e.g.*, diffusivity, fracture strength, and elastic modulus, have attracted extensive attention from the scientific community. Therefore, a thorough understanding of both fundamental aspects of concrete materials is essential for addressing the challenges encountered in marine conditions.

Concrete is a material with a complex internal structure spanning multiple length scales, from nanoscale to the macroscale, where the material constituents, *e.g.*, molecular C-S-H, C-S-H matrix, pores, hydration products, cement paste, sand, interfacial transition zone, mortar, and coarse aggregates, in order of increasing length scale, contribute to the overall material heterogeneity to varying degrees (Pellenq et al., 2009; Cusatis et al., 2014; El Awad, 2020; Pushpakumara and Fernando, 2023). Early studies were conducted to investigate macroscopic properties of concrete and to develop relevant continuum or constitutive models to meet general engineering needs, but they ignore material heterogeneity and lack microscopic evidence (Luping and Gulikers, 2007; Papanikolaou and Kappos, 2007). To address this limitation, subsequent studies consider concrete at finer scales, treating it as various multi-phase

composites at the scale of interest. The overall behaviour of concrete is found to be influenced by inherent nature of its constituent materials (Mačiulaitis et al., 2009; Okumu, 2017; Dastgerdi et al., 2019). Among all length scales, the mesoscale is considered more accessible in practice than other scales. At this scale, concrete or mortar can be regarded as a three-phase composite consisting of the matrix (mortar or cement paste), aggregates (coarse or fine), and interfacial transition zone (ITZ) between them (Thilakarathna et al., 2020; Wu et al., 2021a). In addition, the representative material heterogeneities can be captured at this scale, providing an accurate representation of the internal evolution and local response within concrete (Thilakarathna et al., 2020). Therefore, the mesoscale can be considered the most practical and effective choice for investigating the fundamental properties of concrete by identifying the underlying microscopic mechanisms.

The transport and mechanical behaviours of conventional concrete have been widely investigated through numerical and experimental approaches, with particular focus on the influence of concrete heterogeneity at the mesoscale by considering the content, material properties, and morphology of its constituents, *e.g.*, mortar or cement paste, ITZ, and fine or coarse aggregates, (Zhang, 2013b; Zhang et al., 2014a; Zhang and Zhang, 2014; Thilakarathna et al., 2020; Wu et al., 2021a; Ren et al., 2023; Pan et al., 2025; Tong et al., 2025). Among material constituents, the ITZ and aggregates have received more attention regarding concrete behaviour, such as diffusivity and fracture. Due to its thickness of 10-50μm, the ITZ is difficult to access experimentally and remains debated in terms of its representation in mesoscale models (Maleki et al., 2020), and current experimental or numerical approaches have not achieved further breakthroughs in this area to date. For aggregates, the solid fraction (Liu et al., 2018; Jin et al., 2022a), size (Jin et al., 2022b; Guo et al., 2024), and shape (Abyaneh et al., 2013; Du et al., 2014; Naderi et al., 2021) are key focuses in many mesoscale studies. Many studies can effectively control the aggregate solid fraction and size distribution, providing a deep and comprehensive understanding of their effects on concrete performance. Aggregate shape remains a challenging factor in experimental investigations due to difficulties in control. Consequently, greater attention to the effect of aggregate shape has been given in numerical investigations, where simple shapes, such as spheres (or circles), ellipsoids (or ellipses), or polygons (or polyhedron), have been used to model aggregates (Abyaneh et al., 2013; Du et al., 2014; Liu et al., 2014; Wang et al., 2016b; Chen et al., 2018). However, these shapes cannot represent the real morphology of aggregates and fail to fully reflect the shape effects in terms of macroscopic properties and local responses within the material. Thus, it is necessary to

address this gap to shed new light on the effects of aggregate shape and to better capture the realistic response of concrete under specific loading, thereby enhancing our understanding of mesoscale heterogeneity in marine environments.

1.2 Research objectives

With respect to marine challenges, the fundamental transport and mechanical behaviours of concrete containing realistically shaped aggregates are investigated using mesoscale modelling. The internal microstructure variations and local responses within the concrete are examined to provide quantitative evidence for the underlying mechanisms. The research objectives are:

- To study the effects of aggregate morphology on the ionic diffusivity of concrete;
- To understand how realistic aggregate shapes affect the static fracture behaviour of concrete under simple and complex stress conditions; and
- To enhance the understanding of the dynamic fracture behaviour of concrete with a focus on influencing factors that are difficult to access or control in practice.

1.3 Thesis outlines

The structure of the thesis is as follows. Chapter 2 presents a comprehensive literature review, with a particular focus on the transport and mechanical behaviours of concrete related to marine challenges. Corrosion is a major concern for the durability performance of concrete. In terms of transport behaviours, some fundamental processes, including diffusion, permeation, and absorption, have been reviewed in terms of their correlation to corrosion and their varying contributions to corrosion along the elevation of structures exposed to different environmental zones. The influence of concrete microstructure on diffusivity across varying length scales will be systematically reviewed. For some sudden events, such as ship impacts or rogue waves, the mechanical behaviours of concrete, including uniaxial and multiaxial static fracture, fatigue, time-dependent behaviour, *e.g.*, creep, and dynamic behaviour, will be provided relevant fundamental theory. Their associated mechanical properties, in particular concrete strength and elastic modulus, are discussed in relation to exposure conditions and material heterogeneity across different length scales. To ensure serviceability, management of concrete performance

in terms of monitoring, protection, and maintenance is provided. Various experimental and numerical methods are introduced for related investigations.

Chapter 3 focuses on ion-induced corrosion related to the durability performance of concrete, which is primarily governed by diffusion. Most existing studies have only considered regular aggregate shapes in mesoscale models of concrete materials, resulting in an insufficient understanding of the influence of aggregate morphology. Therefore, this chapter employs the finite element method (FEM) to numerically investigate the diffusion behaviour of cement-based composites, which are simplified as systems consisting of cement paste and aggregates, with the ITZ assumed to be embedded within the cement paste. Realistic aggregate shapes, characterised by fractal dimensions, are generated for two-phase mesoscale model to highlight the effect of aggregate morphology across different aggregate solid fractions. The relationship between effective diffusivity and aggregate solid fraction is validated against analytical solutions. The results further demonstrate the influence of aggregate shape on effective diffusivity and are analysed in relation to geometrical indices of aggregate shape and the associated tortuosity of diffusion paths.

Chapter 4 is concerned with the mechanical performance of concrete. Although these properties have been widely studied under uniaxial loading conditions, such stress states are idealised compared to the multiaxial loads typically encountered in marine environments. To represent more realistic and complex conditions, mesoscale modelling via FEM is conducted to investigate the static fracture of concrete under triaxial loading, in which confining pressure is uniformly applied to all surrounding faces. The mesoscale structure of cubic concrete specimen is generated as a three-phase composite consisting of mortar, ITZ, and aggregate. Realistic aggregate shapes are used to highlight the effect of aggregate morphology on the stress–strain response under triaxial stress conditions, with particular emphasis on the relationship between concrete strength and confining pressure. This relationship is validated against experimental data. Local responses within the concrete, including stress distribution, damage evolution, and crack patterns, are analysed to provide quantitative evidence supporting the influence of aggregate shape on concrete strength.

Chapter 5 discusses the dynamic fracture of concrete to account for sudden loading scenarios in marine environments, such as ship impacts and rogue waves. These loadings are typically unpredictable and difficult to reproduce in laboratory settings, making certain loading factors inaccessible or challenging to measure experimentally. To address this, a numerical

model of the Split Hopkinson Pressure Bar (SHPB) test is developed to investigate the dynamic behaviour of concrete. A three-phase mesoscale structure of the cylindrical concrete specimen, incorporating realistic aggregate shapes, is generated to capture more realistic material responses. The macroscopic analysis focuses on the relationship between the dynamic increase factor (DIF) and strain rate from different aspects, including loading ramp rate, internal friction, and confining pressure. Analyses of internal strain rate and local damage are conducted to provide microscopic evidence and to highlight their roles in each aspect.

The final chapter will first summarise the key findings of the thesis, with particular focus on the different concrete behaviours investigated, including effective diffusivity, triaxial fracture, and dynamic fracture. The chapter will highlight both the macroscopic responses and the associated microscopic mechanisms revealed through mesoscale modelling, emphasising how aggregate morphology, material heterogeneity, and loading conditions influence concrete performance. The contribution of these findings to practical engineering applications will also be highlighted. In addition, the chapter will outline the current limitations of this work and explore possible directions for future research involving more complex loading scenarios.

CHAPTER 2 Literature Review

This chapter provides an overview of the response of concrete to various complex loadings in marine environments. The structure of the relevant content is as follows. Section 2.1 introduces concrete materials, focusing on their heterogeneity across different length scales and the challenges faced by coastal infrastructure in marine environments. To understand the reactions of concrete to these challenges, Sections 2.2 and 2.3 respectively review the transport and mechanical behaviours of concrete in terms of basic mechanisms, relevant properties under varying exposure conditions, and the influence of microstructures. Strategies for monitoring, protecting, and maintaining concrete structures are also presented in Section 2.4. Finally, Section 2.5 provides an overview of the analytical, experimental, and numerical approaches employed in existing studies.

2.1 Concrete materials

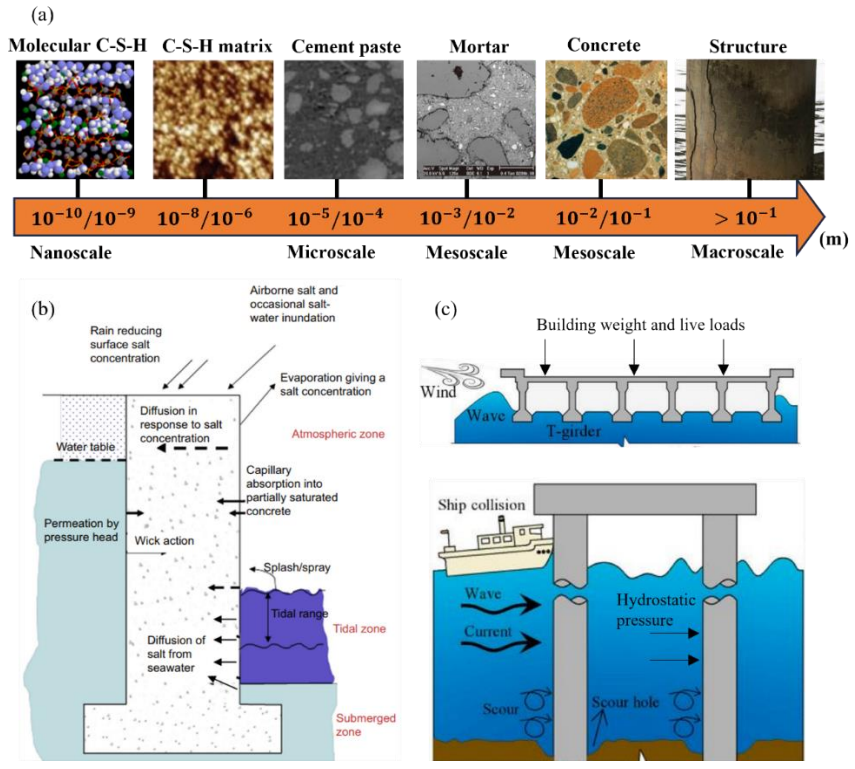

Figure 2.1. Concrete structures in marine environments: (a) Material heterogeneity of concrete across varying length scales (Pellenq et al., 2009; Cusatis et al., 2014; El Awad, 2020; Pushpakumara and Fernando, 2023), (b) chemical loading *i.e.*, corrosion (Santhanam and Otieno, 2016) and (c) mechanical loading, *e.g.*, wind, tidal waves, and ship impact, for reinforced concrete structure (Xu et al., 2023).

2.1.1 Concrete materials across length scales

As a common construction material, concrete is a complex composite that exhibits heterogeneity across various length scales, each associated with distinct material constituents, as shown in Figure 2.1(a). At the nanoscale (around $10^{-10}\sim10^{-9}$m), calcium-silicate-hydrate (C-S-H) exists as globular particles, which form the higher-level granular composite known as C-S-H gel at the scale around $10^{-8}\sim10^{-6}$ m, in both low- and high-density forms, distinguished by gel porosities of around 24% and 37%, respectively (Jennings, 2000; Constantinides and Ulm, 2004; Shahrin and Bobko, 2017). At the microscale (around $10^{-5}\sim10^{-4}$m), in addition to the C-S-H matrix, the composition of cement paste also includes pores, calcium hydroxide (CH), un-hydrated cement grains, and others, contributing to its heterogeneity (Ulm et al., 2004). The pores in cement paste are randomly distributed, interconnected, and vary in size. The morphology of pore structures can be characterised by the porosity, average pore diameter, pore size distribution, pore surface area, and pore connectivity, which are also considered key parameters that affect the performance of cement paste in different ways (Kumar and Bhattacharjee, 2003; Li et al., 2018a).

When the scale increases to the mesoscale, it can be classified on the order of $10^{-3}\sim10^{-2}$ m and $10^{-2}\sim10^{-1}$m. At the former scale, the mortar is considered a three-phase composite, including the cement paste, fine aggregate (or sand), and the interfacial transition zone (ITZ) between them (Wang et al., 2019b). At the latter scale, *i.e.*, the largest aggregate scale, a complete view of conventional concrete can be observed, where the mortar phase is treated as a matrix hosting the coarse aggregates surrounded by ITZs (Naderi et al., 2021). The ITZ, consisting of thin layers, exhibits porosity that decreases from the aggregate surface toward the mortar or cement paste. The morphology of the ITZ has been given with a particular focus on its thickness, which is difficult to define precisely but is generally considered to range from 10-80μm (Winslow et al., 1994; Tu and Lu, 2011). Aggregate type, *e.g.*, natural (Naderi et al., 2021), recycled (Mazzucco et al., 2018) or coral (Wu et al., 2021b) aggregates), solid fraction (Stock et al., 1979), size (Jin et al., 2022a), and shape (Zheng et al., 2012; Wei et al., 2020b) are also widely studied as influencing factors in accounting for the heterogeneity of concrete or mortar. Aggregate shape has been characterised using multiple shape indices, including sphericity, elongation, convexity, irregularity, surface roughness, fractal dimension, and relative roughness (Hu and Stroeven, 2006; Wei et al., 2020b). Sometimes, concrete is even modelled with more than three phases, including initial defects, *e.g.*, macro-pores or air voids

(Wang et al., 2016b), or admixtures, *e.g.*, steel fibres (Naderi and Zhang, 2022). From the nanoscale to the mesoscale, the morphology and physical properties of material constituents at each scale differ from one another, but they all collectively influence the macroscopic performance of concrete at scale on the order of $>10^{-1}$m.

2.1.2 Challenges to coastal concrete infrastructure

The marine environment poses severe challenges, such as chloride salts, fluctuations in temperature and humidity, alternating wet-dry cycles, and persistent wind and wave action (Alexander and Nganga, 2016; Zhang, 2025), which can be considered as chemical, environmental, chemical and mechanical loading to initiate or accelerate the deterioration of coastal concrete infrastructure, as shown in Figure 2.1(b) and (c). As a result, this raises concerns about the durability and mechanical performance of concrete under marine exposure. Among them, a few particular concerns have attracted significant attention from the scientific community (Qu et al., 2021):

- Corrosion-induced deterioration represents a major challenge to the durability of reinforced concrete in marine environments, and can even incur approximately 2.5 trillion dollars in global annual losses (Loto and Cleophas, 2021). This is mainly due to the chemical loading, *i.e.*, chloride penetration, which can lead to electrochemical degradation of embedded steel reinforcement and concrete cracking (Qu et al., 2021). Chloride penetration into concrete occurs differently under various environmental loadings, such as exposure to seawater, waves and tidal actions, or the atmosphere. Meantime, freeze-thaw (Jiang et al., 2018), carbonations (Li et al., 2018b) and sulphate attack (Ma et al., 2023), also as concerns to concrete durability, may occur simultaneously with chloride penetration, further exacerbating the weakening of concrete durability caused by corrosion.
- Coastal infrastructure in marine environments is also exposed to mechanical loading from seawater. For instance, the complex interplay between external hydrostatic pressure and internal water pressure from infiltration can generate strain and causes the fragmentation of the concrete (Takahashi et al., 2021). Submerged concrete structures in deep-sea regions are subjected to high hydrostatic pressure, which increases internal stress and thereby accelerates cracking (Slowik and Saouma, 2000; Cui et al., 2017; Kunawisarut et al., 2025). Such stresses on coastal concrete structures are usually

multiaxial, presenting considerable challenges for ensuring the mechanical reliability of concrete.

- Extreme ocean waves, *e.g.*, rogue waves or tsunamis, or occasional ship impacts can impose sudden and intense dynamic loads on concrete structures, potentially causing the significant loss of structural stability or even collapse (Wilson, 2003; Sundar, 2017), and resulting in substantial financial costs for repair or replacement. For instance, the 2004 Indian Ocean tsunami caused an estimated $1.22 billion in direct damage, and about $10 billion was needed for the reconstruction and repair of coastal infrastructure (Inderfurth et al., 2005). Most of these extreme cases are difficult to prevent or avoid, which increases concerns about the material performance of concrete under the complex stress conditions of the marine environment.

Considerable progress has been made in advanced technologies for predicting marine climate changes (Cole et al., 2019), monitoring structural stability (Votsis et al., 2018), and providing protective coating (Verma et al., 2019) or measures (Klanac and Varsta, 2011) to mitigate or prevent long or short-term, or sudden marine challenges. However, relying solely on these external approaches is far from sufficient. It is even more necessary to gain a comprehensive understanding of the material responses to these loadings to provide a theoretical basis for the potential improvement of material performance. Most of the marine challenges listed above are related to the transport and mechanical behaviours of concrete, and both will be reviewed in the relevant literature in the following sections.

2.2 Transport behaviours

Durability performance under chemical loading is mainly reflected in transport behaviour of concrete and depends on the material resistance to the ingress of aggressive ions such as chloride, sulphate, and carbon dioxide. These chemicals can cause varying degrees of degradation in coastal infrastructures through different transport processes. As a major concern to durability, this section will focus on the corrosion-related transport behaviours of concrete. Chloride ions from the marine environment penetrate the concrete cover and reach the embedded rebar. Corrosion initiates once the chloride concentration at the depth of the rebar exceeds a threshold value. For such a concrete deterioration, the transport mechanism, their correlation with corrosion, exposure conditions and the influence of concrete microstructure will be reviewed.

2.2.1 Mechanisms of ionic transport

Ionic transport through the concrete microstructure is mainly governed by processes, such as diffusion, absorption and permeation, which are driven by various mechanisms. The following provides a general review of these processes with fundamental theories, as below:

2.2.1.1 Ionic diffusion

Diffusion is the process by which gases, liquids, or ions penetrate and move through the pores of concrete, primarily from areas of high concentration to low concentration. This is one of the main driving mechanisms for the movement of chloride ions, particularly those from de-icing salts or marine environments, before they reach the rebar depth and initiate corrosion (Dobrescu and Vasilescu, 2015). Accordingly, models for concrete involving diffusion typically incorporate Fick's first and second laws to describe steady-state and non-steady-state flow, as shown below (Rorschach et al., 1973; Delagrave et al., 1996):

$$J = -D\frac{dc}{dx}, \tag{2.1}$$

$$J = \frac{\partial c(x)}{\partial t} = -D\frac{\partial^2 c}{\partial x^2}, \tag{2.2}$$

where J is the total diffusion flux ($\mathrm{mol/m^2/s}$), c is the ionic concentration ($\mathrm{m^3/mol}$), x is the depth (m), dc/dx is concentration gradient ($\mathrm{mol/m^4}$) and D is the diffusivity ($\mathrm{m^2/s}$). Typically, concrete effective diffusivity is typically found on the order of $10^{-12}\mathrm{m^2/s}$. The second law is commonly used to analyse chloride profiles (concentration versus depth), where concentrations are often expressed as the percentage of chloride by mass of cement.

2.2.1.2 Absorption

Absorption in concrete is the process by which liquids, such as water, penetrate the pores of the material through capillary action. This transport of liquid in porous solids is driven by surface tension within the capillaries (Bentz et al., 1999). Absorption depends not only on the pore structure of the sample but also on its moisture condition, and it becomes particularly important in concrete exposed to freeze-thaw cycles or when harmful agents, such as chlorides, are dissolved in water that frequently contacts the structural member (Richardson, 2023). In

relevant studies, absorption in concrete is commonly determined using the following equation (Richardson, 2023):

$$V_p/A_p = S_p t^{0.5}, \quad (2.3)$$

where V_p is the volume of material absorbed in time t (mm^3), A_p is the cross-sectional area of sample in contact with water (mm^2), and S_p is sorptivity rate ($\mathrm{mm/s}^{0.5}$).

2.2.1.3 Permeation

Permeation in concrete is the movement of liquids or gases through its porous structure, driven by a pressure gradient. Its relevance in concrete service is generally limited to cases where the element is under a hydrostatic head (Basheer et al., 2001; Richardson, 2023). Pressure-induced flow is normally laminar rather than turbulent due to the presence of very small pores, *i.e.*, capillary pore with sizes on the order of 10^{-7}m (Zhang, 2013b). This process is commonly described using Darcy's law, as shown below (Richardson, 2023):

$$\frac{Q}{A} = -\frac{\kappa p g}{\eta}\frac{\Delta h}{L}, \quad (2.4)$$

where Q is flow rate (m^3/s), A is cross-sectional area of the sample, κ is intrinsic permeability (m^2) and is a property of porous materials independent of fluid properties, p is density of fluid ($\mathrm{kg/m}^3$), g is acceleration of gravity (9.81 m^2/s), η is the viscosity of fluid ($\mathrm{Ns/m}^2$), Δh is head loss across the sample (m), and L is thickness of sample (m).

2.2.2 Correlation of ionic transports with corrosion

The above transport processes, including diffusion of free chloride ions, absorption of chloride-enriched liquids, and permeation of salt solutions, are all related to chloride ingress into concrete. The transport mechanisms within concrete may act individually, simultaneously, or one may dominate at different times. The occurrence of these mechanisms generally depends on the internal conditions of the concrete. For example, in relatively dry capillary pores within concrete, absorption is the primary mechanism for chloride transport, whereas in fully saturated capillary pores, diffusion becomes the dominant mode (Basheer et al., 2001). Moreover, the transport mechanism can vary with location within the concrete. When chloride penetrates the near-surface layer through non-steady permeation, capillary action dominates along the larger

capillaries at the leading edge, and the subsequent diffusion of free ions results in a more uniform distribution of ions deeper within the cement paste (Basheer et al., 2001).

During chloride ingress through the pore space of concrete, chloride ions exist in two forms: free and bound. Only free chlorides can penetrate to the rebar depth and initiate corrosion. Bound chlorides are retained in two ways: (i) physical binding by adsorption on the surface of calcium–silicate–hydrate (C-S-H), and (ii) chemical binding, where chloride ions react to form Kuzel's salt ($Ca_4Al_2(OH)_{12}Cl(SO_4)_{0.5} \cdot 5H_2O$) or Friedel's salt ($Ca_2Al(OH)_6Cl \cdot 2H_2O$) at a low or high chloride concentration, respectively (Arya et al., 1990; Tang, 1996; Hirao et al., 2005). When the free chloride concentration at the rebar depth reaches a critical threshold, the passive layer protecting the steel breaks down, allowing water and oxygen to react with the steel and initiate electrochemical corrosion (Cai et al., 2020; Qu et al., 2021; Ma et al., 2023). This is followed by the propagation stage, where corrosion products, *e.g.*, rust, accumulate and occupy a volume 2-6 times greater than the original iron. The rust expansion induced stresses can weaken the steel-concrete bond (Duffó et al., 2004; Sun et al., 2024a). This eventually leads to concrete cracking, which accelerates chloride and oxygen ingress and further deteriorates the concrete (Khatami et al., 2021). The time-to-corrosion initiation, as well as the extent of corrosion after long-term propagation, is highly dependent on the rate of chloride ingress (Kiesse et al., 2020; Mahi and Ridoy, 2025), which is influenced by exposure conditions and the concrete microstructure . These factors will be reviewed in the following section.

2.2.3 Ionic transport under varying exposure conditions

In marine environments, concrete structures from low to high altitude are generally exposed to the seawater, tidal waves, or air, under which ionic transport leads to varying degrees of corrosion-induced deterioration (Cai et al., 2020). Accordingly, environmental conditions on concrete can be classified as submerged, tidal and splash, and atmospheric zones, where different transport processes may occur independently or together (Cai et al., 2020; Ma et al., 2023).

In the atmospheric zone, which is above the sea level, chloride ions in the air are transported by wind and deposited on the surface of marine concrete structures and then followed by airborne chloride penetration into the concrete through diffusion and absorption (Yang et al., 2017). Although the chloride concentration in this zone is relatively low and

presents a limited corrosion risk to concrete structures compared with zones frequently exposed to seawater (Cai et al., 2020), The transport process through concrete is influenced by complex and variable environmental conditions. For instance, higher wind speed, temperature, and relative humidity can accelerate chloride transport, as shown in Figure 2.1(a-c), which indicates increased chloride profiles with depth or higher diffusivity (Meira et al., 2006; Chen et al., 2013; Zhang et al., 2021b; Xu et al., 2024). Besides, carbonation is also a concern for corrosion in this zone. It is a chemical process in which atmospheric carbon dioxide diffuses and permeate into concrete and reacts with calcium compounds in the pore structure to form calcium carbonate (Basheer et al., 2001; Ma et al., 2023). This can release chlorides into the pore solution, increasing their concentration and accelerating their further penetration into the concrete (Basheer et al., 2001; Qu et al., 2021).

In the tidal and splash zones, where the most severe wetting-drying cycles occur, concrete structures are alternately immersed and exposed to normally result in the highest level of corrosion of reinforced concrete (Cai et al., 2014; Richardson, 2023). The number of wetting-drying cycles is a key factor influencing chloride transport, as shown in Figure 2.2(d), where higher chloride concentrations with depth can be observed with an increasing number of wetting-drying cycles (Gang et al., 2015). In the tidal zone, the rising and falling of tides maintain a relatively stable and sufficient chloride content, creating favourable conditions for chloride ingress and reinforcement corrosion (Cai et al., 2014; Cai, 2017). However, the situation is different in the splash zone. The surface concentration of chloride ions is higher than in the atmospheric zone but still lower than in the tidal zone. The chloride source in this zone is unstable due to the unpredictable number of cycles but accelerated chloride diffusion remains evident under the action of wetting-drying cycles (Costa and Appleton, 1999). Besides the chemical actions of seawater, concrete in the tidal and splash zones is also subjected to the physical actions of freezing-thawing cycles, which is the repeated process of water freezing and expanding within the pores to lead microcracks and facilitate deeper penetration of chloride ions (Yi et al., 2020).

In the submerged zone, marine concrete is completely immersed in seawater and is normally considered saturated (Qu et al., 2021). Chloride penetration into the concrete is primarily driven by diffusion, which is rarely influenced by wetting-drying cycles (Nilsson et al., 1997; Cai et al., 2020). Although seawater contains a high concentration of chloride ions, after a certain period of exposure the surface chloride concentration stabilises as it reaches

equilibrium with the surrounding seawater (Yu et al., 2002; Zhao et al., 2006). Compared with other exposure zones, corrosion-induced damage is relatively minor due to reduced environmental fluctuations, resulting in less significant chloride penetration (Luping, 2003; Lindvall, 2007; Luping, 2008).

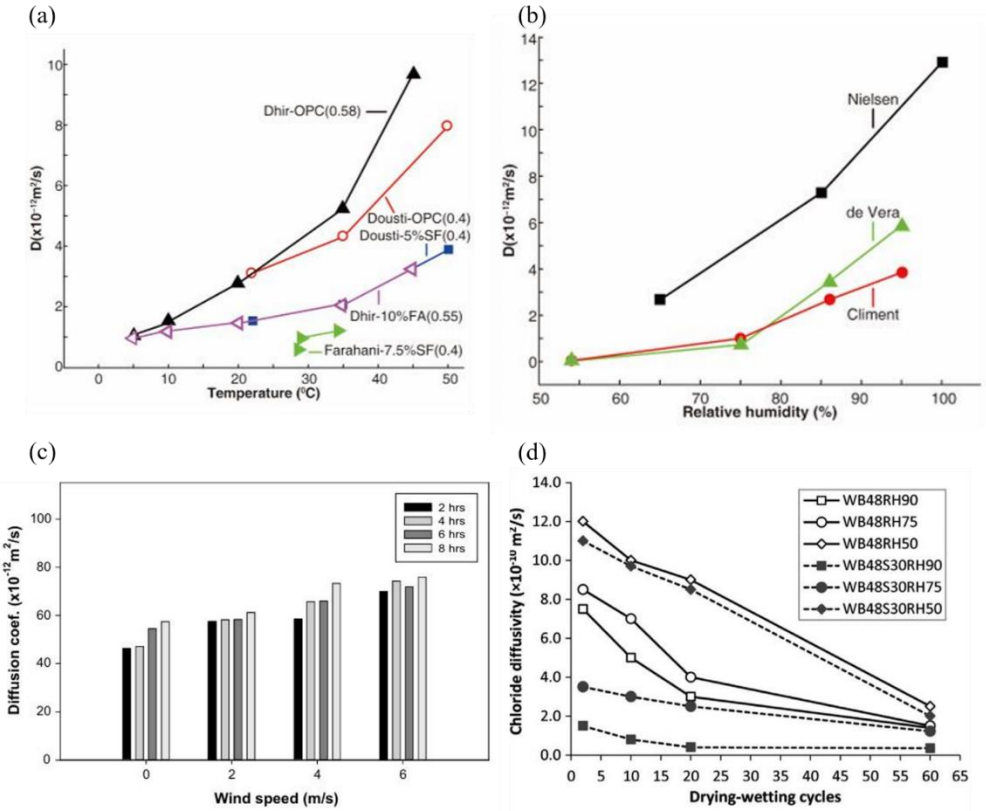

Figure 2.2. Factors influencing the diffusivity of mortar or concrete at the macroscale: (a) temperature (Zhang et al., 2021b), (b) relative humidity (Zhang et al., 2021b), (c) wind speed (Xu et al., 2024), and (d) drying (D)-wetting (W) cycles with D/W ratio of 1:5 and varying cycle numbers of 5,10,20,30,40 and 50 (Gang et al., 2015).

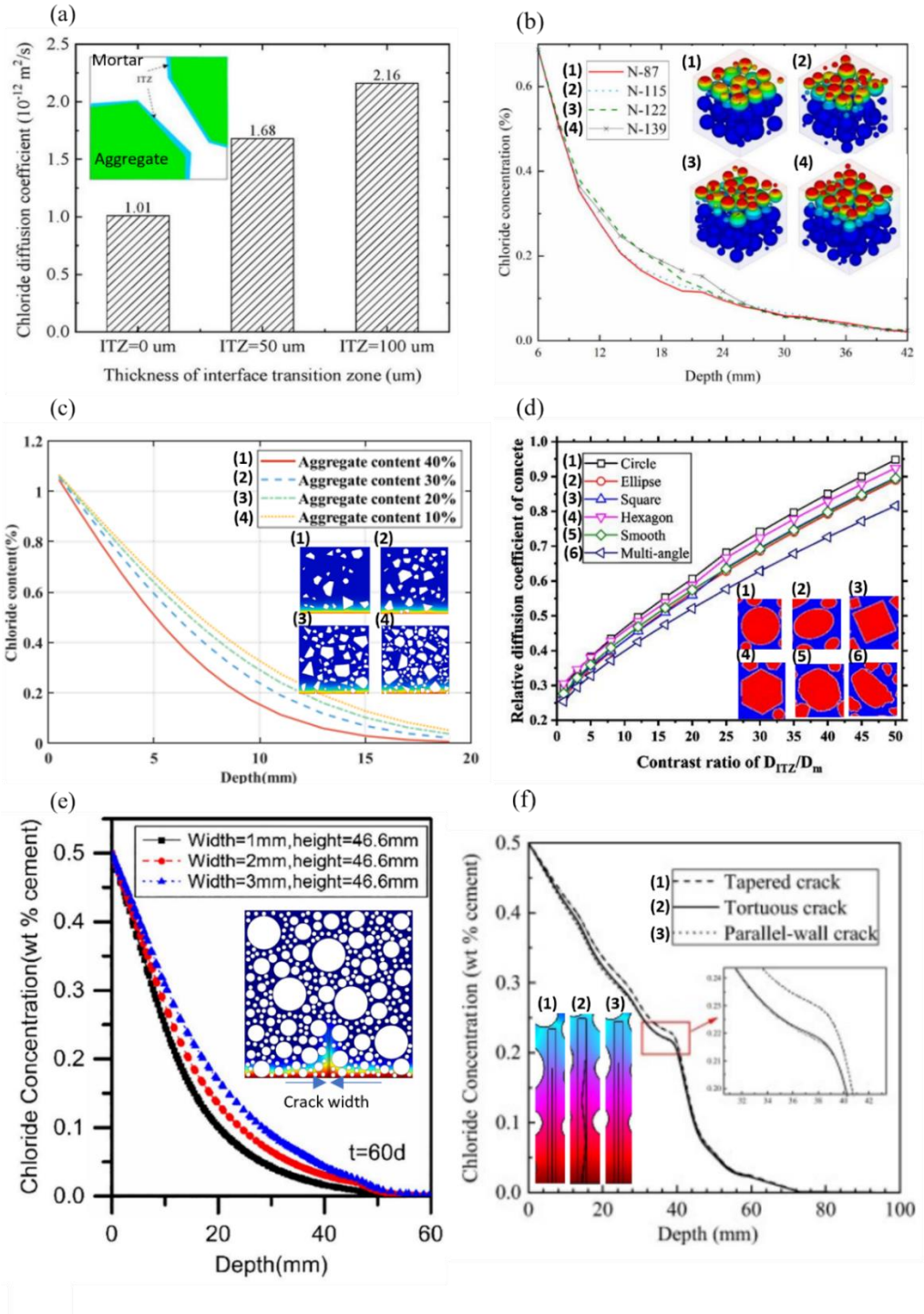

Figure 2.3. Factors influencing the diffusivity of mortar or concrete at the mesoscale: (a) ITZ thickness (Liu et al., 2022b), (b) aggregate size distribution (Sun et al., 2022), where N87 corresponds to 87 aggregates, N-115 corresponds to 115 aggregates, N-122 corresponds to 122 aggregates, N-139 corresponds to 139 aggregates, (c) aggregate solid fraction (Yang et al., 2025), (d) aggregate shape (Liu et al., 2018), (e) crack width (Xu et al., 2020) and (f) crack shape (Peng et al., 2019).

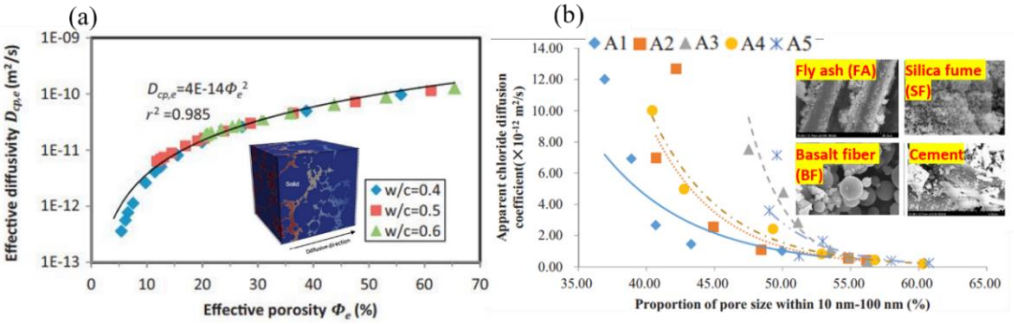

Figure 2.4. Factors influencing the diffusivity of cement paste at the microscale: (a) total porosity (Zhang et al., 2014b), (b) pore size distribution (Zhang et al., 2022), where A1-A5 represent cement paste itself, cement with BF, SF, FA, and a combination of SF and FA.

2.2.4 Influence of microstructure across length scales

As a concern to concrete corrosion, the transport behaviours have been given with specific focuses on the influence of morphology or physical properties of material constituents across varying length scales, and give more attention on chloride diffusivity than other properties, as it is main transport mechanism of chloride ingress relevant to corrosion. The relevant content will be reviewed in this section, varying from the nano- to mesoscale.

At the nanoscale, a considerable amount of research has been devoted to the development and exploration of nanoparticles, *e.g.*, nano-silica, nano-TiO_2, nano-alumina, to refine the microstructure for improving the durability performance of concrete (Safiuddin et al., 2014; Adesina, 2019, 2020; Udumulla et al., 2024). This will be further discussed in the following sections. When the scale increases to the microscale and insight into cement paste, research on chloride diffusivity primarily focuses on the influence of pore structure (Sakai, 2019; Zhang et al., 2022). Total porosity provides pathways for chloride ion transport; pore connectivity determines the extent to which pores are interconnected to form continuous channels; and tortuosity reflects the length and complexity of these transport routes (Hu and Du, 2013; Sakai, 2019; Liu et al., 2021; Tong et al., 2025). An increase in total porosity can lead to higher chloride diffusivity, as shown in Figure 2.4(a) (Zhang et al., 2014b), due to more diffuse paths, which could be highly interconnected (Chen et al., 2013). In addition, pore size (or size distribution), which also influences tortuosity, plays an important role in chloride ingress. As shown in Figure 2.4(b), for any types of cement pastes, a higher proportion of smaller pores or a finer pore size distribution creates a finer pore network, providing more tortuous diffusion

paths for chloride ions and effectively limiting chloride penetration (Zhang et al., 2022), and this is also supported by other studies (Hu and Du, 2013; Tong et al., 2025).

Some characteristics of pore structure vary with the degree of hydration (Moon et al., 2006), curing time (Zhang et al., 2018b), water-to-cement ratio (w/c ratio) (Zhang et al., 2014b), admixtures, *e.g.*, fly ash (Zhang et al., 2022), all of which are widely considered important for the performance of cement paste during concrete production. The cement paste, especially its hydration products, can physically or chemically bind chloride ions, reducing their concentration in the pore solution and thereby slowing diffusion (Moon et al., 2006). To capture this effect, the non-linear relationship between free and bound chloride concentrations, commonly described using Langmuir and Freundlich isotherms, has been used to account for the influence of chloride binding on diffusivity (Ishida et al., 2009; Shazali et al., 2012). As hydration progresses, capillary pores (10-100nm) gradually close and a more refined microstructure forms, causing chloride diffusion to occur mainly through smaller gel pores (<10 nm) and thereby lowering the ingress rate, particularly at later curing ages (Yang, 2006; Islam et al., 2016). Similar results can also be observed with a lower water-to-cement ratio, which densifies the pore structure (Chen and Wu, 2013), or with the addition of admixtures that consume calcium hydroxide through a pozzolanic reaction (Yu et al., 2017).

The influencing factors of cement paste associated with pore structure manifest in mortar or concrete as the length scale increases. At the mesoscale, concrete heterogeneity requires consideration of other material constituents such as ITZ and aggregates, whose effects on overall transport behaviour have received significant attention. The ITZ is a highly porous and less dense region between cement paste and fine aggregate, or between mortar and aggregate, and can accelerate the ingress of free chlorides into cement-based materials (Shane et al., 2000). The diffusivity of the ITZ is normally around 3 to 100 times higher than that of the bulk paste, with both values on the order of $10^{-12}\ \mathrm{m^2/s}$ (Chen and Wu, 2013). In addition, ITZ morphology, *e.g.*, thickness, is a significant factor in ionic transport. Increased ITZ diffusivity (Liu et al., 2018) and greater ITZ thickness (Liu et al., 2022b) can raise the overall chloride diffusivity of concrete, as shown in Figure 2.3 (a) and (d), respectively.

For fine or coarse aggregates, which are impermeable phases in mortar or concrete, an increasing solid fraction can lower concentration profile versus depth as shown in Figure 2.3(c) (Yang et al., 2025) and cause a decrease in the chloride diffusivity of cement-based materials (Delagrave et al., 1997; Jie et al., 2017). However, this is different for recycled aggregates,

which are widely considered as an option to replace natural aggregates. A higher replacement fraction can increase chloride diffusivity, as the new mortar and new ITZ surrounding recycled aggregates have higher diffusivity than natural ones (Wu and Xiao, 2018; Yu and Lin, 2020). Regardless of aggregate types, the effects of aggregate morphology, *i.e.*, size and shape on the chloride diffusivity of concrete have been investigated. For the aggregate size distribution, increasing the number of aggregates while maintaining a constant solid fraction tends to increase chloride diffusivity in concrete. This results in smoother chloride diffusion profiles, as shown in Figure 2.3(b), due to the increased surface area, which creates more interfacial transition zones (ITZ) that accelerate chloride transport (Sun et al., 2022). Early mesoscale studies considered circles in 2D or spheres in 3D to represent aggregates and ignored the effect of aggregate shape. This gap motivates relevant investigation. For instance, when the aspect ratio of elliptical particles increases beyond a certain value, the chloride diffusivity in concrete decreases (Zheng et al., 2012). Interestingly, when aggregates are represented by other shapes, such as ellipses and polygons, concrete exhibits similar chloride concentration profiles with depth, indicating an insignificant effect of aggregate shape on chloride diffusivity. However, in the numerical work of Liu et al. (2018), aggregates are represented by multi-angle shapes, resulting in lower concrete diffusivity, and this effect becomes more pronounced at higher ratio of diffusivity of ITZ to cement or mortar, as shown in Figure 2.3(d). Different conclusions have been reached regarding the effect of aggregate shapes, which requires further investigation in the future for verification.

All the studies mentioned above consider only the transport properties of concrete in the first stage of corrosion, where chloride ions migrate toward the rebar without causing damage or cracks. Once corrosion initiates and gradually induces expansive stress leading to cracking or spalling, chloride transport during this stage, *i.e.*, corrosion propagation can continue in cracked concrete. Generally, cracking dramatically increase the transport properties of concrete by creating preferential pathways for aggressive agents like water, ions and gases (Li and Li, 2019). This effect is more pronounced in cases with higher-density of cracks in mortar or concrete (Gérard and Marchand, 2000; Wang et al., 2016a). It is also strongly dependent on the characteristics of individual cracks and has received significant attention at the mesoscale. For instance, a larger crack width can lead to a higher concentration profile versus depth, as shown in Figure 2.3(e), indicating higher chloride diffusivity (Xu et al., 2020). The effect of crack shape on chloride transport is insignificant, as shown in Figure 2.3(f), where similar concentration profiles are observed in cases with tapered, tortuous, and parallel-wall cracks

(Peng et al., 2019). The appearance or propagation of cracks poses a serious threat to the durability of concrete. To address this issue, a basic understanding of the mechanical behaviours of concrete is needed, and the relevant content will be reviewed in the following.

2.3 Mechanical behaviours

As a load-bearing construction material, concrete is often subjected to complex conditions in marine environment, such as deep-water pressure, hurricanes, tsunamis, high or low temperature and etc. The corresponding mechanical responses of concrete to specific condition, which is simulated in experiment or numerical studies, have been investigated to provide valuable guidance for effective concrete design. Generally, concrete is considered as a quasi-brittle material, which has the rupture process governed by damage induced by interior stresses. However, analyses based solely on macroscopic behaviour or observations of failure patterns in earlier studies are often insufficient to fully understand the mechanical behaviour of concrete. A deeper understanding requires microscopic evidence, including the initiation and propagation of damage, as well as local stress and deformation. These aspects are strongly influenced by the material composition and the interactions among constituent phases across multiple length scales, which account for the inherent heterogeneity of concrete. To provide a comprehensive review of the mechanical behaviour of concrete, the following sections discuss some fundamental mechanisms, related mechanical properties under different exposure conditions, and the influence of concrete microstructure.

2.3.1 Mechanical mechanisms

Mechanical behaviours of concrete can be classified based on its responses to various types of loads, such as dead loads, live loads, concentrated loads, repeated loads, sustained loads. These include fracture or cracking, fatigue and creep, which will be reviewed in the following sections.

2.3.1.1 Fracture or cracking

The concrete fracture or cracking commonly reflects the stress-strain or force-displacement response under compressive (Yankelevsky, 2024), tensile (Gatuingt et al., 2013), or flexural loading (Megahed et al., 2023). This section does not account for repeated, sustained, and dynamic loading. It typically includes an initial elastic-to-plastic ascending branch, a peak

representing the material strength, and a descending or softening branch as damage occurs (Gatuingt et al., 2013; Megahed et al., 2023; Yankelevsky, 2024). The behaviour can be clearly distinguished as ductile in compression and brittle in tension (Özakça et al., 2016). It can be further classified based on concrete response to uniaxial, multiaxial, static and dynamic loadings. Under uniaxial loading, concrete is subjected to non-zero stress in one principal direction ($\sigma_1 \neq 0$) and zero stress in other two directions ($\sigma_2 = \sigma_3 = 0$), leading to the formation of microcracks due to stress concentrations, particularly at the interface between aggregates and mortar (Ren et al., 2008). As the load increases, localised zones of intense cracking develop, forming crack bands or shear planes inclined to the loading direction (often around 30 to 45°) in compression (Yankelevsky, 2024), while in tension, cracks align perpendicular to the loading direction and eventually link up to form a dominant fracture (Gatuingt et al., 2013). A substantial fundamental understanding of stress-strain behaviours has been gained through uniaxial tests. However, these tests do not accurately reflect the mechanical response of concrete structures under more complex stress states. Despite the challenges in replicating realistic stress conditions, notable progress has been made in studying the multiaxial behaviour of concrete.

Under multiaxial loading, concrete experience nonzero stresses in more than one principal direction, *i.e.*, $\sigma_1, \sigma_2, \sigma_3 \neq 0$. The interaction among these stress components significantly alters its strength and failure characteristics compared to uniaxial conditions. When lateral compressive confinement is applied, crack initiation is delayed as confinement suppresses tensile microcrack opening. The concrete exhibits enhanced compressive strength, as confining or lateral pressure restrains volumetric expansion and delays localisation (Chen et al., 2023b; Morger et al., 2024). Unmodified (Richart et al., 1928) and modified Mohr-Coulomb (Sovják et al., 2013), Newman (Newman, 1979), Leon-Pramono (Binici, 2005) criterions and others (Hsieh et al., 1982) are developed to predict the relation between concrete strength and confining pressure. The failure mechanism changes with the variation in the degree of multiaxial stress. For instances, under biaxial compression, *i.e.*, $\sigma_1 > \sigma_2 > \sigma_3 = 0$, the failure surface transitions from axial splitting to shear or compression-shear failure (Zhang et al., 2021a), whereas under triaxial compression, *i.e.*, $\sigma_1 > \sigma_2 > \sigma_3 > 0$, failure is governed by shear-dominated cracking along inclined planes; with increasing confinement, the stress-strain behaviour becomes more ductile, characterised by distributed microcracking rather than abrupt brittle fracture (Rong et al., 2018). Additionally, other multiaxial fracture mechanisms, although less frequently occurring, have also been investigated. These include biaxial tension-

compression, *i.e.,* $\sigma_1 < 0$ for tension, $\sigma_3 > 0$ for compression, $\sigma_3 = 0$, and triaxial tension-compression-compression, *i.e.*, $\sigma_1 < 0$ for tension, $\sigma_2, \sigma_3 < 0$, where the tensile stress tends to initiate axial splitting cracks perpendicular to the tensile direction (Shang et al., 2014b).

2.3.1.2 Fatigue

Concrete fatigue is gradual weakening and damage of concrete from repeated and cyclical loads that are less than the static strength of material (Kachkouch et al., 2022). In marine environments, it typically occurs due to the wind and vehicle transportation. Under loading, stress concentrations around small flaws or discontinuities can cause localised stresses to become very high (Naik et al., 1993; Riyar and Bhowmik, 2023). Cracks often initiate in these areas due to the progressive deterioration of the bond between the coarse aggregate and the matrix, and continue to propagate even when the applied stresses are below the elastic limit. As the intact portion of the structure becomes unable to sustain the applied load due to the reduced stress-resisting area, rapid crack growth occurs, leading to sudden failure (Naik et al., 1993). Depending on the failure characteristics, concrete fatigue can be classified as low-cycle or high-cycle fatigue. Low-cycle fatigue involves the application of high stress levels over a relatively low number of cycles, while high-cycle fatigue corresponds to a large number of cycles at lower stress levels (Naik et al., 1993). In a marine environment, high-cycle fatigue damage induced by increased transportation demands or wind should be given careful consideration throughout the service life of reinforced concrete structures (Fang et al., 2023).

2.3.1.3 Time-dependent behaviour

Concrete creep is a time-dependent phenomenon in which concrete undergoes permanent deformation over time under a sustained and constant load less than yield stress of material, and eventually results in a change in the size and shape of the material after long-term exposure (Neville, 1995; Hassan et al., 2023; Hong et al., 2023). Creep primarily occurs in the cement paste, as the progressive increase in strain (also known as plastic flow) is caused by the slow movement and re-arrangement of calcium silicate hydrate (C-S-H) within the paste. The aggregate phase typically resists creep (Neville, 1995). There are three stages of creep after normal strain under loading: primary, secondary, and tertiary stages (Ahmed and Wahab, 2024; Sattar et al., 2024). During the primary stage, strain hardening causes an initially high creep rate to decrease over time. The second stage is reached when a balance between strain

hardening and softening processes results in a nearly constant creep rate, during which significant deformation occurs. In the tertiary stage, the onset of internal or external damage processes leads to a reduction in load-bearing resistance or a significant increase in the net section stress. This causes necking and the formation of cavities, and the creep rate begins to increase, eventually leading to rupture. Concrete creep occurs over a short period during the primary stage, but it is mostly governed by the secondary stage throughout its service life. The tertiary stage is usually not considered, as it indicates imminent failure (Ahmed and Wahab, 2024; Sattar et al., 2024).

2.3.1.4 Dynamic behaviour

The dynamic behaviour of concrete occurs under rapid loading from events such as ship impacts, explosions, or tsunamis, where the stress-strain behaviour is characterised by strain-rate sensitivity. In conventional tests, static and dynamic fracture of concrete are primarily distinguished by strain rate. Static fracture occurs under a slowly applied load, with a strain rate of approximately 10^{-6} to 10^{-4} s^{-1} in the direction of the principal stress, resulting in low apparent strength (Mosig and Curbach, 2020). This leads to gradual crack propagation and ultimately produces a smoother fracture surface with few or no bifurcations (Guo et al., 2023b). In contrast, at higher strain rate, the dynamic strength of concrete is considerably higher than its static strength, a property quantified by the dynamic increase factor (DIF), which is the ratio of dynamic to static strength, as shown in Figure 2.5(b). The relation between DIF and strain rate typically exhibits distinct low and high slopes in the regions of low strain rate, *i.e.*, around 10^{-3} to 10 s^{-1}, and high strain rate, *i.e.*, around > 10 s^{-1}, respectively (Fan et al., 2023). In the high strain-rate region, inertial forces and stress wave propagation play significant roles (Ožbolt et al., 2011; Fan et al., 2023). A running crack may initiate and propagate rapidly, often producing a fracture surface with bifurcations (Ožbolt et al., 2011; Kantar et al., 2017). The failure pattern can shift from a single crack to more complex branching cracks compared to static fracture (Sun et al., 2021b). Dynamic fracture toughness is generally higher than static fracture toughness, and this ratio increases with the strain rate (Shi and Chen, 2018; Liu et al., 2023).

2.3.2 Mechanical properties under varying exposure conditions

The mechanical properties of concrete, which is reflected in its load-displacement response, either in specific regions or throughout the entire process, have been extensively studied in the scientific community to ensure structural stability, with strength receiving more attention than other properties. However, these properties can vary depending on several exposure conditions, including external stress states and environmental factors, *e.g.*, temperature, humidity, and chemical exposure, all of which will be reviewed in the following sections.

Typically, normal-strength concrete has an elastic modulus ranging from approximately 30 to 50 GPa (Sun and Fanourakis, 2022) and a 28-day compressive strength of about 30 to 45 MPa (Zhou et al., 2015). These values are commonly obtained from uniaxial static tests and represent the basic performance required for practical engineering applications. However, both properties are known to vary under different stress conditions (Zhou et al., 2015; Sun and Fanourakis, 2022). For instance, under split tensile or flexural loading, concrete generally exhibits tensile strengths of around 2-5 MPa, which are typically proportional to its compressive strength (El-Maaty, 2016), as shown in Figure 2.5(a). Higher strengths are observed under confined stress states, *e.g.*, biaxial or triaxial, and at increased strain rates, as illustrated by the relationship between the dynamic increase factor (DIF) and strain rate under uniaxial and triaxial loading in Figure 2.5(b) (Chen et al., 2023b).

The marine environment is characterised by various fluctuating conditions, to which the mechanical properties of concrete respond in different ways. High temperatures can reduce the compressive strength of concrete, as shown in Figure 2.5(c), due to dehydration and the decomposition of calcium hydroxide, which weaken the internal structure (Shoukry et al., 2011). A similar reduction is observed in the elastic modulus. The curing process of concrete is also sensitive to moisture content, and increased moisture can reduce both the strength and elastic modulus of concrete (Hou et al., 2012; Yang et al., 2022b). Under freeze-thaw (FT) cycles, a higher number of cycles leads to decreased concrete strength, as shown in Figure 2.5(d) (Shang et al., 2014a), due to expansion pressure from freezing water and the formation and propagation of microcracks. Chloride-induced corrosion also threatens the mechanical properties of concrete; after corrosion initiation, rust expansion generates high internal stresses that result in microcracking (Taheri-Shakib and Al-Mayah, 2023). In addition to these external factors, mechanical properties of concrete are also highly dependent on the property and

morphology of material constituents across different length scales, which will be reviewed in the following section.

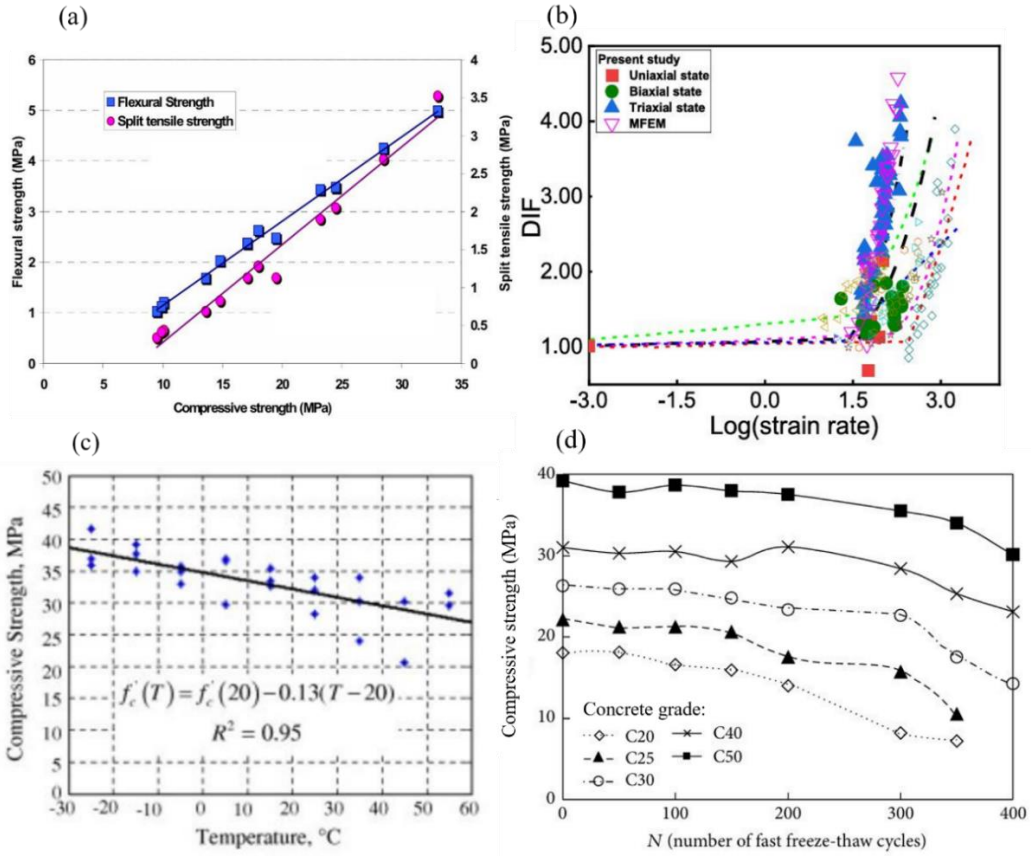

Figure 2.5. Factors influencing concrete strength at the macroscale: (a) compressive, tensile, and flexural stress conditions (El-Maaty, 2016), (b) dynamic and confined stress conditions (Chen et al., 2023b), (c) temperature effects (Shoukry et al., 2011), and (d) the number of freeze–thaw cycles (Shang et al., 2014a).

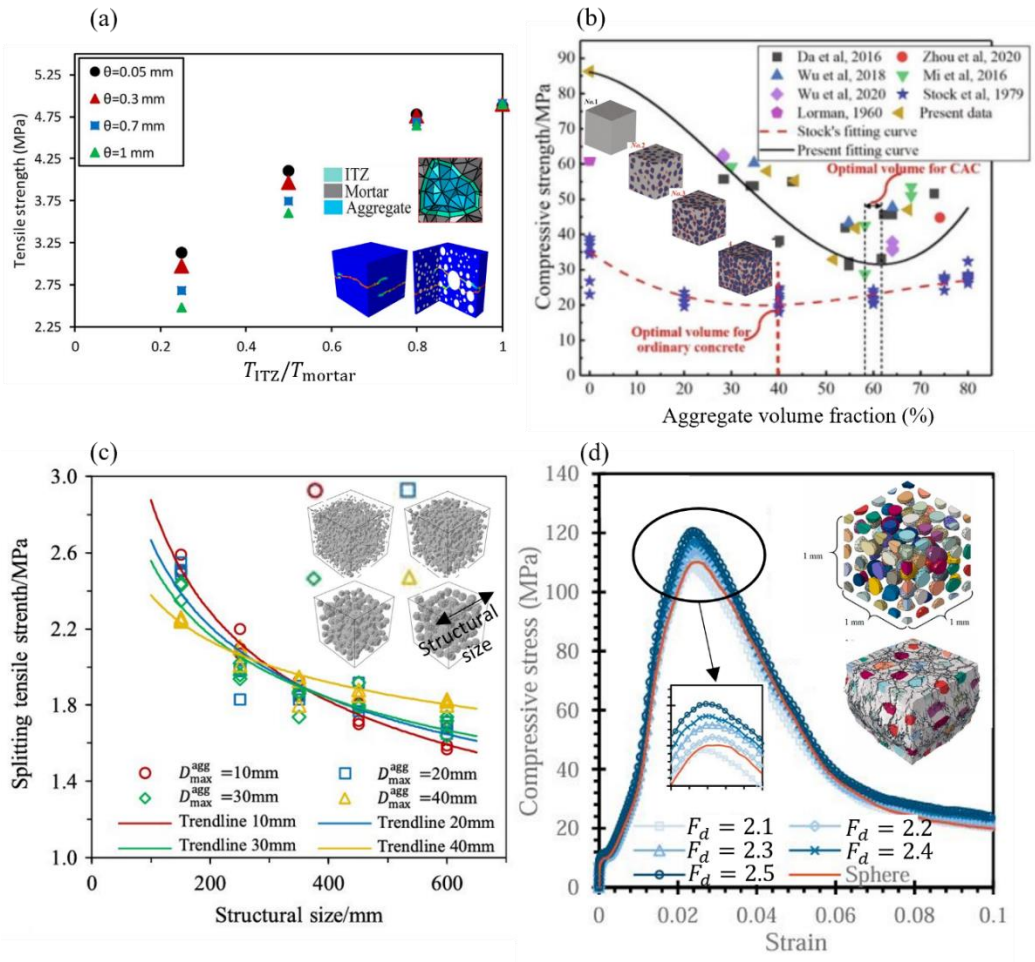

Figure 2.6. Factors influencing concrete strength at the mesoscale: (a) ITZ thickness (θ) and ITZ/mortar strength ratio ($T_{\mathrm{ITZ}}/T_{\mathrm{mortar}}$) (Maleki et al., 2020), (b) aggregate volume fraction (Wu et al., 2021b), (c) aggregate size distribution with focus on maximum aggregate size $D_{\mathrm{max}}^{\mathrm{agg}}$ (Jin et al., 2020a), and (d) aggregate shape characterised with fractal dimension F_d (Wei et al., 2020b).

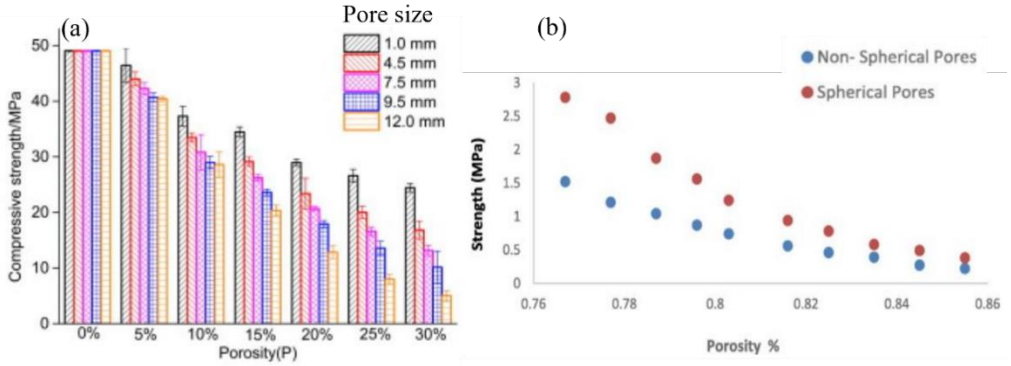

Figure 2.7. Factors influencing concrete strength at the mesoscale: (a) porosity and pore size (Zhang et al., 2020a) and (b) pore shape (Ghahremani et al., 2023).

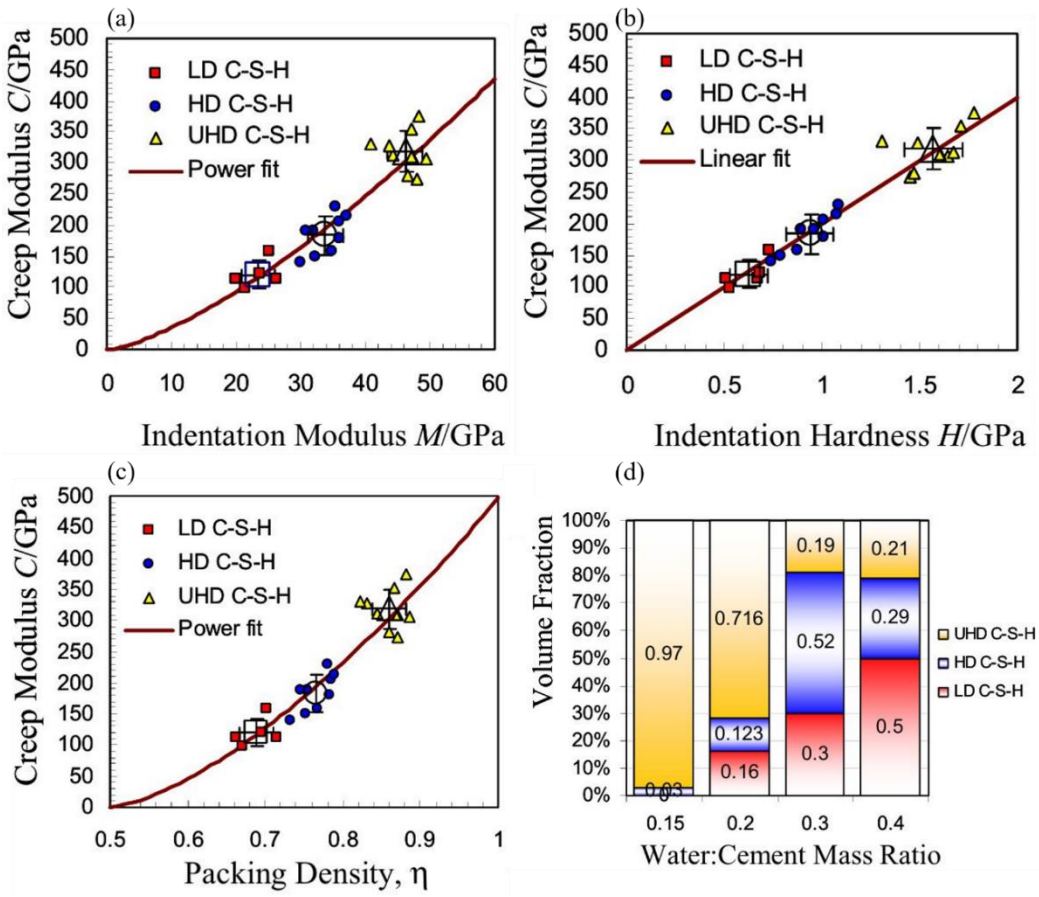

Figure 2.8. Factors influencing concrete creep at the nanoscale with a particular focus on C-S-H: relationship between creep modulus and (a) indentation modulus (M), (b) indentation hardness, and (c) packing density of C-S-H; (d) volume fraction of C-S-H with different packing densities, *e.g.*, low-density (LD), high-density (HD), and ultra-high-density (UHD), under varying water-to-cement (mass) ratios (Vandamme and Ulm, 2009).

2.3.3 Influence of microstructure on mechanical properties

The influence of concrete heterogeneity on its mechanical properties has been extensively investigated in numerous studies. However, it is not possible to cover all the properties of concrete in this section, with greater emphasis placed on concrete strength than on other properties. Representative results are presented to highlight the influence of the morphology and physical properties of its constituents from the nano- to meso-scale.

At the nanoscale, significant progress has been made in the work of Vandamme and Ulm, which mainly focuses on logarithmic creep as an intrinsic property of calcium-silicate-hydrate (C-S-H), investigated using nanoindentation (Vandamme and Ulm, 2008; Vandamme and Ulm, 2009; Vandamme and Ulm, 2013). C-S-H exists in forms with different packing densities, *e.g.*,

low-density (LD), high-density (HD), ultra-high-density (UHD), all of which exhibit intrinsic logarithmic creep depending on the packing of 5 nm-sized particles (Vandamme and Ulm, 2009). For the composition of cement paste, lowering the water-to-cement (w/c) ratio reduces the volume of hydration products, while a higher w/c ratio increases overall gel porosity. This variation arises from changes in the proportions of LD, HD, and UHD C-S-H, which differ in packing density. As shown in Figure 2.8(d), reducing the w/c ratio increases the volume fraction of UHD C-S-H. The rate of logarithmic creep is found to follow a unique scaling with indentation modulus, indentation hardness, and packing density (Vandamme and Ulm, 2013), as shown in Figure 2.8(a-c), respectively. The contact creep modulus is introduced to assess the rate of logarithmic creep, with larger indicating a lower rate of logarithmic creep. These scaling laws are found to be independent of processing, mix proportion, indenter geometry, and load history (Vandamme and Ulm, 2013). In other nanoscale-related studies, various nanomaterials have been incorporated into concrete to maintain or enhance its mechanical performance. Further details are provided in the following section.

At the microscale, among all these factors, significant attention has been paid to the influence of pore structure in the cement paste. When a load is applied, stress becomes concentrated at the edges of pores, which can cause the local stress to exceed the concrete strength and initiate cracking (Li et al., 2022b). Cracks tend to propagate more easily through networks of interconnected pores (Zhu et al., 2025). These effects occur not only in concrete fracture but also in fatigue. In particular, larger pores weaken the structure, making it more susceptible to crack initiation and propagation (Chandrappa and Biligiri, 2019; Shi and Zhao, 2022). For pore size distribution, a high number of small pores can lead to more surface cracks, while larger pores are more likely to connect, forming extensive crack networks (Zhu et al., 2025). The influence of pore structure on concrete cracking has already been considered in some numerical models, which treat the cement paste or mortar as an inhomogeneous phase accounting for the spatial distribution of pores (Wang et al., 2016b).

With respect to related mechanical properties, as shown in Figure 2.7(a), increasing porosity and pore size reduces the strength of concrete (Zhang et al., 2020a), due to the decrease in load-bearing area. The effects of pore size become even more pronounced at higher porosity. Similar trends also happen to the elastic modulus (Zhu et al., 2025). Pore shape can also influence mechanical properties. As illustrated in Figure 2.7(b), non-spherical pores result in significantly lower compressive strength compared to spherical pores, although this effect

becomes less significant at higher porosities (Ghahremani et al., 2023). Liu et al. (2022a) report similar findings, noting that stress concentrations tend to occur along irregular pore edges, making damage more likely when pores are not perfectly round.

The factors related to cement paste have been widely investigated experimentally, including curing time (Cakir, 2022), temperature (Kim et al., 1998), degree of hydration (De Schutter and Taerwe, 1996), water-to-cement ratio (Popovics and Ujhelyi, 2008), and supplementary cementitious material (SCM), *e.g.*, chemical admixture, *e.g.*, superplasticizers (Nagrockiene et al., 2013), silica fume (Mazloom et al., 2004), fly ash (Nath and Sarker, 2011). These factors can refine the microstructure by modifying and densifying the pore structure, or by altering the chemical composition of the cement paste, in order to enhance or maintain its mechanical performance. The influence of these factors is also reflected in mortar and concrete as the length scales of interest increase. Depending on compressive strength, which is influenced by whether SCMs are used, mortar (or concrete) can be classified as normal-strength or high-strength.

At the mesoscale, other material phases, *e.g.*, the ITZ and aggregates, have also received considerable attention for their influence on the mechanical performance of concrete. The ITZ exhibits mechanical properties closely related to its porosity, which can be affected by the properties or morphology of the cement paste, mortar, or aggregates. It is a susceptible region for concrete fracture, being the weakest among all material phases (Chen et al., 2022a). Although the ITZ is challenging to represent or access in numerical and experimental studies, some progress has been made in understanding its role in concrete fracture under various stress conditions (Maleki et al., 2020; Zhou et al., 2021b; Korouzhdeh et al., 2022), where the influence of ITZ properties or morphology varies. As a representative result as shown in Figure 2.6(a), an increase in ITZ strength can lead to higher concrete fracture strength. When the ITZ/mortar strength ratio increases, the inverse relationship between ITZ thickness and concrete strength becomes more pronounced (Maleki et al., 2020). Effects of the ITZ have also been studied in concrete creep. As ITZ thickness increases or its elastic modulus decreases, the effective elastic modulus of concrete decreases, resulting in higher effective creep (Song et al., 2024).

In ordinary concrete, natural fine or coarse aggregates are generally the hardest material phase. However, both recycled aggregates (RAs) (He and Zhang, 2014; Silva et al., 2015) and coral aggregates (Wu et al., 2021b; Zhou et al., 2021a) are typically weaker due to factors such

as adhered mortar on RAs and the low strength and high porosity of coral. Concrete becomes weaker in terms of strength (He and Zhang, 2014; Silva et al., 2015) and elastic modulus (Li et al., 2024) as the replacement proportion of these aggregates increases. Recycled aggregate concrete exhibits increased creep due to the porous nature of the adhered mortar on the aggregate, which results in a weaker aggregate-paste bond (Akono et al., 2021). It can also reduce fatigue life, residual strength, and residual stiffness (Peng et al., 2018). In addition to material properties, other aggregate-related factors, such as solid fraction and morphology, *i.e.*, size and shape, have also been widely studied.

For ordinary mortar or concrete, increasing solid fraction of natural aggregate can enhance elastic modulus of concrete (Stock et al., 1979). However, it becomes different to concrete strength (Stock et al., 1979). According to the results of Wu et al. (2021b), as shown in Figure 2.6(b), the compressive strength of concrete gradually decreases as the aggregate solid fraction increases from around 0% to 40%, since the aggregates are mostly separated from each other and the increased contact area between the cement paste or mortar and the aggregate weakens the strength. After reaching its minimum at a solid fraction of about 40-50%, the strength rebounds at an increasing solid fraction, as the aggregates come into contact and the load can be transferred between them, thereby increasing the bearing capacity. Concrete with coral aggregates exhibits a similar influence of solid fraction, but the optimal solid fraction corresponding to the lowest compressive strength is higher.

Under the same solid fraction of aggregates, the maximum aggregate size is typically used as an indicator of the aggregate size distribution. Smaller maximum sizes lead to higher concrete strength at small structural (or specimen) length, whereas the effect of aggregate size is reversed at larger structural lengths (Jin et al., 2020a), as shown in Figure 2.6(c). This contrasting influence of aggregate size is also observed in the elastic modulus of concrete at w/c ratios of 0.3 and 0.4 (Wang et al., 2024d). For aggregate shape, experiments have shown that crushed aggregates with more irregular shapes lead to higher concrete strength compared to rounded aggregates (Rocco and Elices, 2009). This effect has also been further examined in numerical studies. In the work of Wei et al. (2020b), irregular aggregates, with greater surface roughness characterized by a higher fractal dimension F_d, induce higher stress concentrations than spherical aggregates and enhance the concrete strength. This, in turn, promotes greater fracture propagation into the aggregates once the ITZ begins to fracture, thereby enhancing the overall concrete strength, as shown in Figure 2.6(d).

Most studies have focused on single or simplified stress conditions to highlight the influence of microstructural factors at different scales on concrete performance. However, such conditions are relatively rare in practical engineering. Increasing efforts have been made to incorporate more realistic stress environments, such as multiaxial loading (Naderi et al., 2021), dynamic loading (Jin et al., 2019; Fan et al., 2023), or even a combination of both (Chandrabhan and Kumar, 2024). Under these conditions, the influence of microstructural factors becomes either more pronounced or remains largely consistent with that found under reference simple loading. In addition, interactions may exist between material constituents. For instance, the effect of one constituent on the physical properties of concrete may be amplified or reduced in the presence of another, highlighting the need to consider the combined effects of multiple constituents (Maleki et al., 2020). These studies have yielded significant insights into the influence of complex material heterogeneity in concrete under realistic stress conditions. However, further research is still needed to expand and deepen this field.

2.4 Managements of concrete performance

2.4.1 Monitoring

To date, techniques for monitoring the transport and mechanical behaviours of concrete have been well developed to ensure structural longevity. Concrete corrosion is typically assessed by measuring parameters such as chloride ion concentration, concrete pH, reinforcement potential, concrete resistivity, and corrosion current. These measurements help either predict corrosion initiation or evaluate ongoing corrosion activity (Hu et al., 2022; Ali et al., 2024; Sai et al., 2024; He, 2025). For instance, embedded sensors integrated into the concrete during construction can continuously monitor parameters such as chloride concentration and pH levels (Ismail et al., 2011). For mechanical performance, other types of embedded sensors, such as fiber Bragg grating (FBG) sensors, have been widely used to monitor strain changes (Davis et al., 1997). Stiffness and internal damage can be assessed using the ultrasonic pulse velocity (UPV) method (Roobankumar and SenthilPandian, 2025).

Besides these techniques, which are mainly used for a single aspect of concrete, some methods can monitor both the transport and mechanical aspects. For example, acoustic emission (AE) can detect internal damage caused by corrosion or stress in real time by capturing high-frequency elastic waves generated by cracking and material degradation

(Papaelias et al., 2019; Yang, 2020). More advanced techniques, such as X-ray computed tomography (XCT) (Han et al., 2013) and ground-penetrating radar (GPR) (Wang et al., 2014), are used for detailed structural analysis, providing highly detailed information about the internal condition of structures, *e.g.*, voids, cracks, to support monitoring.

2.4.2 Protection

Based on the understanding of the influence of concrete heterogeneity, significant progress in protection of concrete structure has been made through enhancing durability and mechanical performance of concrete. This has been extensively implemented in concrete mix design. Reducing the water-to-binder ratio (Chen and Wu, 2013; Takiya et al., 2015) and incorporating supplementary cementitious materials (SCMs), *e.g.*, silica fume, fly ash, ground granulated blast-furnace slag, and metakaolin (Skibsted and Snellings, 2019; Fantilli and Jóźwiak-Niedźwiedzka, 2021), can densify the pore structure, thereby enhancing the concrete resistivity to corrosion and its fracture strength. As an alternative protection strategy, the addition of corrosion inhibitors, *e.g.*, calcium nitrite (CNI) and combinations of amines and esters, is considered an effective method to increase the chloride threshold, thereby reducing the corrosion rate through chemical buffering. However, this approach does not directly enhance the mechanical performance of concrete but rather prevents its degradation caused by corrosion (Al-Amoudi et al., 2003; Abosrra et al., 2011; Elsener and Angst, 2016).

Protection of concrete performance can also be achieved by incorporation with nanoparticles, *e.g.*, nano-silica, nano-TiO_2, nano-alumina, which refine the microstructure by densifying the pore structure in several ways (Land and Stephan, 2015; Reches, 2018; Laím et al., 2020). Nanoparticles act as nucleation sites for cement hydration products (C-S-H), accelerating early hydration, and producing more C-S-H gel faster (Land and Stephan, 2015); Nanoparticles are extremely fine (1-100 nm), much smaller than cement particles, can fill micro-voids and capillary pores in the cement matrix (Reches, 2018); Nanoparticles, *e.g.*, nano-silica, react with calcium hydroxide ($Ca(OH)_2$) to form additional C-S-H gel (Laím et al., 2020). Other nanotechnologies, such as bacterial-agent-based concrete, have been found to heal microcracks and block the ingress of harmful ions. However, the practical application of such techniques still requires further development in the future (Ahmad et al., 2025).

Protective strategies have been developed not only for the internal structure of concrete but also externally through surface treatments, which can be classified into three groups: pore

liners (Basheer and Cleland, 2006; Rahman et al., 2013), pore blockers (Tibbetts et al., 2021; El-Reedy, 2022), and coatings (Almusallam et al., 2003; Shi et al., 2012; Yuan and Li, 2015). These methods can improve the durability, the mechanical performance, or both aspects of concrete. The pore liner is normally made of silanes and siloxanes, and penetrates the concrete pores and capillaries, forming a water-repellent (hydrophobic) but vapor-permeable barrier that protects against water and chloride ingress without sealing the surface or affecting its appearance (Basheer and Cleland, 2006; Rahman et al., 2013). Pore blockers react with internal concrete components to form insoluble products, filling and sealing pores, which can improve strength and reduce permeability (Tibbetts et al., 2021; El-Reedy, 2022). Coatings are used to shield the structure from chlorides and prevent corrosion from reaching the concrete reinforcement. Epoxy resins, acrylic, and polyurethane have been widely used as common coating materials to form a physical film on the concrete surface, typically 300μm to 1mm thick. Specific surface treatments or materials are chosen based on application needs, depending on exposure conditions, *e.g.*, submerged, tidal-splash, atmospheric zones, and types of aggressive chemicals, *e.g.*, carbon dioxide or chloride. Their effect on mechanical properties is primarily related to adhesion, and how they can prevent surface cracking, particularly exposed to temperature (Almusallam et al., 2003; Shi et al., 2012; Yuan and Li, 2015).

2.4.3 Maintenance

Deterioration of concrete, *e.g.*, cracking, is a major concern for maintenance. Relevant repair strategies should be appropriately considered to ensure the durability and mechanical performance of concrete throughout its service life, such as patching (Eldho et al., 2016), structural strengthening (Röös and Uddmyr, 2017), and crack repair (El-Hawary et al., 2000). The first two mainly focus on wide or severely deteriorated areas, while the third addresses small crack regions. Patching involves removing all loose and damaged concrete to expose a sound surface, after which the area is repaired with a marine-grade mortar. This method is suitable for localised issues, particularly concrete spalling (Eldho et al., 2016). Fiber-reinforced polymer (FRP) jackets are widely used for structural strengthening. Damaged piles can be encapsulated in jackets made of fiberglass or carbon fibre to restore their structural capacity (Röös and Uddmyr, 2017).

Epoxy resin has been widely used as a crack repair method. It can fill cracks and voids and is effective for non-moving cracks, providing structural bonding that may exceed the

strength of the original concrete. In addition, the resin forms a polymer plug that seals the cracks, preventing the ingress of water, chlorides, carbon dioxide, sulphates, and other aggressive agents (El-Hawary et al., 2000). Repaired structures are usually subjected again to the same environmental conditions that initially caused their deterioration (El-Hawary et al., 2000). Therefore, to some extent, epoxy used for concrete is affected by environmental factors. For instance, extreme heat can soften the epoxy, while cold temperatures can prevent it from curing properly (Czaderski et al., 2012; Yuxin et al., 2023), and moisture can interfere with adhesion (Zhou et al., 2017a). In marine environments, these factors become challenges for applying epoxy resin under appropriate conditions or ensuring its proper performance.

Besides the concrete itself, steel rebar requires special care, as it is the first to corrode due to chloride transport, producing rust that compromises the performance of reinforced structures. Electrochemical techniques have been developed to reverse the corrosion process and protect steel reinforcement, such as electrochemical chloride extraction (ECE) (Fajardo et al., 2006; Jin et al., 2018) and cathodic protection (CP) (Wilson et al., 2013; Byrne et al., 2016). In ECE, a temporary electrical field drives negatively charged chloride ions out of the concrete toward an external anode. This process also increases the concrete alkalinity around the rebar, re-establishing its protective layer (Fajardo et al., 2006; Jin et al., 2018). CP is a rehabilitation technique that provides a long-term solution for corrosion in salt-contaminated structures. It works by applying a protective current, which is generated either by an adjustable permanent power source with long-lasting inert anodes, or through passive self-sacrificing zinc/aluminium anodes that gradually deplete to maintain the rebar in a non-corroding state (Wilson et al., 2013; Byrne et al., 2016).

2.5 Research methods

To investigate the transport and mechanical responses of concrete, previous studies have employed analytical methods, experimental testing, and numerical modelling to examine the underlying mechanisms across different length scales and loadings. These approaches are reviewed in this section.

2.5.1 Analytical approaches

The analytical solution is a fast approach to predict the behaviour of concrete in various aspects. For instance, Fick's law has been used to capture the diffusion profile, *i.e.*, ionic

concentration versus depth inside the material, where the diffusion coefficient can vary to account for the influence of factors such as temperature and humidity, based on experimental or numerical data diffusivity (Xu et al., 2024). In addition, other physical models for sorption and permeation can be used to estimate their respective conductivities (Richardson, 2023). For mechanical behaviour, the standard stress-strain response under various stress conditions can be defined according to established design codes, such as the Model Code 2010 (MC2010) and the Chinese Code for Design of Concrete Structures (GB5010). In addition, various semi-empirical or empirical relations have been developed to estimate the strength under confinement (Candappa et al., 1999) and dynamic loading (Fan et al., 2023). However, these early solutions treat concrete as a homogeneous material, when predicting macroscopic behaviour.

Approximations of the effective properties of concrete, *e.g.*, conductivity and elastic modulus, are derived using homogenisation techniques that treat cement paste or concrete as a two-phase material. The earliest one is the Wiener bounds (Van Eekelen, 1973), which are based on simple one-dimensional parallel and series configuration assumptions of the two constituents and are valid for arbitrary microstructures, whether isotropic or anisotropic. However, these bounds are often relatively wide to be of practical predictive value (Pabst and Gregorová, 2014). In contrast, using a variational principle, Hashin and Shtrikman (Hashin and Shtrikman, 1962, 1963) derive possible upper and lower bounds to refine the range of the effective properties of isotropic two-phase systems, relying on the volume fraction and material properties of each phase. Besides, more rigorous solutions have also been developed, such as the Maxwell approximation (MA) (Markel, 2016), effective medium approximation (EMA) (Choy, 2015). However, most of original solutions are limited to relatively simple cementitious systems. Later developments have extended some of them to three-phase or multiphase cementitious materials or have introduced semi-analytical solutions based on reasonable assumptions, as well as experimental or numerical data, to account for more complex microscale factors such as ITZ (Sun et al., 2011), pores (Zhou et al., 2024b), particle size (Stoyanov et al., 2001) and shape (Zhou et al., 2018).

2.5.2 Experimental approaches

Conventional experiments at the early stage, such as rapid diffusion and standard mechanical test, are mainly developed to measure the macroscopic response of concrete.

However, these became inadequate for exploring underlying microscopic evidence. Later, advanced non-destructive testing techniques, such as micro- or X-ray Computed Tomography (CT) (Marzec and Tejchman, 2019), Scanning Electron Microscopy (SEM) (Akçaoğlu et al., 2005), Digital Volume Correlation (DVC) (Hong et al., 2020), Mercury Intrusion Porosimetry (MIP) (Han et al., 2022), X-ray Diffraction (XRD) (Uzbas and Aydin, 2020), and others (Zhao et al., 2018), have been developed and widely used to evaluate the microstructure of cementitious materials in studies on durability or mechanical behaviours based on the information provided by testing equipment.

For ion-related transport behaviours, X-ray CT in the case of chloride-induced corrosion of reinforced concrete has been applied to quantitatively characterise corrosion pits at the concrete-steel interface, enabling investigation and monitoring of the corrosion initiation stage (Van Steen et al., 2019). As an example of other techniques, in the work of Ranger et al. (2025), to evaluate chloride binding during the diffusion process, the microstructure of cement paste specimens was studied using MIP, which can provide information on porosity and pore size distribution to determine the relationship between the occurrence and magnitude of microstructural changes and the binder type. Also, the chemical composition of the cement paste was investigated based on the ionic ratios of Si/Ca, Al/Ca, and Al/Si obtained from XRD, to quantify the amount of chloride binding as a function of binder type.

To interpret the evolution of the internal structure of concrete under various stress conditions, in addition to those used for studying concrete durability, other techniques, such as acoustic emission (AE) (Chen et al., 2020a), ultrasonic methods (Wang et al., 2024b), etc, can also offer new experimental possibilities for microscopic investigation. Among them, X-ray CT is a commonly used technique that can be combined with in-situ mechanical tests to characterise the material constituents before and after concrete fracture. As shown in the work of Huang et al. (2015) and Huang et al. (2022), X-ray CT has also proven effective in tracking and identifying internal damage or deterioration within the concrete microstructure. Despite these advantages, it lacks standardised scan resolution for specific applications and is limited by the trade-off between sample size and 3D image resolution (Lorenzoni et al., 2022). As an alternative, digital volume correlation (DVC), which can be used to estimate the full field strain over the entire concrete volume (Chateau et al., 2018), has been shown to be a feasible technique for detecting damage below the image resolution. In the work of Chateau et al. (2018), micro-cracks as small as one-tenth of a voxel in concrete images were successfully detected

using DVC, enabling the identification of early-age cracks that cannot be captured by X-ray CT.

For the above techniques, especially when investigating the influence of material properties or morphology, it becomes more difficult to control these factors, and analysis can typically only be performed at a specific time point or in a specific region of each sample. This results in repetitive sample preparation and the time-consuming use of complex equipment. Additionally, the obtained data are often indirect indicators, which can only be used to infer the desired microscopic physical or chemical mechanisms, while the directly related microscopic physical quantities cannot be extracted for quantitative analyses. In such cases, numerical investigation can be considered as a more appropriate alternative.

2.5.3 Numerical modelling

Early modelling generally treated concrete as a homogeneous medium and was mainly used to develop constitutive laws for predicting its transport (Zheng et al., 2010) and mechanical behaviours (Le Thanh et al., 2022). Later, with increasing attention to the material heterogeneity of concrete, modelling efforts began to focus on more directly capturing information about its internal structure, based on the concrete microstructure with a representative size. The following sections present the modelling framework, the concept of the representative elementary volume, and the generation of concrete microstructures using both image-dependent and image-independent approaches.

2.5.3.1 Modelling framework

The modelling can be broadly categorised into two approaches: discrete and continuum modelling. The former one can treat the material as a system consisting of individual components, *i.e.*, spheres or lattice beams, which are typically implemented using discrete element methods (Beckmann et al., 2012; Nitka and Tejchman, 2020) or lattice-type methods (Schlangen and Garboczi, 1997), respectively. The latter approach considers the material as a continuous medium, and have been mainly solved using finite element method (FEM) (Thilakarathna et al., 2020). In comparison, one of the challenges with discrete modelling is determining the equivalent model parameters for the bonds between individual components, which need to be carefully chosen through calibration based on macroscopic responses using extensive trial-and-errors (Xiong et al., 2020a). In addition, other discrete approaches, such as

lattice-type models, produce results that strongly depend on the lattice geometry (Thirumalaiselvi et al., 2019). However, such issues can potentially be avoided by using continuum modelling.

When concrete is modelled as a multiphase microstructure, its material heterogeneity can be characterised by assigning distinct material properties to each constituent phase. For transport behaviour, the Poisson equation is typically implemented in numerical frameworks to simulate chloride-induced corrosion. For mechanical behaviour, the finite element method (FEM) is more commonly used, where the targeted response of concrete is simulated using appropriate constitutive models, such as concrete damaged plasticity (CDP) (Naderi et al., 2021), cohesive interface element (CIE)-based methods (Naderi and Zhang, 2021a), the Holmquist-Johnson-Cook (HJC) model (Wu et al., 2023a), the K&C model (Chen et al., 2023a), or others (Pan et al., 2025).

2.5.3.2 Representative elementary volume of concrete microstructure

Representative elementary volume is the smallest volume of concrete microstructure and is widely considered in measurement or modelling to capture the representative macroscopic properties, as it is impractical to computationally generate the sample at full length scales. Among all the requirements, two of them are quite important as follows (Rozenbaum and du Roscoat, 2014): (1) The REV must be large enough to include enough microstructural features to accurately represent the macroscopic property; (2) The REV is defined for a specific property and is generally independent of the location within the material where it is sampled. The REV is determined by the length scale of the features of interest, which can range from the nanoscale to the aggregate scale. At a given scale, fluctuations in the target property decrease as the sampling volume increases, and the REV is defined as the volume at which these fluctuations become negligible (Rozenbaum and du Roscoat, 2014; Zhang et al., 2025).

2.5.3.3 Image-based generation of concrete microstructure

Image-based approach uses X-ray CT to create a microstructure with structural properties that closely resemble reality (Huang et al., 2015; Huang et al., 2016). It can visualise the internal features of concrete and capture digital images of the microstructure, which can then be transformed into numerical models (Coleri et al., 2013; Mostafavi et al., 2013). By taking advantage of such models, comparison with experimental results helps obtain more appropriate

material properties of concrete constituents for simulation, laying the groundwork for subsequent model analysis (Wei et al., 2020b). In addition, further progress can be made toward understanding the local mechanisms that drive macroscopic mechanical behaviours (Zhang et al., 2021c). The key challenge in X-ray CT lies in image segmentation for phase identification, which focuses on accurately delineating material boundaries based on specific grey values in the images (Mazzucco et al., 2021; Stamati et al., 2021). Another issue is that reliance on images allows only a limited number of microstructure models to be generated, which is insufficient for statistical characterisation. This also results in a lack of flexibility in adjusting the microstructure (Naderi and Zhang, 2021a).

2.5.3.4 Non-image-based generation of concrete microstructure

Owing to higher efficiency and better adjustability, computer-based packing algorithms have been developed as an alternative image-independent approach to generate packings of variously shaped particles, which represent the spatial distributions of pores (Yang et al., 2022a), sand (or fine aggregate) (Hou et al., 2021), or aggregates (Abyaneh et al., 2013) depending on the scale of interest. Among all existing works, the latter two have received more attention when investigating diffusivity or fracture of concrete microstructure. To satisfy the predefined packing density and size distribution curves for various application purposes, numerous packing algorithms have been developed or extended for generating concrete microstructures, such as the take-and-place method (Wang et al., 2015a), random extension methods (Ma et al., 2016) and the graphical method (Caballero et al., 2006). However, most representative shapes used in packing are oversimplified shapes, such as circles, ellipses, or polygons in 2D (Wang et al., 2015b) , and spheres, ellipsoids, or polyhedron in 3D (Wang et al., 2016b). These fail to accurately represent the realistic particle morphology, which would lead to underestimating or overestimating concrete performance.

In existing algorithms, non-dimensional geometric parameters have been incorporated to characterise particle morphology (Pan et al., 2022; Zheng et al., 2022). Their definitions have been widely derived from aggregates or soil particles related studies that use image-based approaches to analyse shape. The sphericity, flatness and convexity are introduced to capture the overall forms of particle and can be defined based on the width to length ratio, diameter, area or volume (Wadell, 1932a; Mora and Kwan, 2000; Ferellec and McDowell, 2008; Zheng and Hryciw, 2015). At a finer scale, the roundness (or angularity) is used to account for local

features of the particle shape (Mollon and Zhao, 2012; Zheng and Hryciw, 2015; Wei et al., 2020b). At the smallest observation scale, roughness is used to describe the texture of the aggregate surface (Zheng and Hryciw, 2015; Guida et al., 2020). However, its implementation is very challenging in practice. According to Mollon & Zhao (2012), the surface roughness can alternatively be defined by the regularity, which considers the round-off errors in the floating-point algorithm to approximate the convex envelope. These traditional geometric parameters can only quantify particle shape at a single scale.

To achieve more realistic particle morphology, incorporating Voronoi tessellations, the Fast Fourier Transformation (FFT) is employed to generate the 2D irregular shape, based on the Fourier spectrum $F_n \propto n$, where F_2, F_3 and F_8 are key Fourier descriptors used to control the elongation, irregularity, and roughness of particles, respectively, as demonstrated in the work of Mollon and Zhao (2012). In their later work, Mollon and Zhao (2014) extend this Fourier descriptor-based method from 2D to 3D by incorporating random field theory. Instead of controlling the particle shape using multiple F_n, when the spherical harmonic is employed as an alternative to generate the 3D irregular shape in the work of Wei et al., the fractal dimension F_d, which is a multiscale geometric index, is introduced to bridge the linear relation between the Fourier descriptor F_n and n in a log-log scale for $n > 2$, as defined below:

$$F_n = F_2 \left(\frac{n}{2}\right)^{2F_d - 6}. \tag{2.5}$$

Additionally, based on the Parseval formula, relative roughness R_r is derived to quantify how globally different the irregular shape is from an equivalent sphere, as shown below (Wei et al., 2020a):

$$R_r = \sqrt{\sum_{n=2}^{\infty} \left(F_2 \left(\frac{n}{2}\right)^{2F_d - 6}\right)^2}. \tag{2.6}$$

2.6 Summary

In summary, the transport and mechanical behaviours of concrete, focusing on their fundamental mechanisms, exposure conditions, the influence of material microstructures, and the management of their performance, have been reviewed in this section. Various methods for related investigations have also been provided. Several insights are identified which enrich our

understanding of concrete behaviour under marine challenges and, at the same time, inspire our research work.

For the concrete responses under various loadings, significant experimental and numerical progress has been achieved across different material length scales. Certain factors at specific length scales remain difficult to investigate experimentally but are more accessible through numerical approaches. This provides further motivation for our research. Although material constituents at different length scales all contribute to the overall performance of concrete, the mesoscale provides direct access to the overall behaviour of concrete in practice. In mesoscale modelling, when aggregates are treated as the impermeable and strongest phase among the material constituents of conventional concrete, related factors, *e.g.*, solid fraction and morphology, are the focus of investigations into concrete performance. In particular, aggregate morphology is important because it affects the tortuosity and stress distribution within the concrete microstructure. However, realistic aggregate shapes are less frequently used in concrete models compared to regular shapes representing aggregates. Although crushed and rounded aggregate shapes have been employed to investigate the effect of aggregate shape in experimental studies, the conclusions require revision due to the limited variation in shape irregularity. Consequently, the effects of aggregate shape remain insufficiently explored, and the realistic response within concrete cannot be fully captured. Some existing studies, whether incorporating irregularly shaped aggregates or not, quantify shape effects only in terms of macroscopic properties, without sufficient quantitative evidence from internal variations or local responses within concrete. These gaps concerning the effect of realistic aggregate shapes need to be addressed in this thesis.

Fourier-descriptor-based methods are employed to generate mesoscale structures with realistic aggregate shapes for the investigation of specific concrete behaviours. From our review, many transport and mechanical behaviours of concrete are related to marine challenges; however, not all of them will be considered in this project. Among these behaviours, the most relevant and representative are ionic diffusion leading to chloride-induced corrosion and structural durability under complex stress conditions, corresponding to the transport and mechanical performance of concrete, respectively. The effect of aggregate shape will receive particular attention within these investigations using mesoscale modelling via FEM, which has been widely proven to be an efficient tool for simulating the transport and mechanical behaviours of concrete. At a given aggregate solid fraction, the variation in concrete diffusivity

due to aggregate shape irregularity will be highlighted. For quasi-static fracture, to better approximate complex stress conditions encountered in practice, the effect of aggregate shape on concrete strength under various confining pressures in triaxial loading will also be examined. In addition, the dynamic fracture behaviour of concrete will be analysed, with emphasis on local responses under various stress conditions, considering different loading ramp rates, internal friction, and confining pressures. As quantitative evidence, the local responses of concrete, including aggregate-shape-induced tortuosity, stress distribution, damage, and strain-rate distribution, will be analysed to support our findings, *e.g.*, diffusivity, triaxial strength versus confining pressure, dynamic strength, for the related concrete behaviours. Both macro- and microscopic analyses of the effects of aggregate shape on the concerned concrete behaviours will be conducted in the following sections.

Chapter 3 Mesoscale Modelling of Diffusion in Concrete

In this chapter, to account for diffusion-driven corrosion, we apply the finite element method (FEM) to investigate diffusion behaviour of 2D cement-based composites. Realistic multi-scale aggregate shapes, characterised by fractal dimension (F_d) and relative roughness (R_r), are generated to highlight the influence of aggregate morphology on the effective diffusivity. The spatial distribution is evaluated by the disorder index. From numerical results, samples with a larger disorder index, indicating a broader throat size distribution, show smaller effective diffusivities. Meanwhile, aggregate shape irregularity causes much smaller effective diffusivities, highlighting the necessity of the realistic concave particle shapes in numerical simulations. Sensitivity studies show F_d and R_r are more related to the effective diffusivity than other single-scale classical shape parameters. At last, a model with only these two shape parameters is proposed to predict effective diffusivity. This work further improves the understanding of the role of aggregate morphology on the effective diffusivity, towards applications in ionic-induced corrosion in two-phase composites.

This chapter has been devoted to the following paper:

Liu, Q., Wei, D., Zhang, H., Zhai, C., Gan, Y., 2022. A numerical investigation on effective diffusion in cement-based composites: the role of aggregate shape. *Transport in Porous Media* 143(3), 681-702.

3.1 Introduction

The presence of aggregates in cement-based composites, *e.g.*, concrete, has gained insights from many scientific and engineering communities for many decades, and it is generally accepted that the size, shape, and texture of aggregates well influence the properties of the fresh and hardened mixtures. Recent studies have been conducted widely towards the influence of aggregate morphology, *e.g.*, shape and size, on structural performances (Denis et al., 2002; Rocco and Elices, 2009), transport properties (Krejsová et al., 2018; Santos et al., 2020; Ueno and Ogawa, 2020), viscosity (Erdoğan et al., 2008; Westerholm et al., 2008) and flowability (Cui et al., 2020) of cement-based composites. The influences of aggregate size, content and shape on effective properties are demonstrated. Several shape indices have been adopted, such as elongation, surface roughness and fractal dimension, exhibiting notable effects on the mechanical responses (Wei et al., 2020b). However, the study on how shape factors of aggregates affect effective transport properties, in particular ironic diffusion, remains relatively unexplored.

Effective diffusivity is one of most important transport behaviours in terms of concrete durability issues (Gjørv, 2011). The chloride-induced ionic transport in the cement-based composite is mainly driven by diffusion (Bastidas-Arteaga et al., 2011). Either bulk diffusion or migration tests have been developed to quantify the diffusion coefficient in the Fick's law (Luping and Gulikers, 2007). In experiments, the diffusivities have been widely tested by considering the cement content (Pae et al., 2021), aggregate size distribution (Shafikhani and Chidiac, 2019) and solid fractions (Delagrave et al., 1996). Especially for aggregate particles, their existence is to necessarily account for the tortuosity of diffusive paths (Patel et al., 2016). Image analysis (IA) is developed to determine the shape of coarse aggregates for the interpretation of aggregate geometrical parameters, *e.g.*, elongation, (Fernlund, 2005). It is intuitive that geometrical parameters can significantly affect the durability of the concrete (Kwan et al., 1999). However, few experiments targeting to correlate diffusivities and geometrical parameters have been conducted due to the limited control of particle morphology.

Effective diffusivity is analytically developed by upscaling from heterogenous to a continuous homogenous medium (Hornung, 1996). The modification of Hashin-Shtrickman upper and lower bounds is derived for the effective diffusivity of the two-phase isotropic composite media, under the given aggregate fraction, these bounds are reached when the

inclusion in the matrix is shaped to be sphere (Torquato and Haslach Jr, 2002). Alternative solutions of effective diffusivity are based on effective medium approximation (EMA), *e.g.*, Maxwell and self-consistent approximations, which also account for simplified microscale information (Choy, 2015; Hoch, 2015). For instance, the homogenization is applied to account for pore structures for the diffusivity of cement paste, and a self-consistent scheme is adopted to evaluate the effective diffusivities in the cement-based composite. Also, multiscale modelling by N-layered spherical inclusion theory still assume aggregates to be spheres (Sun et al., 2011). Therefore, it is desirable to develop the analytical model to account for geometrical parameters, besides the first order approximation accounting for volume content and size of aggregates.

In addition to the theoretical approaches, several numerical methods are proposed to model the diffusivity in cement-based composites, such as Lattice Boltzmann Method (LBM) (Zhang et al., 2012b, 2014a) and Finite Element Method (FEM) (Idiart et al., 2011; Liu et al., 2012; Zheng et al., 2012; Xu and Li, 2017; Xiong et al., 2020a). LBM modelling is chosen to be an appropriate micro-solver for complex boundary problems, when the heterogeneity of cement paste, *e.g.*, pore structures, is considered (Zhang, 2013a). However, parameters at pore scale were neglected in this study, and cement paste is assumed to be homogenous. FEM modelling is straightforwardly conducted for the diffusion study based on Fick's Law, where Monte-Carlo algorithm has been widely applied to generate the meso-structure by construction of random packing with regular particle shapes (Du et al., 2014; Liu et al., 2014). Randomness, *e.g.*, aggregate positions, is seldom quantitatively evaluated in the investigation on the effective diffusivity, though disordered inclusion positions in the matrix phase has been demonstrated to be one of influencing factors to the transport properties (Laubie et al., 2017a; Cui et al., 2019; Wang et al., 2019c). In numerical modelling, representative elementary volume (REV) size of the periodical structure for the aggregate packing is also a concern to the simulation (Zhou et al., 2014; Ma et al., 2016). Regardless of REV size, it has been found that diffusion profiles for different idealized convex aggregate shapes, *e.g.*, square, regular pentagon, hexagon, and circle, are almost identical (Xiao et al., 2012). Representative aggregate shapes in most FEM modelling of diffusivity are usually oversimplified, which may not be able to represent the morphologies of real aggregates. It is found that aggregate elongation, *e.g.*, for elliptical aggregates, can reduce effective diffusivity (Zheng et al., 2012; Zheng et al., 2016).Nevertheless, due to the elongation, it is unclear to see how the orientation of elliptical aggregates affects the diffusivity variance (Abyaneh et al., 2013). In addition to elongation, 2D

particle shape can be quantified by other traditional and scale-dependent geometrical parameters, such as roundness and roughness (Zheng and Hryciw, 2015). Among these geometrical parameters, none of them is able to fully describing all aspects of morphology of the aggregate shape (Kwan et al., 1999). Fractal dimension has been introduced to be a novel global index summarising all geometrical characterises, and improved spherical harmonics based on the fractal dimension is used to construct the 3D irregular shape (Wei et al., 2018). Moreover, fast Fourier transformation (Mollon and Zhao, 2012) and pixel-based method (Liu et al., 2018) are also alternative solutions to generate irregular shapes, which can be feed into numerical models with well-controlled shape indices to identify the key parameters and establish isolated cause-effect relations.

This study presents an FEM investigation on diffusivities of cement-based composites, emphasizing on the effects of aggregate stochastics, in terms of spatial distributions, elongation, and morphology features. The main contents are outlined as follows. In Section 3.2, packing processes for the virtual concrete sample consisting of various of aggregate shapes are firstly introduced. The disorder index is introduced to quantitively measure the aggregate position randomness. Then, how the irregular aggregate is generated using Fast Fourier Transformation (FFT) via two compressed shape factors, relative roughness (R_r) and fractal dimension (F_d), is described. Subsequently, key details about FEM simulation of one-way steady-state diffusion based on Fick's first law are illustrated. Results and relevant discussions focusing on influencing factors on effective diffusivity, such as disorder index, elongation and aggregate shapes, are demonstrated in Section 3.3. Sensitivity study is also conducted for the relations between different length-scaled geometrical parameters of irregular aggregate and effective diffusivity. Inspired by the sensitivity study, a promising prediction model is proposed with only two shape parameters (R_r and F_d) for specific aggregate fraction. Finally, some conclusions are drawn in Section 3.4.

3.2 Methods

For modelling the effective diffusivity of cement-based composites, mesoscale numerical samples consisted of the cement and aggregates should be established. It is noted that the grain size distribution of aggregates (or aggregate sieving) is also an important factor in transport properties and can be seen elsewhere (Liu et al. 2018; Xiong et al. 2020; Wu and Xiao 2018). Thus, the aggregate grading is not the focus of this study and only mono-sized aggregates are

applied for isolating grading effects. The basic underlying assumption of this mesoscale level analysis is that only large aggregates in the same grading are explicitly represented in cementitious material, while the rest fine aggregates are represented as homogenous 'cement' paste. The fundamental parameters contributed to the construction of aggregates in cement paste in this study are the aggregate fraction, shapes, and spatial arrangement.

3.2.1 Packing structure of aggregates

3.2.1.1 Ordered packing

To investigate the effect of aggregate shape on the effective diffusion, hexagonal packing is employed to construct 2D composite structures, in which aggregates with the same size are inserted into cement paste. The maximum solid fraction equal to $\frac{\sqrt{3}\pi}{6}$ can be achieved for 2D mono-sized circular packing (Hales, 1992). The overall shape of the aggregates, *e.g.*, elongation, is the dominant morphological parameter controlling packing structure (Hafid et al., 2016). The hexagonal packing can increase the aggregate spacing and avoid the aggregate overlaps for the other shapes, *e.g.*, ellipse, polygon, and irregular shape.

Contact check is required to avoid the intersection between aggregates caused by the rotation of non-circular aggregates. For either polygonal or irregular aggregate, each vertex of shapes should be checked to determine whether it is contacted with others. It can be implemented by using the built-in function of inpolygon in MATLAB (Zhang et al., 2017). Meanwhile, to guarantee at least one-mesh size space between aggregates, the aggregate area for contact check is 2% more than the targeted aggregate area. The choice of REV and hexagonal packing results in 120 aggregates in the sample. Each taken aggregate at the position of hexagonal packing is randomly rotated and placed into REV size of cement paste. Geometrical periodicity is ensured in both horizontal and vertical directions.

3.2.1.2 Disordered packing

In terms of the disordered packing, only circular shape is used to check the effects from the spatial arrangement of aggregates. The way to quantitively describe the overall effect of aggregate position is based on the original disorder index I_d (Laubie et al., 2017a). It not only affects the mechanical properties (Laubie et al., 2017a; Laubie et al., 2017b), but also impacts the fundamental understanding of fluid transport properties (Holtzman, 2016; Fantinel et al.,

2017). However, the original disorder index I_d tends to ignore the small perturbations, which is less sensitive to the specific solid mechanics problems. As the Voronoi tessellation is quite sensitive to such small disturbances, the disorder index I_v modified to cooperate with Voronoi tessellation is used in this paper. It can be defined as (Cui et al., 2019):

$$I_v = \sqrt{\frac{\sum_{k=1}^{N_a}(\phi_k - \phi)^2}{N_a - 1}}, \tag{3.1}$$

where N is the number of aggregates in the domain of cement paste, ϕ_k is local solid fraction within the Voronoi cell, ϕ is the overall solid fraction in the cement paste.

Disordered packing is introduced by Monte-Carlo movement of each circular based on the initial hexagonal packing (Wang et al., 2019c). To stabilize the I_v around a specific value, sufficient iterations are required to assure the uncertainty less than 5%.

3.2.2 Generation of aggregate shapes with multi-scale morphology features

Mesoscale models of cement-based composites are usually generated with regular shapes, such as circle, ellipse and polygon (Du et al., 2014). To construct more realistic aggregate morphology, discrete Fourier transform of the contour of the grain can be used (Mollon and Zhao, 2012). In the 2D case, with the aggregate particle centre O, the contour of the aggregate particle is discretised by N_p points P_i, with a constant polar angle $\theta_P = 2\pi/N_P$. The distance between P_i and O is defined as l_i, and the discrete signal $l_i(\theta_i)$ can be expressed by:

$$l_i(\theta_i) = l_0 + \sum_{n=1}^{N}[X_n \cos(n\theta) + Y_n \sin(n\theta)], \tag{3.2}$$

where n is the number of discrete signal, N is the total number of discrete signal and equal to 64 in the present study (Wang et al., 2019a), and l_0 is the average of discrete signals. The spectrum X_n and Y_n of the discrete signal after Fourier transformation are defined as:

$$X_n = \frac{1}{N}\sum_{i=1}^{N}[l_i \cos(i\,\theta_i)], \tag{3.3}$$

$$Y_n = \frac{1}{N}\sum_{i=1}^{N}[l_i \sin(i\,\theta_i)]. \tag{3.4}$$

The most sensitive term to the irregular shape is normalized amplitude F_n for each discrete signal number n, defined as:

$$F_n = \frac{\sqrt{{X_n}^2 + {Y_n}^2}}{p_0}, \tag{3.5}$$

For $n = 0$, F_0 is normally set to 1 for the normalization. F_n for $n = 1$ is equal to 0 ensuring that the aggregate is centred at the position of point O. F_2 controls the elongation of aggregate particles, and F_n for $3 \leq n < 8$ are used to represent irregularity of aggregates while F_n for $n \geq 8$ are related to the roughness of the particle surface. For natural aggregates, normalized amplitude F_n is roughly linearly decreased with the discrete signal number n. This linear relationship can be denoted with the combination of fractal dimension F_d for $n \geq 2$ in the log-log scale, which is a global geometrical index describing the aggregate shape at multiscale (Wei et al., 2018). The exponential relation between the normalized amplitude F_n and discrete signal number n can be expressed by:

$$F_n \propto n^{-2H}, \tag{3.6}$$

where -2H is the slope of $\log(F_n)$ and $\log(n)$, and H is the Hurst coefficient associated with fractal dimension F_d,

$$F_d = 2 - H. \tag{3.7}$$

Therefore, the normalized amplitude F_n can be modified with F_d for $n \geq 2$, defined as:

$$F_n = F_2 \left(\frac{n}{2}\right)^{2F_d - 4}. \tag{3.8}$$

The relative roughness R_r can be used to compute how globally different the irregular aggregate shape is from l_0 determined equivalent circle (Wei et al., 2020c). R_r derived from Fourier series is deduced in Appendix A, and defined as:

$$R_r = \sqrt{\sum_{n=2}^{\infty} \left({F_2}^2 \left(\frac{n}{2}\right)^{4F_d - 8} \right)}. \tag{3.9}$$

The influence of F_d and R_r on the morphology of irregular shape has been illustrated in Figure 3.1(a). It has been found that both increases in F_d and R_r results in more fractal shape with rougher surfaces.

3.2.3. FEM Modelling effective diffusivity

The finite element method (FEM) is applied to simulate the one-way steady-state diffusion based on Fick's first law, shown as:

$$J = -D_{eff}\frac{dc}{dx}, \tag{3.10}$$

where J is the total diffusion flux (mol/s), $\frac{dc}{dx}$ is concentration gradient (mol/m^2), and D_{eff} is the effective diffusivity (m^2/s). As reported by Savvas et al. (2016), simulation results of cement-based composite properties can be influenced by the selection of REV size. With the increasing volume of the cement-based structure, the dispersion or fluctuation of studied properties becomes small or less influenced by the size of REV (Zhou et al., 2014; Savvas et al., 2016; Xu et al., 2017). In terms of effective diffusivity, regardless of aggregate shapes, RVE size is determined to be at least 5 times larger than the maximum size of aggregates (Liu et al., 2018). For this study, numerical simulation of steady-state diffusion is conducted with diffusion coefficients of cement $D_c = 1 \times 10^{-12} m^2/s$ and of aggregate $D_a = 0\, m^2/s$. The REV size is considered as 10 times of the maximum aggregate size, as shown in Figure 3.1(b), to compute more stable value of effective diffusivity D_{eff} and save the computational efforts.

In Figure 3.1(b), irregular aggregates with $F_d = 1.65$ and $R_r = 0.357$ are packed in REV size of cement at the solid fraction of 50%, and it has been chosen as an example to illustrate the numerical simulation of effective diffusivity. More details of aggregate packing in REV size of cement paste will be introduced in the following section. To eliminate the influence of value fluctuation at the boundary, REV size of geometry is doubled in the diffusion direction. The chloride concentration at left boundary is set as 1 mol/m^3,while it is set as 0 mol/m^3 at the right end. Meanwhile, periodical boundary conditions have been given on the top and bottom boundary. The mesh layout particularly for the space between irregular shape has been shown in Figure 3.1(c), where the relative mesh size (the ratio of mesh size to aggregate size in diameter) is less than 0.03. D_{eff} is computed from the middle section to minimise the boundary effects.

This middle section (A-B) of the samples can be homogenised by setting up a moving window with the width of about 3 area-equivalent circle diameters of aggregate. Note that all aggregates in cement paste are of the same area. The window is moved by a step size of 1/5 of its length for calculating concentration, c, at the horizontal displacement, x. The reference

evolution of concentration gradient, $\frac{dc}{dx}$, is shown in Figure 3.1(d). Meanwhile, the total flux J for this middle section can be computed from FE software COMSOL to calculate the value of effective diffusivity, D_{eff}. In following sections, D_{eff} is converted into the dimensionless form $\frac{D_{eff}}{D_0}$, where D_0 is the effective diffusivity of the regularly hexagonal packing of circular aggregates.

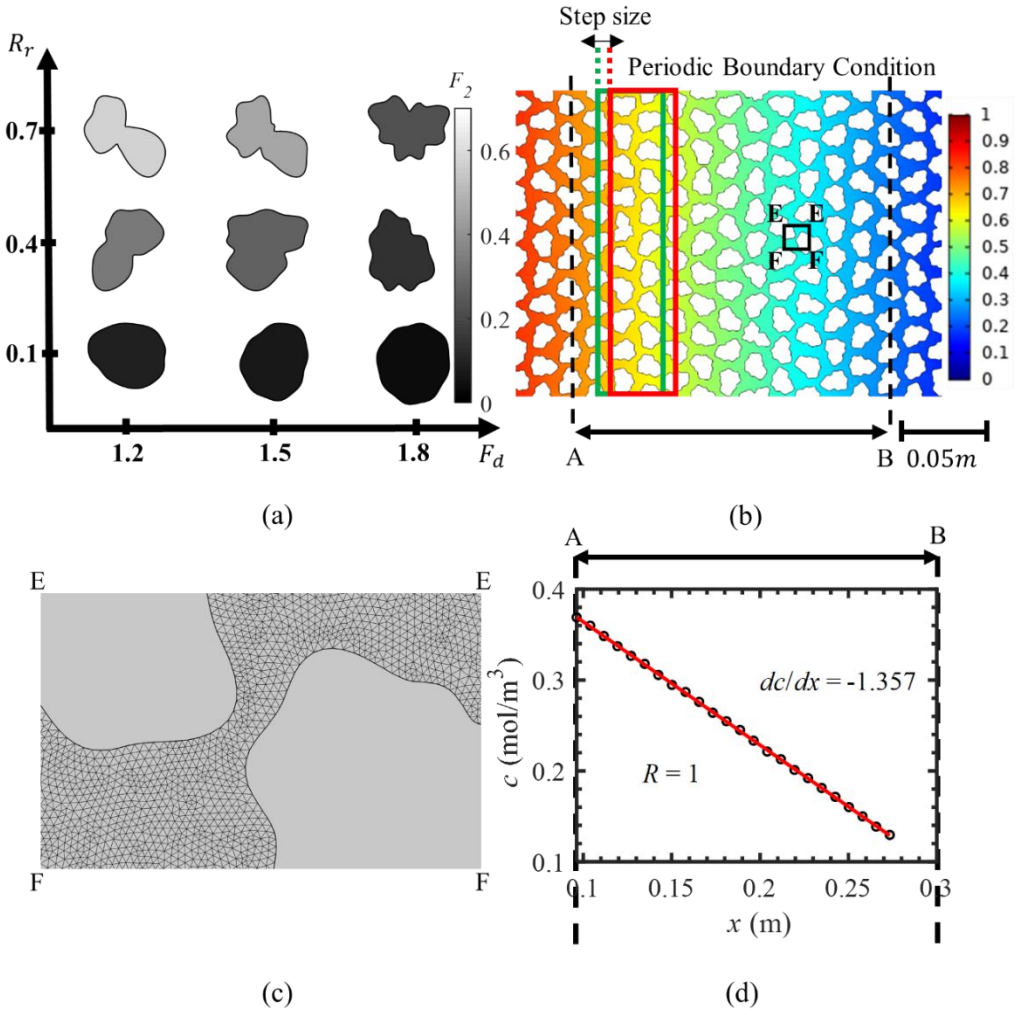

Figure 3.1: (a) Variation of irregular shapes with fractal dimension F_d and relative roughness R_r, (b) illustrations of FE diffusivity modelling of 2D hexagonal packing of irregular aggregate with $F_d = 1.65$ and $R_r = 0.357$, (c) Mesh layout and (d) Concentration profile along the horizontal displacement.

3.3. Results and discussion

3.3.1. Spatial distribution of aggregates

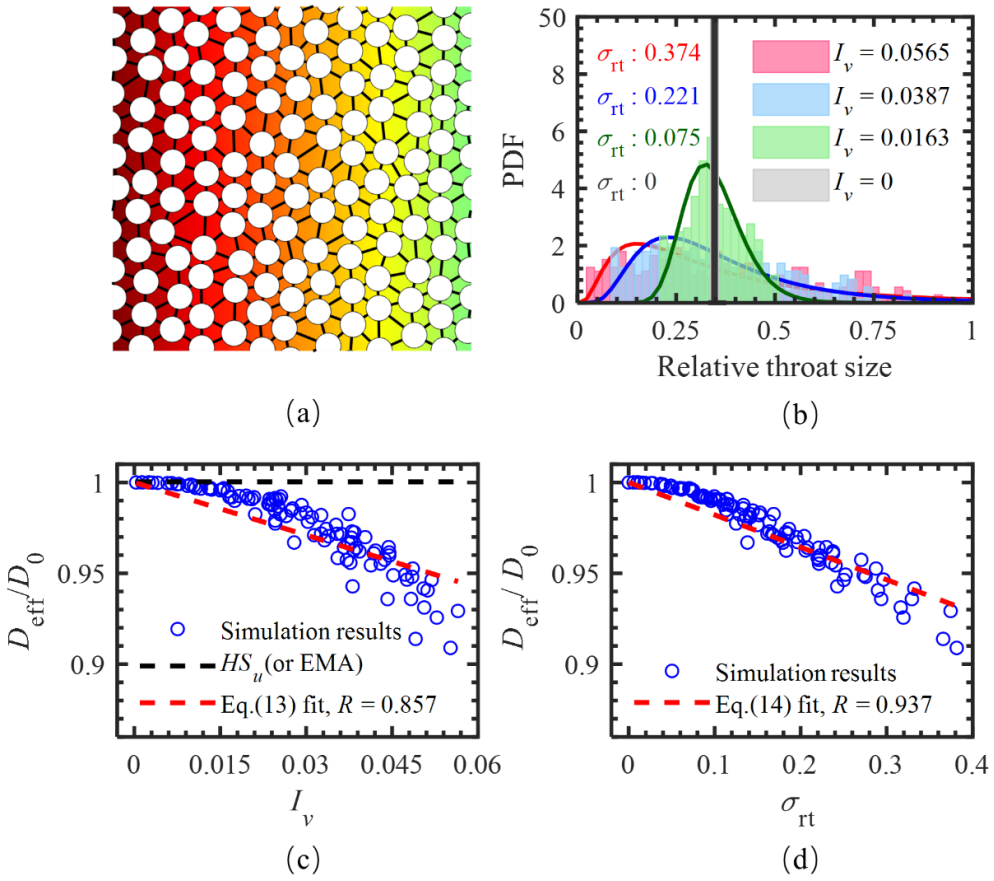

Figure 3.2:(a) FE modelling results for random packing of circular aggregates at $I_v = 0.0387$, and black solid lines denote throats between circular aggregates, (b) Histogram of probability density function (PDF) of relative throat sizes at I_v of 0, 0.0163, 0.0387 and 0.0565, and their corresponding plots of lognormal distribution fitting in black, red, blue and green solid lines, and each fitting is given with the standard deviation of relative throat size σ_{rt}, (c) Relations between $\frac{D_{\mathrm{eff}}}{D_0}$ and I_v at solid fraction ϕ of 50%, and HS_u (or EMA) is the Hashin-Shtrikman upper bound of Equation 3.11 at ϕ of 50% and (d) Relations between $\frac{D_{\mathrm{eff}}}{D_0}$ and standard deviation of relative throat size distribution σ_{rt}.

Randomness of aggregate positions due to Monte-Carlo iterative movement is characterized by I_v. It is controlled by apparent diameter $d_{\mathrm{ap}} = \gamma d$ with associated $\gamma \in$

$[1, \frac{\sqrt{3}\pi}{6}]$, where d is original diameter of circular aggregate. Note that when d_{ap} reaches to the maximum at $\gamma = \frac{\sqrt{3}\pi}{6}$, circular aggregates are placed in the hexagonal packing. To compute the variation of $\frac{D_{\mathrm{eff}}}{D_0}$ with I_v, 100 disordered spatial distributions of circular aggregates at $I_v \in [0.01, 0.06]$ are generated at $\phi = 50\%$. Figure 3.2(a) is an example of the FEM modelling for a random packing of circular aggregates at $I_v = 0.0387$. The throat size between two grains is defined as the shortest distance between points on each neighbour grain boundaries. Figure 3.2(b) presents probability density function (PDF) of relative throat size, defined as the ratio of throat size to circular aggregate diameter, at $I_v = 0, 0.0163, 0.0387$ and 0.0565. The corresponding standard deviations of lognormal fittings for them are: $\sigma_{\mathrm{rt}} = 0,\ 0.075, 0.221$ and 0.374. The higher I_v induces the larger σ_{rt} due to the wider range of throat sizes. After involving in all disordered packings, Figure 3.2(c) indicates the relation between $\frac{D_{\mathrm{eff}}}{D_0}$ and I_v. For the diffusivity of two-phase composite of which aggregate phases are impermeable, the well-known narrow Hashin-Shrinkman (HS) upper bound, derived by the variational theorems (Hashin and Shtrikman, 1962), is

$$HS_u(\phi) = \frac{D_c}{(1+\phi)D_0}. \tag{3.11}$$

More information about the derivation can be referred to Appendix B. Notably, HS_u, defined the same as EMA in terms of Maxwell approximation for 2D effective diffusivity (Jóhannesson and Halle, 1996; Torquato and Haslach Jr, 2002), is shown in Figure 3.2(c). At $I_v = 0$, HS_u well matches our simulation result, while $\frac{D_{\mathrm{eff}}}{D_0}$ decreases obviously with the increase of I_v and below the HS_u. As $I_v \in [0.01, 0.06]$, $\frac{D_{\mathrm{eff}}}{D_0}$ fluctuates within a range of around 10%. Since I_v is quite sensitive to throat size, the relation between $\frac{D_{\mathrm{eff}}}{D_0}$ and σ_{rt} is also shown in the Figure 3.2(d), where $\frac{D_{\mathrm{eff}}}{D_0}$ generally decreases with the increase of σ_{rt}. Evidently, $\frac{D_{\mathrm{eff}}}{D_0}$ can be correlated to I_v or σ_{rt}. For the simplicity, both correlations in Figure 3.2(c) and (d) are defined by linear fittings, starting from $\frac{D_{\mathrm{eff}}}{D_0} = 1$ at $I_v = 0$ and $\sigma_{\mathrm{rt}} = 0$:

$$\frac{D_{eff}}{D_0}(I_v) = a_1 I_v + 1, \tag{3.12}$$

$$\frac{D_{eff}}{D_0}(\sigma_{rt}) = a_2 \sigma_{rt} + 1, \tag{3.13}$$

where $a_1 = -0.956$ and $a_2 = -0.177$ are fitting parameters. Relative to the I_v, σ_{rt} is a more effective factor to determine effective diffusion because of its higher correlation coefficient.

3.3.2. Aggregate elongation

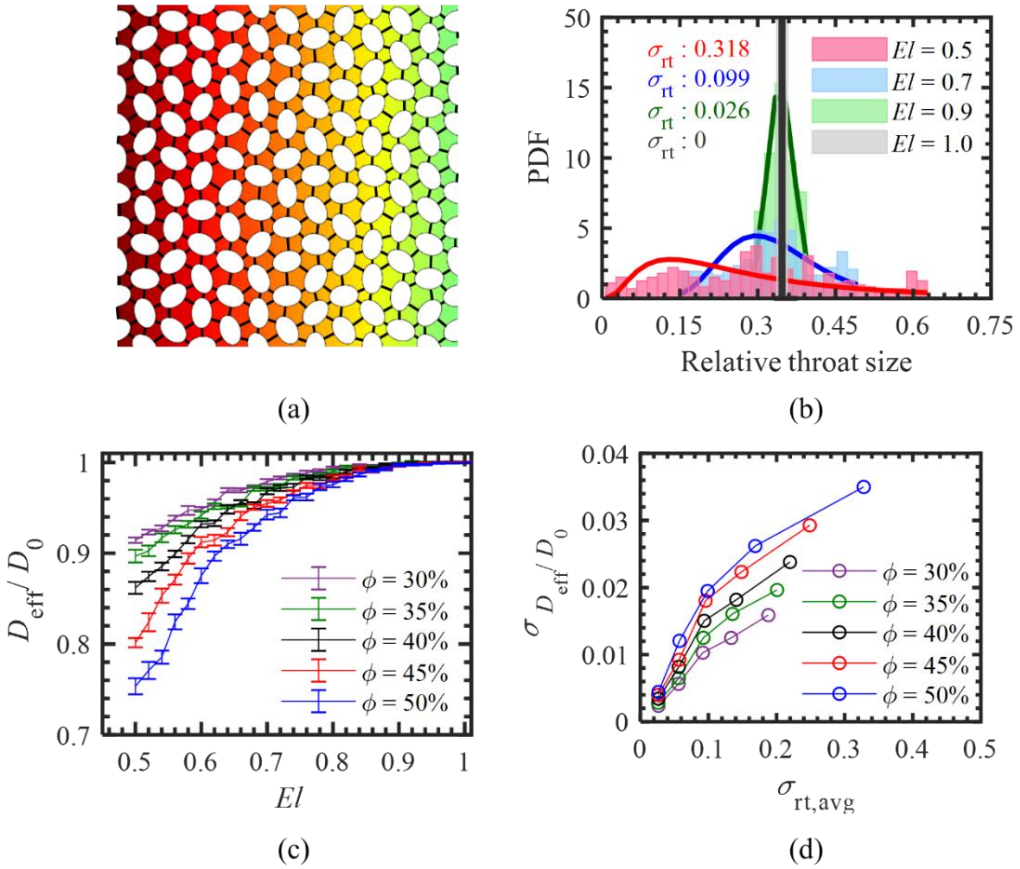

Figure 3.3: (a) FE modelling results for the hexagonal packing of elliptical aggregate with elongation (El) of 0.7 at solid fraction ϕ of 50%, where black solid lines mean throat sizes between elliptical aggregates, (b) Histogram of probability density function (PDF) of relative throat sizes at El of 0.5, 0.7, 0.9 and 1, and corresponding plots of lognormal distribution fitting in red, blue, green and black solid lines with the standard deviation of relative throat size distribution σ_{rt}, (c) Relations between $\frac{D_{\mathrm{eff}}}{D_0}$ and El at ϕ of 30%, 35%, 40%, 45% and 50%, and (d) Relation between standard deviation of effective diffusivities $\sigma_{\frac{D_{\mathrm{eff}}}{D_0}}$ and average value of all standard deviation of relative throat size distribution $\sigma_{\mathrm{rt,avg}}$ at ϕ of 30%, 35%, 40%, 45% and 50%, and five points at the same ϕ is referred to values at the elongation of 0.9, 0.8, 0.7, 0.6 and 0.5 from left to right.

To investigate the influence of elongations on the degree of effective diffusivity, elliptical aggregate is preferred to isolate other geometry factors. With the packing process described in Section 2 in hand, the different ϕ, *e.g.*, 30%, 35%, 40%, 45% and 50%, is readily achieved. For each ϕ , the number of aggregates and aggregate size are kept the same in the hexagonal packing. Meanwhile, elongations from 0.5 to 1 with an increment of 0.02 are selected, where the elongation of 1 means circular aggregate. Notably, all the elliptical aggregates, placed in the hexagonal packing, with the same elongation can be rotated randomly within $\theta \in [0, \pi]$ without contacting each other. Figure 3.3(a) is an example of FEM modelling results for the hexagonal packing of elliptical aggregates with the elongation (El) of 0.7 at the ϕ of 50%. Figure 3.3(b) shows the probability density function of relative throat size at El of 0.5, 0.7, 0.9 and 1. Meanwhile, the standard deviation of relative throat size, σ_{rt}, approximated by lognormal distribution, increases with smaller El.

All FEM modelling results, in terms of $\frac{D_{\mathrm{eff}}}{D_0}$ versus El, are illustrated in Figure 3.3(c), where each error bar is calculated from 15 samples at each El increment. It is found that at each ϕ, $\frac{D_{\mathrm{eff}}}{D_0}$ is decreased with the smaller elongation, which is consistent with those in previous studies (Zheng et al., 2012; Abyaneh et al., 2013; Zheng et al., 2016). This tendency becomes more obvious at larger ϕ. At ϕ of 50%, El of 0.5 even causes around 25% reduction in $\frac{D_{\mathrm{eff}}}{D_0}$ compared with circular inclusions. From error bars, it is also found that the smaller elongation causing a wider range of throat size induces the larger fluctuation in $\frac{D_{\mathrm{eff}}}{D_0}$. To further investigate the elongation induced fluctuation in $\frac{D_{\mathrm{eff}}}{D_0}$, at each El 50 samples are used, of which the standard deviation of effective diffusivities, $\sigma_{\frac{D_{\mathrm{eff}}}{D_0}}$, and the average value of all standard deviations of relative throat size distribution, $\sigma_{\mathrm{rt,avg}}$, are computed. In Figure 3.3(d), $\sigma_{\frac{D_{\mathrm{eff}}}{D_0}}$ is plotted with $\sigma_{\mathrm{rt,avg}}$ at different ϕ ,which indicates smaller $\sigma_{\mathrm{rt,avg}}$ causes the smaller $\sigma_{\frac{D_{\mathrm{eff}}}{D_0}}$. When considering random orientation angles, elliptical aggregates with the larger El tends to be closer to circular aggregates, resulting in $\sigma_{\mathrm{rt,avg}}$ closer to zero and more stable $\frac{D_{\mathrm{eff}}}{D_0}$. In addition, it is more obvious both El and ϕ influence $\sigma_{\frac{D_{\mathrm{eff}}}{D_0}}$ much. In the conditions of smaller El, aggregate fractions can much vary $\frac{D_{\mathrm{eff}}}{D_0}$ and induce higher $\sigma_{\frac{D_{\mathrm{eff}}}{D_0}}$. When aggregate fraction is very limited,

e.g., $\phi \approx 0$, $\sigma_{\frac{D_{\text{eff}}}{D_0}}$ is nearly zero regardless of the rotation angles. Furthermore, at El of 0.5 and ϕ of 50%, $\sigma_{\frac{D_{\text{eff}}}{D_0}}$ shows the maximum value less than 4%, which is a very small disturbance compared to the elongation induced reduction in $\frac{D_{eff}}{D_0}$ (around 25%). Based on above discussions, especially for composites of high solid fractions, small aggregate elongation can cause an obvious reduction in effective diffusivity, in which the fluctuation can be ignored.

3.3.3. Global aggregate morphology features

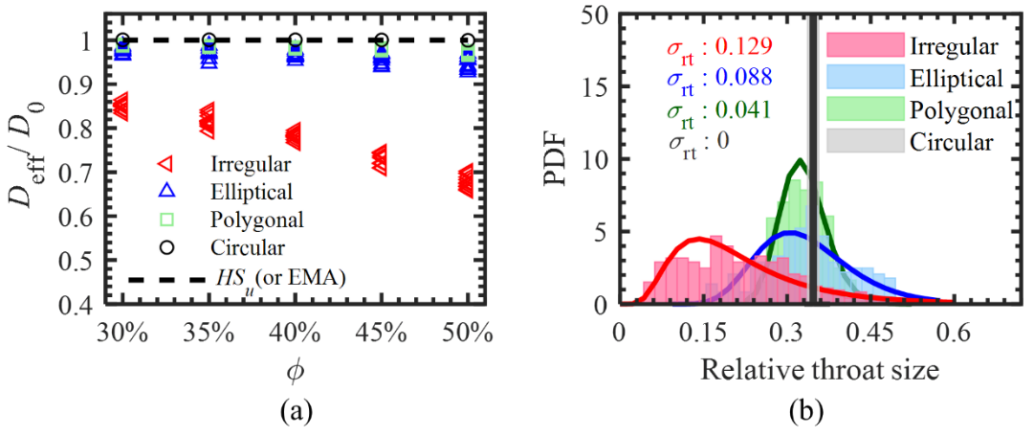

Figure 3.4: (a) Influence of aggregates shapes on effective diffusivities $\frac{D_{eff}}{D_0}$ at the solid fraction ϕ of 30%, 35%, 40%, 45% and 50%, where F_d = 1.85 and R_r = 0.99 are used to generate the irregular aggregates, and El of each irregular shape is slightly varied around 0.7; (b) Probability density function (PDF) of relative throat sizes of irregular, elliptical, polygonal and circular aggregates at $\phi = 50\%$, and corresponding plots of lognormal distribution fitting in red, blue, green and black solid lines.

Circular, polygonal, elliptical, and irregular aggregates are used to investigate the influence of aggregate shapes on $\frac{D_{eff}}{D_0}$ at $\phi \in [30\%, 50\%]$ with an increment of 5%. For each ϕ of packings contained distinctively shaped inclusions, aggregate area is the same. To perform this investigation more accurately, it is necessary to eliminate influences of aggregate spatial distributions and elongations. Mass centres of aggregates in different cases are at the same position of standard hexagonal packing. Meanwhile, irregular and elliptical aggregates have the same Els and orientation angles.

In Figure 3.4, it can be found that an increase in ϕ causes a decrease in $\frac{D_{eff}}{D_0}$ for all shapes of aggregates, which is quite consistent with Li et al. (2012). Meanwhile, 2D HS_u is perfectly matched with $\frac{D_{eff}}{D_0}$ for the hexagonal packing of circles at ϕ of 30% to 50%, proving the efficiency of our simulation results. It is also found that $\frac{D_{eff}}{D_0}$ values are almost the same for circular, polygonal and elliptical aggregates, as in relevant studies (Du et al., 2014; Jie et al., 2017). However, the polygonal aggregate causes a slightly lower $\frac{D_{eff}}{D_0}$ than circular aggregates, due to smaller sized throats caused by sharp corners around its circumference. There is also a very small fluctuation (<1%) of $\frac{D_{eff}}{D_0}$ for polygonal aggregates, since the cement-based structure with polygonal aggregates is slightly different from each other due to random rotation angles and length of polygonal aggregates. Elliptical aggregates display a little smaller $\frac{D_{eff}}{D_0}$ than polygonal and circular aggregates, that is because the elliptical aggregate is a more elongated aggregate and randomly orientated. Furthermore, as ϕ increases, it is more apparently seen that the irregular aggregate shows much smaller $\frac{D_{eff}}{D_0}$ than other regular shapes, *e.g.*, circle, polygon, and ellipse. At the ϕ of 50%, when irregular and elliptical aggregates are placed at the same position with the same elongation and orientation angles, irregular aggregate still results in around 20% reduction in $\frac{D_{eff}}{D_0}$. The main reason is that only irregular aggregates in this study contain the concave shapes, increasing the effective length of diffusive path, due to decreasing the average and enlarging the scope of relative throat size (Figure 3.4(b)). Furthermore, similar to previous discussion in Section 3.2, elongation induced fluctuation in $\frac{D_{eff}}{D_0}$ can also be negligible when compared to concave shape induced reduction in $\frac{D_{eff}}{D_0}$. Irregular aggregates with the concave shape affecting $\frac{D_{eff}}{D_0}$ will be further discussed in terms of geometrical characteristics in the following Section 3.4.

3.3.4. Correlating shape indices to effective diffusivity

Table 3.1: List of geometric parameters for regression studies

Feature No.	Feature name	Feature definition
1	Fractal dimension (F_d)	Equation 3.7
2	Relative roughness (R_r)	Equation 3.9
3	Elongation	$\frac{S}{L}$
4	Circularity	$\sqrt{\frac{r_{\text{insc}}}{r_{\text{circ}}}}$
5	Area sphericity	$\frac{A_s}{A_{\text{cir}}}$
6	Perimeter sphericity	$\frac{P_c}{P_S}$
7	Diameter sphericity	$\frac{d_c}{d_{\text{cir}}}$
8	Roundness	$\frac{\sum r_c}{n_c r_{\text{insc}}}$
9	Regularity	Log ($\frac{P_s}{P_s - P_{\text{conv}}}$)

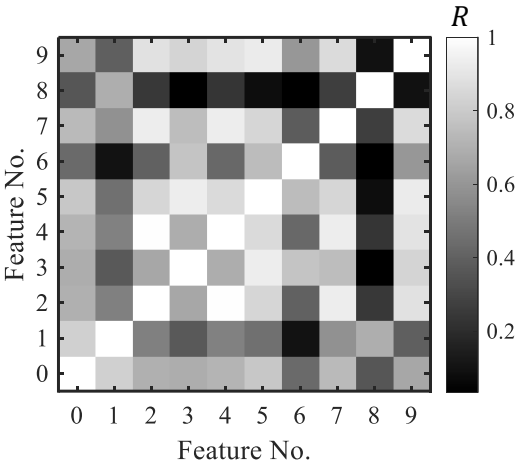

Figure 3.5. A heatmap of correlation between a different pair of features. Feature 0 is $\frac{D_{eff}}{D_0}$, and other feature numbers refer to Table 1. Notations: A_s is the projected area of an aggregate particle (m^2); A_{cir} is the area of the minimum circumscribing circle (m^2); d_c is the diameter of a circle having the same projected area as the particle (m); d_{cir} is the diameter of the minimum circumscribing circle (m); r_{circ} is the radius of the minimum circumscribing circle (m); P_c is the perimeter of a circle having the same projected area as the particle (m); r_{insc} is the radius of the largest inscribed circle in the particle (m); r_c is the radius of the circles that approximate the corners of the particles contour (m); P_S is the perimeter of the aggregate particles (m); P_{conv} is the convex perimeter of the particle (m); S and L are the width and length of an aggregate particle (m).

With the development of high-resolution cameras, 2D aggregate outline is of very easy access to be achieved. It is very promising to correlate 2D shape indices to effective diffusivity in cement composites. As previous illustration, the morphology of the irregular aggregate is generated just by two compressed factors, F_d and R_r. F_d is a global geometrical parameter introducing how the morphology feature is altered at every length scale. R_r is another geometrical index to describe the overall irregularity of aggregates, which defines how the irregular shape is different from the area-equivalent circle. Other common single-length

geometrical parameters are also included to describe the morphology of irregular shape, as shown in Table. 3.1. In Guida et al. (2020), three non-dimensional shape parameters are introduced over the range of experimentally accessible scales: i) aggregate shape at the macro-scale, ii) aggregate roundness at the mesoscale, and iii) aggregate texture (surface roughness) at the micro-scale. The overall form carries information on the proportions of the particle, *i.e.*, how isometric or elongated the particle is; roundness (angularity) accounts for local features of the aggregates (Wadell, 1932b; Ferellec et al., 2008). Furthermore, similar to Guida et al. (2020), three scale-dependent shape factors, such as sphericity, roundness and roughness, have been defined, and the sphericity has been defined in five ways including area sphericity, diameter sphericity, circle ratio sphericity, perimeter sphericity, width to length ratio sphericity (or elongation) (Zheng and Hryciw, 2015). According to Mollon and Zhao (2012), regularity can be used to measure the roughness alternatively. Sensitivity studies are performed to inspect the correlation with $\frac{D_{\mathrm{eff}}}{D_0}$ in the following.

For the sensitivity study, F_d is controlled to be varied from 1.05 to 1.85 with the increment of about 0.04, and R_r is varied from 0.06 to 0.99 with an increment of about 0.05. Meanwhile, for the existence of irregular aggregates in hexagonal packing at ϕ of 50%, only 179 pairs of F_d and R_r with F_2 no more than 0.26 are selected, as F_2 mainly controls the elongation of irregular aggregates. After that, the linear regression analysis is needed to calculate the correlation indices between geometrical parameters and $\frac{D_{\mathrm{eff}}}{D_0}$ .All possible geometrical parameters discussed above have been summarised in Table 1, all of which are less or more correlated with each other (Mora and Kwan, 2000). Furthermore, sensitivity studies between geometrical parameters are conducted. The heatmap in Figure 3.5 lists the score of correlation for each pair of features.

From Figure 3.5, Feature 3-9 are referred to the mostly used classical single-length-scale geometrical parameters, where Feature 3-7 describe the forms of irregular aggregate in five different ways as in previous discussion (Zheng and Hryciw, 2015). Among these five different forms (Feature 3-7), they are almost highly correlated with each other, except for the correlation between perimeter sphericity (Feature 6) and diameter sphericity (Feature 7). Furthermore, roundness (Feature 8) is almost rarely correlated with these five different descriptions about forms (Feature 3-7). That is also consistent with the previous statement that roundness is one of three scale-dependent geometrical factors (Zheng and Hryciw, 2015). Also, regularity (Feature 9) to characterise the surface roughness of irregular aggregate should be

independent of these five aspects of forms (Feature 3-7) and roundness (Feature 8). However, it is found to be correlated with five different forms (Feature 3-7). Look back to the definition of regularity, in which perimeter is included, thus it is for general shape in the length scale of form, which is larger than roundness. While roughness denotes geometry smaller than roundness, we claim that regularity is not appropriate to describe roughness, contradicting Guida et al. (2020). Geometrical parameters except for perimeter sphericity (Feature 6) and roundness (Feature 8) are relatively highly sensitive to the $\frac{D_{eff}}{D_0}$ (Feature 0). F_d and R_r are the two most sensitive shape indices to effective diffusivity.

As in Equation 3.9, F_d and R_r are independent of each other, and able to describe the morphology of the irregular aggregate shape at multiscale by including all traditional geometrical parameters. Furthermore, either F_d (Feature 1) or R_r (Feature 2) also highly correlated to $\frac{D_{eff}}{D_0}$ (Feature 0). This indicates that the prediction equation of $\frac{D_{eff}}{D_0}$ can be effectively deduced only using F_d and R_r without including other shape factors. Therefore, $\frac{D_{eff}}{D_0}$ (Feature 0) due to the irregular aggregate will be further analysed only with F_d (Feature 1) and R_r (Feature 2) in the following part.

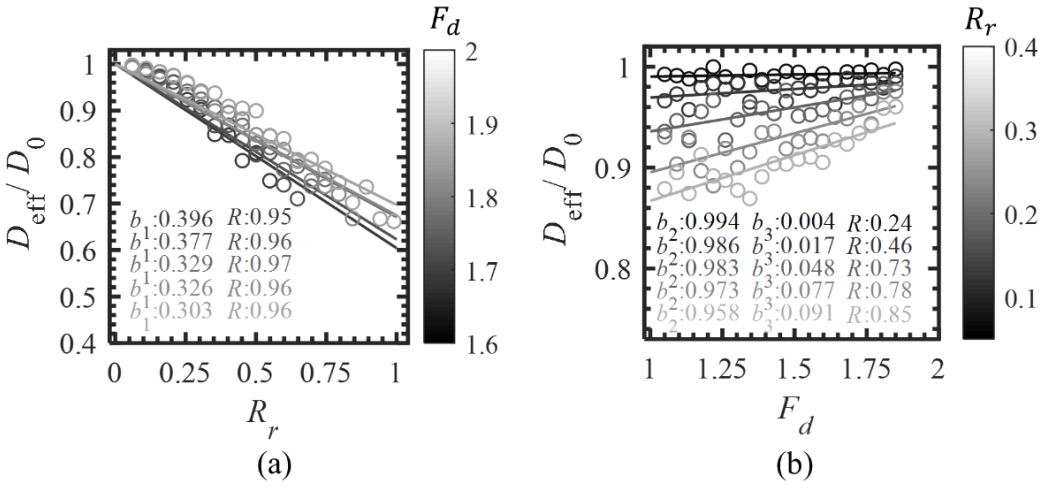

Figure 3.6: (a) Relation between R_r and $\frac{D_{eff}}{D_0}$ at $F_d \in [1.65\ 1.85]$ with the fitting of Equation 3.14 and (b) relation between F_d and $\frac{D_{eff}}{D_0}$ at $R_r \in [0.06\ 0.26]$ with fitting of Equation 3.15.

Here we take $\phi = 50\%$ as an example, of which the derivation process can be extended to ϕ of other values. In Figure 3.6 (a) and (b), R_r versus $\frac{D_{eff}}{D_0}$ at $F_d \in [1.65\ 1.85]$ and F_d versus $\frac{D_{eff}}{D_0}$ at $R_r \in [0.06\ 0.26]$ are selected to plot. As $R_r \to 0$, irregular aggregates become circular,

causing $\frac{D_{\text{eff}}}{D_0} \to 1$. Furthermore, the maximum value of F_d is restricted to 2 in Equation 3.8, because of our 2D studies. We apply the linear fitting of each relation:

$$\frac{D_{eff}}{D_0}(R_r) = 1 - b_1 R_r, \tag{3.14}$$

$$\frac{D_{eff}}{D_0}(F_d) = b_2 - b_3(2 - F_d), \tag{3.15}$$

where b_1, b_2 and b_3 are fitting parameters. For negative correlation between R_r and $\frac{D_{\text{eff}}}{D_0}$ shown in Figure 3.6(a), the correlation coefficients of each fitting are all above 0.9. Note that the b_1 value is increased at the larger F_d. For F_d versus $\frac{D_{\text{eff}}}{D_0}$, linear fitting shows a small correlation coefficient of R at small R_r. At $R_r \to 0$, indicating irregular grain shapes approximate circular, the decreases in the F_d shows the small fluctuation below $\frac{D_{\text{eff}}}{D_0} = 1$. As R_r increases, Figure 3.6(b) shows a more apparent positive correlation between F_d and $\frac{D_{\text{eff}}}{D_0}$. Furthermore, b_3 is increased at larger R_r. In addition, b_3 value is decreased as increased R_r causes aggregate shape more irregular. Both b_2 and b_3 in Equation 3.15 are dependent on R_r, whilst only b_1 in Equation 3.14 is dependent on F_d. Therefore, by combining the two, the relation between F_d, R_r and $\frac{D_{\text{eff}}}{D_0}$ can be simply defined as:

$$\frac{D_{eff}}{D_0}(F_d, R_r) = 1 - (m_1 + m_2(2 - F_d))R_r, \tag{3.16}$$

where $m_1 = 0.286$ and $m_2 = 0.230$ are two fitting parameters. Among all 179 generated two-phase composites, the relation between F_d and R_r and $\frac{D_{\text{eff}}}{D_0}$ in Figure 3.7(a) shows that increasing both F_d and R_r can even result in an almost 40% reduction in $\frac{D_{\text{eff}}}{D_0}$ at $\phi = 50\%$. Also, the plane fitting of Equation 3.16 has the correlation coefficient $R = 0.948$, which proves fitting accuracy as well as the strong correlation of F_d and R_r to $\frac{D_{\text{eff}}}{D_0}$. It can be further explained that due to the throat size influenced by the concave shape, the standard deviation of relative throat size distribution σ_{rt} for irregular aggregate is also dependent on F_d and R_r, as in Figure 3.7(b). It can be found that σ_{rt} is decreased by an increase in F_d and decrease in R_r. Furthermore, the relation σ_{rt} and $\frac{D_{\text{eff}}}{D_0}$ in Figure 3.7(c) shows that an increase in σ_{rt} causes the decrease in $\frac{D_{\text{eff}}}{D_0}$. Therefore, $\frac{D_{\text{eff}}}{D_0}$ is highly affected by both F_d and R_r, which change the

morphology of aggregate shape and further change the throat size for diffusive paths, as in Figure 3.4(b).

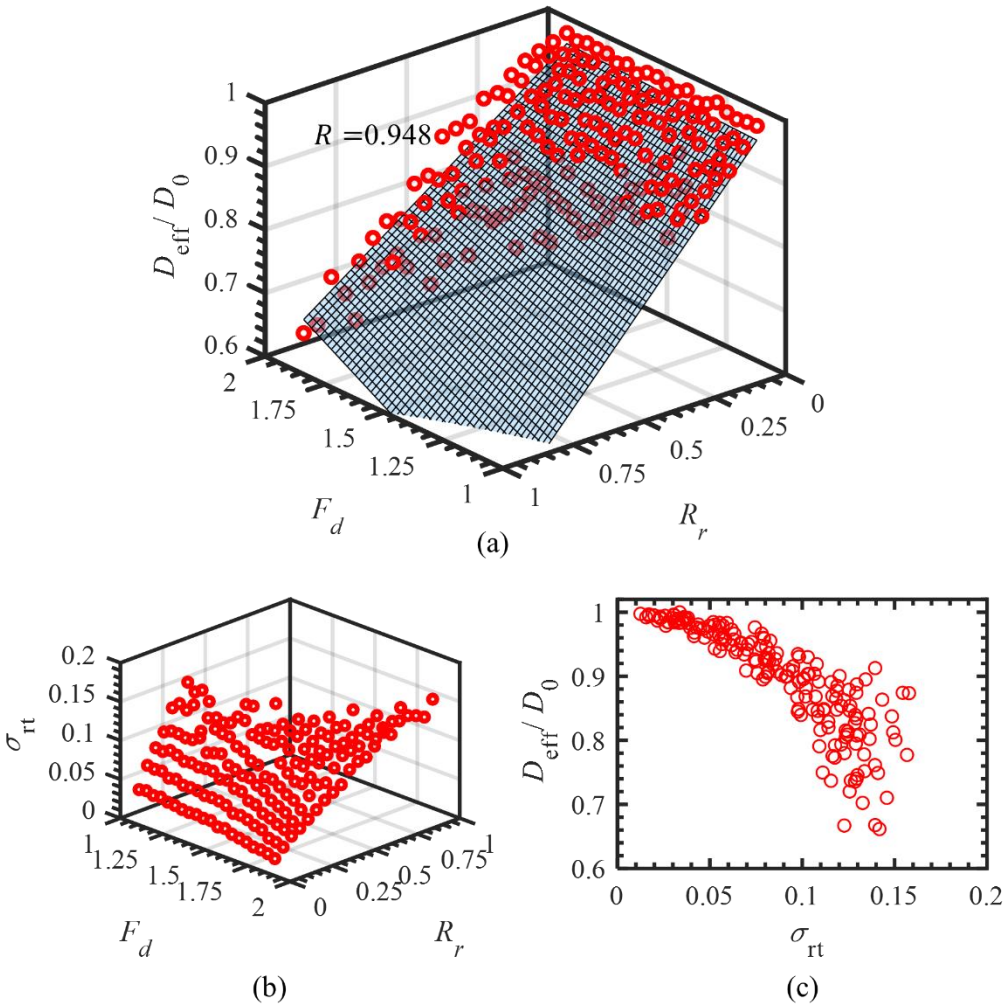

Figure 3.7: (a) 3D plot of relation between F_d, R_r and $\frac{D_{\text{eff}}}{D_0}$ with the plane fitting of Equation 3.16, and (b) 3D plot of relation between F_d, R_r and σ_{rt} and (c) plot of σ_{rt} and $\frac{D_{\text{eff}}}{D_0}$.

3.4. Summary

In this chapter, the steady-state diffusion is modelled through FEM using Fick's first law. The influence of aggregate characteristics on the effective diffusivity of the cement-based composite has been specifically investigated. Main conclusions of this study can be drawn as:

- More disordered packing has a larger standard deviation of throat size distribution. Larger disorder index and standard deviation of throat size distribution both induce the

lower effective diffusivity, while throat size is more sensitive to and the first factor determining effective diffusivity.

- Lower aspect ratio contributes to decreasing effective diffusivity, especially at the higher aggregate fraction. Furthermore, smaller aspect ratio causes the larger standard deviation of relative throat size distribution, resulting in larger fluctuation in effective diffusivity. However, when compared with the reduction in effective diffusivity induced by low elongation, the fluctuation can be negligible.
- The irregular aggregate with the concave shape causes significantly smaller, *e.g.*, even to about 30%, effective diffusivity than the other regular shapes of the same aggregate fraction. Fractal dimension and relative roughness are relatively more sensitive geometrical parameters to the effective diffusivity than other classical single-length parameters. At specific aggregate fraction, one promising prediction model for effective diffusivity can be proposed with only the two shape factors.

This work has highlighted the role of irregularly shaped aggregates on effective diffusivity, which can be further interpreted through tortuosity, as quantified by the throat size distribution. Future work can be undertaken to further develop this investigation by addressing the limitations as follows: (1) The current study is limited to 2D modelling, which may result in more obstructed and tortuous diffusion compared to 3D cases, where pore connectivity is enhanced due to the availability of out-of-plane diffusion paths. The quantitative differences between 2D and 3D cases should be systematically evaluated; (2) This work considers only mono-sized aggregates with uniform packing to assess the effect of aggregate shape. The differences in diffusivity between artificially generated models (based on FFT) and realistic concrete microstructures should be further investigated; (3) More rigorous validation should be conducted using scanned images to reconstruct realistic concrete models, which can then be compared with corresponding experimental results. This would enable more reliable calibration of material properties for subsequent parametric studies on shape effects using FFT-based models; (4) The current study considers anisotropy only through one-way diffusion. Diffusivity in multiple directions should be investigated to fully capture anisotropic behaviour.

Chapter 4 Mesoscale Modelling of Triaxial Concrete Fracture

In this chapter, acknowledging the complex stress conditions experienced by marine structures, mesoscale modelling using the finite element method (FEM) is conducted to first investigate the three-phase concrete fracture behaviour subjected to triaxial compression with the presence of confining pressure. The realistic aggregate shape, characterised by the fractal dimension, is generated to emphasise the effects of aggregate morphology on the concrete strength under varying confining pressures. Quantitative evidence from a microscopic perspective on local stress, damage evolution, and crack patterns is provided to support macroscopic observations. As a result, similar to uniaxial tests, rougher aggregate with the higher fractal dimension leads to greater compressive strength of concrete. With increasing confining pressure, this effect can be amplified. We further find that the data for uniaxial-strength-normalised triaxial strength and confining pressure of concrete specimens with various aggregate shapes are well-calibrated with experimental results and can collapse onto a single universal curve. As microscopic evidence shows, the heterogeneity of stress distribution for aggregate shapes, which deviates from each other at initial loading, finally converges. Local damage exhibits a universal competition between the ITZ and aggregates, with increasing fractal dimension of aggregates, under varying confining pressures, and explains the occurrence of the scaling law in the relationship between triaxial compressive strength and confining pressure. The same competition extends to macro-cracks and is reflected in crack volume (or area) and cluster size. The effort in systematic mesoscale modelling enriches the understanding of the influence of material heterogeneity in concrete under complex stress conditions in marine environments.

This chapter has been devoted to the following paper:

Liu, Q., Wei, D., Gan, Y., 2025. Mesoscale Modelling of Triaxial Concrete Fracture: The Role of Aggregate Shapes. *International Journal of Mechanical Sciences*, 110570.

4.1. Introduction

As a typical example of the matrix-inclusion composites containing hard particulates, concrete has emergent characteristics different from its components. Concrete industries have a worldwide consumption of about 17 billion metric tonnes per year (Ashby, 2012). Due to the presence of mismatched mechanical behaviour with the material constituents, one of the fundamental challenges is to quantitatively relate the microscale information to the emergent macroscopic properties (Sun et al., 2024b). It is well acknowledged that representing concrete as a homogenous material, with the advancement and development of non-local theory (Pijaudier-Cabot and Bažant, 1987) and strain gradient models (Sun and Poh, 2016), has made significant progress. Nevertheless, the spatial heterogeneity is hard to be captured by such kind of mean-field approximations. The quasi-brittle behaviour of concrete is strongly influenced by the heterogeneity of its material constituents and interactions manifested over a large range of length scales (Garboczi and Bentz, 1993): from nano- to meso-scale, namely nanometre (hydrated cement paste (Vandamme and Ulm, 2009)) to centimetre (the largest aggregate scale (Garboczi, 2002)). Zaitsev and Wittmann (Zaitsev and Wittmann, 1981) conduct pioneering study on concrete as a hierarchical structure with various length scales of inhomogeneities. The primary inhomogeneity of concrete is found at the mesoscale, which has been widely treated as the most sought-after scale to focus on the influence of heterogeneity on macro mechanical response (Kim and Al-Rub, 2011). At such a scale, besides voids, concrete is composed of three phases, namely mortar matrix, coarse aggregates, and interfacial transition zone (ITZ) jointed the two phases. Even under uniform loading conditions, the heterogenous internal stress field could be encountered, resulting in severe stress concentrations, which are of high possibility to cause crack initiation at the weakest phase—ITZ (Chen et al., 2024). Note that the multi-scale approach dedicated to the collective mechanical response can also be realised by upscaling the underlying mesoscale information as a constitutive law to the macroscopic scale to minimise the phenomenological assumptions and fitting parameters.

For experiments, a significant portion of the fundamental understanding of concrete fracture behaviour is derived from the results of simple uniaxial tests (Wu et al., 2021a). However, uniaxial tests fail to reflect the real mechanical responses of concrete structures subjected to complex multiaxial stress conditions. Although replicating the real stress conditions of concrete in experimental studies is challenging, some progress has still been made in the study of triaxial fracture of concrete (Papanikolaou and Kappos, 2007). As a rock-like

material, some empirical failure criterions or stress-strain relations (such as the Mohr-Coulomb criterion), inspired by rock mechanics, are developed to predict the peak compressive stress of concrete; among them, three categories of stress-strain curves can be summarised: proper rational fraction, improper rational fraction, and polynomial equations (Ouyang et al., 2022). Similar to the famous Hoek-Brown criterion (Brown, 1970; Hoek and Martin, 2014) in rock mechanics community, in conventional triaxial tests on cylindrical concrete domain, influences of σ_2 on compressive strength cannot be specifically included, with σ_1, σ_2, and σ_3 being principal stresses and $\sigma_1 > \sigma_2 = \sigma_3$. Meanwhile, the true triaxial compression tests, that are closer to real concrete stress conditions with the macro stress anisotropy, $\sigma_1 > \sigma_2 > \sigma_3$, are of higher priority when morphology anisotropy comes into play. Bridging length scales, a few studies have highlighted the influence of meso-scale heterogeneity in concrete on macroscopic failure criterion, with a particular focus on aggregate type, *e.g.*, natural and recycled aggregates, (He and Zhang, 2014) and aggregate morphology (Wang et al., 2022). However, there is insufficient evidence to support the changes in the microscale localisation and failure mechanisms within the concrete due to differences in aggregate properties. For this concern, one of studies employs X-ray computed tomography (CT) combining with in situ tests to identify the strain localisation and crack network development within local regions, *e.g.*, mortar, aggregate and pore, of concrete under triaxial stress conditions (Wu et al., 2023a). However, none of the tests consider the effects of aggregate shape, when local damage and failure of concrete are investigated under uniaxial or triaxial stress conditions. From the overview of experiments, conducting the refined study on the effects of aggregate shape and eliminating disturbance of other factors remain challenging. Additionally, achieving a controlled variation in the shape irregularity of aggregate is also difficult. Considering the above concerns, the effects of aggregate shape on the underlying micro-mechanics rooted in grain-scale heterogeneity remains to be emphasised, in order to clarify the rigorousness and validity of macroscopic findings.

Mesoscale simulations have been proven as an effective alternative to experimental approaches to reveal the influences of local heterogeneities on the complex global response (Zaitsev and Wittmann, 1981). Up to now, mesoscale studies on concrete fracture behaviour can be classified into three categories, namely the finite element method (FEM) in the context of continuum mechanics, the discrete element method (DEM) and the combination of such two methods. Due to the maturity and rigorousness of continuum mechanics, many continuum-fashion mesoscale models have been proposed, such as the truss model (Bažant et al., 1990)

and the lattice model (Schlangen and Van Mier, 1992). Considering that substantial cracks could initiate, grow, and coalesce and much more input energy is consumed by frictional contacts at these cracks than the newly created fractures themselves (Zhai et al., 2019), accurate simulations of fracture evolutions in concrete require careful considerations of a large number of discrete contacts. Since then, DEM featured with contact searching and determining becomes popular in concrete-like-composite crack modelling; cracks are enriched in the bonds between connected elementary spheres in 3D (or circles in 2D) DEM. However, many physically meaningless local parameters in DEM parallel bond models are required to be fitted. The primary bulk elasticity, in terms of Young's modulus and Poisson's ratios, is highly dependent on element packing structures; albeit the same calibrated parameters are utilised, the elasticity can no longer be warranted (André et al., 2019) when the packing structure is alternated. The combined finite and discrete element method (FDEM) (Wei et al., 2020b), importing the capability of DEM to handle contacts to explicit FEM framework with crack initiations and evolutions, fits within the context of the accurately simulating fracture behaviour of mesoscale concretes.

Mesoscale concrete models often require topological reconstructions of different material phases. The bottom-up method—a dense or loose random packing of artificially shaped and sized aggregates with mortar matrix filling the space between them—may be the most popular among others (Huang et al., 2023). Due to the resulting loose packing structure, the target solid fraction of aggregates is typically achieved by mechanical compressions, such as the die compaction, which could induce strong strain localisations or even shear bands within the domain, hindering the investigation of heterogeneity-influenced concrete fracture behaviour with the natural adequacy. By contrast, during the real concreting process, coarse aggregates are homogenously suspended within the mortar phase, with less variances in local aggregate fractions. Moreover, aggregate shapes utilised in most of such bottom-up methods are simple convex shapes, *e.g.*, spheres, polyhedrons and ellipsoids (Wang et al., 2016b). Natural grains have fractal-like shapes with higher irregularities on their surfaces, where more stress concentrations can be induced on the joints between the mortar and the aggregate phases. In recent years, with the development of non-destructive 3D imaging techniques (including magnetic resonance imaging (MRI), and X-Ray and neutron tomography), real meso-morphologies became accessible. It has to be mentioned that in situ (Landis and Keane, 2010) and ex situ (Poinard et al., 2012) X-Ray mechanical tests are also conducted on quasi-static localised deformation on mesh-scale concrete. However, unavoidable, yet large creep strains

are encountered in the small-scale concrete specimen due to the long durations required form imaging towards full 3D spatial evolutions. Although the scanned 3D heterogeneity of concretes with packed aggregates can be readily imported into numerical models, the subsequent mechanical analysis is highly sensitive to the randomly packing structure (Wang et al., 2016b). Consequently, the numerical method seems to be a plausible alternative to isolate effects of heterogeneity rooted in aggregate morphology on concrete strength from other dominant factors. Another type of method in numerically modelled mesoscale heterogeneity is based on the top-down fashion. In these methods, global descriptors, such as aggregate fraction, specific formulations of the two-point correlation function, and more microscale statistical information extracted from the real 3D images, are realised by randomised processes (Zhang and Torquato, 2013). Before the net homogenous distribution of aggregates is ready, unphysical, although hard to determine, features must be removed (Tahmasebi et al., 2017), followed by separating or labelling single aggregates from the whole solid phase. These steps could bring additional uncertainties in these aggregate shapes, such as their sizes, and even the aggregate grading cannot be exactly sustained as the target distribution, as the first mesoscale factor to determine the concrete strength (Stock et al., 1979). To capture realistic heterogeneously-localised deformations of mesoscale concrete specimens, an explicit method must be proposed to account for both the homogenously packing structures of aggregates and the high-fidelity aggregate morphology features.

For the mesoscale modelling of concrete fracture, the inherent heterogeneity of the mesoscale structure can be characterised by assigning distinct material properties to the mortar, aggregate, and interfacial transition zone (ITZ) phases (Zhou et al., 2024a; Zhu et al., 2024; Ge and Chen, 2025; Wu et al., 2025). This is based on constitutive laws implemented in various numerical models, such as the CDP model (Naderi et al., 2021; Cai et al., 2025), cohesive element method (Naderi and Zhang, 2021b; Wang and Xu, 2024), Johnson–Holmquist Concrete (JHC) model (Wu et al., 2023a; Wu et al., 2023b) and others (Pan et al., 2025). Interestingly, a novel combination of numerical models has been adopted in some studies, where the CDP model is used for the solid elements of mortar and aggregates, while zero-thickness cohesive elements considering the ratio of shear to normal strength are applied to represent the ITZ phase (Wang et al., 2020; Wang et al., 2021). Given appropriate material properties for each material phase, mesoscale models can effectively capture the stress–strain response of concrete and have been widely used to investigate fracturing processes under various stress conditions, including static (Naderi and Zhang, 2021b; Chandrabhan and Kumar,

2024; Ren et al., 2024), dynamic (Chandrabhan and Kumar, 2024; Singh and Gupta, 2024; Ning et al., 2025), uniaxial (Naderi and Zhang, 2021b; Wang et al., 2024c; Wang and Xu, 2024; Zhang et al., 2024a) and multiaxial (Chandrabhan and Kumar, 2024; Singh and Gupta, 2024; Wang et al., 2025c) loadings. The 3D mesoscale structures of concrete in these studies are generated using either scan-dependent, *i.e.*, X-ray computed tomography or scan-independent approaches, *i.e.*, computer-based packing algorithms. The influence of material properties or the morphology of material constituents, such as the ITZ (Maleki et al., 2020; Yang et al., 2024), aggregates (Yang et al., 2024; Wang et al., 2025a), and pores (Wang et al., 2016b), on concrete fracture has been extensively studied. Although digital imaging allows the mesoscale structure to capture greater heterogeneity in concrete, including pores in the mortar phase, which significantly affect the formation of crack networks (Huang et al., 2015; Huang et al., 2022; Huang et al., 2023), few studies focus on the influence of aggregate shape. This is more commonly explored using the latter approach, such as the take-in-place method (Wang et al., 2020; Wang et al., 2021; Liu et al., 2024b; Wang et al., 2024c), random extension method (Ren et al., 2023; Gao et al., 2024; Wei et al., 2024), and Voronoi-tessellation-based method (Wei et al., 2020b; Zhang et al., 2023; Su et al., 2024; Wang et al., 2024a; Liang et al., 2025), which generate particle packings through computer programming.

Some studies have highlighted the effects of aggregate shape on concrete strength (Wang et al., 2016b; Wei et al., 2020b; Naderi et al., 2021; Naderi and Zhang, 2021b), local damage mechanisms (Wang et al., 2016b; Wei et al., 2020b), and failure patterns (Wang et al., 2016b; Naderi et al., 2021; Naderi and Zhang, 2021b). For instance, compared to cases with spherical aggregates, Wei et al. (2020b) concluded that more concave and irregular aggregate shapes can induce higher stress concentrations and enhance the compressive strength of concrete. Moreover, this study quantitatively analysed the relationship between local damage and concrete strength, showing that with more concave aggregate shapes, cracking tends to occur more within the aggregates and less in the ITZ. On another note, although some studies have compared the failure patterns of concrete with different aggregate shapes, these comparisons often rely heavily on visual observations and lack quantitative evidence (Naderi et al., 2021; Naderi and Zhang, 2021b). While stress distribution in the host matrix is used as an indicator of the fracture behaviour of heterogeneous materials (Laubie et al., 2017b), it has not yet been applied to analyse the influence of aggregate shape. Looking at existing literature on mesoscale studies on the influence of aggregate morphology, most are only dedicated to uniaxial compression or tension. Although some numerical progress has been made in investigating the

triaxial failure of concrete, these efforts have primarily focused on stress-strain responses (Qin and Hua, 2012; Singh and Gupta, 2024), without incorporating realistic aggregate shapes in concrete models. Moreover, assessing the effect of aggregate shape only based on macroscopic responses is insufficient. It is essential to support such assessments with comprehensive and quantitative analysis of the local responses of concrete at the microscopic level. However, such investigations under triaxial loading conditions are still lacking.

Based on the above discussions, in this study, we conduct mesoscale FEM modelling on triaxial compression induced fracture behaviour of three-phase concretes. The aggregates are generated with realistic shapes and are assumed to be distributed in a homogeneous mortar, without considering the influence of pores. The effect of aggregate shape on concrete strength under triaxial loading is investigated. We aim to enrich the understanding of this effect, with a focus on local responses, including stress distributions, local damage, and crack patterns, which may provide insights into variations in macroscopic strength. The reminder of this paper is structured as follows. In Section 2, the packing/parking process is firstly introduced for the 3D mesoscale concrete structure containing the irregularly shaped aggregates; with the target size distribution in hand, their positions and orientations are inherited from the Voronoi tessellation of the domain, while specific morphology features are realised by the combined method of random field and Fast Fourier Transformation. The FEM mesh generation and constitutive models, including the damage laws for cohesive interface elements of ITZ and concrete damage plasticity (CDP) of both aggregate and mortar elements, are also provided. Section 3 validates our numerical results by comparing them with some existing experimental results, and then demonstrates the macroscopic stress-strain curves under both uniaxial and triaxial compression loading conditions. The universality of aggregate-shape-influenced triaxial strength is analysed by quantitative statistics of microscopic stress distributions, evolutions of local damages, and crack patterns. Main conclusions are finally summarised in Section 4.

4.2. Methodology

In this section, the mesoscale modelling of concrete fracture under the triaxial stress condition is conducted in two stages. Mesoscale structures with irregularly shaped aggregates are generated to represent the cubic concrete specimen in Section 4.2.1. For the packing algorithm, the Voronoi tessellation as well as generation of fractally shaped aggregates within a predefined cubic space are illustrated in Section 4.2.1.1 and 4.2.1.2, respectively. The

construction of the mesoscale structure of a three-phase cubic concrete specimen, including mortar, ITZ and aggregate, is then provided in Section 4.2.1.3. Section 4.2.2 introduces the constitutive laws for mesoscale structure of concrete including the CDP for mortar and aggregate in Section 4.2.2.1 and cohesive element method for ITZ in Section 4.2.2.2, which are employed for the finite element modelling. In Section 4.2.3, boundary conditions for simulating the quasi-static triaxial tests are described.

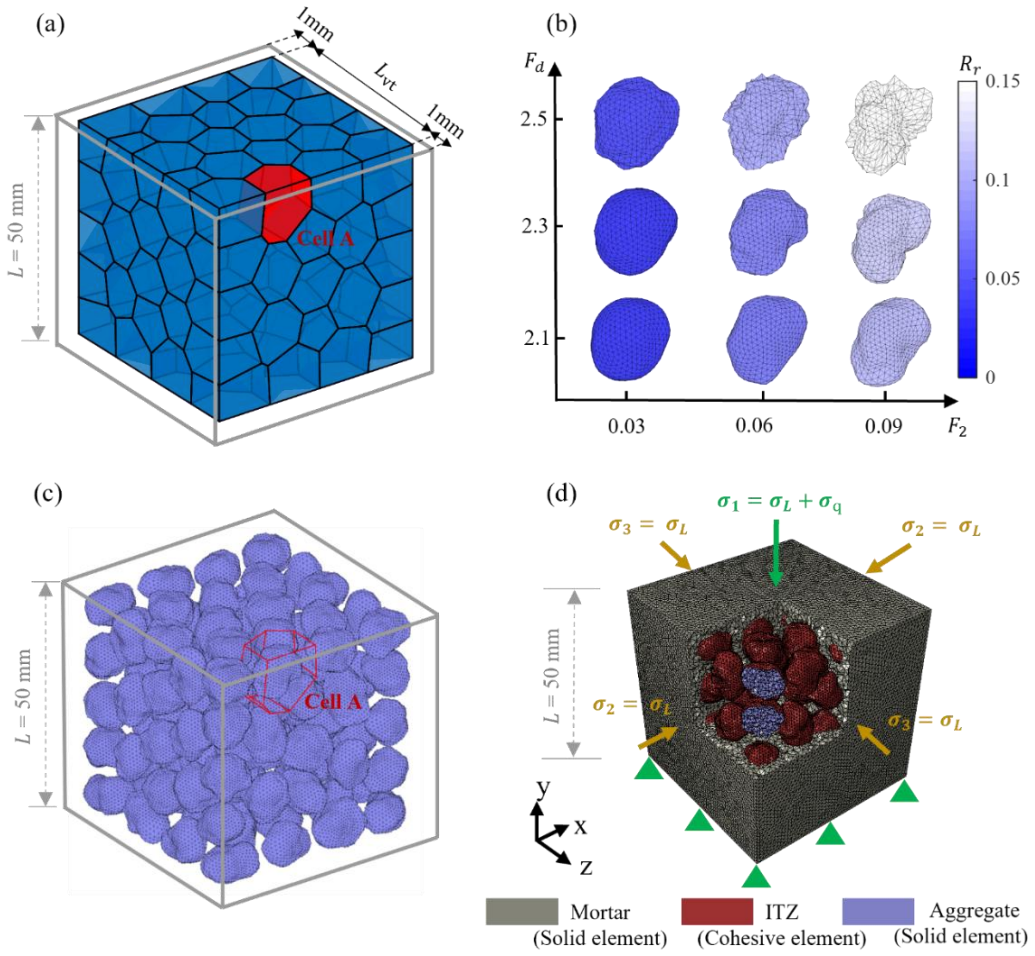

Figure 4.1: (a) A typical Voronoi tessellation, (b) irregular aggregate shapes varying with fractal dimension, F_d, and the normalised second Fourier descriptor, F_2, in Cell A of (a), of which the colour bar is used to denote the relative roughness, R_r, (c) packing of irregularly shaped aggregates corresponding to the Voronoi tessellation in (a), and (d) schematic diagram of finite element (FE) modelling of the triaxial test, with arrows indicating the directions of the principal stresses of σ_1, σ_2 and σ_3.

4.2.1. Mesoscale structure of concrete

The effects of aggregate shape under triaxial stress conditions are investigated using a cubic concrete specimen, where the aggregates are assumed to be non-contacting and fully contained within the specimen domain. The key to generate the mesoscale structure is to produce initial aggregation packing within a reasonable range of packing density. To handle the packing problem of realistic shaped aggregates beyond idealised convex shapes, we have referred to the work of Mollon and Zhao (2014). A specific cubic space can be divided into Voronoi cells. Then, the irregular aggregate shape characterised by the fractal dimension, F_d, is generated fully inside each Voronoi cell. By such packing processes, any contact or overlapping can be avoided. As shown in Figure 4.1(a-c), when the aggregate shapes are varied within the same Voronoi cell, the spatial distribution and orientation, which are factors affecting the mechanical performance of heterogeneous materials (Laubie et al., 2017b; Liu et al., 2024a), are kept the same for the generated shape. This can refine the investigation into the effects of aggregate shape. Mesoscale structures of concrete are typically generated in accordance with the Fuller curve to achieve a more realistic aggregate grading, which has been shown to significantly affect concrete strength, particularly with regard to the effects of maximum aggregate size (Jin et al., 2021; Jin et al., 2022a). To minimise interference from such effects in this study, nearly mono-sized aggregates are assumed in the concrete specimens to maintain consistent grading across different aggregate shapes, while still preserving the main heterogeneity of concrete. Although these assumptions allow us to control only the aggregate shape, they lead to a simplified mesoscale structure that does not fully represent real concrete. This is a limitation that will be addressed in future work by incorporating aggregate characteristics under more realistic conditions.

4.2.1.1 Voronoi tessellation

In the 3D domain space $\Omega \subset R^3$, a Voronoi tessellation $\{VT_i\}_{i=1}^{M}$ is a partition of Ω into M regions close to a set of seeds $\{S_i\}_{i=1}^{M} \subset \Omega$, if $VT_i \cap VT_j = \emptyset$ for $i \neq j$ and $\bigcup_{i=1}^{M} VT_i = \Omega$. Each Voronoi cell VT_i corresponding to the seed S_i is defined in Equation 4.1 (Zhang et al., 2012a). The Voronoi cell VT_i consisted of every point x in the region:

$$VT_i = \{x \in \Omega, ||x - S_i|| \leq ||x - S_j||, \text{for } j > 1,\ j \neq i\}, \tag{4.1}$$

where $||\cdot||$ denotes a Euclidean distance in R^3. The energy functional associated to sets of $\{VT_i\}_{i=1}^M$ and $\{S_i\}_{i=1}^M$ is used to introduce the differences of Voronoi cell geometry (Zhang et al., 2012a):

$$Q(\{S_i\}_{i=1}^M, \{VT_i\}_{i=1}^M) = \sum_{i=1}^M \int_{VT_i} \rho_{vt}(x)||x - S_i||\, dx, \tag{4.2}$$

where $\rho_{\mathrm{vt}}(x)$ is a density function over a domain. Clearly, the Q is minimised only if Voronoi tessellation has the seed S_i coincided with the mass centroid of Voronoi cell $C_i = \int_{VT_i} x\rho_{\mathrm{vt}}(x)dx / \int_{VT_i} \rho_{\mathrm{vt}}(x)dx$, *i.e.*, Centroid Voronoi tessellation. Meanwhile, the Voronoi cell geometry becomes the most stable. Arbitrarily chosen seeds are usually not the mass centroids of their associated Voronoi cells, and reaching the coincidence is very difficult. The Lloyd iteration is used in this study to minimise Q by alternately moving the seed to the mass centroid of the Voronoi cell (Du et al., 1999). The number of Lloyd iterations N_l is a key factor to control the aggregate size and will be determined with the appropriate value later.

4.2.1.2 Packing for irregular aggregate shapes

In the 3D case, the existing method, *i.e.*, a combination of the random field and Fourier-shape-descriptor based method, from the work of Mollon and Zhao (2014), is employed to generate the irregularly shaped aggregate inside each Voronoi cell. In the current paper, based on the codes (MATLAB program accessible via http://guilhem.mollon.free.fr), we have improved this method by introducing the fractal dimension, F_d, which is a multiscale geometric index to characterise the aggregate shape. For the Fourier descriptor, F_n, the F_0 is normally set to 1 for the normalisation, $F_1 = 0$ ensures that the aggregate centroid has been properly chosen. F_2, F_n for $3 \leq n < 8$ and $n \geq 8$ are used to control the elongation, irregularity and surface roughness of aggregate particles, respectively. For the natural aggregate, F_n for $n \geq 2$ has a roughly linear decrease with the n in the log-log scale. According to Wei et al (2018), the exponential relation between F_n and n can be described using the Hurst coefficient, H, which is associated with fractal dimension, F_d, as follows:

$$F_n \propto n^{-2H}, \tag{4.3}$$

$$F_d = 3 - H, \tag{4.4}$$

where -2H is the slope of relation between log (F_n) and log (n). Thus, F_n can be controlled by F_d and F_2, as below (Wei et al., 2018):

$$F_n = F_2(\frac{n}{2})^{2F_d-6}. \quad (4.5)$$

The relative roughness, R_r, can be used to compute how globally different the irregular aggregate shape is from r_0, the mean radial length (Wei et al., 2020b), as below:

$$R_r = \sqrt{\sum_{n=2}^{\infty}(F_2\left(\frac{n}{2}\right)^{2F_d-6})^2}. \quad (4.6)$$

Given an example of Voronoi cells, *i.e.*, Cell A, in Figure 4.1(a), Figure 4.1(b) shows the aggregate shapes generated at different combinations of F_d and F_2, and we can see higher values of F_d and F_2 causing the aggregate shape with the rougher surface. The size scaling of aggregate from its mass centre is required to not only reach the given packing density but also ensure the aggregate particle completely located inside the respective Voronoi cell. Consequently, any contact or overlapping between aggregate boundaries can be avoided. Then, the packing for irregularly shaped aggregates characterised by the fractal dimension is completed and used to produce the mesoscale structure for the concrete specimen in the following.

4.2.1.3 Generation of material components for the mesoscale model

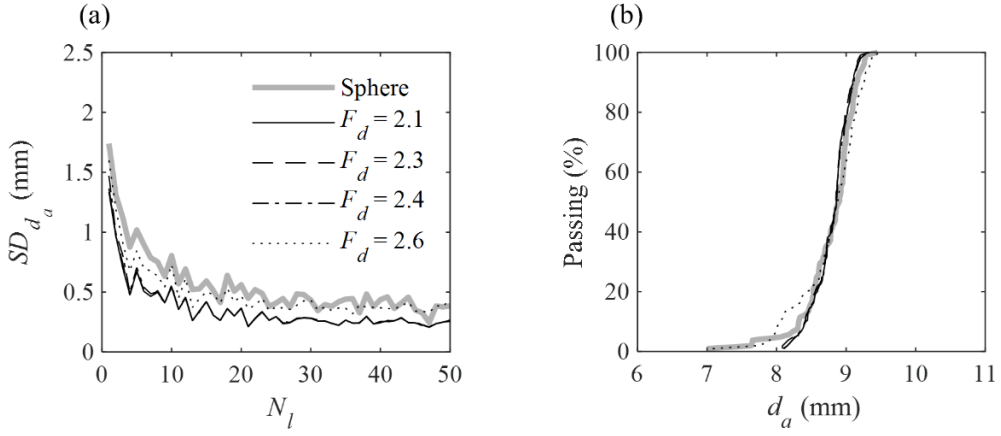

Figure 4.2: (a) Influence of the number of Lloyd iterations, N_l, on the standard deviation of aggregate size, SD_{d_a} and (b) aggregate size distribution curves at $N_l = 50$, with the same legend in (a).

The cubic concrete specimen with the side length of L is used for the modelling of triaxial tests. To prevent aggregate boundaries from contacting with the borders of concrete specimen, the cubic space for the Voronoi tessellation has the side length of L_{vt} is slightly smaller than L as in Figure 4.1(a). Then, if the target solid fraction of aggregate is SF_a, the packing density is required to reach the $SF_a(L/L_{\mathrm{vt}})^3$. For this study, all the mesoscale structures for concrete specimen are constructed with $L = 50$ mm. In some mesoscale models of concrete (Zhou et al., 2017b; Naderi et al., 2021; Naderi and Zhang, 2021b; Chen et al., 2022b; Zhou and Xu, 2023), the aggregate solid fraction often reaches a certain high value exceeding 35%. It is challenging to isolate the influence of a single aggregate characteristic from others. To conduct a refined investigation, the effects of aggregate shape are investigated under a relatively low solid fraction (at 30%), allowing variation of aggregate shape without any overlaps between aggregates. In the virtual samples, the solid fraction, size distribution, and spatial distribution are kept the same across different shapes to emphasis on the effects of aggregate morphology. As mentioned in Naderi et al (2021), L needs to be guaranteed at least three to five times of the maximum aggregate size to be representative. To satisfy this condition and keep $SF_a = 30\%$, our concrete specimen is designed to contain 105 aggregates, as illustrated in Figure 4.1(c). Here, we have defined the aggregate size d_a as the volume-equivalent sphere diameter to within a concrete specimen. Based on the standard deviation of d_a, SD_{d_a}, the effects of the number of Lloyd iterations, N_l, on d_a is investigated, when various aggregate shapes are considered for the mesoscale structure of concrete specimen. As shown in Figure 4.2(a), an increase in N_l leads to a decrease in SD_{d_a} and a more uniform aggregate size distribution. To minimise fluctuations in aggregate size within the concrete specimen, $N_l = 50$ is decided for the Voronoi tessellation. For different aggregate shapes, this results in similar size grading curves as shown in Figure 4.2(b), with d_a mostly varying from around 8 to 9 mm, closely approximating a mono-sized aggregate. Thus, the influence of aggregate size distribution can be minimised in this study.

Given the Voronoi tessellation with 105 seeds and 50 Lloyd iterations as shown in Figure 4.1(a), an example of packing of irregularly shaped aggregates with F_d = 2.3 and F_2 = 0.06 as in Figure 4.1(c) is made for illustrative purposes. It is important to ensure that the meshing of aggregates can capture the shape-induced stress concentration effects. The aggregate surface is defined with 642 vertices and discretised into 1280 nearly uniform surficial triangular meshes, directly generated using the published code from the work of Mollon and Zhao (2014), which incorporates the concept of geodesic structure. The number of surficial meshes is even more

than adequate compared to that used in the work of Wei et al. (2020c), where around 400 uniformly surficial triangular meshes are defined for the irregular aggregate surface and found sufficient to demonstrate the effects of aggregate shape. Therefore, mesh sensitivity for the aggregate will not be a concern in our case. Then, we import aggregate surfaces, as solid geometries, into the Finite Element Software, ABAQUS/Explicit. On another note, the aggregate shapes are artificially generated based on the statistical information obtained from the actual aggregate shapes (Mollon and Zhao, 2014; Wei et al., 2019; Wei et al., 2021). The actual geometry may differ from the experimental and virtual samples, and our modelling effort focuses on demonstrating the influence of these statistical differences which were observed from experimental datasets. A future study using in situ XCT can supplement our current numerical methods by capturing temporospatial information for detailed validations, which represents a gap to be addressed. The mortar phase is generated by cutting the cubic space with $L = 50$ mm using all the solid aggregates. Here, we assume that the mortar phase is homogeneous, without considering the distribution of pores. Based on the surficial mesh size given on the aggregate surface, the tetrahedral element with the size of about 1 mm is used to mesh all solid entities including aggregates and mortar. Representation of ITZ has been debated to the date. The typical value of ITZ thickness varies between 10~50 μm (Maleki et al., 2020). It is challenging to represent the ITZ with physical thickness by the small-scale solid elements (Naderi et al., 2021). In this study, fracture of ITZ is simulated by the zero-thickness cohesive elements, inserted between the mortar phase and aggregates. Eventually, the meshed mesoscale structure of the concrete specimen is generated as in Figure 4.1(d), with about 1,420,000 solid elements and about 135,000 cohesive elements for the ITZ. According to Wang et al. (2016b), 236,260 solid elements are sufficient for the modelling of concrete fracture behaviour, when the mesoscale structure of concrete specimen is of $L = 50$ mm and $SF_a = 30\%$. Therefore, no additional effort is dedicated to the mesh sensitivity study. The simulations are conducted in the High-Performance Computing (HPC) platform.

4.2.2 Constitutive laws for mesoscale model of concrete

Normal-strength concrete is considered here for the modelling of triaxial tests. The respective constitutive models for mortar, aggregate and ITZ have been decided to appropriately present concrete responses. The concrete damage plasticity (CDP) model has been widely used to simulate concrete damage behaviours (Naderi et al., 2021). This study focuses only on triaxial tests with low confining pressure, which is significantly lower than the

uniaxial strength of normal-strength concrete (approximately 30-40 MPa (Yankelevsky, 2024)). Although the entire concrete specimen is subjected to the specified confining pressure, some elements in local regions might experience extremely high pressure, for which we did not optimise the CDP model. For simplicity, as in a previous study (Zhang et al., 2020b), the built-in CDP model can be directly considered for our mesoscale structure to capture the general trend of the confined stress–strain response. Greater emphasis is placed on how different aggregate shapes affect the concrete strength under various low confining pressures, rather than on the stress–strain response in a specific region. Here, the built-in CDP model is implemented to the damage behaviour of both mortar phase and aggregates, whereas aggregates are considerably stronger than mortar matrix in normal-strength concrete. The cohesive interface element (CIE) with the traction-separation law is employed to represent ITZ behaviours. Compared with the mortar, ITZ is relatively weaker, partially due to its more porous structures, which is the main reason why crack initiation of concrete generally occurs at ITZ (Maleki et al., 2020). In the following subsections, the CDP model and cohesive element method are briefly illustrated. More details can be seen in ABAQUS documentation.

Table 4.1: Material properties of concrete constituents.

Component	Material property	Value
Mortar/Aggregate (Concrete damage plasticity, CDP)	Density, $\rho(\mathrm{kg/m^3})$	2200/2600
	Young's modulus, E (GPa)	30/70
	Poisson's ratio, v	0.2/0.2
	Ultimate strength in compression, σ_{cu} (MPa)	45/80
	Ultimate strength in tension, σ_{t0} (MPa)	4/10
ITZ (Cohesive interface element, CIE)	Initial stiffness, k_{n0}, k_{s0}, k_{t0} $(\mathrm{N/m^3})$	1×10^{13}
	Normal strength, t_{n0}, (MPa)	2.4
	Shear strength, t_{s0}, t_{t0} (MPa)	7.2
	Fracture energy, $G_{f,n}, G_{f,s}, G_{f,t}$ (N/m)	30
Fracture (Broken CIE)	Friction coefficient	0.3

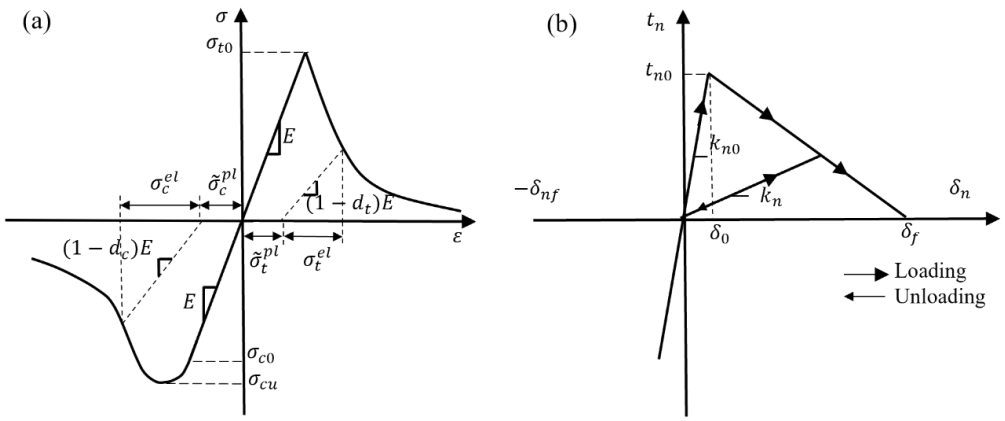

Figure 4.3: Schematic diagrams of (a) stress-strain relationship of the CDP model and (b) bilinear traction-separation law of the cohesive element in the normal direction.

4.2.2.1 CDP model for mortar and aggregate

Compression crushing and tension cracking are considered to be main failure mechanisms given in the CDP model, as in first and third quadrants of Figure 4.3(a), respectively. The stress-strain in both quadrants follow the linear elastic relation before ultimate strength in tension, σ_{t0}, and yield stress in compression, σ_{c0}. The compressive response between yield stress, σ_{c0}, and ultimate strength, σ_{cu}, is defined to be strain hardening. For the issue of mesh sensitivity, which is induced by strain localisation (Maleki et al., 2020), it is suggested in some studies to define tensile softening behaviour by specifying stress–displacement curves using the fracture energy criterion instead of stress–strain (Chen et al., 2018; Maleki et al., 2020; Jin et al., 2021). Such considerations are important when using small solid elements in local regions, which are more susceptible to strain localisation and may even lead to unreasonable numerical results (Chen et al., 2018). In the current study, our concrete model is meshed with a nearly uniform size, which can be sufficiently used to present the aggregate morphology. Thus, our cases can follow similar works (Wang et al., 2020; Xiong et al., 2020b; Wang et al., 2021) and directly use stress–strain to define both compressive and tensile softening behaviour in the CDP model, aiming to obtain an acceptable overall trend in the stress–strain response of concrete, rather than calibrating the model for a specific region. According to Code for Design of Concrete Structures (GB 50010-2010), the compressive strain hardening and softening behaviour are defined as:

$$\frac{\sigma_c}{\sigma_{cu}} = \begin{cases} a_a \frac{\varepsilon_c}{\varepsilon_{cu}} + (3 - 2a_a)\left(\frac{\varepsilon_c}{\varepsilon_{cu}}\right)^2 + (a_a - 2)\left(\frac{\varepsilon_c}{\varepsilon_{cu}}\right)^3, \frac{\sigma_c}{\sigma_{cu}} \geq 0.4 \; and \; \frac{\varepsilon_c}{\varepsilon_{cu}} \leq 1, \text{harderning} \\ \frac{\frac{\varepsilon_c}{\varepsilon_{cu}}}{a_d\left(\frac{\varepsilon_c}{\varepsilon_{cu}} - 1\right)^2 + \frac{\varepsilon_c}{\varepsilon_{cu}}}, \frac{\varepsilon_c}{\varepsilon_{cu}} > 1, \text{softening} \end{cases}, \tag{4.7}$$

where σ_c and ε_c are compressive stress and strain, ε_{cu} is the strain at σ_{cu}, $a_a = 2.4 - 0.0125\sigma_{cu}$ and $a_d = 0.157{\sigma_{cu}}^{0.785} - 0.905$.

For the tension, beyond the ultimate strength, σ_{t0}, the softening behaviour can be expressed as:

$$\frac{\sigma_t}{\sigma_{t0}} = \frac{\frac{\varepsilon_t}{\varepsilon_{t0}}}{\alpha_t(\frac{\varepsilon_t}{\varepsilon_{t0}} - 1)^{1.7} + \frac{\varepsilon_t}{\varepsilon_{t0}}}, \tag{4.8}$$

where σ_t and ε_t are tensile stress and strain, ε_{t0} is the strain at σ_{t0}, and $\alpha_t = 0.312{\sigma_{t0}}^2$.

The stress-strain as defined above can be also converted into the stress-plastic strain curve, by following equations:

$$\tilde{\varepsilon}_c^{pl} = \tilde{\varepsilon}_c^{in} + \varepsilon_{0c}^{el} - \varepsilon_c^{el}, \tag{4.9}$$

$$\tilde{\varepsilon}_t^{pl} = \tilde{\varepsilon}_t^{ck} + \varepsilon_{0t}^{el} - \varepsilon_t^{el}, \tag{4.10}$$

where $\tilde{\varepsilon}_c^{pl}$ and $\tilde{\varepsilon}_t^{pl}$ are equivalent plastic strain tensor in compression and tension, $\tilde{\varepsilon}_c^{in}$ and $\tilde{\varepsilon}_t^{ck}$ are inelastic strain in compression and cracking strain in tension, and ε_{0c}^{el}, ε_c^{el}, ε_{0t}^{el} and ε_t^{el} are defined as below:

$$\varepsilon_{0c}^{el} = \frac{\sigma_c}{E}, \varepsilon_c^{el} = \frac{\sigma_c}{(1-d_c)E}, \tag{4.11}$$

$$\varepsilon_{0t}^{el} = \frac{\sigma_t}{E}, \varepsilon_t^{el} = \frac{\sigma_t}{(1-d_t)E}, \tag{4.12}$$

where d_c and d_t are damage variables for compression and tension, respectively, and E is Young's modulus. Eventually, the stress-strain relation under tension and compression loading can be obtained as below:

$$\sigma_c = (1 - d_c)E\left(\varepsilon_c - \tilde{\varepsilon}_c^{pl}\right), \tag{4.13}$$

$$\sigma_t = (1 - d_t)E\left(\varepsilon_t - \tilde{\varepsilon}_t^{pl}\right), \tag{4.14}$$

where $\varepsilon_c = \varepsilon_{0c}^{el} + \tilde{\varepsilon}_c^{in}$ and $\sigma_t = \varepsilon_{0t}^{el} + \tilde{\varepsilon}_t^{ck}$.

For material properties of mortar and aggregate, most inputs for the CDP are given with acceptable values from previous literature (Yılmaz and Molinari, 2017; Maleki et al., 2020; Naderi et al., 2021), as listed in Table 4.1. Additionally, other five parameters for the CDP model, the dilation angle, plastic potential eccentricity, ratio of compressive strengths under biaxial and uniaxial loading, ratio of the second stress invariant on the tensile meridian to that on the compressive meridian, and viscosity parameter, have the corresponding values of 35°, 0.1, 1.16, 0.667 and 0.0005 (Maleki et al., 2020; Naderi et al., 2021), and are used for both concrete phases here.

4.2.2.2 Cohesive interface element method for ITZ

For the cohesive element, the traction-separation law illustrates that one normal and two shear tractions acting on adjacent surfaces result in separations, such as crack initiation and evolution (Barenblatt, 1962). For simplicity, we consider the bilinear traction-separation law to describe the response of cohesive elements, as in Figure 4.3(b). The linear elastic behaviour after the damage initiation is followed by linear softening. It is noted for Figure 4.3(b) that here only shows the normal direction with the notation $*_n$. The first quadrant of Figure 4.3(b), if $*_n$ is replaced by $*_s$ and $*_t$ as shown in context, can be also used as first and third quadrants of schematic diagram to illustrate the traction-separation in two shear directions, and the corresponding diagrams in both directions are not provided here. In this study, the criterion for damage initiation is the quadratic nominal stress law, as given by:

$$\left\{\frac{\langle t_n \rangle}{t_{n0}}\right\}^2 + \left\{\frac{t_s}{t_{s0}}\right\}^2 + \left\{\frac{t_t}{t_{t0}}\right\}^2 = 1, \tag{4.15}$$

where t_n is normal traction, t_s and t_t are two shear tractions, t_{n0}, t_{s0} and t_{t0} are corresponding cohesive strengths and critical values for damage initiation, and $\langle \cdot \rangle$ is the Macaulay bracket defined as:

$$\langle t_n \rangle = \begin{cases} t_n, t_n \geq 0 & \text{(tension)} \\ 0, \ t_n < 0 & \text{(compression)} \end{cases}. \tag{4.16}$$

Fracture energy, G_f, is the area under the curve representing separation, δ, and traction, $t(\delta)$, and it can be determined using the cohesive strength, t_0, and failure separation, δ_f, in either normal or shear directions, as below:

$$G_f = \int_0^{\delta_f} t(\delta)d\delta = \frac{1}{2}t_0\delta_f. \tag{4.17}$$

The damage variable, d_{CIE}, as function of effective relative displacement, δ_m, is introduced to describe the linear softening branch representing the damage evolution, and defined as:

$$d_{CIE} = \frac{\delta_{mf}(\delta_m - \delta_{m0})}{\delta_m(\delta_{mf} - \delta_{m0})}, \tag{4.18}$$

$$\delta_m = \sqrt{\langle\delta_n\rangle^2 + {\delta_s}^2 + {\delta_t}^2}, \tag{4.19}$$

$$\langle\delta_n\rangle = \begin{cases} \delta_n, \delta_n \geq 0 & \text{(tension)} \\ 0, \ \delta_n < 0 & \text{(compression)} \end{cases}, \tag{4.20}$$

where δ_n, δ_s and δ_t are separation in one normal and two shear directions, δ_{m0} and δ_{mf} are effective relative displacement at damage initiation and final failure. During the damage evolution, the stiffness degradation is controlled by d_{CIE}, and the current stiffness in one normal and two shear directions k_n, k_s, k_t are given by:

$$k_n = (1 - d_{CIE})k_{n0}, k_s = (1 - d_{CIE})k_{s0}, k_t = (1 - d_{CIE})k_{t0}, \tag{4.21}$$

where k_{n0}, k_{s0} and k_{t0} are initial cohesive stiffness correspondingly, and $k_{n0} = k_{s0} = k_{t0}$ is assumed in this study. Damage-affected tractions, t_n, t_s and t_t, are defined as:

$$t_n = \begin{cases} (1 - d_{CIE})\overline{t_n}, & \overline{t_n} \geq 0 \\ \overline{t_n}, & \overline{t_n} < 0 \end{cases},$$

$$t_s = (1 - d_{CIE})\overline{t_s}, \tag{4.22}$$

$$t_t = (1 - d_{CIE})\overline{t_t},$$

where $\overline{t_n}$, $\overline{t_s}$ and $\overline{t_t}$ are traction components calculated based on the elastic-displacement behaviour for the current separations without damage.

For the ITZ, input values for material parameters of the cohesive element are listed in Table. 4.1, as in some studies (Yılmaz and Molinari, 2017; Maleki et al., 2020; Naderi et al., 2021). The energy-based crack evolution is considered for the linear softening region. The Benzeggagh-Kenane criterion (1996) is used for the mixed mode behaviour, and for simplicity, fracture energy G_f are assumed to be the same in normal $G_{f,n}$ and two shear directions $G_{f,s}$ and $G_{f,t}$, $G_f = G_{f,n} = G_{f,s} = G_{f,t}$.

4.2.3 Triaxial loading conditions

As shown in Figure 4.1(d), the concrete model is loaded under triaxial compressive stresses of σ_1, σ_2 and σ_3 , where σ_1, σ_2 and σ_3 are referred to principal stresses. In this study, $\sigma_1 > \sigma_2 = \sigma_3 = \sigma_L \geq 0$ MPa and only confining pressure, σ_L, less than uniaxial compressive strength of concrete are considered. Though the explicit scheme is used here for its efficiency of handling multiple contacts, the modelling focuses on the quasi-static triaxial test. As the ABAQUS/Explicit is a dynamic solver, the loading rate on the concrete model needs to be carefully selected to avoid considerable initial effects; we have ensured that the ratio of the total kinetic energy to internal energy is always below 5% in all simulations.

The loading is implemented in two steps, which are carried out sequentially in the simulation without any coupling settings. As shown in Figure 4.1(d), all nodes at the bottom are fixed in the direction of σ_1, *i.e.*, the y-direction. In the first step, the confining pressure, σ_L, is applied to the top and side faces of the cubic concrete specimen, linearly increasing to the given value within 0.001 s. In the second step, the stress σ_1 for the top surface is increased to $\sigma_1 + \sigma_{\mathrm{q}}$, where σ_{q} is the deviatoric stress applied using a velocity-controlled method. Meanwhile, confining pressure σ_L keeps acting to other confined faces, *i.e.*, $\sigma_2 = \sigma_3 = \sigma_L$, as propagated from the end of first step. The velocity of the nodes on the top surface is linearly ramped up to 25 mm/s within 0.001 s and then held constant until the end of the second step. In this study, the given confining pressures $\sigma_L = 0, 5, 10, 15, 20, 25$ MPa are considered, unless otherwise emphasised. To obtain the stress-strain data under different σ_L, the entire time of the second step is set to 0.02 s. It is noted that the uniaxial compression tests correspond to cases with $\sigma_L = 0$ MPa.

4.3. Results and discussion

In this section, using our established model, numerical analyses are performed to investigate the macro- and micro-mechanical responses of concrete under various confining pressures and aggregate shapes. The macroscopic responses of concrete under uniaxial and triaxial stress conditions are presented in Section 4.3.1. Particular focus is placed on the relation between the macro-strength of concrete and confining pressure, which will be compared with existing experimental data. To explore the underlying micro-mechanisms behind the influence of aggregate shape on these relations, quantitative evidence is examined through local stress distribution, local damage and crack clusters in Sections 4.3.2 to 4.3.4, respectively.

4.3.1 Stress-strain responses

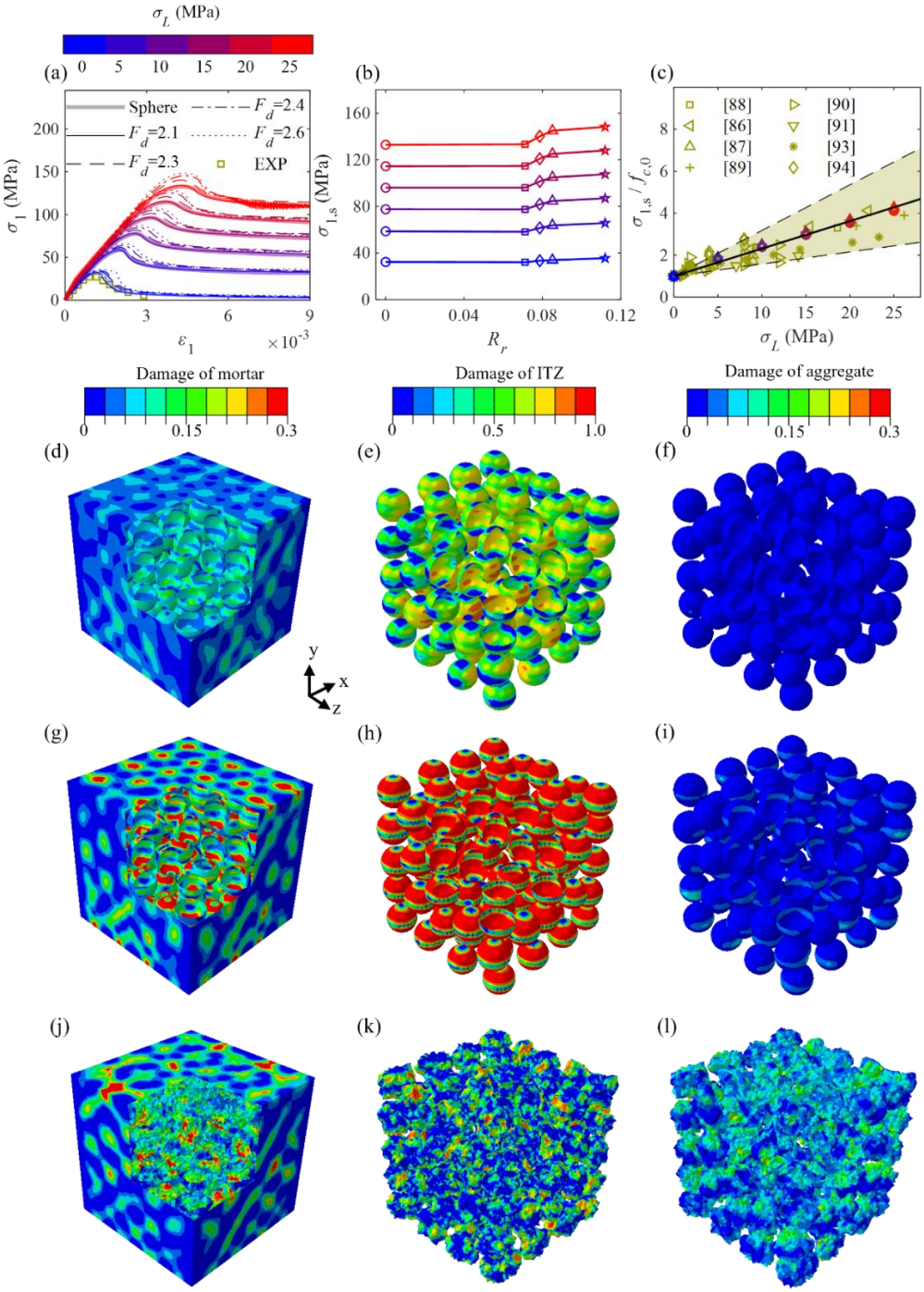

Figure 4.4: (a) Typical axial stress-strain curves for different aggregate shapes and confining pressures, where EXP shows results from the experiments of Lowes (1999), (b) compressive strength, $\sigma_{1,s}$, versus relative roughness, R_r, where the markers from left to right represent cases of sphere, $F_d = 2.1$, $F_d = 2.3$, $F_d = 2.4$ and $F_d = 2.6$, respectively, (c) relations between normalised strength, $\sigma_{1,s}/f_{c,0}$,and confining pressure, σ_L, where the black line fits

FEM simulations, and dashed black lines are for fitted upper and lower bounds of experimental data, and (d-l) damage field distributions of mortar, ITZ and aggregate at the compressive strength, where (d-f) are for the uniaxial test, (g-l) are for the triaxial test with $\sigma_L = 25$ MPa; (d-i) are for the sphere and (j-l) are for aggregates with $F_d = 2.6$.

Based on the above-established modelling, firstly we can obtain the σ_L-influenced axial stress (σ_1) − strain (ε_1) curves for the concrete with various shaped inclusions, as the specimens with sphere, $F_d = 2.1$, $F_d = 2.3$, $F_d = 2.4$, and $F_d = 2.6$ shown in Figure 4.4(a). Therein, σ_1 is defined as F/A, with F being the sum of nodal reaction force on the top boundary where the velocity boundary condition is inserted, and $A = 50 \times 50\ \mathrm{mm}^2$ is the initial cross-section area, and ε_1 is calculated as the ratio of nodal displacement to the initial side length of the specimen. For the obtained stress–strain curves, our results for uniaxial tests show good agreement with the experimental work of Lowes (1999). For the triaxial tests, it is challenging to find experimental results that exactly match the same combination of aggregate solid fraction, aggregate size, specimen dimensions, and confining pressures used in our model. We acknowledge this as a limitation in validating our model from the stress–strain perspective. Thus, Figure 4.4(a) is primarily used to demonstrate that our model can capture the general characteristics of the triaxial response of concrete. As an alternative approach for model validation, the relation between concrete strength and confining pressure, as our main basis of investigation into the influence of aggregate shape, will be compared with existing data in the following.

As shown in Figure 4.4(a), with a rising confining pressure, the peak value of σ_1, *i.e.*, compressive strength, $\sigma_{1,s}$ are increased, and the post-peak softening turns to be flatter. Such an increase of $\sigma_{1,s}$ in the triaxial test can be explained by severer damage in all three phases as shown in Figure 4.4(g-i), when compared to the uniaxial test in Figure 4.4(d-f). In Figure 4.4(a), another noticeable point is that rougher aggregate shapes with higher F_d result in higher $\sigma_{1,s}$. That is because higher F_d induces higher stress concentrations near aggregate surfaces, which may lead to more fractures propagating across the strongest phase, aggregate, rather than along the weakest phase-ITZ, as demonstrated in Figure 4.4(g-l); as a result, the macroscopic strength of concrete is enhanced. This influence could be further enhanced by higher confining pressure, σ_L, as illustrated in Figure 4.4(b). Wei et al. (2020b) also found more roughness-induced higher uniaxial compressive strength, $f_{c,0}$, in numerical uniaxial tests on mesoscale concrete samples.

This pronounced effect due to increased confining pressure may be rooted in more stress concentrations under triaxial states.

The combined effects of confining pressures and aggregate morphology features, $f_{c,0}$-normalised $\sigma_{1,s}$ versus σ_L are provided in Figure 4.4(c). Our numerical results are also plotted against some existing experimental works focusing on various strength-dependent factors including normal (Kotsovos and Newman, 1980; Imran and Pantazopoulou, 1996; Sfer et al., 2002; Mazzucco et al., 2021) or high-strength concrete (Candappa et al., 2001; Lu and Hsu, 2007), confinement (Attard and Setunge, 1996), supplementary materials (Xie et al., 1995), and dynamic loading impacts (Chen et al., 2010). Besides the consistence with the experimental results, it is surprising that all data pertinent to various inclusion shapes and confining pressures collapses well onto a single line with $R^2 \approx 1$, as below:

$$\sigma_{1,s}/f_{c,0} = k \cdot (\sigma_L/\sigma_0) + 1, \tag{4.23}$$

where σ_0 is 1 MPa for normalisation, and $k = 0.13$ is the fitting parameter. Failure criterions have been analytically or empirically proposed to predict $\sigma_{1,s}$ by σ_L, such as unmodified (Richart et al., 1928) and modified Mohr-Coulomb (Sovják et al., 2013), Newman (Newman, 1979), Leon-Pramono (Binici, 2005) criterions and others (Hsieh et al., 1982). Compared with all these criterions, our model only contains one fitting parameter. The following sections are dedicated to untangling why and how the macroscopic scaling law bridging $\sigma_{1,s}$ and σ_L holds for concrete with distinctive inclusions, with the micro perspectives of local stress, damage evolutions and crack patterns.

4.3.2 Local stress distributions

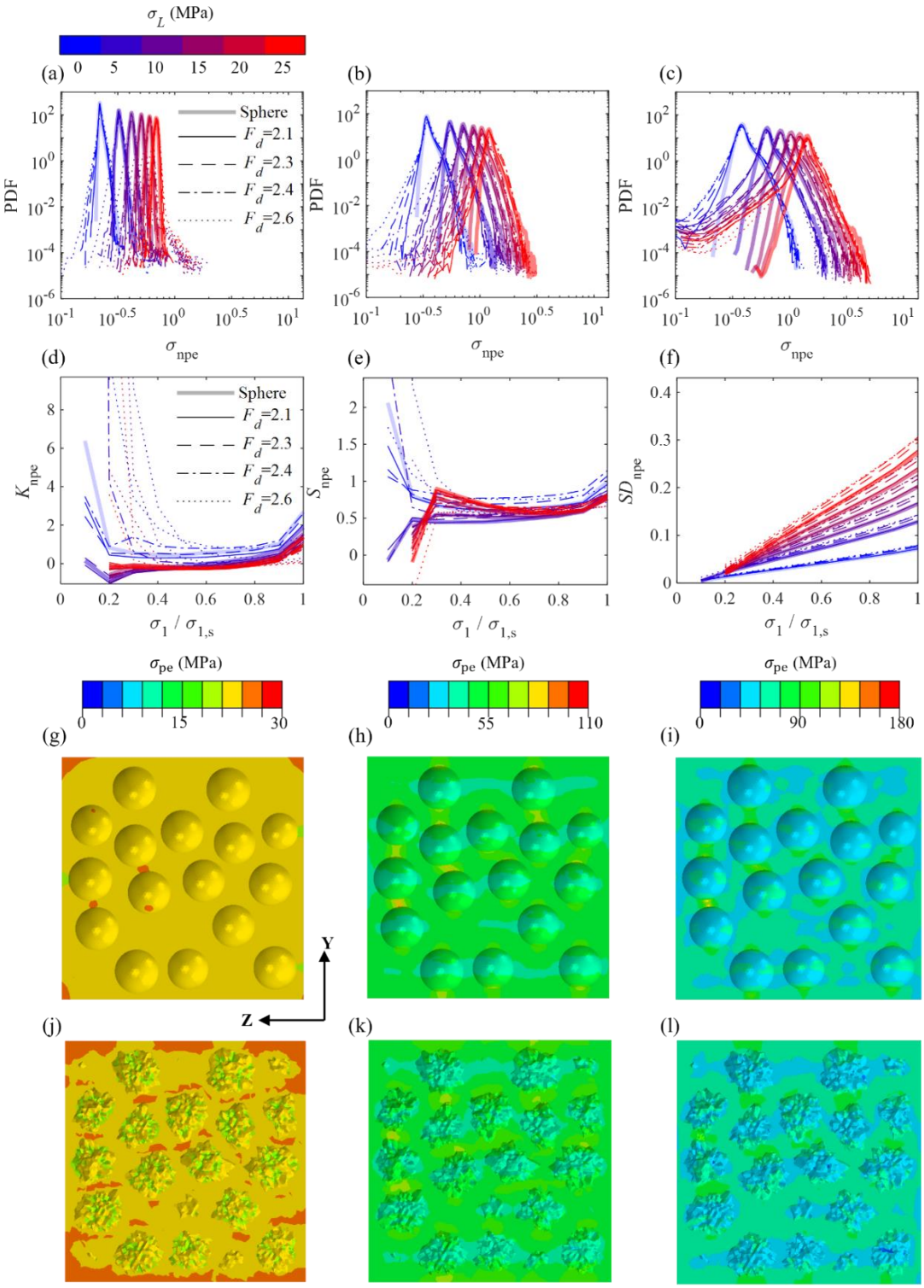

Figure 4.5: Probability density functions (PDFs) of normalised mean stress, σ_{npe}, of mortar elements at (a) $\sigma_1/\sigma_{1,s} = 0.2$, (b) $\sigma_1/\sigma_{1,s} = 0.8$ and (c) $\sigma_1/\sigma_{1,s} = 1$, all using the legends from (a), and variations of (d) kurtosis, K_{npe}, (e) skewness, S_{npe}, and (f) standard deviation, SD_{npe}, of σ_{npe} with $\sigma_1/\sigma_{1,s}$, all using the legends from (d), and (g-l) distribution of mean stress, σ_{pe},

in mortar on the y-z plane, *i.e.*, midplane of the concrete specimen, at $\sigma_L = 25\text{MPa}$: (g) and (j) are for $\sigma_1/\sigma_{1,s} = 0.2$, (h) and (k) are for $\sigma_1/\sigma_{1,s} = 0.8$, (i) and (l) are for $\sigma_1/\sigma_{1,s} = 1$, (g-i) and (j-l) are for cases of sphere and $F_d = 2.6$, respectively.

The stress distribution and its evolution during triaxial loading are focused on the mortar phase. As a continuous medium connecting discretely distributed aggregates surrounded by the ITZ, the mortar has the stress distribution that results from aggregate-to-aggregate and aggregate-to-mortar interactions, in addition to external loading, thus reflecting the influence of aggregate shape. The stress distribution in the host matrix has been successfully used to explain the 2D macro failure of materials with a disordered spatial distribution of circular flaws (Laubie et al., 2017b). Such an approach using the stress distribution will be extended to more general cases of concrete, where the mortar is taken as host matrix containing the aggregate and surrounding ITZ, to gain the insight into the fracture process of concrete with different aggregate shapes. Here, the evolution of stress distribution in the mortar is focused during the loading with an increasing ratio of macroscopic stress to compressive strength, $\sigma_1/\sigma_{1,s} \in [0.1,1]$, where the confining stage, *i.e.*, $\sigma_1 \leq \sigma_L$, is excluded. Given the mean stress of element in the mortar phase, σ_{pe}, obtained from the simulation results, probability density function (PDF) is plotted for its normalised value, $\sigma_{\text{npe}} = (\sigma_{\text{pe}} + 2\sigma_{t,0})/f_{c,0}$, where $\sigma_{t,0}$ is tensile strength as given in Table. 4.1, and the shift of $2\sigma_{t,0}$ is used to remove the negative value and allows the PDF of σ_{npe} plotted in log-log scale, $f_{c,0}$, *i.e.*, $\sigma_{1,s}$ at $\sigma_L = 0\,\text{MPa}$, is uniaxial strength of concrete with the influence of aggregate shapes in terms of relative roughness, R_r, as shown in Figure 4.4(b), and normalising $f_{c,0}$ scales element stress to minimise the quantitative differences between aggregate shape, making it more effective for focusing on how the aggregate shape affects the heterogeneity of stress distribution during the triaxial loading. The PDF at each $\sigma_1/\sigma_{1,s}$ is calculated based on the element volumes, showing its dependences on the aggregate shape and confining pressure by log-log plots, as shown in a few examples in Figure 4.5(a-c). To characterise the PDF, the following statistical indices are introduced for Figure 4.5(d-f) as:

$$\text{Kurtosis: } K_{npe} = \frac{\frac{1}{n}\sum_{i=1}^{n}\left(\sigma_{npe}-M_{npe}\right)^4}{\left(\frac{1}{n}\sum_{i=1}^{n}\left(\sigma_{npe}-M_{npe}\right)^2\right)^2} - 3\,, \tag{4.24}$$

$$\text{Skewness: } S_{npe} = \frac{\frac{1}{n}\sum_{i=1}^{n}\left(\sigma_{npe}-M_{npe}\right)^3}{\left(\sqrt{\frac{1}{n}\sum_{i=1}^{n}\left(\sigma_{npe}-M_{npe}\right)^2}\right)^3}\,, \textit{and} \tag{4.25}$$

Standard deviation: $SD_{npe} = \sqrt{\frac{1}{n-1}\sum_{i=1}^{n}\left(\sigma_{npe} - M_{npe}\right)^2}$, (4.26)

where the M_{npe} is the mean value of element-level stress σ_{npe}.

At almost linear elastic regime ($\sigma_1/\sigma_{1,s}$= 0.2), PDF in Figure 4.5(a) shows that most element stresses σ_{npe} are concentrated within a small range. The kurtosis, K_{npe}, and skewness, S_{npe}, which is used to indicate the heterogeneity of stress distribution in mortar, exhibit significant variation across different aggregate shapes, as shown in the Figure 4.5(d) and (e), respectively. That is due to the presence of extreme values of σ_{npe} in the right tails of PDF, showing a dependency on the aggregate shape. The rougher aggregates induce the higher concentrated stresses on mortar elements adjacent to their boundaries and can result in greater heterogeneity of stress distribution in mortar, as also evidenced by higher value of K_{npe} and S_{npe}. In triaxial tests with increasing confining pressure, although the stress near aggregate boundaries intensifies and shifts the PDF to the right, the overall trend of PDF in Figure 4.5(a) remains nearly unchanged for all aggregate shapes, showing decreasing dependency on the shapes. This is also reflected in insignificant variation of K_{npe} and S_{npe} at $\sigma_1/\sigma_{1,s}$= 0.2 across different confining pressures, suggesting the similar influence of aggregate shape on heterogeneity of stress distribution in mortar.

Beyond the elastic region, as $\sigma_1/\sigma_{1,s}$ increases, the overall stress in the mortar improves to varying degrees, leading to a broader range of the PDF of σ_{npe}, as seen in the comparison between Figure 4.5(b) or (c) and (a). Simultaneously, the standard deviation, SD_{npe}, shows a continuous increase, accompanied by a progressively more pronounced effect of confining pressure. This is because the stress in the mortar tend to increase and propagate in a restricted direction due to the confining pressure, leading to a more heterogeneous stress distribution. The difference in the PDF between aggregate shapes may be reduced, as indicated by K_{npe} and S_{npe}, which converge to their respective values. This suggests that although the initial influence of aggregate shape on the heterogeneity of stress distribution gradually weakens, the relative differences can still be observed under different confining pressures. As seen in Figure 4.5(g-l), with increasing $\sigma_1/\sigma_{1,s}$, the enhanced stress gradually propagates to other regions of the mortar, causing the heterogeneity of the stress distribution to extend over a wider high-stress area, where the shape-induced stress concentration effects on mortar elements become less pronounced compared to those at the initial loading stage.

When $\sigma_1/\sigma_{1,s}$ approaches 1 (or approaching the respective uniaxial compressive strength), the confining pressure becomes a more dominant factor influencing the heterogeneity of stress distribution, showing a universality across different aggregate shapes, as more apparently evidenced by SD_{npe} in Figure 4.5(e).

Finally, at $\sigma_1/\sigma_{1,s}$=1, the heterogeneity of stress distribution in mortar is similar across different aggregate shapes, and this aligns with the universal scaling law expressed by Equation 4.23 and in Figure 4.4(c). However, this similarity in stress heterogeneity does not explain the reason that rougher aggregates lead to a greater overall concrete strength, as illustrated in Figure 4.4(b). When concrete approaches its failure strength, it transitions from linear to non-linear regions with possible damage initiation or propagation within the material phases. The influence of material properties and / or morphology have been used to analyse damage mechanisms to interpret how the evolution of internal structure affects the macroscopic behaviour of concrete (Wei et al., 2020b; Naderi et al., 2021). It is worth noting here that our focus on the stress distribution in the mortar alone is intended to determine whether this approach, similar to that of Laubie et al. (2017b), is applicable to our analysis. The investigation of the heterogeneity of stress distribution will not be extended to other material phases of concrete. We found that while this approach effectively explains the universal scaling law, it fails to account for the influence of aggregate shape on the macroscopic strength of concrete. Therefore, it is necessary to investigate the underlying reasons for both issues from an alternative perspective, focusing on the assessment of local damage, as discussed in the following section.

4.3.3 Damage evolutions

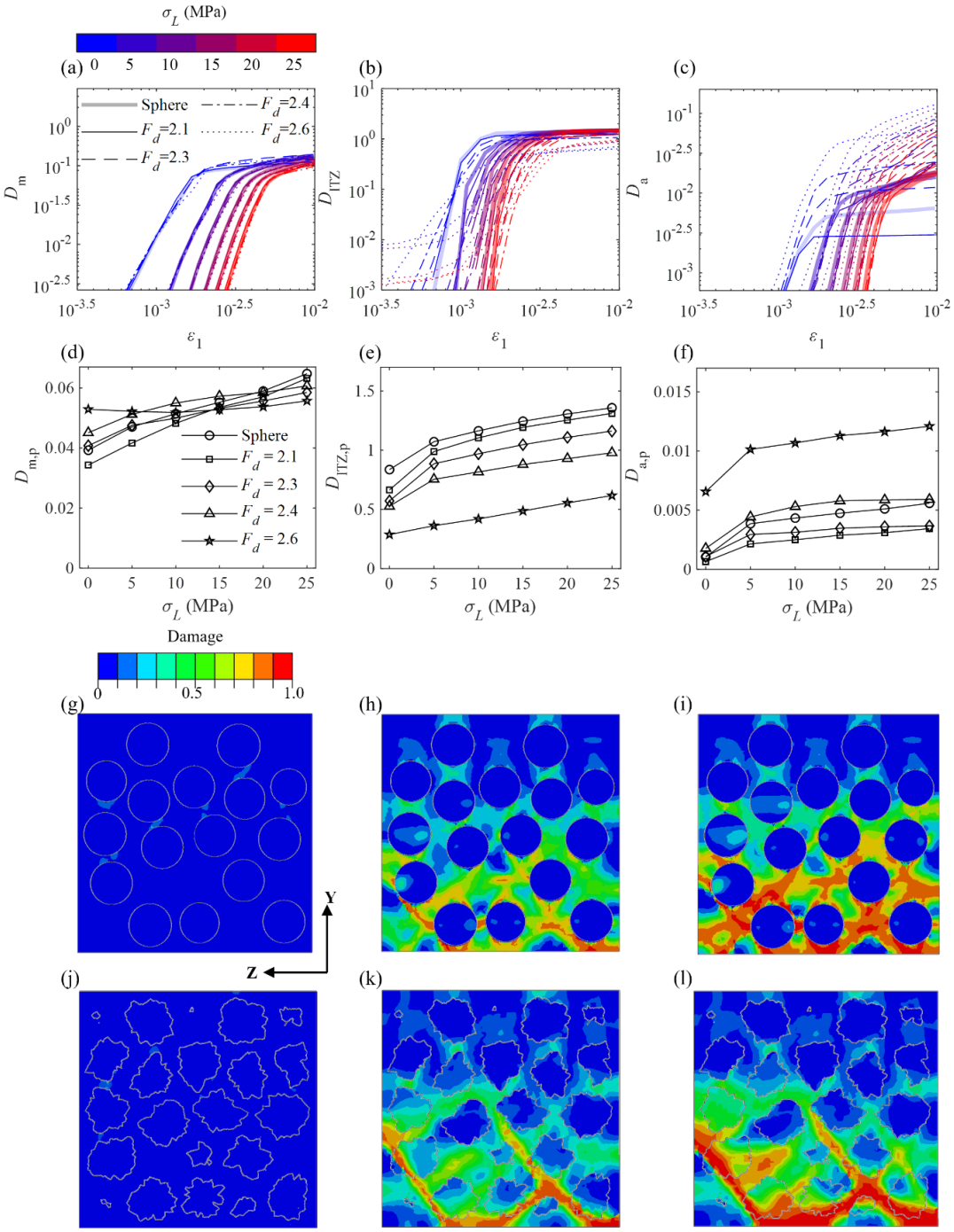

Figure 4.6: (a-c) Evolutions of damage in mortar, ITZ and aggregate with the axial strain, ε_1, all using the legend from (a), and (d-f) variation in damage in mortar, ITZ and aggregate corresponding to the compressive strength with σ_L, all using the legends from (d), and damage field distribution on y-z plane, *i.e.*, midplane of the concrete specimen, at $\sigma_L = 25$MPa: (g) and (j) are for $\varepsilon_1 = 0.003$, (h) and (k) are for $\varepsilon_1 = 0.006$, (i) and (l) are for $\varepsilon_1 = 0.009$, (g-i) and (j-l) are for cases of sphere and $F_d = 2.6$.

The local damage of concrete is investigated to understand how different material phases contribute to the damage, providing a more accurate representation of the macroscopic behaviour to illustrate its universality. Here, the damage in different material phases, mortar, ITZ, and aggregate are expressed as D_{m}, D_{ITZ}, and D_{a}, respectively, and can be quantified as below:

$$\frac{\sum_{i=1}^{N} d_i V_i}{V_c} \; or \; \frac{\sum_{i=1}^{N} d_i S_i}{S_c}, \tag{4.27}$$

where d_i is the element-level damage of i-th element, V_i is the volume of i-th solid element for mortar or aggregate, S_i is the area of i-th cohesive interface element (CIE) representing the ITZ, and V_{c} and S_{c} are the volume and surface area of cubic specimen of concrete, respectively.

To investigate whether damages have any universality during triaxial loading, the evolution of D_{m}, D_{ITZ} and D_{a} are computed using values at 30 uniform increments within the range of axial strain, $\varepsilon_1 \in [0.0005, 0.01]$. Figure 4.6(a-c) in log-log scale highlight effects of confining pressure and aggregate shape. When damages increase with the strain, D_{ITZ} evolves fastest and reaches the maximum first due to the weakest intrinsic fracture strength, followed by D_{m} and D_{a}. This also explains why damage originates from areas adjacent to aggregate boundaries and then spreads to other regions of the material phases, as shown in Figure 4.6(g-l). With an increased σ_L, a significant delay in the damage evolution can be observed. That is because the enhanced material strength due to σ_L makes it less prone to inelastic deformation, and the failure mode of the material becomes more ductile, typically requiring greater deformation of elements for the onset of damage. Among all material phases, only the damage evolution of mortar remains quite similar across aggregate shape, exhibiting a universal behaviour governed by the confining pressure σ_L. However, this universality is absent in the damage evolution of the ITZ and aggregates due to significant variations in aggregate shapes, as shown in Figure 4.6(b-c). In particular, under larger strain, greater damage propagation from the ITZ into the aggregates is observed in cases with rougher aggregate shapes, as seen in Figure 4.6(g-l). These observations contradict the universality of the scaling law expressed in Equation 4.21. To address this, the following focus will be on investigating how material phases respond at a specific point, *i.e.*, the concrete strength, instead of the entire loading process.

To find underlying reasons behind the scaling law, damages in mortar, $D_{\mathrm{m,p}}$, ITZ, $D_{\mathrm{ITZ,p}}$, and aggregate, $D_{\mathrm{a,p}}$, at the respective ultimate compressive strength are provided in Figure 4.6(d-f). When an increase of confining pressure, σ_L, enhances the concrete strength, it also results in greater damage within each material phases. It is because at higher σ_L, reaching the compressive strength requires more deformation, as shown in Figure 4.4(a), during which the intensified overall stress within the material phases promotes the initiation or propagation of damage within elements. With an increasing value, the $D_{\mathrm{m,p}}$ shows insignificant dependency on the aggregate shape, due to the similar heterogeneity of stress distribution in the mortar at the compressive strength, *i.e.*, $\sigma_1/\sigma_{1,s} = 1$, in Figure 4.5, indicating comparable levels of damage. More noticeable effects of aggregate shape can be observed in $D_{\mathrm{ITZ,p}}$ and $D_{\mathrm{a,p}}$, which shows the competitive relation with an increasing F_d of aggregate. This aligns with the findings of Wei et al. (2020b), which focused only on uniaxial compressive tests. However, this study also find that this competition extends to triaxial tests and remains universal across various confining pressures.

For rougher aggregates, higher stress concentration can be induced. The presence of confining pressure further amplifies this effect by preventing the material from expanding laterally and increasing localised stresses. This further promotes the fracture propagation from the ITZ to the aggregates. As a result, with an increasing F_d of the aggregate, $D_{\mathrm{ITZ,p}}$ decreases while $D_{\mathrm{a,p}}$ increases. The tendencies become more pronounced as overall damage increases with increasing σ_L. The relative damage change in different phases explains why rougher aggregates cause the more significantly enhanced concrete strength at higher σ_L, as shown in Figure 4.4(b). Due to its fully convex shape, damage in spherical aggregate, which is even greater than in some realistic aggregates, causes $D_{\mathrm{ITZ,p}}$ and $D_{\mathrm{a,p}}$ to deviate from the competitive relation for realistic shapes. The greater surface roughness of realistic aggregate with higher F_d causes fracture propagation to concentrate in more localised areas, *e.g.*, sharp corners or edges, resulting in an almost proportional increase in $D_{\mathrm{a,p}}$. The universality of the competitive relation between damage levels in ITZ and aggregates across σ_L indicates that the effect of aggregate roughness on concrete strength can be mapped from triaxial to uniaxial tests. Thus, when the $\sigma_{1,\mathrm{s}}/f_{c,0}$ is used in Equation 4.23, it can reduce the dependence of relation between σ_L and $\sigma_{1,\mathrm{s}}$ on the aggregate shape, allowing Equation 4.23 to be applied to predict the σ_L-dominated concrete strength for different aggregate shapes, whilst the shape effects being fully captured by the uniaxial compressive strength.

4.3.4 Crack patterns

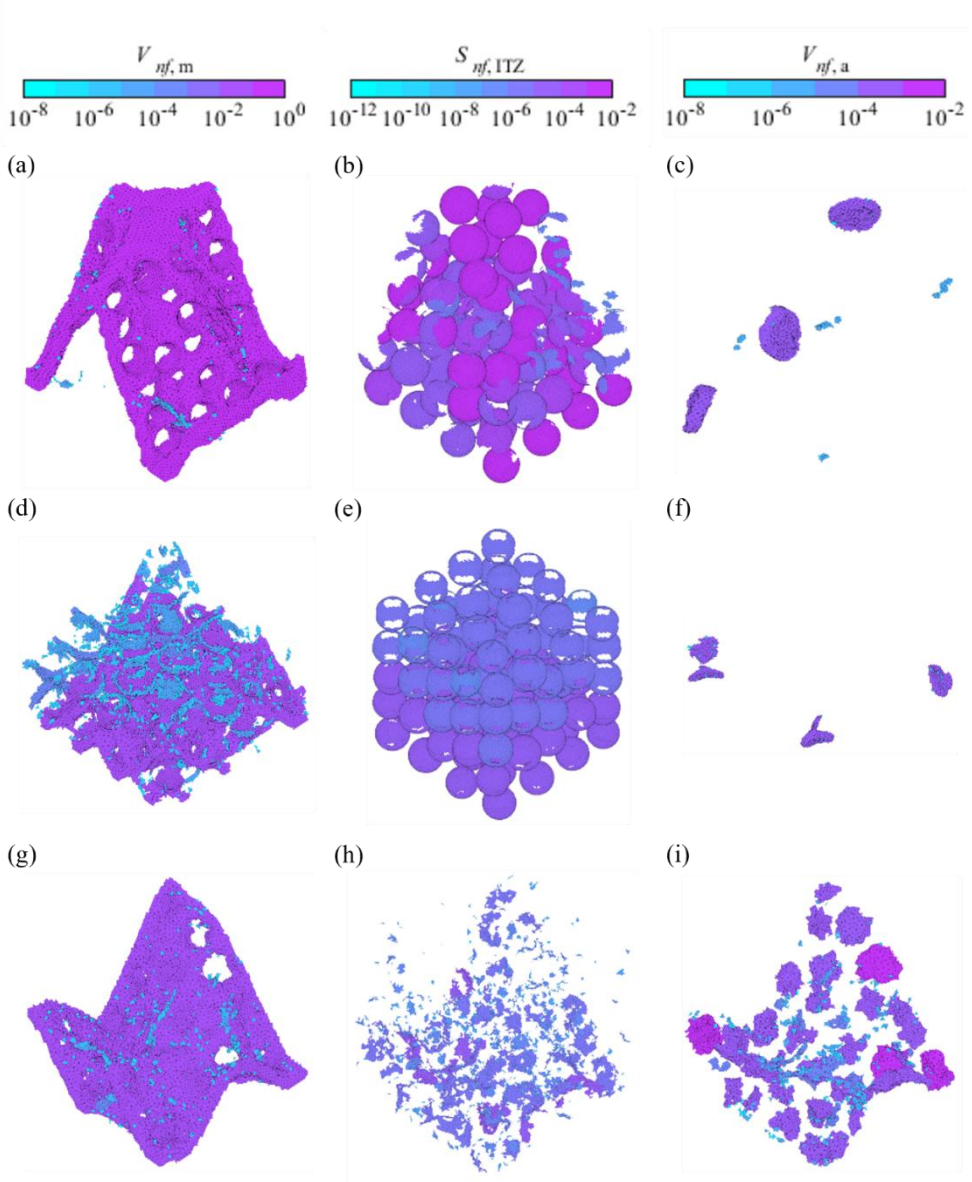

Figure 4.7: Crack patterns of mortar, ITZ and aggregate, where (a-c) are for the uniaxial test, (d-i) are for the triaxial tests with $\sigma_L = 25$ MPa, (a-f) are for the sphere and (g-i) are for aggregates with $F_d = 2.6$, and three colours bars from left to right sequentially represent the relative size, *i.e.*, area/volume, of crack cluster of mortar, $V_{nf,\mathrm{m}}$, ITZ, $S_{nf,\mathrm{ITZ}}$ and aggregate, $V_{nf,\mathrm{a}}$.

At the final loading stage, we assess the crack pattern of concrete subjected to triaxial loading. Most existing mesoscale studies rely only on visual observation to compare and discuss crack patterns (Wang et al., 2016b; Naderi et al., 2021). We attempt to improve such an investigation by introducing quantitative analyses of the crack clusters in each material

phase. Here, the macro-crack is assumed to form at the axial strain, $\varepsilon_1 = 0.009$. In the modelling, there is no precisely defined damage threshold for identifying cracked elements. However, some existing numerical studies have used the damage value of elements to characterise cracking patterns in concrete, commonly adopting a threshold of 0.9 (Wang et al., 2020; Naderi et al., 2021; Wang et al., 2021; Zhou and Xu, 2023). Following this convention, solid elements or CIEs with damage values exceeding this threshold, considered as cracked elements, are isolated from each material phase of concrete. The contact between crack clusters in mortar and aggregate is determined by the face-to-face contact of solid elements, while in the ITZ, it is determined by the edge-to-edge contact of zero-thickness CIEs. Our in-house algorithm for both contact detection methods, which are implemented in MATLAB, follows the main workflow outlined below:

(1) All cracked elements of each material phase are collected into a set, $T_E = \{E_i | i = 1,2,..n\}$, where i is the element index. Each solid element or CIE can be represented using a 4×3 or 3×2 matrix, where each row contains node indices representing the face or edge of the element.

(2) We check whether any single element in T_E is in contact with other elements. The contact criterion is defined as follows: any two solid elements (or CIEs) that share the same row of node indices are considered to be in face-to-face (or edge-to-edge contact).

(3) The connection elements are identified as clusters for different material phases.

Once the above processes are completed, each cluster size of mortar, $V_{f,\mathrm{m}}$, ITZ, $S_{f,\mathrm{ITZ}}$, or aggregate, $V_{f,\mathrm{a}}$ is determined by summing the volume or area of elements within the same cluster. The normalisation is conducted as $V_{nf,\mathrm{m}} = V_{f,\mathrm{m}}/V_c$, $S_{nf,\mathrm{ITZ}} = S_{f,\mathrm{ITZ}}/S_c$, and $V_{nf,\mathrm{a}} = V_{f,\mathrm{a}}/V_c$, shown in Figures. 4.7 and 4.8.

For cases with spherical aggregates, cracks in the uniaxial test freely develop along inclined planes, forming distinct V-shaped branches that cross diagonally, particularly prominent in the mortar, as shown in Figure 4.7(a). As observed in the comparison between Figure 4.7(d-f) and Figure 4.7(a-c), differences in crack morphology between uniaxial and triaxial tests are primarily found in the mortar and ITZ, while negligible in the aggregate due to the minimal crack volume. With $\sigma_L = 25$MPa, along the increased crack area in the ITZ,

cracks in the mortar become less inclined and exhibit a more diffuse pattern, as shown in Figure 4.7(d), due to the constraint on lateral deformation imposed by the confining pressure.

For the cases with realistic aggregate under triaxial loading, damage during the post-peak stage continues to intensify in the already affected local regions at or around the sharp corners or edges of aggregates, and propagates along these regions deeper into the aggregate, leading to the new cracks or the expansion of existing cracks into larger areas within aggregates. When $\varepsilon_1 = 0.009$, as shown in Figure 4.7(d-f), cracks in the ITZ are distributed in spatially dispersed clusters, while a considerable volume of cracks is observed within the aggregates. In contrast, as shown in Figure 4.7(e-f) for cases with spherical aggregates, due to lower stress concentration, damage tends to be more uniform on the spherical surface, leading to spatially continuous and extensive cracks in the weakest phase—ITZ. In the strongest phase—aggregate, only a few local regions reach the critical damage threshold, *i.e.*, 0.9, and form cracks.

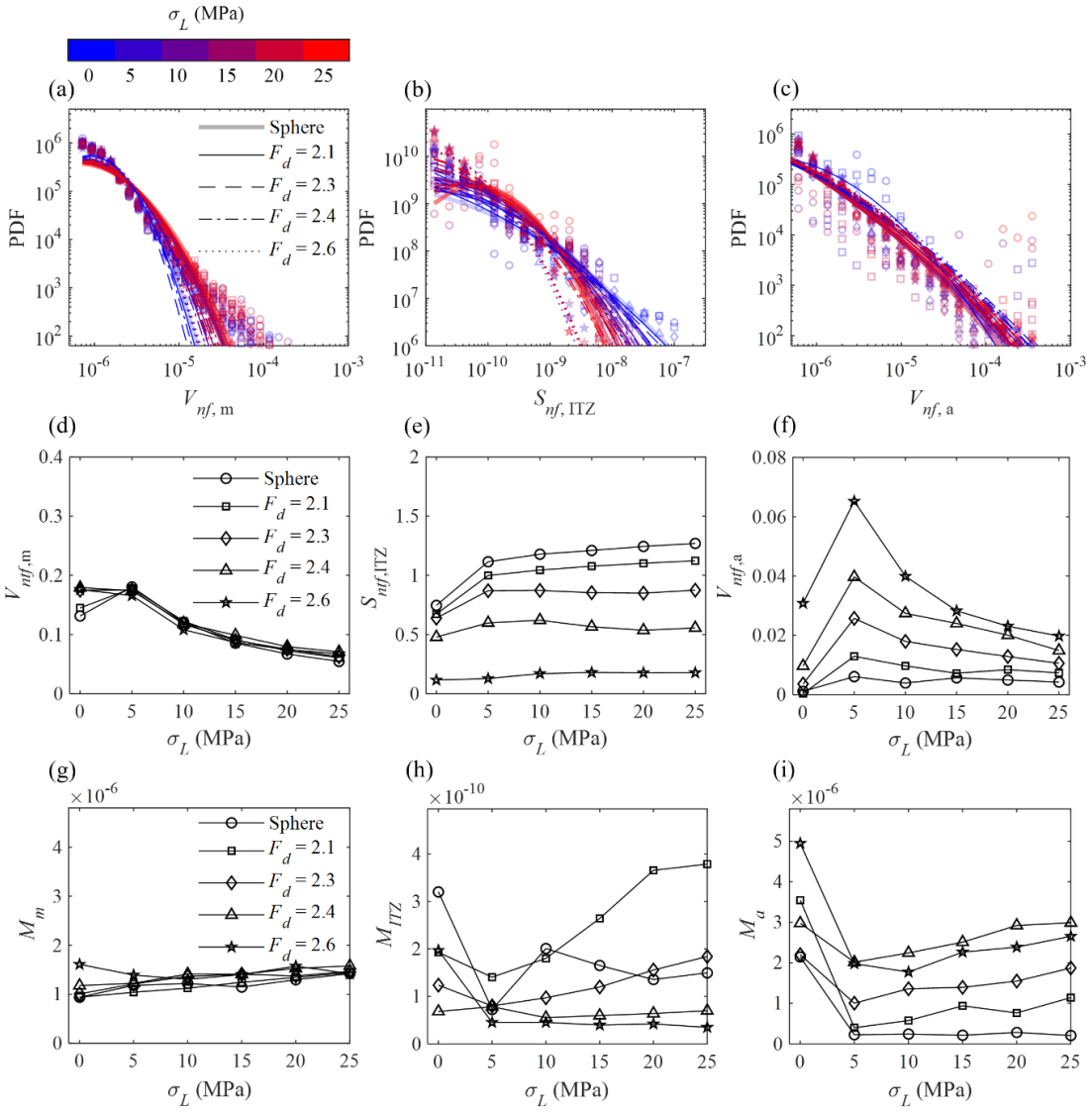

Figure 4.8: (a-c) Probability distributions of relative size of crack clusters of mortar, ITZ and aggregate, maker shapes for data point follow the legend in (d), legends in (a) for lognormal fittings is also used for (b-c), (d-f) variations in relative total crack volume/area of mortar, ITZ and aggregate with respect to σ_L, all using the legends from (d), and (g-i) variations in mean value of lognormal fittings to PDF for mortar, ITZ and aggregate with respect to σ_L, all using the legends from (g).

PDF is plotted for the relative crack cluster size, which is evenly divided in logarithmic space. It is calculated based on the cluster counts within each bin width and provided in Figure 4.8(a-c). The PDFs reveal that smaller relative crack cluster sizes occur more frequently in material phases, as stress tends to concentrate more often in small local regions, making these areas more susceptible to damage. The relative total crack volume or area for mortar, $V_{ntf,\mathrm{m}}$, ITZ, $S_{ntf,\mathrm{ITZ}}$, and aggregate, $V_{ntf,\mathrm{a}}$, are computed by summing relative cluster sizes. Their

variations with respect to σ_L are provided in Figure 4.8(d–f). To explicitly describe the variation of the PDFs with confining pressure and aggregate shape, the lognormal fitting, $f_{ln}(x_s)$, is applied to effectively capture the overall trend of the PDF, as below:

$$f_{ln}(x_s) = \frac{1}{x_s \sigma_s \sqrt{2\pi}} \exp\left(-\frac{(Inx_s - \mu_s)^2}{2{\sigma_s}^2}\right) \tag{4.28}$$

$$M = \exp\left(\mu_s + \frac{{\sigma_s}^2}{2}\right) \tag{4.29}$$

where μ_s and σ_s are the fitting parameters of the lognormal fitting, x_s is the random variable for the PDF, which can be replaced by $V_{nf,\mathrm{m}}$, $S_{nf,\mathrm{ITZ}}$ and $V_{f,\mathrm{a}}$. The analysis of the PDF based on this fitting uses Equation 4.29 to calculate its mean value, M, which can be replaced by M_{m} for mortar, M_{ITZ} for ITZ, and M_{a} for aggregate, as introduced in Figure 4.8(g-i). This mean value of fitting is used to indicate the central tendency of the relative cluster size.

With increasing the confine pressure σ_L, the damage level in mortar, $V_{ntf,\mathrm{m}}$, in Figure 4.8(d) shows a nearly continuous decrease, whilst $S_{ntf,\mathrm{ITZ}}$ and $V_{ntf,\mathrm{a}}$ in Figure 4.8(e) and (f), respectively, exhibit different trends in response to σ_L. We note that, compared to the uniaxial test, low confining pressures, *e.g.*, 5 MPa, can even cause increases in damage levels in ITZ and aggregates, $S_{ntf,\mathrm{ITZ}}$ and $V_{ntf,\mathrm{a}}$, because the lateral constraint is insufficient to prevent fracture initiation or propagation in both material phases, driven by intensified overall stress. Nevertheless, confining pressure can restrict the growth direction of cracks, making them more likely to be confined to localised areas and resulting in smaller crack clusters, as evidenced by the reductions in M_{ITZ} and M_{a} in Figure 4.8(h) and (i), respectively, in contrast to uniaxial test, where crack can freely develop. As σ_L increases beyond 5 MPa, damage levels in mortar and aggregates, $V_{ntf,\mathrm{m}}$ and $V_{ntf,\mathrm{a}}$ in Figure 4.8(d) and (f), respectively, progressively decrease. This is because the greater lateral constraint becomes more dominant, restraining deformation in the axial loading direction and potential shear failure. This significantly increases the strength required for material fracture, reducing the regions of experience severe damage. However, although the strength of the ITZ improves with higher σ_L, as described in the material model, it remains the weakest phase and is still the most susceptible to cracking. Therefore, $S_{ntf,\mathrm{ITZ}}$ is not significantly inhibited for increasing level of confine pressure, as shown in Figure 4.8(e).

Among all material phases, the mortar phase, $V_{ntf,\mathrm{m}}$ and M_{m} as shown in Figure 4.8(d) and (g), respectively, exhibits similar damage behaviour for different aggregate shapes, reflecting the universality of crack properties in mortar across varying confining pressures. The dependencies of $S_{ntf,\mathrm{ITZ}}$ and $V_{ntf,\mathrm{a}}$ on aggregate shapes are evident through their competition as F_d increases. Although the decrease in $V_{ntf,\mathrm{a}}$ with increasing σ_L, as shown in Figure 4.8(f), makes this competition less pronounced, it remains universal under varying confining pressures. This also indicates that higher level of stress concentration induced by rougher aggregates, whether in uniaxial tests or amplified in triaxial tests, persists during the post-peak regime and continues to promote the fracture propagation from the ITZ to aggregates. The mean of cracked region sizes, M_{ITZ} and M_{a} as shown in Figure 4. (h) and (i), respectively, exhibit no significant variation with increasing σ_L but still generally display universal competition between two material phases. This suggests that, in the case of rougher aggregates under confining pressures, cracking in the ITZ is constrained to propagate in smaller and more localised areas, leading to the more frequent formation of smaller clusters. When promoting fracture propagation into aggregates, higher stress concentration can also expand the fractured area within the aggregates, increasing the likelihood of forming larger crack clusters.

4.4. Summary

In this chapter, the triaxial fracture behaviour of concrete, which contains aggregates with realistic shapes, is studied using mesoscale modelling based on the finite element method. The effect of aggregate shape on the macro strength of concrete under varying confining pressures is specifically investigated, with a focus on exploring the underlying microscopic information from the local response of concrete. These micromechanical features, such as distribution and evolution of stress, local damage, and crack clusters, are analysed to illustrate the universality observed in macroscopic mechanical responses.

Rougher aggregates lead to higher compressive strength of concrete, and this effect becomes more pronounced under higher confining pressure. The relation between confining pressure and normalised compressive strength for all aggregate shapes can be describe by the scaling law with only a single fitting parameter. It is found that the universal law in the triaxial loading regime relies on uniaxial responses, which are strongly dependent on the aggregate shape.

At the initial loading stage, rougher aggregates induce higher concentrated stress within the adjacent mortar phase, resulting in a significant difference in the heterogeneity of stress across samples with different aggregate shapes. As the loading increases toward compressive strength, this heterogeneity becomes universal across varying confining pressures. Confining pressure amplifies the stress concentration effects caused by rougher aggregates, further promoting fracture propagation from the ITZ into the aggregates and resulting in greater concrete strength. The competition among damage evolution in concrete phases across varying confining pressures allows the effects of aggregate shape on concrete strength to be reflected from triaxial to uniaxial tests and enables the scaling law to include the shape effects through normalisation while predicting concrete strength under confining pressure. The competition between the ITZ and aggregates also extends to crack and damage evolutions, illustrating that shape-induced stress concentration effects on fracture propagation from the ITZ to aggregates persist even in the post-peak regime. Under confining pressures, the competition in terms of crack clusters indicates that, for rougher aggregates, the ITZ tends to fracture into smaller clusters, while higher stress concentrations can expand the fractured zones within the aggregates, leading to larger fracture clusters.

In summary, the role of aggregate shapes on fracture behaviour of concrete under triaxial stresses has been comprehensively understood by examining local responses within the material phases. The adopted universal scaling law can improve the prediction of concrete strength under triaxial stress conditions, as it accounts for the effect of confining pressure while minimising the influence of aggregate shape. In addition, this study can provide a valuable insight for practical engineering applications, especially in concrete mixture design, where shape irregularity of aggregate associated with concrete strength and damage should be carefully considered. Our mesoscale model can be improved by considering the following aspects in future research: (1) More reliable material parameters will be obtained from corresponding experimental studies in future work, rather than relying on reported values or assumptions from the existing literature; (2) The current work considers an idealised mesoscale concrete model, assuming mono-sized and non-contacting aggregates, as well as homogeneous material phases. More realistic concrete models, incorporating higher aggregate volume fractions, pre-existing cracks, and pores in the mortar, should be considered to better assess the effect of aggregate shape; (3) The idealised confining pressure conditions will be extended to more complex multiaxial stress states, i.e., $\sigma_1 > \sigma_2 > \sigma_3$.

Chapter 5 Mesoscale Modelling of Dynamic Fracture of Concrete

In this chapter, to account for sudden impact accidents occurring in marine environments, mesoscale modelling based on the finite element method (FEM) is employed to simulate Split Hopkinson Pressure Bar (SHPB) tests on three-phase concrete with realistic aggregate shape, to investigate the effects of loading ramp rate, internal friction, and confining pressure on the dynamic increase factor (DIF). Microscopic evidence to explain these effects is explored through analysing the distributions of the internal strain rate and local damage. As key results, increasing loading ramp rates, internal friction, and confining pressure can generally leads to higher DIF values. Only a higher loading ramp rate significantly amplifies the strain-rate effect on the DIF, as evidenced by pronounced increases in both internal strain rate and damage in the mortar and aggregate phases. In contrast, higher internal friction and confining pressure weaken the strain-rate effect on the DIF. Both can be attributed to the mortar phase, which shows a less pronounced increase in damage with increasing strain rate. These systematic mesoscale studies deepen our understanding of the dynamic fracture behaviour of concrete and provide a stronger theoretical basis for predicting sudden dynamic accidents in marine environments.

This chapter has been devoted to the following paper:

Liu, Q. and Gan, Y., 2026. Mesoscale modelling of confined split-Hopkinson pressure bar tests on concrete: effects of internal damage and strain rates, Engineering Fracture Mechanics, 339, p.112079.

5.1. Introduction

As the most widely used construction material worldwide, concrete plays an essential role across a wide range of onshore and offshore infrastructure applications, such as bridges (Branco and Mendes, 1993), tunnels (Gong et al., 2017), concrete dams (Bukenya et al., 2014), and offshore wind turbines (Mathern et al., 2021). Throughout their service life, concrete structures are exposed to extreme weather and complex geotechnical conditions and may suffer natural or accidental events, such as earthquakes (Takeda et al., 1970; Shakib and Alemzadeh, 2017), rockfall events (Tian et al., 2025; Wang et al., 2025b) , tsunamis (Petrone et al., 2020; Tagle et al., 2021) and ship impacts (Wan et al., 2019; Wu et al., 2021a), leading to potentially huge and irreversible damage to concrete structures. Thus, characterisation of concrete behaviour under dynamic loading is a prerequisite for safe and efficient structural design (Mazars and Millard, 2009; Mo, 2013; Malvern and Ross, 1986). Various types of dynamic loading, e.g., impact (Li et al., 2025a), blast (Zhang et al., 2019), seismic (Zhang et al., 2018a), and cyclic loadings (Sinaie et al., 2015), have been considered. As applied stress conditions become more complex to reflect practical scenarios, it becomes progressively more challenging to precisely control over the loading conditions for investigating the dynamic response of concrete to external conditions. In addition to the vastly existed unconfined experimental cases, confined dynamic loading has also received increasing attention (Cui et al., 2018; Chen et al., 2023b). As a typical heterogeneous material, concrete has a microstructure spanning length scales from the nano- to the macroscale (Vandamme and Ulm, 2009; Cusatis et al., 2014; El Awad, 2020), and its complicated internal structure of concrete poses challenges in identifying the underlying mechanisms of dynamic fractures. The mesoscale allows concrete to be treated as a three-phase composite consisting of mortar, aggregates, and the interfacial transition zone (ITZ), making it possible to represent the main material heterogeneity of concrete and to capture its overall and local responses (Ren et al., 2023). Yet, due to the intrinsic complexities in the material phases and temporospatial variations of the strain rates, there is still a lack of investigations on bridging microscopic information to the macroscopic findings under dynamic stress conditions.

The dynamic response of concrete over a wide range of strain rate has been investigated using various approaches, such as drop hammer tests (Hughes and Watson, 1978), Split Hopkinson Pressure Bar (SHPB) tests (Ross et al., 1995), bullet impact tests (Jamnam et al., 2020), and explosion tests (Kušter Marić et al., 2024). For the broadly focused strain rate range

relevant to the infrastructure applications (around 10^{-5}~10^{3} s^{-1}), the SHPB test is the most widely regarded approach and has been used to characterise the overall response of concrete at strain rates of about 10~10^{3} s^{-1} (Ross et al., 1995), whereas drop hammer tests are typically used for lower strain rates up to around 10 s^{-1} (Hughes and Watson, 1978). As commonly observed, with increasing strain rate, the stress-strain behaviour of concrete becomes more ductile with its instantaneous material properties changing accordingly. The most notable effect is the significant increase in concrete strength (Al-Salloum et al., 2015), quantified by the dynamic increase factor (DIF) as the ratio of dynamic to static strength (Abrams, 1917). Based on the available experimental data, many attempts have been made to capture the relationship between DIF and strain rate through empirical models, such as those proposed by the International Federation for Structural Concrete (FIB) (CEB-fib, 2013), Bischoff and Perry (Bischoff and Perry, 1995), and Ross and Tedesco (Ross et al., 1995). The strain rate dependency of concrete strength can be divided into low and high strain rate regions, characterised by the low and high rate sensitivity, respectively, and separated by a critical strain rate (Cusatis, 2011). Due to the heterogeneous nature of concrete, the relationship between the DIF and strain rate has also been investigated with respect to various properties related to the material constituents, including mortar strength (Sun et al., 2021a), aggregate type (e.g., coral (Li et al., 2025b) or recycled (Selyutina and Smirnov, 2023) aggregate), aggregate morphology (e.g., size (Kim et al., 2019) and shape (Jiang and Shen, 2022)). Besides the interest in the macroscopic dynamic performance of concrete, advanced precision instruments, e.g., X-ray computed tomography (XCT) (Krčmářová et al., 2025) and ultra-high-speed imaging camera (Ghosh et al., 2025), have been widely used to investigate the microscopic effects. Nevertheless, analyses based on the available experimental data do not intuitively reflect the damage evolution of the internal material constituents. Direct evidence of the local response of concrete is needed to explain the macroscopic performance.

In SHPB tests, the specimen strain rate is often governed by the magnitude of the stress wave (Al-Salloum et al., 2015), and other factors associated with the impact wave, such as wave shape due to the presence of the pulse shaper between the striker and incident bars, have rarely been assessed in experiments. The main function of the pulse shaper in SHPB tests is to produce a longer and smoother ramp-like stress wave, characterised by the loading ramp rate, magnitude and duration of the stress wave (Lv et al., 2017). As it is difficult to control the wave shape using a pulse shaper in experiments, this issue could be addressed using numerical approaches. It is shown that the stress wave impacting the incident bar can be prescribed in a

waveform, allowing the wave shape to be defined in the SHPB model (Ayhan and Lale, 2022). When different wave shapes are used to assess the dynamic response of concrete, they may also result in different ramp rates, the effects of which have been neglected and remain to be quantified.

To understand concrete responses under realistic dynamic stress conditions, various confined conditions have been taken into consideration. Confining pressure can be applied using active confinement methods, e.g., liquid- or air-pressurised hydraulic vessels (Christensen et al., 1972; Gran et al., 1989), or passive confinement methods, e.g., shrink-fit metal sleeve (Chen and Ravichandran, 1996; Chen and Ravichandran, 1997). Generally, the confinements can improve the concrete strength but cause lower strain rate sensitivity compared to unconfined cases (Christensen et al., 1972; Gran et al., 1989; Chen and Ravichandran, 1996; Chen and Ravichandran, 1997). Coupling dynamic loading with confinement is experimentally challenging, requiring a complex test setup and implementation. Consequently, it is difficult to maintain a constant confining pressure throughout the dynamic deformation of the concrete specimen, leading to an inaccurate estimation of the intended confining pressure. Numerical work on confined loading scenarios is quite limited and has mainly focused on developing well-calibrated models by comparing a single dynamic strength under unconfined and confined loading cases (Li et al., 2022a; Singh and Gupta, 2024) or under different confinement methods (Cui et al., 2018). Systematic assessments of the overall and local responses of concrete under progressively increasing confinement levels are still lacking. For the abovementioned the loading ramp rate and confinement, their influences require further attention in SHPB-related studies.

Considering the different material phases of concrete, representing its internal structure using mesoscale models has been given particular attention. Generally, these models can be generated by either image-dependent approach, i.e., XCT (Huang et al., 2023), or image-independent approaches, i.e., computer based packing algorithms (Wei et al., 2020b; Xiong et al., 2020a; Liu et al., 2025). The former can be used to obtain the digital images of the concrete specimen and then convert them into the mesoscale structure of concrete (Huang et al., 2023). Such an approach is highly affected by image resolution (Li and Li, 2015). The image segmentation may fail to delineate some aggregate boundaries when encountering aggregate overlapping (Li and Li, 2015). Alternatively, the latter makes it possible to overcome this issue by generating the spatial distribution of aggregates using various packing algorithms, such as

take-in-place methods (Wang and Jivkov, 2015), random extension methods (Ma et al., 2016) and graphical methods (Caballero et al., 2006). These approaches can achieve a predefined packing density while simultaneously satisfying the specified Fuller curves for the aggregate size distribution. However, aggregates are represented using simplified and regular shapes, such as spheres, ellipsoids, or polyhedron (Xiong et al., 2020a), which fail to capture the realistic morphology of aggregates and may induce unrealistic stress concentrations compared with realistic shapes. Detecting aggregate-to-aggregate contact in packing is a challenging task for realistically shaped aggregates. For an effective approach, spherical harmonics (Wei et al., 2020b) or Fourier descriptor-based methods (Mollon and Zhao, 2014; Liu et al., 2025), combined with Voronoi tessellation for predefined spaces, have been adopted to generate realistic aggregate shapes within the cells, characterised by multiscale geometrical indices such as fractal dimension and relative roughness (Wei et al., 2020b; Liu et al., 2025).

Appropriate numerical methods and constitute laws need to be carefully considered for mesoscale models to reflect realistic dynamic fracture behaviour in concrete. Generally, numerical methods fall into two categories including discrete approaches and continuum approaches. Compared with the latter, the former requires extensive trial-and-error during calibration to determine the parameter values for the bonds between individual components, e.g., spheres in the discrete element method (DEM), as reported in some studies (Zhou et al., 2022). This issue can be avoided by using continuum modelling, which treats the system as a continuous medium rather than a collection of individual components (Thilakarathna et al., 2020). The most representative continuum approach is the finite element method (FEM). Among the constitutive models implemented in FEM, such as concrete damaged plasticity (CDP) (Xiong et al., 2020a), cohesive interface element (CIE) methods (Wei et al., 2020b), and the K&C model (Guo et al., 2020), some have been used to account for the dynamic nature of concrete and to predict its stress-strain behaviour under different strain rates. For the characterisation of material heterogeneity in mesoscale modelling, distinct material parameter values can be assigned to each material constituent, by assuming all have the same dynamic constitutive framework (Liu et al., 2019). Alternatively, different constitutive models can be used for different material phases, such as combining the cohesive element method for the ITZ and CDP model for the mortar and aggregate (Wang et al., 2020; Liu et al., 2025).

The well-established mesoscale modelling framework, considering morphological and material heterogeneities, has been employed to assess the dynamic response of concrete. These

numerical works are generally conducted using two loading schemes, velocity and stress wave controlled. The first approach is to apply the velocity boundary conditions directly to the specimen (Yu et al., 2023). The other approach is to use the impact wave in SHPB tests, generated by the striker impacting the incident bar (Cui et al., 2018), which has become more popular as it allows the investigation of the dynamic response at even higher strain rates. Relevant mesoscale modelling has been conducted to investigate the various interior and exterior influencing factors, such as low temperature (Su et al., 2023), confined condition (Cui et al., 2018), specimen size (Yu et al., 2023) and shape, lightweight aggregate (Duan et al., 2023), aggregate solid fraction (Zhang et al., 2021c) and size (Jin et al., 2020b). Although damage or failure in different material phases can be visualised, such microscopic investigations are insufficient to explain macroscopic findings due to the lack of statistical and correlative analyses. As shown in the work of Liu et al. (Liu et al., 2025), which focuses on the quasi-static triaxial failure of concrete, statistical parameters obtained from PDF analyses of microscopic information can provide more evident support for the results. These model-based analyses must be properly calibrated and benchmarked (Cui et al., 2018), including the material parameters and internal contact model between post-failure segments. When velocity-controlled loading or impact waves are applied to the concrete model through a loading plate (Yu et al., 2023) or SHPB bars (Cui et al., 2018), the interaction with the concrete specimen is normally treated as frictional contact (Cui et al., 2018; Yu et al., 2023). Internal friction between and within different material phases, as an inherent property of concrete that is inaccessible in experiments, should also be incorporated into the model (Wei et al., 2020b; Liu et al., 2025). However, its effects are often neglected in many studies and need to be quantified to enhance the understanding of the realistic responses of concrete material constituents to dynamic loading.

Despite based on the mesoscale structure of concrete, most numerical SHPB models emphasis on macroscopic dynamic responses, without providing sufficient information from microscopic analyses. During the loading process, the internal strain rate within the specimens exhibits temporospatial distributions due to the presence of material heterogeneities and interfaces (Blatny et al., 2022). Further, as additional microscopic information, local damage can effectively reflect the responses within concrete and explain the variation in its strength [63]. Both strain rate and damage aspects are rarely evaluated statistically or quantitively to provide direct evidence on the dynamic behaviour of concrete. For exploring the effects of loading ramp rate, internal friction, and confining pressure, a comprehensive numerical

investigation of their respective effects is required, with particular attention given to analyses of internal strain rate and local damage to provide microscopic evidence supporting variations in the macroscopic dynamic response of concrete materials.

To address these research gaps discussed earlier, in this study, FEM modelling of SHPB tests is conducted to investigate the dynamic response of concrete. Here, concrete is represented as a three-phase mesoscale structure with realistic aggregates embedded in a homogeneous mortar matrix. The mesoscale model is used to explore the roles of internal strain rate and local damage in the DIF-strain rate relationship from different aspects, including loading ramp rate, internal friction, and confining pressure. The remainder of the paper is organised as follows. Section 5.2 presents the generation of a mesoscale concrete model with realistic aggregate shapes, followed by the implementations of strain-rate-dependent constitutive models and SHPB loading conditions. Model validations against experimental data are then conducted. Section 5.3 will assess each aspect by investigating the relationship between DIF and strain rate, through microscopic analyses of internal strain rates and damage states. Finally, conclusions are drawn in Section 5.4.

5.2. Methods

In this section, the mesoscale modelling of SHPB tests on concrete is conducted. Consistent with our previous work (Liu et al., 2025), concrete at the mesoscale is still treated as a three-phase composite consisting of mortar, the ITZ, and aggregates. Here, we assume each material phase to be a homogeneous medium, ignoring any pores and pre-existing microcracks, although these normally appear in the material constituents and affect the mechanical performance of concrete (Zhang, 1998; Xie et al., 2016). The cylindrical concrete sample is represented as a mesoscale structure packed with realistically shaped aggregates, then, the material constitutive laws are described, combining the concrete damage plasticity model for the mortar and aggregates and the cohesive element method for the ITZ, capturing the dynamic properties of concrete. The loading conditions for modelling the SHPB test are presented. Based on the data processing, the validation of our numerical results against existing experimental data is provided.

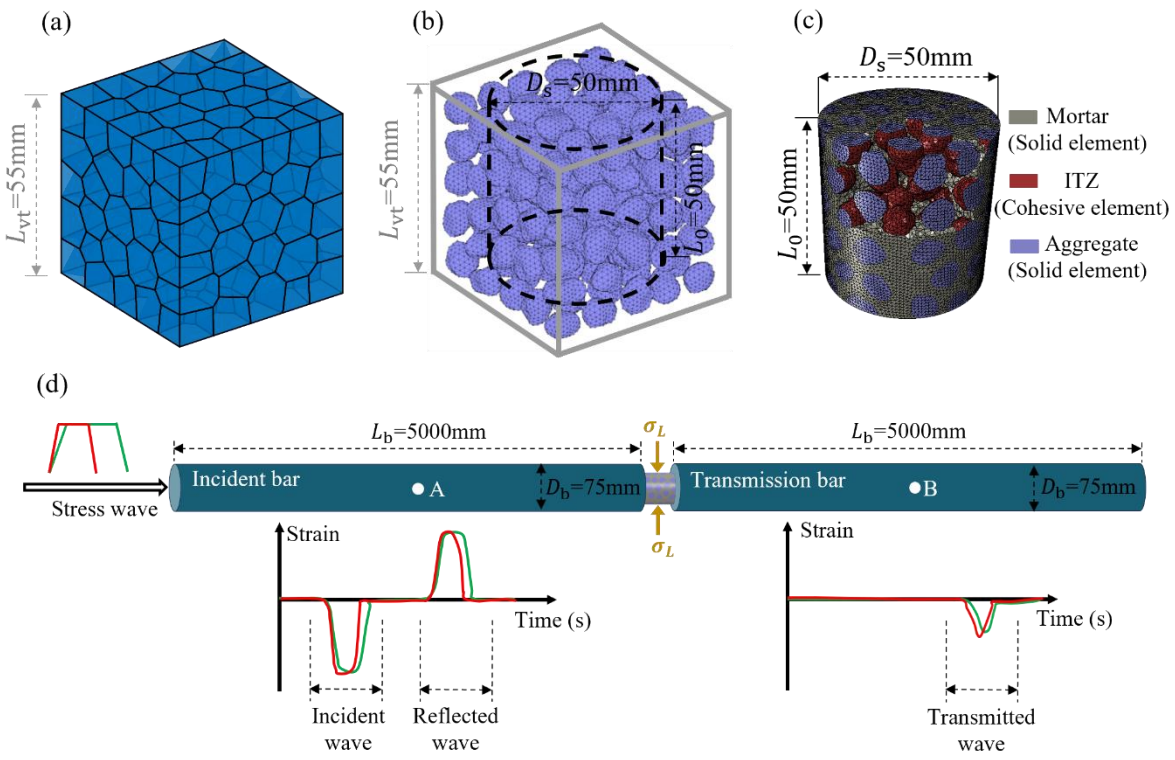

Figure 5.1. Mesoscale modelling of SHPB tests on concrete: (a) Typical Voronoi tessellation for packing processes; (b) Spatial distribution of irregularly shaped aggregates corresponding to the initial tessellation in (a); (c) A cylindrical specimen extracting from (b) containing three concrete phases and finite element meshes; and (d) Schematics of FE model of the SHPB test with a confining pressure of σ_L and the wave records at points A and B.

5.2.1. Mesoscale sample generation

To generate the concrete model containing realistic aggregate shapes, this study uses the packing algorithms (Liu et al., 2025), i.e., combination of Voronoi tessellation and the Fourier-descriptor-based methods. This approach has been improved by introducing the fractal dimension F_d as a multiscale geometrical index to characterise the realistic aggregate shape. Given a target packing density, an appropriate size scaling of aggregates from their mass centres is also required to achieve a packing of realistically shaped aggregates without any contact or overlap within a predefined cubic space. As our early works have explored the effects of aggregate morphology, and the samples with $F_d = 2.3$ have been found to be the most representative case and only one geometrical model is used in all simulations due to the neglectable sample variation found previously.

The mesoscale structure of a cylindrical concrete specimen with a diameter of $D_s = 50$ mm and a length of $L_0 = 50$ mm is used for our numerical investigation, consistent with the standard sample size used in the work of Cui et al. (2018). We first achieve aggregate packing within a predefined cubic space with a side length of 55 mm ($> L_0$), shown in Figure 5.1(a), which is more than five times larger than the maximum aggregate size, as suggested by Naderi et al. (2021). The aggregates are then cut for generating the cylindrical concrete specimen. In the initial cubic space, 120 nearly mono-sized aggregates are generated using the adopted packing algorithm to achieve a packing density (or aggregate solid fraction, SF_a) of 30%. Generating realistic aggregate shapes with $F_d = 2.3$ in each cell produces the approximately mono-sized aggregate packing shown in Figure 5.1(b), with a mean equivalent volume diameter of around 9.3 mm.

The aggregate surface is defined by 162 vertices and discretised into 320 nearly uniform triangular surficial meshes, which are directly generated using the published code from the work of Mollon and Zhao (2014) that incorporates the concept of geodesic structures. A similar number of surficial meshes was also used in the work of Wei et al. (2020b), and has been shown to sufficiently highlight the effects of aggregate surface roughness, as characterised by the prescribed fractal dimension. The aggregate surfaces are then imported as solid geometries into the finite element software ABAQUS/Explicit. The solid aggregates are then cut using a cylindrical space with $D_s = 50$ mm and $L_0 = 50$ mm, whose centroid is aligned with the centre of the cubic space. As a result, 81 aggregates intersected by the cylindrical space are cut, while 39 aggregates remain entirely inside the domain. The mortar phase is then generated by filling the cylindrical space around these aggregates.

For meshing the cylindrical sample geometry directly cut from the initial cubical space, appropriate pre-treatment must first be applied to resolve the complex intersections among the elements, interfaces and exterior boundary. Cutting the aggregates with the cylindrical space may subdivide some triangular surface elements into small fragments, which induce excessively fine meshes around aggregate interfaces during the meshing process. This can be resolved by generating a more uniform mesh layout to replace the undesired fine meshes and prevent potential numerical errors. While preserving the geometry of the aggregate cuts, some vertices of the small mesh fragments need to be removed through trial and error. This pre-treatment can eventually enable the aggregate cut to retain the inherent morphology characterised by the prescribed fractal dimension while preventing unrealistic stress

concentrations. After this, the entire solid geometry of mortar and aggregate can be successfully discretised using tetrahedral elements with an edge size of approximately 1 mm, as shown in Figure 5.1(c). More effective approaches are recommended for future work to avoid such meshing issues arising from aggregate cutting. The zero-thickness cohesive interface element (CIE) is used to represent the ITZ, following our previous work (Liu et al., 2025). The meshed mesoscale structure of the cylindrical concrete specimen is shown in Figure 5.1(c), containing around 418,000 solid elements for the mortar and aggregates and around 34,000 CIEs for the ITZs. In this study, an average tetrahedral element size of approximately 1 mm (≈1/10 of the characteristic aggregate size) was adopted and has been shown to be sufficient to ensure numerical accuracy in our previous work through mesh sensitivity analyses (Liu et al., 2025) and existing concrete fracture studies (Wang et al., 2016b; Naderi et al., 2021). In addition, this element size is much less than the stress wavelength and allows the capture of stress-wave propagation without potential numerical dispersion.

5.2.2 Constitutive models for dynamic fracture

Different constitutive laws for concrete materials are considered to simulate dynamic fracture. Here, the concrete damage plasticity (CDP) model is used for both mortar and aggregate, with respective sets of material parameters. For the ITZs, the traction-separation law is used to describe the mechanical response of the CIEs. The key aspects of the constitutive laws and the relevant strain rate effects are also discussed in this section.

Table 5.1: Material properties of concrete constituents.

Constituents	Material property	Value
Mortar/Aggregate (Concrete damage plasticity, CDP)	Density ($\mathrm{kg/m^3}$)	2200/2600
	Young's modulus (GPa)	30/70
	Poisson's ratio	0.2/0.2
	Ultimate strength in compression (MPa)	45/80
	Ultimate strength in tension (MPa)	4/10
	Fracture energy, GFI_{ts} (N/m)	50/60
ITZ (Cohesive interface element, CIE)	Initial stiffness ($\mathrm{N/m^3}$)	1×10^{13}
	Normal strength (MPa)	2.4
	Shear strength (MPa)	7.2
	Fracture energy (N/m)	30

Steel SHPB bar	Density (kg/m^3)	7850
	Young's modulus (GPa)	200
	Poisson's ratio	0.3

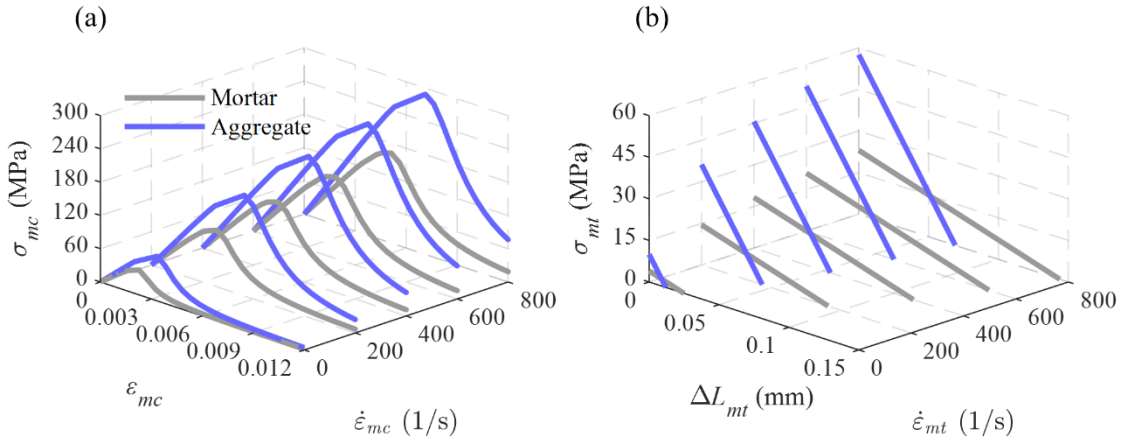

Figure 5.2. Dynamic responses of the material phases: (a) Compressive stress (σ_{mc}) -strain (ε_{mc}) under varying compressive strain rates $\dot{\varepsilon}_{mc}$, and (b) Post-peak tensile stress (σ_{mt})–crack opening (ΔL_{mt}) under varying tensile strain rates, $\dot{\varepsilon_{mt}}$.

5.2.2.1 Concrete damage plasticity (CDP) model

The CDP model defines compression and tension as the two primary failure mechanisms, based on the concepts of isotropic damage together with isotropic plasticity to describe the inelastic behaviour of concrete (Lubliner et al., 1989). The compressive stress-strain relationship is defined using the FIB Model Code 2010 (FIB-MC2010) (CEB-fib, 2013), in which the stress (σ_{mc})-strain (ε_{mc}) curve is linear elastic up to the onset of damage, followed by strain-hardening and strain-softening stages (CEB-fib, 2013; Yu et al., 2023). For tension, specifying the stress-strain curve may lead to mesh-size dependency in the numerical results (Chen et al., 2020b; Chen et al., 2022a). To address this issue, the tensile behaviour can alternatively be defined by directly specifying the tensile strength and fracture energy in the CDP model to characterise the tensile stress (σ_{mt}) - crack opening (ΔL_{mt}) response (Chen et al., 2020b; Chen et al., 2022a). The corresponding material parameters have been previously calibrated with sets of experimental data as summarised in Table 5.1 (Liu et al., 2025). In addition, five other parameters of the CDP model, which are dilation angle, plastic potential eccentricity, ratio of biaxial to uniaxial compressive strength, ratio of the second stress invariant on the tensile meridian to that on the compressive meridian, and viscosity parameter,

are taken to be the same for both the mortar and aggregate phases, with values of 35°, 0.1, 1.16, 0.667, and 0.0005, respectively (Liu et al., 2025).

5.2.2.2 Cohesive element method for ITZ

A bilinear traction-separation law is employed to model the response of the cohesive elements, exhibiting linear behaviour after damage initiation, followed by energy-based linear softening (Geubelle and Baylor, 1998). Damage initiates when the stresses in the normal and shear directions reach their critical values, as defined by a quadratic stress criterion. Once damage is initiated, the tractions gradually decrease with increasing separation, representing softening and energy dissipation through fracture. The fracture energy corresponds to the total energy required to fully separate the CIE. When the separation reaches the ultimate fracture displacement, the CIE is completely damaged. Benzeggagh-Kenane (BK) criterion (Benzeggagh and Kenane, 1996) is adopted to account for mixed-mode behaviour. The material parameters for the CIE (Liu et al., 2025) have been previously calibrated as in Table 1. Element deletion is considered for both solid elements and CIEs, with a default maximum degradation threshold of 1.0.

5.2.2.3 Strain rate effects

The constitutive models for concrete materials should be adapted to respond to the real-time strain rate at each incremental step to accurately account for the dynamic response of concrete. This rate-dependent response is reflected in mechanical properties such as compressive and tensile strength, elastic modulus, and strain at peak stress (Liu et al., 2019; Chen et al., 2020b), several of which are well defined in FIB-MC2010 (CEB-fib, 2013). Among these properties, the influence of strain rate on concrete strength is the most significant and is therefore taken as the main consideration in mesoscale modelling (Liu et al., 2019; Chen et al., 2020b). This can be achieved by adapting strengths of material constituents to the real-time strain rates, assuming that they exhibit a similar strain rate behaviour as the overall concrete strength (Liu et al., 2019; Chen et al., 2020b). The compressive and tensile strengths of both mortar and aggregate are defined as strain-rate dependent based on the formulas in FIB-MC2010 (CEB-fib, 2013), as shown below:

Compression:

$$\frac{\sigma_{mc,d}}{\sigma_{mc,s}} = \left(\frac{\dot{\varepsilon}_{mc}}{\dot{\varepsilon}_{mc,s}}\right)^{0.014}, \dot{\varepsilon}_{mc} \leq 30\ \mathrm{s}^{-1} \quad (5.1)$$

$$\frac{\sigma_{mc,d}}{\sigma_{mc,s}} = 0.012\left(\frac{\dot{\varepsilon}_{mc}}{\dot{\varepsilon}_{mc,s}}\right)^{1/3}, \dot{\varepsilon}_{mc} > 30\ \mathrm{s}^{-1} \quad (5.2)$$

Tension:

$$\frac{\sigma_{mt,d}}{\sigma_{mt,s}} = \left(\frac{\dot{\varepsilon}_{mt}}{\dot{\varepsilon}_{mt,s}}\right)^{0.018}, \dot{\varepsilon}_{mt} \leq 10\ \mathrm{s}^{-1} \quad (5.3)$$

$$\frac{\sigma_{mt,d}}{\sigma_{mt,s}} = 0.0062\left(\frac{\dot{\varepsilon}_{mt}}{\dot{\varepsilon}_{mt,s}}\right)^{1/3}, \dot{\varepsilon}_{mt} > 10\ \mathrm{s}^{-1}, \quad (5.4)$$

where $\sigma_{mc,s}$ and $\sigma_{mt,s}$ are the static compressive and tensile strengths (MPa), $\dot{\varepsilon}_{mc,s} = 30 \times 10^{-6}\mathrm{s}^{-1}$ and $\dot{\varepsilon}_{mt,s} = 1 \times 10^{-6}\mathrm{s}^{-1}$ are the reference static strain rates in compression and tension, $\sigma_{mc,d}$ and $\sigma_{mt,d}$ are dynamic compressive and tensile strength (MPa) at their respective strain rate $\dot{\varepsilon}_{mc}$ and $\dot{\varepsilon}_{mt}$ (s^{-1}). The subscription, m, indicates the corresponding material constituent.

As suggested by Snozzi et al. (Snozzi et al., 2011), the strain-rate effects on the tensile fracture energy are defined in this study to ensure that the tensile strength and crack opening increase proportionally with increasing strain rate. For simplicity, the fracture energy $\mathrm{GFI}_{mt,d}$ at different strain rates can be calculated by replacing $\frac{\sigma_{mt,d}}{\sigma_{mt,s}}$ with $\frac{\mathrm{GFI}_{mt,d}}{\mathrm{GFI}_{mt,s}}$ in Equations.(5.3) and (5.4), where $\mathrm{GFI}_{mt,s}$ is fracture energy (N/m) at the reference static strain rate.

For the remaining material parameters in Table 5.1, the strain rate effects are considered negligible in the CDP model. Eventually, the compressive stress–strain curves, tensile strengths, and fracture energy for mortar and aggregate can be adapted to increasing strain rates and provided as input to the implemented CDP model. Examples under several compressive and tensile strain rates are shown in Figure 5.2, where the post-peak tensile stress (σ_{mt})–crack opening (ΔL_{mt}) in Figure 5.2(b) is used to demonstrate the effects of strain rate on tensile strength and fracture energy.

Finally, the ITZ is modelled using zero-thickness CIEs and does not possess measurable strain fields, unlike solid phases of mortar or aggregate. The concept of strain rate, defined based on deformation over a finite length and time, is not physically meaningful for zero-thickness CIEs. Although some efforts have been dedicated to developing traction–separation laws that incorporate opening or sliding rate effects for CIEs (Zhao et al., 2021; Zhang et al., 2024b), such a rate dependency can be neglected for our model, due to insufficient

experimental observations reported about dynamic response of ITZ (Liu et al., 2019; Li et al., 2021; Zhao et al., 2025). To provide a certain understanding of the assumption regarding the ITZ, the concrete is also treated as a special case of a two-phase composite consisting only of mortar and aggregates, in which the ITZ is assumed to be embedded in the mortar and to have the same properties as the mortar. This case can be regarded as providing an upper bound for the current modelling assumption, accounting for the infinite strengthening of the ITZ under rate effects. Compared to this two-phase model, which is a fully strain-rate-dependent model, the assumption of strain-rate independence for the ITZ in the current three-phase model may lead to discrepancies in the results, as local responses tend to shift more toward the mortar and aggregate phases, thereby contributing to the macroscopic response.

5.2.3 Loading conditions and wave signal processing

5.2.3.1 Loading conditions

The modelling of the SHPB test on concrete specimens is conducted to investigate the dynamic behaviour of concrete, as shown in Figure 5.1(d). The incident and transmission bars have a diameter of $D_{\mathrm{b}} = 80$ mm and a length of $L_{\mathrm{b}} = 5000$ mm, and both are meshed with around 4 mm sized hexahedral solid elements. The bars are made of steel, with material properties shown in Table 5.1. The cylindrical concrete specimen is positioned between the two bars. The contact between the bar and the specimen surfaces is defined as hard contact with a friction coefficient of 0.5, which is a rounded value adopted from the work of Minh et al. (2021). In confined cases, the confining pressure σ_L is kept below half of the uniaxial compressive strength of concrete under quasi-static conditions. Due to its efficiency in handling contacts, ABAQUS/Explicit is employed as the dynamic solver for all modelling cases.

The loading scheme is conducted in two sequential steps without any additional step coupling. In the first stage, the confining pressure is applied to the lateral surface of the cylindrical specimen and linearly increased to the specified value within 0.001 s, leading to a biaxially isotropic compression state. It then remains constant until the end of the entire simulation. In the second stage (with a duration of 0.0023 s), the stress wave impacting the incident bar is used by a prescribed loading amplitude that defines the variation of stress with time. A trapezoidal loading amplitude is employed to reduce excessive oscillations associated with instantaneous loading, in comparison with other shapes, as noted by Ayhan and Lale (2022). Details of the loading amplitude, such as the maximum stress and duration, are

specified in the following sections for different purposes of interest. The loading ramp rate, describing the increase rate of the stress at the initial rising stage of trapezoidal loading, has been controlled for highlighting the sensitivity of the stress wave shape. To determine the DIF, quasi-static fracture of concrete also needs to be modelled, as provided in Appendix C.

5.2.3.2 Wave signal processing

As shown in Figure 5.1(d), points A and B are the midpoints of the incident and transmitted bars, respectively, where the strain waves $\varepsilon_{\mathrm{w}}(t)$ are recorded over time t to calculate the dynamic stress–strain response of the concrete specimen. When the compressive stress wave impacts the incident bar, it travels along the bar and is recorded at point A as the incident strain wave, $\varepsilon_{\mathrm{w,i}}(t)$. Upon reaching the interface between the incident bar and the cylindrical specimen, a portion of the incident wave is reflected back into the incident bar and recorded at point A as the reflected strain wave, $\varepsilon_{\mathrm{w,r}}(t)$. The remaining portion is transmitted through the specimen and travels back and forth between its two end surfaces of the specimen over several cycles. Finally, the stress wave exits the specimen, propagates along the transmitted bar, and is recorded at point B as the transmitted strain wave, $\varepsilon_{\mathrm{w,t}}(t)$. As an example, the recorded $\varepsilon_{\mathrm{w,i}}(t)$, $\varepsilon_{\mathrm{w,r}}(t)$, and $\varepsilon_{\mathrm{w,t}}(t)$ are presented in Figure 5.3(g). The sum of the incident and reflected waves $\varepsilon_{\mathrm{w,i+r}}(t)$ is nearly consistent with the transmitted wave $\varepsilon_{\mathrm{w,t}}(t)$, confirming the achievement of stress equilibrium.

According to one-dimensional wave theory (Meyers, 1994), the time histories of strain, $\varepsilon(t)$, stress, $\sigma(t)$, and strain rate, $\dot{\varepsilon}(t)$, of the specimen can be calculated as follows:

$$\varepsilon(t) = \frac{C_b}{L_0}\int_0^t [\,\varepsilon_{\mathrm{w,i}}(t) - \varepsilon_{\mathrm{w,r}}(t) - \varepsilon_{\mathrm{w,t}}(t)]\,dt, \tag{5.5}$$

$$\sigma(t) = \frac{E_{\mathrm{b}}A_{\mathrm{b}}[\varepsilon_{\mathrm{w,i}}(t)+\varepsilon_{\mathrm{w,r}}(t)+\varepsilon_{\mathrm{w,t}}(t)\,]}{2A_{\mathrm{s}}}, \tag{5.6}$$

$$\dot{\varepsilon}(t) = \frac{C_b}{L_0}\left[\varepsilon_{\mathrm{w,i}}(t) - \varepsilon_{\mathrm{w,r}}(t) - \varepsilon_{\mathrm{w,t}}(t)\,\right], \tag{5.7}$$

where C_{b} is the wave velocity (mm/s) in the bar and can be calculated as $\sqrt{E_{\mathrm{b}}/p_{\mathrm{b}}}$, E_{b} and p_{b} are the elastic modulus ($\mathrm{N/mm^2}$) and density ($\mathrm{kg/mm^3}$) of bar, respectively, L_0 is the initial length (mm) of the cylindrical concrete specimen, and A_{b} and A_{s} are the cross section area ($\mathrm{mm^2}$) of the bar and cylindrical concrete specimen, respectively. The strain rate of the

concrete specimen is generally not constant throughout the dynamic loading period. For a representative value, the strain rate at the peak stress, $\dot{\varepsilon}_{\mathrm{p}}$, is adopted in this study, as particular emphasis is placed on the dynamic strength in following sections. For the quasi-static condition, the stress is defined as $\sigma = F/A$, where F is the sum of the nodal reaction forces (N) on the top plate, and A is the initial cross-sectional area (mm^2) of the cylindrical specimen. The strain is calculated as the ratio of the nodal displacement (mm) to the initial length (mm) of the specimen. Although the velocity-controlled loading method for the quasi-static case involves a short acceleration phase from zero to the prescribed velocity, this brief period can be neglected, allowing the loading process to be considered as occurring at a constant velocity. Thus, the strain rate at the peak stress for the quasi-static case is 1/s, obtained by dividing the applied maximum velocity (50 mm/s) by the initial specimen length ($L_0 = 50$ mm), in accordance with the approach by Liu et al. (Liu et al., 2019).

5.2.4 Validation

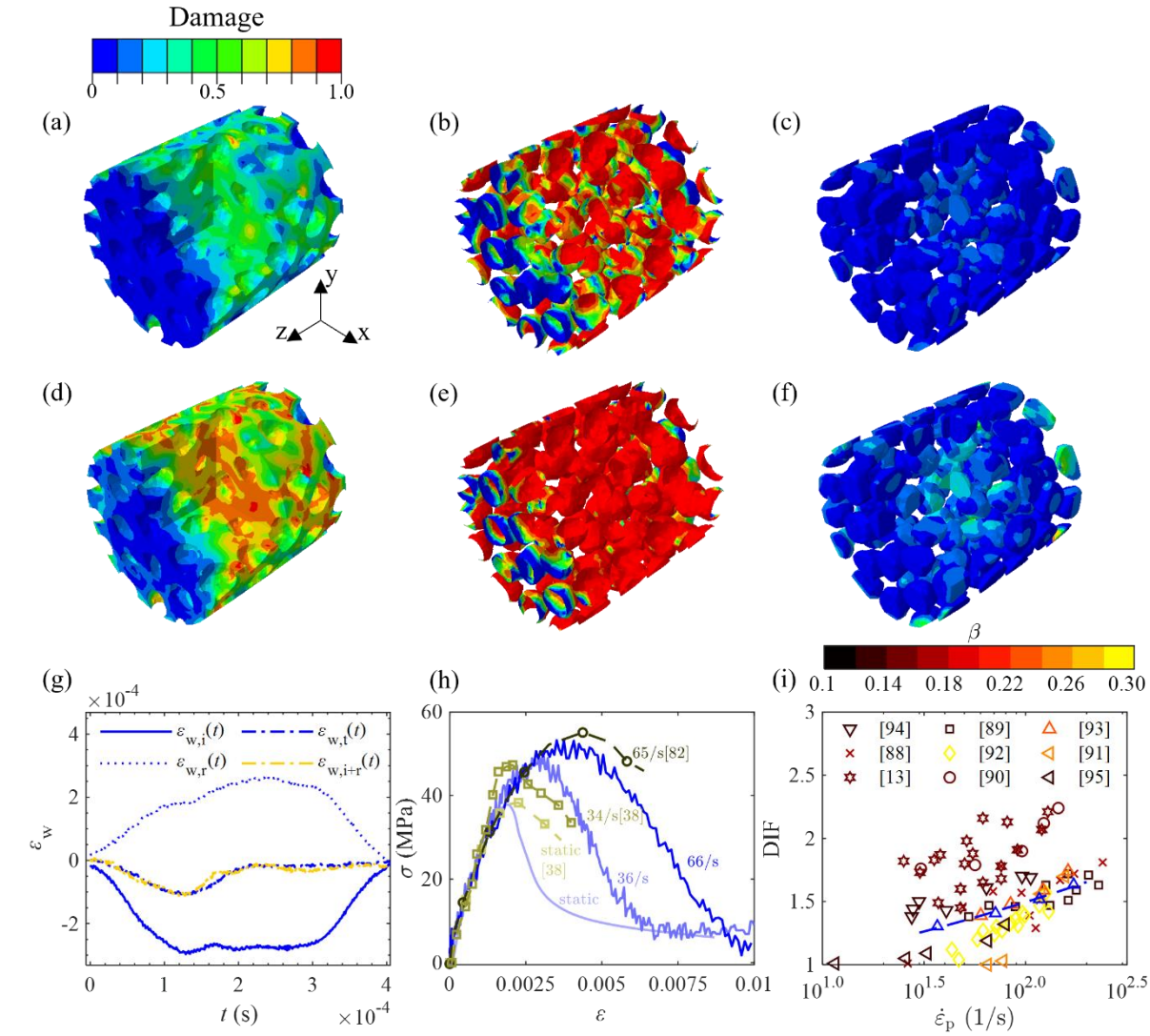

Figure 5.3. Model validation: (a-f) Damage field distributions of mortar, ITZ, and aggregate at the peak dynamic strength, where (a-c) and (d-f) correspond to maximum stress of trapezoidal loading amplitude, $\sigma_{ld,max}$ = 50 and 250 MPa, respectively; (g) A typical incident $\varepsilon_{w,i}(t)$, reflected $\varepsilon_{w,r}(t)$, transmitted $\varepsilon_{w,t}(t)$ waves, along with the sum of the incident and reflected waves $\varepsilon_{w,i+r}(t)$, at $\sigma_{ld,max} = 50$ MPa; (h) Stress (σ)-strain (ε) responses of the concrete specimen under the quasi-static and dynamic cases, with comparable strain rates labelled using different gradual colours for numerical and experimental data; and (i) The dynamic increase factor (DIF) vs the strain rate of the specimen ($\dot{\varepsilon}_p$), where the dashed line represents the fitting to the numerical results, and the colour bar above indicates the corresponding β values of the experimental datasets, represented by marker shape in different colours.

To validate our results, this section focuses only on the rate effects of the unconfined cases. Internal friction within the concrete model is one of the key aspects examined in Section 5.3.2. Through a general contact algorithm, internal frictional contact is applied to elements within each material phase and between different material phases. The contact is defined based on normal and tangential behaviour, with a specified internal friction coefficient. Internal friction is implemented from the initial stage and maintained throughout the entire simulation process, rather than being applied only after the CIEs are completely damaged. Here, an internal friction coefficient of $f_{\mathrm{e}} = 0.1$ is adopted for this section. The trapezoidal loading amplitude for the impact wave is prescribed such that the stress increases linearly to its maximum within 0.0001 s, remains constant for 0.0002 s, and then decreases linearly to zero within 0.0001 s. The maximum stress for the trapezoidal loading amplitude, $\sigma_{\mathrm{ld,max}}$, is specified as 50, 90, 150, and 250 MPa to evaluate the dynamic response of concrete under increasing strain rates. These settings in the SHPB model are adopted for following investigations unless otherwise specified for a particular purpose. The following validation focuses only on comparing our numerical results with experimental data from multiple sources in the existing literature. The corresponding experiments will not be conducted in the current work but could be considered in future studies to provide more rigorous validation and extension of our model.

In Figure 5.3(h), the stress-strain curves are obtained for the quasi-static case and for the dynamic cases with $\sigma_{\mathrm{ld,max}}$ of 50 and 90 MPa, which yield $\dot{\varepsilon}_{\mathrm{p}}$ values of 1, 36, and 66/s, respectively. At higher strain rates, the stress-strain behaviour becomes more ductile, with a significant improvement in concrete strength. To achieve effective validation, the experimental data used for comparison must be obtained at comparable strain rates and from specimen the same slenderness ratio of specimen ($\frac{L_0}{D_{\mathrm{s}}} = 1$). Our results capture the general trend of the limited available stress–strain behaviour reported in experimental studies at different strain rates. For the dynamic cases with higher $\sigma_{\mathrm{ld,max}}$ values of 150 and 250 MPa, which yield higher strain rates of $\dot{\varepsilon}_{\mathrm{p}} = 116$ and 172 /s, we acknowledge the lack of relevant experimental data as a limitation for further validating the model through stress-strain comparisons, in particular at the high strain rate regime. Alternatively, the dynamic increase in concrete strength, as a key concern in dynamic response of concrete, will be compared with existing studies in the following.

The dynamic increase factor (DIF), defined as the ratio of dynamic to static compressive strength of concrete, is computed under varying strain rates, as shown in Figure 5.3(i). As the

DIF increases with increasing strain rate, the damage in the mortar, ITZ and aggregates becomes more severe, as indicated by comparing Figure 5.3(a-c) with (d-f), because higher stresses are imposed on the elements, accelerating the respective damage. This observation regarding local damage is also almost consistent with findings from high-speed imaging studies, in which greater impact loads lead to denser fractures (Pająk et al., 2021; Krčmářová et al., 2025; Pająk and Janiszewski, 2025). Beyond this, further validation of the temporal evolution of fracture morphology is limited. Especially, these evolutions are sensitive to the actual material mix proportions, specimen dimensions, and spatial scale. Our numerical results are plotted against experimental data that consider various influencing factors, such as normal concrete (Dilger et al., 1984; Tedesco and Ross, 1998; Zhang et al., 2009), cement (Lai and Sun, 2009) and aggregate types (Guo et al., 2023a; Gao et al., 2025), additives (Jiao et al., 2009; Tai, 2009), and moisture content (Malvern and Ross, 1986). These existing experimental data are also obtained from SHPB tests. The fitting to the numerical results is proposed in a form similar to Equation (5.2) and achieves an excellent coefficient of determination $R^2 = 0.99$:

$$\mathrm{DIF} = \frac{\sigma_{d,\mathrm{p}}}{\sigma_{s,\mathrm{p}}} = \alpha\left(\frac{\dot{\varepsilon}_{\mathrm{p}}}{\dot{\varepsilon}_{\mathrm{p},0}}\right)^{\beta}, \tag{5.8}$$

$$\frac{\mathrm{DIF}}{\mathrm{DIF}_1} = \frac{\alpha\left(\frac{\dot{\varepsilon}_{\mathrm{p}}}{\dot{\varepsilon}_{\mathrm{p},0}}\right)^{\beta}}{\alpha\left(\frac{\dot{\varepsilon}_{\mathrm{p},1}}{\dot{\varepsilon}_{\mathrm{p},0}}\right)^{\beta}} = \left(\frac{\dot{\varepsilon}_{\mathrm{p}}}{\dot{\varepsilon}_{\mathrm{p},1}}\right)^{\beta}, \tag{5.9}$$

where $\sigma_{\mathrm{d,p}}$ and $\sigma_{\mathrm{s,p}}$ are the dynamic and static strengths of concrete, respectively; $\dot{\varepsilon}_{\mathrm{p}}$ is the strain rate; $\dot{\varepsilon}_{\mathrm{p},0}$ is reference quasi-static strain rate, 1/s, $\alpha = 0.7613$ is the fitting parameter that defines the baseline of the DIF, and $\beta = 0.1466$ is the fitting parameter that characterises the slope of the DIF-$\dot{\varepsilon_{\mathrm{p}}}$. Due to the missing value of $\dot{\varepsilon}_{\mathrm{p},0}$ in some experimental datasets, Equation (5.8) cannot be applied directly to obtain their β values, which are also of particular importance to our validation. For this concern, we normalise the DIF by DIF_1, the first DIF value in the dataset, thereby eliminating the need for $\dot{\varepsilon}_{\mathrm{p},0}$. This enables a fitting with $R^2 > 0.9$ to the experimental data to obtain the β values using Equation (5.9), where $\dot{\varepsilon}_{\mathrm{p},1}$ is the first strain rate of each experimental dataset. In Figure 5.3(i), the numerically obtained DIF values fall within the experimental range, with an acceptable slope when comparing the β values with those of the experimental results shown in the colour bar. This successful validation confirms the reliability of our SHPB models and enables the following investigations and analyses.

5.3. Results and Discussion

Under dynamic loading, both macroscopic and microscopic assessments of concrete are conducted, with particular focus on the effects of loading ramp rate, internal friction, and confining pressure. All these analyses emphases on exploring the role of internal strain rate and damage on DIF through quantitative and statistical analyses of obtained results.

5.3.1. Loading ramp rate

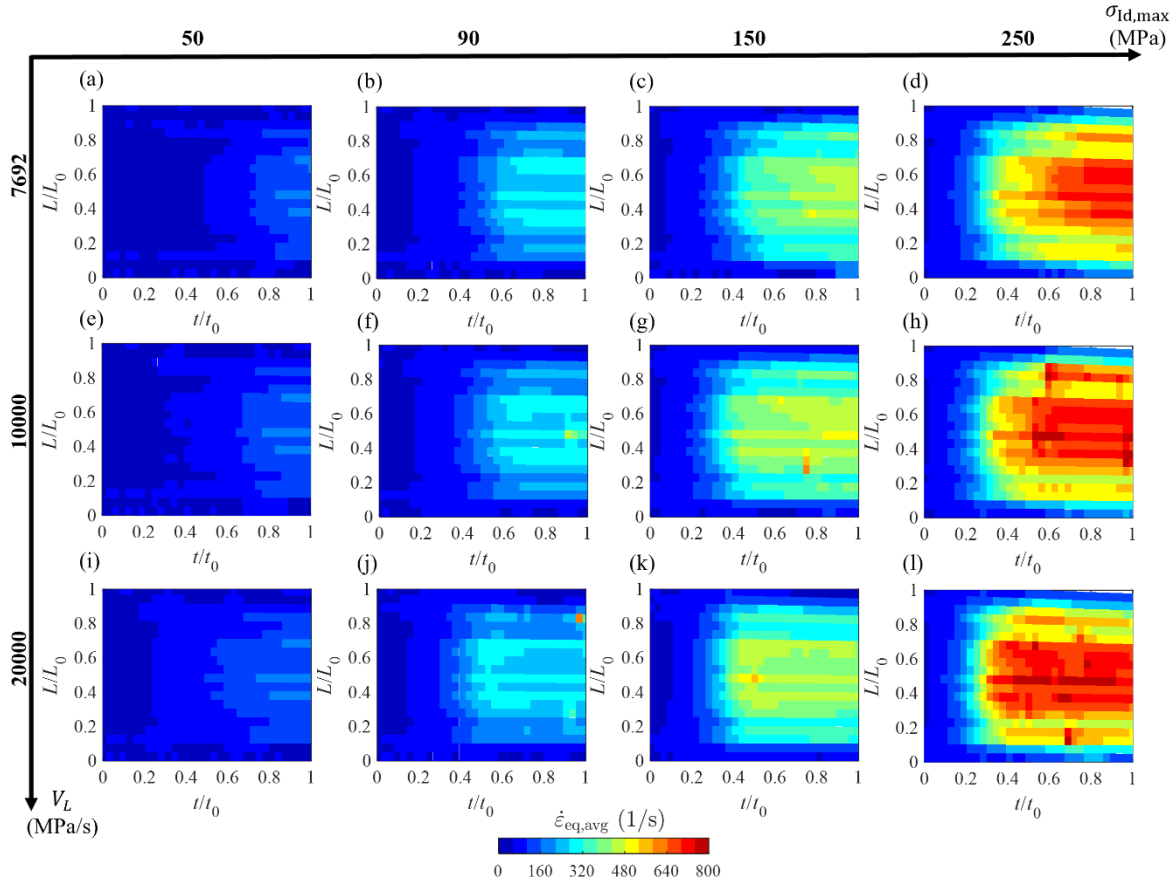

Figure 5.4: Time evolution of the profile of average internal strain rate, $\dot{\varepsilon}_{eq,avg}$, along the length deformed specimen, L/L_0, for different maximum stresses of the trapezoidal loading amplitudes, $\sigma_{ld,max}$, and loading ramp rate, V_L.

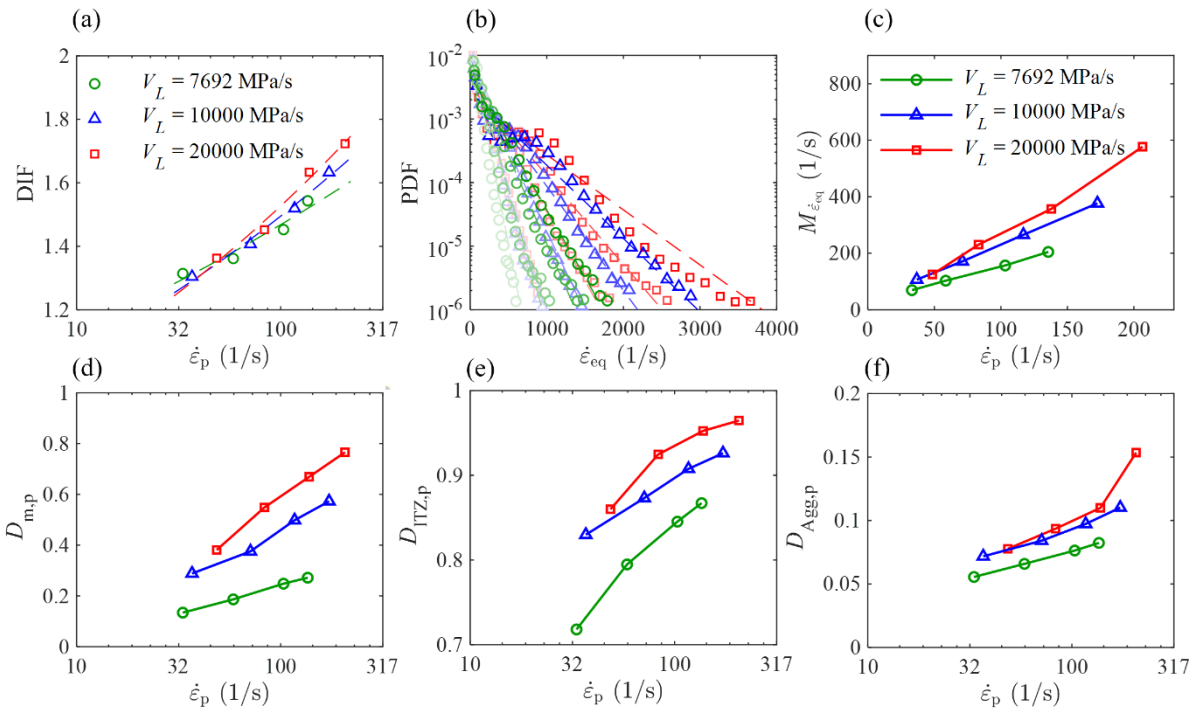

Figure 5.5. Effects of loading ramp rate, $\boldsymbol{V_L}$, on the macro- and micro- responses of concrete: (a) DIF versus $\dot{\varepsilon}_p$ for different V_L, with dashed lines denoting the fits using the Equation (5.8); (b) PDFs of the internal equivalent strain rate, $\dot{\varepsilon}_{eq}$, for different $\sigma_{ld,max}$ and V_L, using the same legend as in (a), with dashed lines denoting exponential fits and colours from light to dark indicating increasing $\dot{\varepsilon}_p$; (c) Mean value, $M_{\dot{\varepsilon}_{eq}}$, from exponential fitting of the PDFs; and (d-f) Damage of mortar, $D_{m,p}$, ITZ, $D_{ITZ,p}$, and aggregate, $D_{Agg,p}$, for the DIF, using the same legend in (c).

Here, we focus on the effect of the loading ramp rate, V_L, resulting from different pulse shapers adopted in different sets of SHPB tests. Our studied cases include maximum stress of $\sigma_{ld,max}$ = 50, 90, 150, and 250 MPa, and the stress magnitude has been kept for 0.0002 s. To vary the loading ramp rate, we include the cases of V_L = 7,692, 10,000 and 20,000 MPa/s in the initial rising stage. After stress waves are recorded, the example with $\sigma_{ld,max}$ = 90 MPa in Figure D.1 of Appendix D shows that a higher V_L can result in a faster increase of the incident waves over the initial rising stage, thereby demonstrating the achievement of precise control over V_L. Using the Equations (5.5-5.6), stress (σ)-strain (ε) curves are calculated in Figure D.2(b) of Appendix D, showing dependences on $\sigma_{ld,max}$ and V_L. Both effects on the concrete strength have been mainly focused by computing the DIF versus $\dot{\varepsilon}_p$ across various V_L in Figure 5.5(a). Using the Equation (5.8), the β values are measured as 0.113, 0.147, and 0.171 for V_L =

7692, 10000 and 20000 MPa/s, respectively. A higher V_L starts to lead to a higher DIF when $\dot{\varepsilon}_{\mathrm{p}}$ increases to a sufficiently large value in the range of $\dot{\varepsilon}_{\mathrm{p}} \in [100{,}200]$ /s, and eventually results in a more significant increase in DIF with increasing $\dot{\varepsilon}_{\mathrm{p}}$, as reflected by the larger β values.

We further explore the microscopic information, i.e., internal strain rate and local damage, emphasising on the inherent heterogeneities and their implications on the macroscopic observations.

For the temporospatial variations of internal strain rate during dynamic loading, we approach this in a manner similar to that used by Blatny et al. (Blatny et al., 2022), who quantified the evolution of the internal strain rate profile along the height of 2D porous media to successfully illustrate compaction patterns. During dynamic loading, although volumetric expansion and tensile splitting may occur, the shear-driven damage mechanism in concrete is generally associated with deviatoric deformation. Therefore, the second invariant of the strain-rate tensor is employed in the present study to quantify the equivalent internal strain rate, $\dot{\varepsilon}_{\mathrm{eq}}$. It provides a non-negative scalar value as compared to the volumetric counterpart, and facilitates the subsequent statistical analysis using the probability density function (PDF) on semi-log plots. The $\dot{\varepsilon}_{\mathrm{eq}}$ for each mortar and aggregate element is calculated explicitly, as shown below:

$$\dot{\varepsilon}_{\mathrm{eq}} = \sqrt{\left[\dot{\varepsilon}_{\mathrm{xx}}{}^2 + \dot{\varepsilon}_{\mathrm{yy}}{}^2 + \dot{\varepsilon}_{\mathrm{zz}}{}^2 + \frac{1}{2}\left(\dot{\varepsilon}_{\mathrm{xy}}{}^2 + \dot{\varepsilon}_{\mathrm{xz}}{}^2 + \dot{\varepsilon}_{\mathrm{yz}}{}^2\right)\right]}, \tag{5.10}$$

where $\dot{\varepsilon}_{\mathrm{xx}}$, $\dot{\varepsilon}_{\mathrm{yy}}$, $\dot{\varepsilon}_{\mathrm{zz}}$, $\dot{\varepsilon}_{\mathrm{xy}}$, $\dot{\varepsilon}_{\mathrm{xz}}$, and $\dot{\varepsilon}_{\mathrm{yz}}$ are the mechanical strain rate components, which are directly obtained from the field output of ABAQUS. We focus only on the time duration of $t_0 = 0.0003$ s from the initial time L_0/C_{b} of stress wave reaching the specimen. The $\dot{\varepsilon}_{\mathrm{eq}}$ values are obtained for 50 time points t, evenly distributed over the duration t_0. A moving window is used to compute the heatmap representing the evolution of the internal strain rate. The window thickness needs to be appropriately selected to adequately present the influence of the factors of interest on the internal strain rate while reducing the computational cost of generating the heatmap, although a smaller thickness may produce a more refined heatmap. Here, a moving window with a fixed thickness of 5 mm is defined along the loading direction at each normalised time point t/t_0. As this window moves in an initial step of 2.5 mm mapped along the deformed specimen length, the average internal strain rate of all solid elements within the

window, denoted as $\dot{\varepsilon}_{\mathrm{eq,avg}}$, is calculated at varying L/L_0, where L is the centroid position of the window and L_0 is the original specimen length. Eventually, the profile of $\dot{\varepsilon}_{\mathrm{eq,avg}}$ along L/L_0 can be obtained for all 50 time points to form the heatmap, as shown in Figure 5.4. In each case, as t/t_0 increases, the stress acting on the solid elements gradually increases, resulting in higher values of $\dot{\varepsilon}_{\mathrm{eq,avg}}$ along L/L_0.

The evolution of the $\dot{\varepsilon}_{\mathrm{eq,avg}}$ profile in Figure 5.4 shows effects of the applied maximum stress in the trapezoidal loading amplitude, $\sigma_{\mathrm{ld,max}}$, and loading ramp rate, V_L. With higher $\sigma_{\mathrm{ld,max}}$, higher stresses imposed on the elements can promote deformation and induce the evolution of the higher $\dot{\varepsilon}_{\mathrm{eq,avg}}$ profile. Comparison of Figure 5.4(e-h) or (i-l) with (a-d) shows that a higher V_L produces a more rapid stress increase, leading to a higher $\dot{\varepsilon}_{\mathrm{eq,avg}}$ profile at an earlier time. Furthermore, this effect becomes more pronounced at higher $\sigma_{\mathrm{ld,max}}$, which can further intensify the stress increase. These observations can be more clearly found in the central region than near the two ends, which experience stronger deformation constraints from the incident and transmission bars. These visualisations can present overviews of the internal strain rate throughout the entire deformation process, and further direct and quantitative evidence at the peak are required to explain the results of DIF-$\dot{\varepsilon}_{\mathrm{p}}$.

The probability density function (PDF) is employed for the statistical analysis of $\dot{\varepsilon}_{\mathrm{eq}}$ for all mortar and aggregate elements at the peak stress. The PDF is calculated based on the element volume to highlight the effects of V_L and $\sigma_{\mathrm{ld,max}}$ by the semi-log plots, as shown in Figure 5.5(b). To explicitly describe these variations in the PDFs, the exponential fitting function, $f_{\mathrm{ex}}(\dot{\varepsilon}_{\mathrm{eq}})$, is applied to effectively capture the overall trend of the distributions, as shown below:

$$f_{\mathrm{ex}}\left(\dot{\varepsilon}_{\mathrm{eq}}\right) = \lambda e^{-\lambda \dot{\varepsilon}_{\mathrm{eq}}}, \tag{5.11}$$

$$M_{\dot{\varepsilon}_{\mathrm{eq}}} = \frac{1}{\lambda}, \tag{5.12}$$

where λ is the fitting parameter of the exponential distribution. Using this fitting, Equation (5.12) is applied to compute the mean value, $M_{\dot{\varepsilon}_{\mathrm{eq}}}$ to characterise the central tendency of the PDFs.

The PDFs and $M_{\dot{\varepsilon}_{\mathrm{eq}}}$ are shown in Figure 5.5(b) and (c), respectively. Increasing $\sigma_{\mathrm{ld,max}}$ and V_L broadens the distribution toward higher $\dot{\varepsilon}_{\mathrm{eq}}$ values, with more elements attaining larger $\dot{\varepsilon}_{\mathrm{eq}}$. ultimately leading to higher $M_{\dot{\varepsilon}_{\mathrm{eq}}}$. These tendencies in PDF and $M_{\dot{\varepsilon}_{\mathrm{eq}}}$ shows similar effects of $\sigma_{\mathrm{ld,max}}$ and V_L to those observed in Figure 5.4, confirming the existence of the similar underlying mechanism governing concrete strength. The enhancement of $M_{\dot{\varepsilon}_{\mathrm{eq}}}$ due to increased $\sigma_{\mathrm{ld,max}}$ or V_L suggests that a greater fraction of elements undergo elevated local strain rates, which in turn promotes overall material strengthening and results in a higher DIF. Increasing $\sigma_{\mathrm{ld,max}}$ intensifies the enhancing effect of higher V_L on $M_{\dot{\varepsilon}_{\mathrm{eq}}}$, leading to more material elements undergo high-strain-rate deformation. Consequently, a higher V_L leads to a more pronounced increase in $M_{\dot{\varepsilon}_{\mathrm{eq}}}$ with respect to $\dot{\varepsilon}_{\mathrm{p}}$, reflecting the observed higher slope of the DIF-$\dot{\varepsilon}_{\mathrm{p}}$ in Figure 5.5(a).

Further, the damages of mortar, ITZ, and aggregate are expressed as $D_{\mathrm{m,p}}$, $D_{\mathrm{ITZ,p}}$, and $D_{\mathrm{Agg,p}}$, respectively, and can be quantified as follows:

$$\frac{\sum_{i=1}^{N} d_i V_i}{\sum_{i=1}^{N} V_i} \text{ or } \frac{\sum_{i=1}^{N} d_i S_i}{\sum_{i=1}^{N} S_i}, \tag{5.13}$$

where V_i is the volume of the i-th solid element (for mortar or aggregate), S_i is the area of the i-th CIE (for the ITZ), and d_i is the damage of the i-th element, obtained from the scalar stiffness degradation in ABAQUS, which indicates the damage caused by both compressive crushing and tensile cracking. The variations of $D_{\mathrm{m,p}}$, $D_{\mathrm{ITZ,p}}$, and $D_{\mathrm{Agg,p}}$ with $\dot{\varepsilon}_{\mathrm{p}}$ for each V_L are computed in Figure 5.5(d-f), respectively.

When the DIF is enhanced at higher $\dot{\varepsilon}_{\mathrm{p}}$, greater damage develops within the different material phases, as the higher stresses acting on the elements due to the increase in $\sigma_{\mathrm{ld,max}}$ can promote fractures. At higher V_L, larger instantaneous stresses are induced, promoting fracture in all material phases, as evidenced by the higher values of $D_{\mathrm{m,p}}$, $D_{\mathrm{ITZ,p}}$, and $D_{\mathrm{Agg,p}}$, generally contributing to a higher DIF. With an increase in $\dot{\varepsilon}_{\mathrm{p}}$, the effect of V_L on damage exhibits inconsistent trends across different material phases. For the ITZ, this effect becomes less significant. This is mainly because, as the weakest zone, the ITZ is more susceptible to damage and gradually reaches a fully damaged state with increasing $\sigma_{\mathrm{ld,max}}$, resulting in reducing differences in $D_{\mathrm{ITZ,p}}$ among different V_L, although a higher V_L still induces higher stress in the elements. In contrast, increasing $\sigma_{\mathrm{ld,max}}$ amplifies the effect of V_L on $D_{\mathrm{m,p}}$ and $D_{\mathrm{Agg,p}}$, results

in more pronounced increases in $D_{\mathrm{m,p}}$ and $D_{\mathrm{Agg,p}}$ at higher V_L. This indicates that fracture in the mortar and aggregate, caused by higher V_L, can be further promoted by increasing $\sigma_{\mathrm{ld,max}}$, ultimately leading to a greater enhancement of the DIF with increasing $\dot{\varepsilon}_{\mathrm{p}}$.

In the following sections, a trapezoidal loading amplitude with V_L = 10000 MPa/s is retained to investigate the additional effects of internal friction and confining pressure. For each effect, the DIF-$\dot{\varepsilon}_{\mathrm{p}}$ remains the main focuses in characterising the overall response of concrete. The same approach to analyse the internal strain rate and local damage will be applied to explore the variations in the DIF-$\dot{\varepsilon}_{\mathrm{p}}$. Thus, the macro- and microscopic responses of concrete will be presented in a format consistent with that of Figure 5.5. The following discussion focuses only information specific to how internal friction and confining pressure affect the DIF and the slope of DIF-$\dot{\varepsilon}_{\mathrm{p}}$.

5.3.2. Internal friction

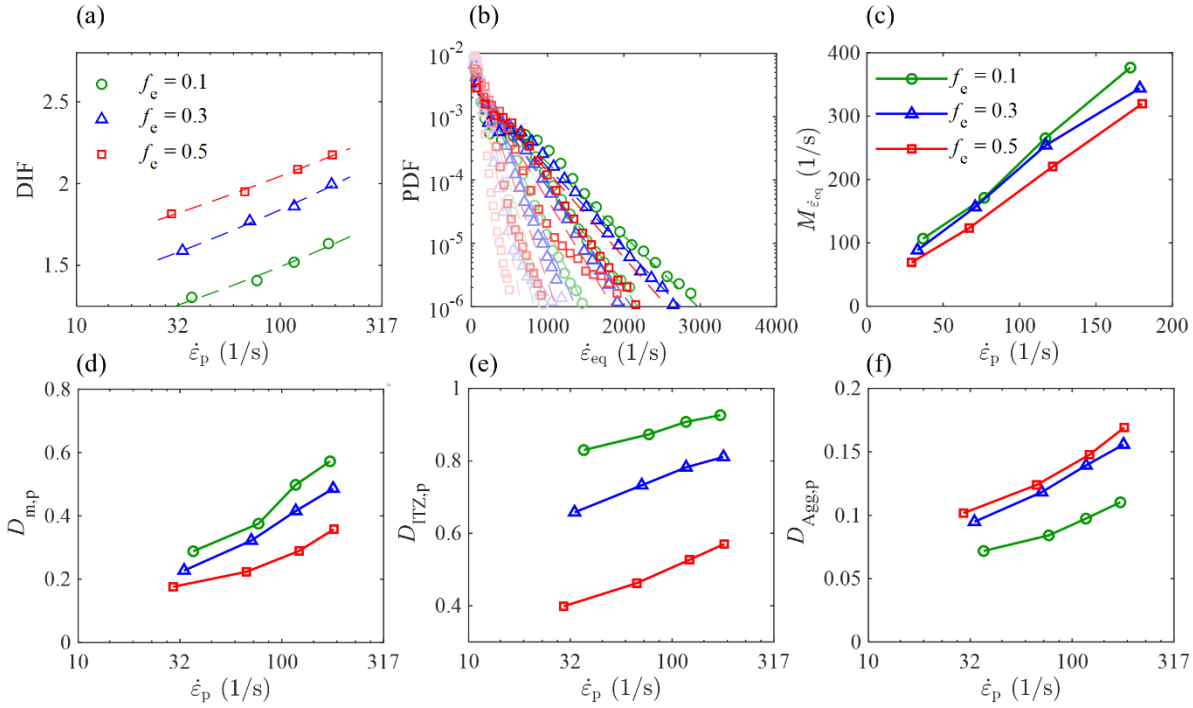

Figure 5.6: Effects of internal friction, f_{e}, on the same macro- and micro- responses of concrete shown in (a) and (b-f), respectively.

Internal friction coefficients of $f_{\mathrm{e}} = 0.1$, 0.3 and 0.5 are considered for the concrete model. Notably, it is difficult to accurately quantify the internal friction of real concrete. The selected

values here are therefore intended only to qualitatively evaluate the effects of internal friction. To achieve more realistic assessments, future work will first conduct experimental investigations to determine the true internal friction of concrete and then incorporate these results into the numerical model for more effective analysis. As in Figure D.2(a) and (b), when the V_L remains the same across different cases, the incident waves are almost identical, while the reflected and transmitted waves dominate the dependence of stress–strain behaviours on f_{e} under a given $\sigma_{\mathrm{ld,max}}$. To highlight the effects of f_{e} on concrete strength for all dynamic cases, the DIF is redefined, with all values calculated relative to the static strength of concrete with $f_{\mathrm{e}} = 0.1$, as shown in Figure 5.6(a), where the β values for the slope of DIF-$\dot{\varepsilon}_{\mathrm{p}}$ are measured as 0.148, 0.132, and 0.101 for cases with $f_{\mathrm{e}} = 0.1$, 0.3, and 0.5, respectively. As observed, when a higher f_{e} leads to higher DIF values, it results in a smaller increase in DIF with increasing $\dot{\varepsilon}_{\mathrm{p}}$, as reflected by the smaller β values.

The evolution of the $\dot{\varepsilon}_{\mathrm{eq,avg}}$ profile is computed for different $\sigma_{\mathrm{ld,max}}$ and f_{e}, as shown in Figure E.1 of Appendix E. The comparison of Figure E.1(a-d) with (e-h) or (i-l) shows that the effect of internal friction on this evolution is insignificant and does not become more pronounced or weakened with increasing $\sigma_{\mathrm{ld,max}}$. However, these observations cannot be directly linked to the peak stress. Alternatively, this aspect has been further investigated using the semi-plot of PDF and $M_{\dot{\varepsilon}_{\mathrm{eq}}}$ in Figure 5.6(b) and (c), respectively, both confirming effects of $\sigma_{\mathrm{ld,max}}$ and f_{e}. Higher f_{e} imposes stronger constraints on local deformation, thereby leading to a contraction of the PDF toward lower values with fewer elements reaching high $\dot{\varepsilon}_{\mathrm{eq}}$ levels, and correspondingly resulting in a smaller $M_{\dot{\varepsilon}_{\mathrm{eq}}}$. Unlike the discussion in Section 5.3.1, this correlation between $M_{\dot{\varepsilon}_{\mathrm{eq}}}$ and f_{e} is unubiquitous for the absolute values of DIF, providing different corresponding quasi-static strengths at different settings of f_{e}. When an increase in $\sigma_{\mathrm{ld,max}}$ induces higher stress acting on the elements, although it results in greater deformation, the constraining effect due to internal friction becomes more pronounced, as evidenced by increased differences in the PDF and $M_{\dot{\varepsilon}_{\mathrm{eq}}}$ among various f_{e}. Ultimately, higher f_{e} results in a less significant increase in $M_{\dot{\varepsilon}_{\mathrm{eq}}}$ with increasing $\dot{\varepsilon}_{\mathrm{p}}$, reflecting a smaller slope of DIF-$\dot{\varepsilon}_{\mathrm{p}}$in Figure 5.6(a).

Variations in local damage with $\dot{\varepsilon}_{\mathrm{p}}$ across different f_{e} are shown in Figure 5.6(d-f). With increasing f_{e}, $D_{\mathrm{ITZ,p}}$ increases while $D_{\mathrm{Agg,p}}$ decreases, reflecting a competitive mechanism between ITZ and aggregate. This means that a higher f_{e} induces stronger stress concentrations

near aggregate surfaces, promoting greater fracture propagation from the ITZ into the aggregate and eventually enhancing the DIF, although a higher f_e can delay fracture initiation and propagation in the mortar and induce a smaller $D_{m,p}$. When local damage increases with increasing $\dot{\varepsilon}_p$, the competition between $D_{ITZ,p}$ and $D_{Agg,p}$ does not become significantly amplified or weakened and therefore cannot explain the effect of internal friction on the slope of the DIF-$\dot{\varepsilon}_p$. This can be attributed to the damage status in mortar. A higher f_e causes a less significant increase in $D_{m,p}$ with increasing $\dot{\varepsilon}_p$. This means that when increasing $\sigma_{ld,max}$ raises contact stresses and promotes greater fracture in the mortar, the constraining effect of internal friction is amplified. Consequently, a higher f_e more strongly inhibits the increase in fracture within the mortar, mapping to a smaller enhancement of the DIF with increasing $\dot{\varepsilon}_p$.

5.3.3. Confining pressure

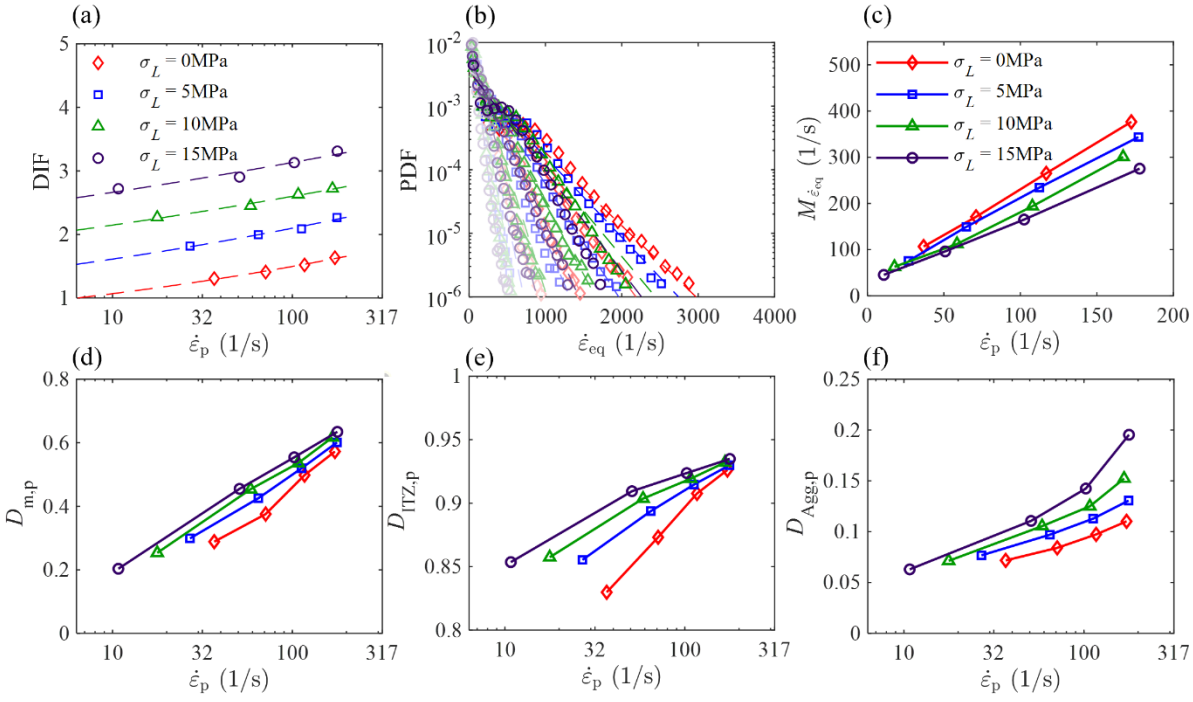

Figure 5.7: Effects of confining pressure, σ_L, on the same macro- and micro- responses of concrete shown in (a) and (b-f), respectively.

Here, we consider the confining pressure σ_L = 0, 5, 10 and 15 MPa to explore the effect of σ_L. It should be noted that applying a constant confining pressure throughout the deformation of concrete is an idealisation compared with triaxial experiments with confining devices. This is because the confinement provided by fluid- or air-pressurised vessels in real

experiments can be affected by the dilation of the concrete specimen and cannot always maintain the predefined confining pressure due to dynamic effects. While in our simulations, the confining pressure has been kept constant throughout the impact event.Increasing σ_L mainly acts on the reflected and transmitted waves, causing a more ductile strain-stress response of concrete, as shown in Figure D.3(a-b) of Appendix D. The DIF is calculated by dividing the dynamic confined strength by the static uniaxial strength of concrete to highlight the effect of confining pressure, as shown in Figure 5.7(a). The $\beta = 0.147$, 0.115, 0.0832 and 0.0707 are obtained for the slope of DIF-$\dot{\varepsilon}_{\mathrm{p}}$ at $\sigma_L = 0$, 5, 10 and 15 MPa, respectively. Compared with the unconfined case, the confined cases exhibit higher DIF values but show a less pronounced increase in DIF with increasing $\dot{\varepsilon}_{\mathrm{p}}$, as evidenced by the smaller β value, similar to findings from experimental studies on confinement (Christensen et al., 1972; Gran et al., 1989; Chen and Ravichandran, 1996; Chen and Ravichandran, 1997).

The evolution of the $\dot{\varepsilon}_{\mathrm{eq,avg}}$ profile for different $\sigma_{\mathrm{ld,max}}$ and σ_L are shown in Appendix E. As increasing σ_L imposes stronger lateral restraint on the element deformation, it shrinks the PDF toward smaller σ_{eq} values, with an increasing proportion of elements concentrated in this range, resulting in a smaller $M_{\dot{\varepsilon}_{\mathrm{eq}}}$ in Figure 5.7(c). With increasing $\sigma_{\mathrm{ld,max}}$, the amplified later restraint makes effects of σ_L on PDF more pronounced, as also reflected by the increasing difference in $M_{\dot{\varepsilon}_{\mathrm{eq}}}$ between different σ_L. Eventually, higher σ_L shows a less significant increase of $M_{\dot{\varepsilon}_{\mathrm{eq}}}$ with an increasing $\dot{\varepsilon}_{\mathrm{p}}$, reflecting a smaller slope of DIF-$\dot{\varepsilon}_{\mathrm{p}}$ in Figure 5.7(a).

Variations in local damage with $\dot{\varepsilon}_{\mathrm{p}}$ across different σ_L are presented in Figure 5.7(d-f). As increasing σ_L requires higher overall stress to promote the initiation and propagation of fractures due to stronger lateral restraint, damage in all material phases increases; meanwhile, the DIF is also enhanced. When damage increases with increasing $\dot{\varepsilon}_{\mathrm{p}}$, $D_{\mathrm{Agg,p}}$ shows more significant effect of σ_L, in contrast to $D_{\mathrm{ITZ,p}}$. This because when increasing $\sigma_{\mathrm{ld,max}}$ drives ITZ to gradually reaches a fully fractured state, more fracture propagates from ITZ to aggregate, causing a much higher $D_{\mathrm{Agg,p}}$ at higher σ_L and retain a higher DIF. Thus, higher σ_L shows a more significant increase of $D_{\mathrm{Agg,p}}$ with an increasing $\dot{\varepsilon}_{\mathrm{p}}$. $D_{\mathrm{Agg,p}}$ cannot directly reflect smaller slope of DIF-$\dot{\varepsilon}_{\mathrm{p}}$ at higher σ_L. This could be attributed to the mortar. Higher σ_L shows a less significant increase of $D_{\mathrm{m,p}}$ with increasing $\dot{\varepsilon}_{\mathrm{p}}$, indicating a weakened strain rate effects and a smaller slope of DIF-$\dot{\varepsilon}_{\mathrm{p}}$.

5.3.4. Discussion

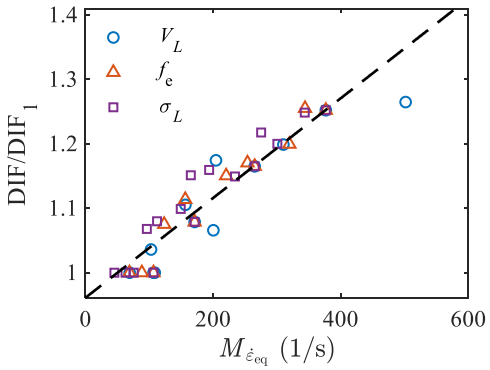

Figure 5.8: Correlation between $M_{\dot{\varepsilon}_{eq}}$ and normalised DIF.

As discussed in all earlier cases all cases with varying loading ramp rates, V_L, internal friction, f_e, and confining pressure, σ_L, there are individual trends between the microscopic statistical index, $M_{\dot{\varepsilon}_{eq}}$, and the overall dynamic strength, DIF. When the distribution of internal strain rate at the peak stress is statistically analysed, variations in $M_{\dot{\varepsilon}_{eq}}$ with $\dot{\varepsilon}_p$ are found to reflect the slope of DIF-$\dot{\varepsilon}_p$ for effects of loading ramp rates, V_L, internal friction, f_e, and confining pressure, σ_L. To further confirm this, $M_{\dot{\varepsilon}_{eq}}$ and DIF are collected from different cases to investigate the correlation between both values, as shown in Figure 5.8. DIF is normalised by DIF_1, the first value of each case, to focus on the relative change respective to the distinct initial values. We found a strong positive correlation between DIF/DIF_1 and $M_{\dot{\varepsilon}_{eq}}$ with a correlation coefficient of $R = 0.94$. Thus, the heterogeneity of internal strain rate can be more confidently considered as microscopic indicator for explaining the strain rate effects on the concrete fractures, highlighting the necessity of mesoscale modelling of concrete.

It is noteworthy that the internal strain rate analysed in this study is obtained from mesoscale modelling results that incorporates the rate-independent response of the ITZ due to the limited available data for the material phase (Liu et al., 2019; Li et al., 2021; Zhao et al., 2025). These aspects remain to be implemented to achieve more realistic predictions and to further highlight the role of internal strain rate in the dynamic response of concrete. Moreover, higher strain rate regions (i.e., $\dot{\varepsilon}_p$>200/s) can be further explored as this range can be of interests for many applications in protective structures. The mesoscale model can be extended to focus on sustainable concrete materials by replacing natural aggregates with coral (Li et al., 2025b), lightweight (Duan et al., 2023) or recycled aggregates (Selyutina and Smirnov, 2023),

to enrich the understanding of the effects of heterogeneities in material and internal strain rate under dynamic loading.

5.4. Conclusion

In this paper, the dynamic fracture of concrete containing aggregates with realistic shapes is investigated through mesoscale modelling of SHPB tests based on the FEM. The macroscopic dynamic response of concrete has been validated, and we focus on the relationship between the DIF and strain rate with respect to loading ramp rate, internal friction, and confining pressure. Particular attention is given to explaining the DIF related results through microscopic analyses based on the distributions and evolutions of internal strain rate and local damage. The main conclusions are summarised as follows:

- As the loading ramp rate increases, the internal strain rate distribution and the local damage both increase, leading to a higher DIF. With an increase in strain rate of concrete specimen, the damage of both mortar and aggregate exhibits rate-dependent trends similar to internal strain rate distribution. Both show enhanced strain rate effects at higher loading ramp rates, contributing to a more significant increase in the DIF with increasing strain rate.
- With increasing internal friction, although the internal strain rate is more strongly suppressed, the competition between damages of ITZ and aggregate indicates higher induced stress concentration, which promotes fracture propagation from the ITZ into the aggregates, resulting in a higher DIF. Such competition cannot explain the variation in the slope of the DIF-strain rate, as it is mainly attributed to the mortar phase, as evidenced by local damage rather than the internal strain rate. Higher internal friction weakens the strain rate effects on damage of mortar, contributing to a less significant increase in the DIF with increasing strain rate.
- Despite higher confining pressure suppressing the internal strain rate, it can still enhance the DIF, evidenced by increased damage in all material phases. As local damage provides more direct evidence than the internal strain rate, it shows that the less significant increase in the DIF with increasing strain rate at higher confining pressure is mainly attributed to the mortar, which exhibits a weakened strain rate effect on damage under higher confining pressure, although fracture is further promoted in the

aggregate than in the mortar at higher strain rates, leading to a more pronounced effect of confining pressure on damage of aggregate.

This mesoscale numerical investigation examines loading and material factors that are difficult or impossible to access experimentally and clarifies their effects on the dynamic response of concrete at both macroscopic and microscopic levels. The analyses of heterogeneities of microscopic information during the dynamic loading provide several insights on explaining the macroscopic observed rate-dependent behaviours. These findings enrich the understanding of strain rate effects in concrete fracture and provide a theoretical basis for improving constitutive relationships of concrete under dynamic loading. Nevertheless, the present work considers only the effects of individual factors, and future studies are required to further develop the mesoscale model to investigate their coupled effects, thereby enabling more accurate predictions of concrete behaviour under complex dynamic conditions. In addition, the model will be further developed to more accurately predict realistic concrete behaviour by incorporating material heterogeneity within each phase (e.g., pores and pre-existing microcracks), strain-rate-dependent ITZ properties, and variations in impact loading conditions.

Chapter 6 Conclusion and Future Work

6.1 Conclusion

This thesis develops a comprehensive mesoscale modelling framework to investigate the transport and mechanical behaviours of concrete under conditions relevant to marine environments. By explicitly accounting for material heterogeneity, this research provides new insights into how realistic aggregate morphology affects concrete performance across multiple physical processes. The main findings are summarised as below:

- The concrete model incorporating realistic aggregate morphologies is well validated against the Hashin–Shtrikman solution for effective diffusivity, as well as experimental data for static triaxial fracture and dynamic fracture of concrete, enabling accurate predictions. Moreover, realistic aggregate morphology is not merely a geometric factor but a governing one that links microstructural characteristics to macroscopic behaviour. Across these different physical processes, aggregate shape systematically influences internal transport paths, stress distribution, internal strain rate, and damage evolution.
- From the perspective of transport behaviour, realistic aggregate shapes can increase the tortuosity of diffusion pathways, as evidenced by a broader throat size distribution between aggregate particles, leading to smaller effective diffusivity compared to other regular shapes. This effect is more pronounced at higher solid fractions, where the effective diffusivity can be considered a function of fractal dimension and relative roughness to account for influence of the aggregate shape. Thus, realistic aggregate morphology should be considered when assessing chloride ingress and long-term durability in marine concrete.
- Rougher aggregate morphology leads to higher concrete strength, and this effect becomes more pronounced under triaxial stress conditions. It is found that the relationship between uniaxial-strength-normalised triaxial strength and confining pressure follows a universal law across different aggregate shapes. This behaviour arises because the initially diverse heterogeneity in stress distribution converges toward a similar stress state at the peak of the stress-strain response. With increasing aggregate roughness, the competitive mechanisms between the ITZ and the aggregates persist under varying confining pressures, manifesting not only in damage at the peak but also in the crack cluster size at post-peak region.

- For the dynamic response of concrete, the roles of internal strain rate and damage have been highlighted in understanding the effects of loading ramp rate, internal friction, and confining pressure on the dynamic increase factor (DIF). A higher loading ramp rate enhances the strain rate effect on DIF due to a more significant increase in internal strain rate and damage in the mortar and aggregate phases. Increasing internal friction and confining pressure both weaken the strain-rate effect on DIF. Although internal strain rate and local damage can explain both effects, local damage is more effectively attributed to the mortar phase.

Overall, this work advances the fundamental understanding of concrete performance in complex loading environments and provides additional theories for material design and assessment. Furthermore, it highlights the importance of considering aggregate morphology in durability evaluation, strength prediction, and safety assessment of marine infrastructure.

6.2 Future work

Despite the advances achieved, several limitations remain. Therefore, the mesoscale modelling framework needs to be further improved, and additional related studies should be considered in future work to enrich the understanding of the transport and mechanical behaviours of concrete under various loading conditions:

- Regarding the concrete model itself, this thesis simplifies the mesoscale structure by adopting nearly mono-sized aggregates. Although realistic aggregate shapes are incorporated, a more realistic aggregate size distribution and aggregate volume fraction should be considered to further improve the representativeness of the mesoscale model. Consequently, the coupled effects of these aggregate-related factors should be assessed simultaneously to better reflect both the overall and local responses of concrete under various loading conditions. In addition, the mesoscale model can be further developed to focus on sustainable concrete materials incorporating coral, lightweight, and recycled aggregates.
- Future work should assess the influence of the ITZ on the effective diffusivity of concrete by treating it as a separate material phase. This can be achieved by comparing the effects of aggregate shape with and without explicit consideration of the ITZ. In addition, with respect to mechanical behaviour, the dynamic properties of the ITZ

should first be informed by experimental data and then incorporated into the mesoscale model. These efforts aim to improve the mesoscale modelling framework for more accurate prediction of both transport and mechanical behaviours of concrete.

- More complex mechanical loading conditions, such as true triaxial stress states and blast loading, should be incorporated in future studies to enrich the understanding of concrete fracture behaviour. Furthermore, other mechanical behaviours that frequently occur in marine environments, such as creep and shrinkage, should also be investigated.
- The transport and mechanical behaviours considered in this thesis were investigated independently, whereas in real marine environments these processes are often strongly coupled, for example through corrosion-induced cracking that simultaneously affects durability and structural performance. In addition, coupling with other degradation processes, such as freeze–thaw cycles and sulphate attack, is also necessary to enhance the predictive capability of the model for complex service environments.

Appendix A: Derivation of Relative Roughness

As irregular aggregates are generated by the discrete Fast transformation, the roughness measured for a specific surface is based on the Parseval's formula of discrete Fast transformation:

$$\frac{1}{\pi}\int_0^{2\pi} l_0 + \sum_{n=1}^{N}[A_n\, cos(n\theta) + B_n sin\,(n\theta)]^2\, d\theta = 2(l_0)^2 + \sum_{n=1}^{\infty} {A_n}^2 + \sum_{n=1}^{\infty} {B_n}^2. \tag{A.1}$$

Since ${A_n}^2 + {B_n}^2 = ({F_n}^2)({l_0}^2)$, we arrive at

$$\frac{1}{\pi}\int_0^{2\pi} l_i(\theta_i)^2 d\theta = 2(l_0)^2 + \sum_{n=1}^{\infty}\left({F_n}^2\right)({l_0}^2). \tag{A.2}$$

Roughness is defined as the difference between generated irregular aggregate shape and l_0-determined circle, and thus after the roughness is normalised by l_0-determined circle, the relative roughness is obtained as:

$$R_r = \frac{\sqrt{2(l_0)^2 + \sum_{n=1}^{\infty}({F_n}^2)({l_0}^2) - 2(l_0)^2}}{l_0}. \tag{A.3}$$

Considering F_1 = 0, Rr can be expressed as,

$$R_r = \sqrt{\sum_{n=2}^{\infty}({F_n}^2)}\,. \tag{A.4}$$

Then substitute $F_n = F_2\left(\frac{n}{2}\right)^{2F_d-4}$ in Section 2 into A.4,

$$R_r = \sqrt{\sum_{n=2}^{\infty}({F_2}^2(\frac{n}{2})^{4F_d-8})}. \tag{A.5}$$

Appendix B: Derivation of Hashin-Shrinkman

According to the Hashin-Shrinkman (HS) variational theorems (Hashin and Shtrikman, 1962), upper $D_{\text{eff,u}}$ and lower $D_{\text{eff,l}}$ bounds of 2D effective diffusivity for the two-phase composite are defined as (Torquato, 1985):

$$D_{eff,u} = D_c \frac{1+\phi D_{a,c}}{1-\phi D_{a,c}}, \tag{B.1}$$

$$D_{eff,l} = D_a \frac{1+(1-\phi)D_{c,a}}{1-(1-\phi)D_{c,a}}, \tag{B.2}$$

where

$$D_{a,c} = \frac{D_a - D_c}{D_a + D_c} \text{ and } D_{c,a} = \frac{D_c - D_a}{D_c + D_a}. \tag{B.3}$$

Additionally, as aggregate phase in the diffusivity modelling assumes to be impermeable and $D_a = 0\ m^2/s$, $D_{\text{eff,u}}$ and $D_{\text{eff,l}}$ are divided by $(1-\phi)$ (Jiao and Torquato, 2012; Liasneuski et al., 2014). Therefore, $D_{\text{eff,l}}$ is zero, and $D_{\text{eff,u}}$ becomes

$$D_{eff,u} = \frac{D_c}{1-\phi}\frac{1+\phi D_{a,c}}{1-\phi D_{a,c}} = \frac{D_c}{1+\phi}. \tag{B.4}$$

Dimensionless HS upper bounds (HS_u) of effective diffusivity can be finally defined as:

$$HS_u = \frac{D_{eff,u}}{D_c} = \frac{D_c}{(1+\phi)D_0}. \tag{B.5}$$

Appendix C: Modelling of Static Fracture of Concrete

To simulate concrete fracture under quasi-static conditions, the loading rate is carefully chosen to minimise initial dynamic effects, ensuring that the ratio of total kinetic energy to internal energy remains below 5% in the simulation. Two steel loading plates, with a side length of $L_p = 60$ mm and a thickness of $t_p = 4$ mm, are placed at both ends of the cylindrical concrete specimen, as shown in Figure C.1, and are meshed using 4 mm hexahedral solid elements. The contact between the loading plate and the specimen is defined as hard contact with a friction coefficient of 0.5. Here, we focus only on the unconfined static cases. The bottom plate is restrained in all directions, while the top plate is allowed to move only in the vertical (loading) direction. The axial stress σ_1 is applied to the top plate using a velocity-controlled method, in which the velocity of the nodes on the top surface is linearly ramped up to 50 mm/s within 0.001 s and then held constant until the end of the simulation. The step duration is set to 0.02 s.

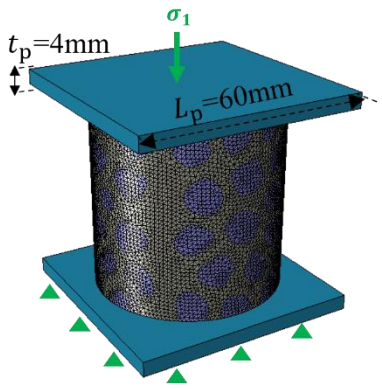

Figure C.1: Schematic diagram of the FE model of quasi-static compressive concrete fracture, where the arrow indicates the direction of the axial loading acting on the plate.

Appendix D: Strain Wave and Stress-Strain Curve

From our numerical results, Figures D.1-D.3(a) show variations in the incident $\varepsilon_{w,i}(t)$, reflected $\varepsilon_{w,r}(t)$, and transmitted $\varepsilon_{w,t}(t)$ strain waves with loading ramp rate V_L, internal friction f_e, and confining pressure σ_L, respectively. These are examples when the maximum stress of trapezoidal loading amplitude $\sigma_{ld,max}$ is 90 MPa. The dynamic stress-strain curves are calculated based on Equations (5.5-5.7) to highlight effects of V_L, f_e, and σ_L under $\sigma_{ld,max}$ = 50, 90, 150, and 250 MPa, as shown in Figures D.1-D.3(b), where colours from light to dark represent increasing $\sigma_{ld,max}$.

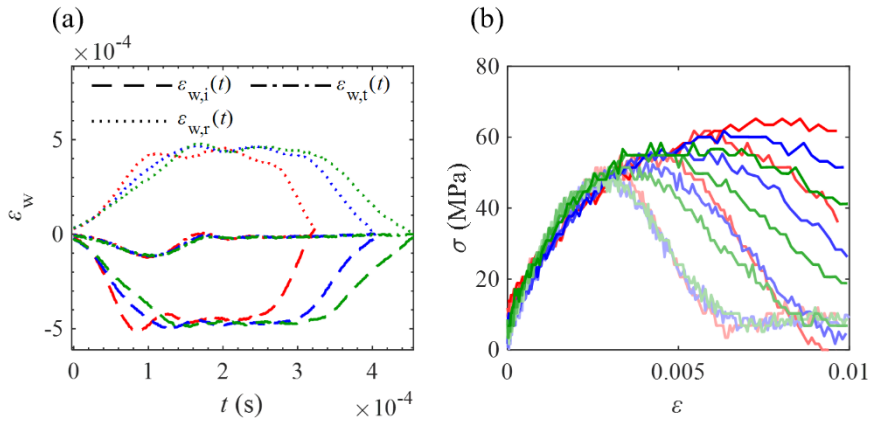

Figure D.1. Effects of $\boldsymbol{V_L}$ on macroscopic dynamic response of concrete: (a) Examples of the incident $\varepsilon_{w,i}(t)$, reflected $\varepsilon_{w,r}(t)$, and transmitted $\varepsilon_{w,t}(t)$ waves; and (b) Stress (σ)-strain (ε) curves for different $\sigma_{ld,max}$ and V_L, where cases with V_L = 7692, 10000 and 20000 MPa/s are shown in green, blue, and red, respectively.

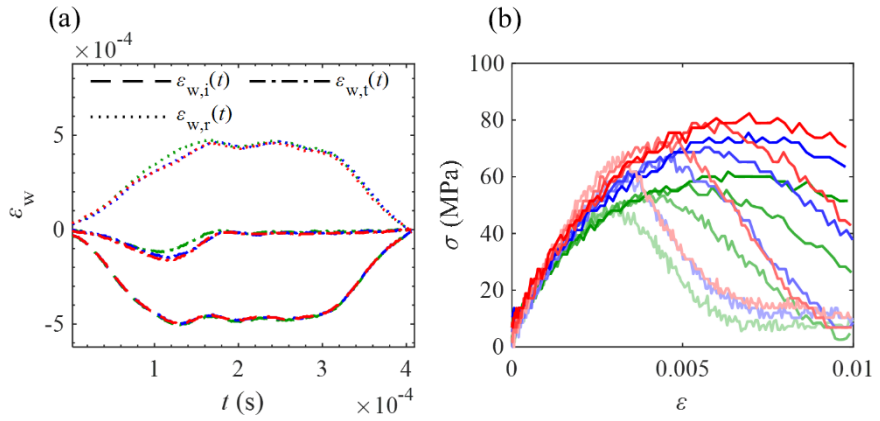

Figure D.2. Effects of f_e on macroscopic dynamic response of concrete: (a) Examples of the incident $\varepsilon_{w,i}(t)$, reflected $\varepsilon_{w,r}(t)$, and transmitted $\varepsilon_{w,t}(t)$ waves; and (b) Stress (σ)-strain (ε) curves for different $\sigma_{ld,max}$ and f_e, where cases with internal friction $f_e = 0.1$, 0.3, and 0.5 are shown in green, blue, and red, respectively.

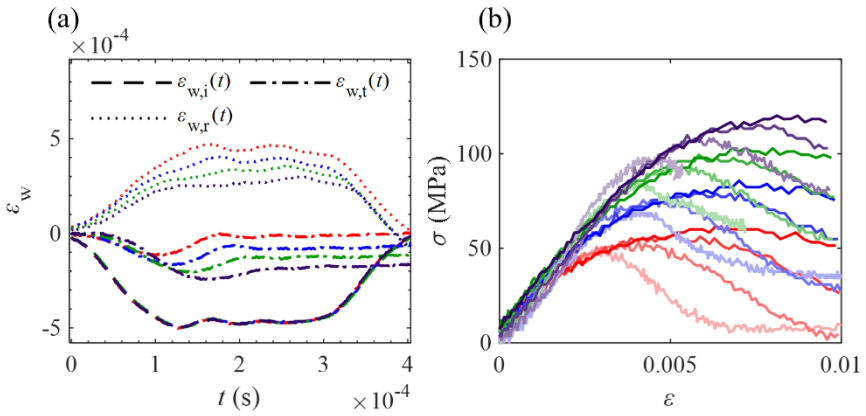

Figure D.3. Effects of $\boldsymbol{\sigma_L}$ on macroscopic dynamic responses of concrete: (a) Examples of the incident $\varepsilon_{w,i}(t)$, reflected $\varepsilon_{w,r}(t)$, and transmitted $\varepsilon_{w,t}(t)$ waves; and (b) Stress (σ)-strain (ε) curves for different $\sigma_{ld,max}$ and σ_L, where cases with confining pressure $\sigma_L = 0$, 5, 10 and 15 MPa are shown in red, blue, green, and purple, respectively.

Appendix E: Distributions of Internal Strain Rate

Figures E.1 and E.2 show the time evolution of the profile of the average internal strain-rate distribution, $\dot{\varepsilon}_{\mathrm{eq,avg}}$, along the length of the deformed specimen. These are computed using the same method as that applied in Figure 4 and exhibit similar patterns. Figures E.1 and E.2 show cases with internal friction values of f_{e} = 0.1, 0.3, and 0.5, and confining pressures σ_L = 0, 5, 10, and 15 MPa, respectively. when $\sigma_{\mathrm{ld,max}}$ = 50, 90, 150, and 250 MPa. Figures. E.1 and E.2 are used to support the discussions in Sections 5.3.2 and 5.3.3.

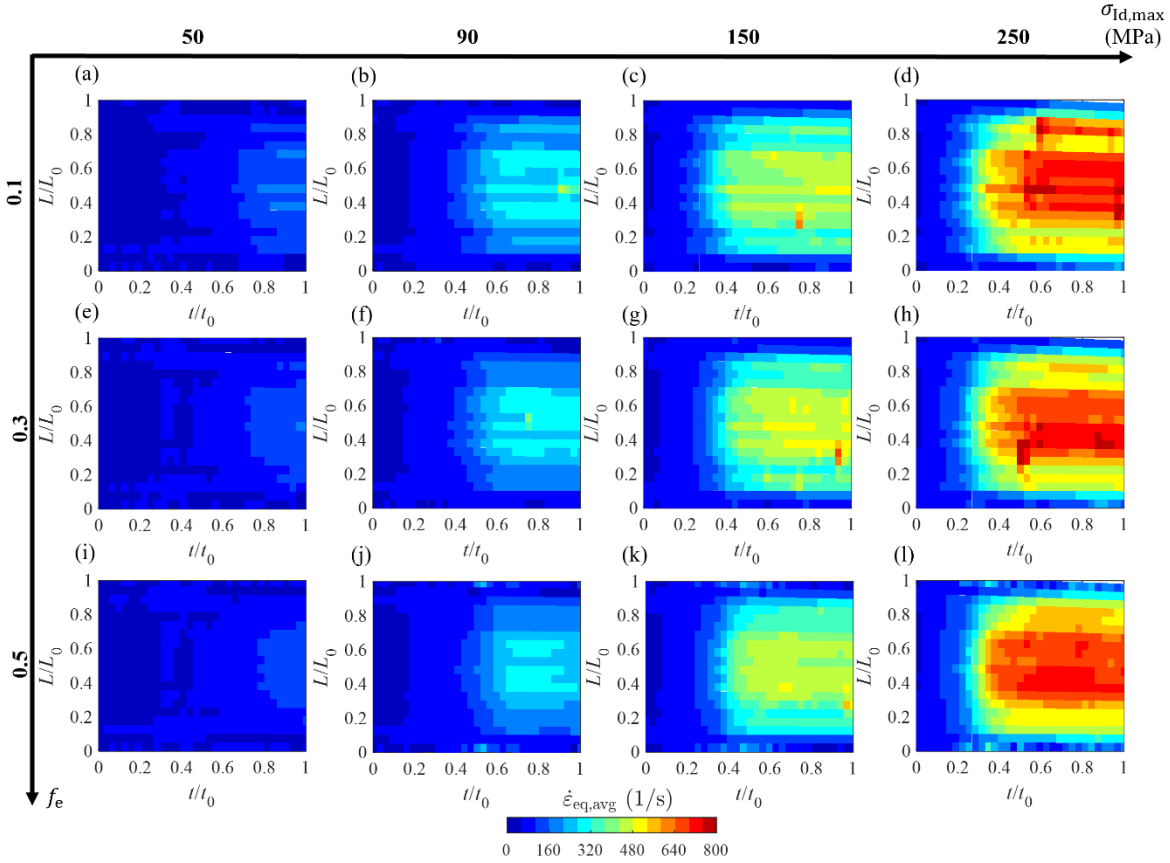

Figure E.1: Evolution of the profile of average internal strain rate, $\dot{\varepsilon}_{\mathrm{eq,avg}}$, along the normalised length, L/L_0, of the deformed concrete specimen for different $\sigma_{\mathrm{ld,max}}$ and f_{e}.

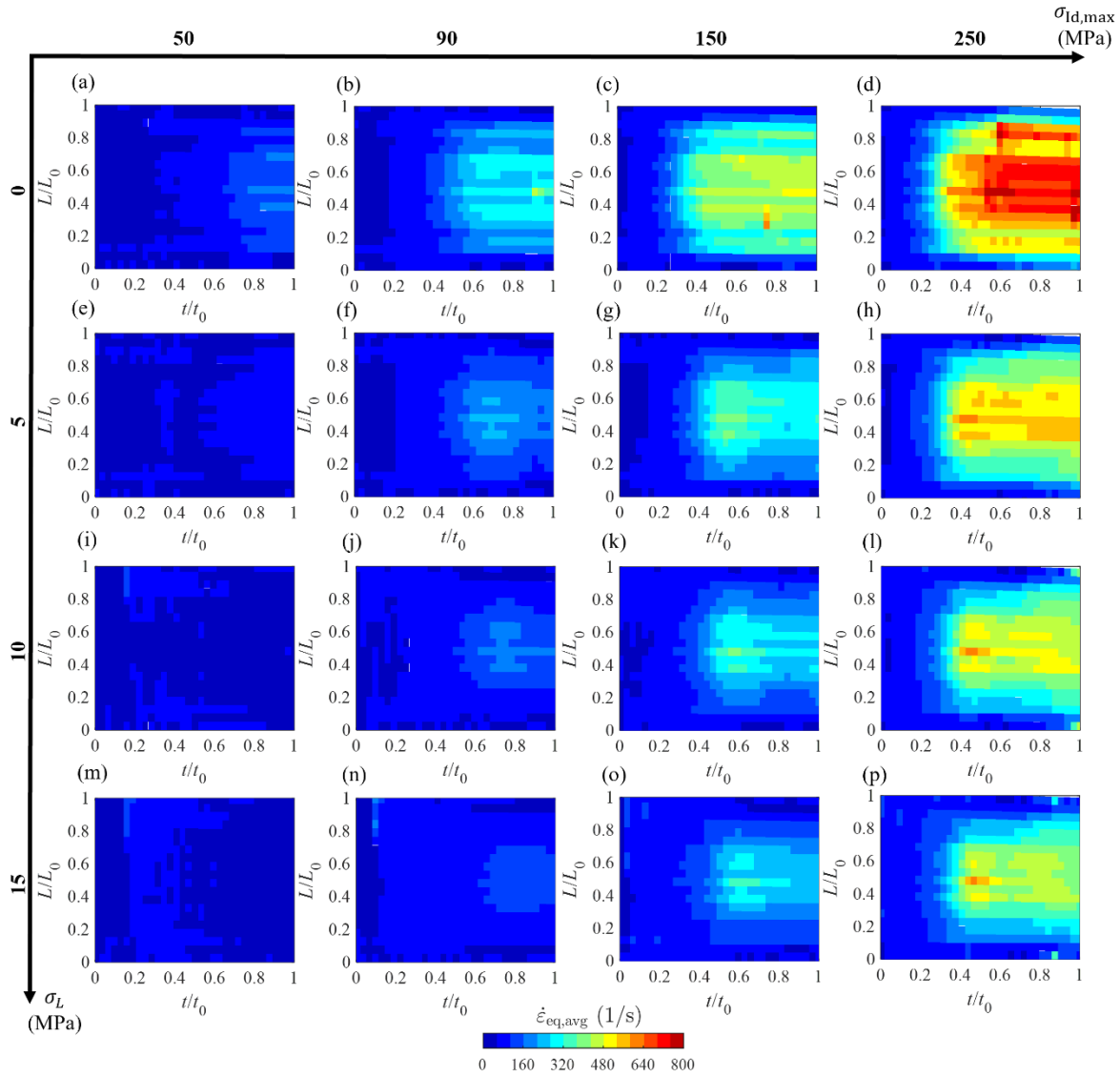

Figure E.2: Evolution of the profile of average internal strain rate $\dot{\varepsilon}_{\mathrm{eq,avg}}$ along the normalised deformed length, L/L_0, of the concrete specimen for different $\sigma_{\mathrm{ld,max}}$ and σ_L.

Bibliography

Abosrra, L., Youseffi, M., Ashour, A.: Effectiveness of calcium nitrite in retarding corrosion of steel in concrete. International Journal of Concrete Structures and Materials **5**(1), 65-73 (2011)

Abrams, D.A.: Effect of rate of application of load on the compressive strength of concrete. In: Proceeding of ASTM 1917, pp. 364-377

Abyaneh, S.D., Wong, H., Buenfeld, N.: Modelling the diffusivity of mortar and concrete using a three-dimensional mesostructure with several aggregate shapes. Computational Materials Science **78**, 63-73 (2013)

Adesina, A.: Durability enhancement of concrete using nanomaterials: an overview. In: Materials Science Forum 2019, pp. 221-227. Trans Tech Publ

Adesina, A.: Nanomaterials in cementitious composites: review of durability performance. Journal of Building Pathology and Rehabilitation **5**(1), 21 (2020)

Ahmad, M.A., Yi, X., Munir, Q., Kärki, T., Wang, J., Deng, X.: Nano-engineered Self-Healing Concrete: Application, Mechanism, Challenge and Prospect. J. Build. Eng., 114179 (2025)

Ahmed, J.A., Wahab, M.A.: A multiscale approach of additive materials processing on the creep behavior analysis of functionally graded thick-walled cylinders. Comprehensive Materials Processing: Volume 1-13, Second edition **6**, V6: 54 (2024)

Akçaoğlu, T., Tokyay, M., Çelik, T.: Assessing the ITZ microcracking via scanning electron microscope and its effect on the failure behavior of concrete. Cem. Concr. Res. **35**(2), 358-363 (2005)

Akono, A.-T., Chen, J., Zhan, M., Shah, S.P.: Basic creep and fracture response of fine recycled aggregate concrete. Constr. Build. Mater. **266**, 121107 (2021)

Al-Amoudi, O.S.B., Maslehuddin, M., Lashari, A., Almusallam, A.A.: Effectiveness of corrosion inhibitors in contaminated concrete. Cem. Concr. Compos. **25**(4-5), 439-449 (2003)

Al-Salloum, Y., Almusallam, T., Ibrahim, S., Abbas, H., Alsayed, S.: Rate dependent behavior and modeling of concrete based on SHPB experiments. Cem. Concr. Compos. **55**, 34-44 (2015)

Alexander, M., Nganga, G.: Introduction: Importance of marine concrete structures and durability design. In: Marine Concrete Structures. pp. 1-13. Elsevier, (2016)

Ali, M., Shams, M.A., Bheel, N., Almaliki, A.H., Mahmoud, A.S., Dodo, Y.A., Benjeddou, O.: A review on chloride induced corrosion in reinforced concrete structures: lab and in situ investigation. RSC advances **14**(50), 37252-37271 (2024)

Almusallam, A., Khan, F., Dulaijan, S., Al-Amoudi, O.: Effectiveness of surface coatings in improving concrete durability. Cem. Concr. Compos. **25**(4-5), 473-481 (2003)

André, D., Girardot, J., Hubert, C.: A novel DEM approach for modeling brittle elastic media based on distinct lattice spring model. Comput. Method Appl. Mech. Eng. **350**, 100-122 (2019)

Arya, C., Buenfeld, N., Newman, J.: Factors influencing chloride-binding in concrete. Cem. Concr. Res. **20**(2), 291-300 (1990)

Ashby, M.F.: Materials and the environment: eco-informed material choice. Elsevier, (2012)

Attard, M., Setunge, S.: Stress-strain relationship of confined and unconfined concrete. ACI Mater. J. **93**(5), 432-442 (1996)

Ayhan, B., Lale, E.: Modeling strain rate effect on tensile strength of concrete using damage plasticity model. Int. J. Impact Eng. **162**, 104132 (2022)

Barenblatt, G.I.: The mathematical theory of equilibrium cracks in brittle fracture. Adv. Appl. Mech. **7**, 55-129 (1962)
Basheer, L., Cleland, D.: Freeze–thaw resistance of concretes treated with pore liners. Constr. Build. Mater. **20**(10), 990-998 (2006)
Basheer, L., Kropp, J., Cleland, D.J.: Assessment of the durability of concrete from its permeation properties: a review. Constr. Build. Mater. **15**(2-3), 93-103 (2001)
Bastidas-Arteaga, E., Chateauneuf, A., Sánchez-Silva, M., Bressolette, P., Schoefs, F.: A comprehensive probabilistic model of chloride ingress in unsaturated concrete. Engineering Structures **33**(3), 720-730 (2011)
Bažant, Z.P., Tabbara, M.R., Kazemi, M.T., Pijaudier-Cabot, G.: Random particle model for fracture of aggregate or fiber composites. J. Eng. Mech. **116**(8), 1686-1705 (1990)
Beckmann, B., Schicktanz, K., Reischl, D., Curbach, M.: DEM simulation of concrete fracture and crack evolution. Structural Concrete **13**(4), 213-220 (2012)
Bentz, D.P., Clifton, J.R., Ferraris, C.F., Garboczi, E.J., Torrents, J.M.: Transport properties and durability of concrete: Literature review and research plan. (1999)
Benzeggagh, M., Kenane, M.: Measurement of mixed-mode delamination fracture toughness of unidirectional glass/epoxy composites with mixed-mode bending apparatus. Compos. Sci. Technol. **56**(4), 439-449 (1996)
Binici, B.: An analytical model for stress–strain behavior of confined concrete. Eng. Struct. **27**(7), 1040-1051 (2005)
Bischoff, P.H., Perry, S.H.: Impact behavior of plain concrete loaded in uniaxial compression. J. Eng. Mech. **121**(6), 685-693 (1995)
Blatny, L., Berclaz, P., Guillard, F., Einav, I., Gaume, J.: Microstructural origin of propagating compaction patterns in porous media. Phys. Rev. Lett. **128**(22), 228002 (2022)
Branco, F.A., Mendes, P.A.: Thermal actions for concrete bridge design. J. Struct. Eng. **119**(8), 2313-2331 (1993)
Brown, E.T.: Strength of models of rock with intermittent joints. Journal of the Soil Mechanics and Foundations Division **96**(6), 1935-1949 (1970)
Bukenya, P., Moyo, P., Beushausen, H., Oosthuizen, C.: Health monitoring of concrete dams: a literature review. J. Civ. Struct. Health Monit. **4**(4), 235-244 (2014)
Byrne, A., Holmes, N., Norton, B.: State-of-the-art review of cathodic protection for reinforced concrete structures. Mag. Concr. Res. **68**(13), 664-677 (2016)
Caballero, A., López, C., Carol, I.: 3D meso-structural analysis of concrete specimens under uniaxial tension. Comput. Method Appl. Mech. Eng. **195**(52), 7182-7195 (2006)
Cai, R.: Study on multi-factor computational models of surface chloride concentration for concrete exposed to marine environment. Guangxi University (2017)
Cai, R., Hu, Y., Yu, M., Liao, W., Yang, L., Kumar, A., Ma, H.: Skin effect of chloride ingress in marine concrete: A review on the convection zone. Constr. Build. Mater. **262**, 120566 (2020)
Cai, R., Yang, L., Yu, B.: Computing model for surface chloride concentration of concrete in marine tidal and splash zones. Ocean Eng **32**(5), 25-33 (2014)
Cai, T., Zhang, Z., Wang, X., Yang, Z., Zhou, C., Li, Y.: A mesoscale approach for the three-dimensional modelling of interfacial debonding between FRP and concrete. Eng. Struct. **327**, 119663 (2025)
Cakir, F.: Effect of curing time on polymer concrete strength. Challenge Journal of Concrete Research Letters **13**(2), 54-61 (2022)
Candappa, D., Sanjayan, J., Setunge, S.: Complete triaxial stress-strain curves of high-strength concrete. Journal of materials in civil engineering **13**(3), 209-215 (2001)

Candappa, D., Setunge, S., Sanjayan, J.: Stress versus strain relationship of high strength concrete under high lateral confinement. Cem. Concr. Res. **29**(12), 1977-1982 (1999)
CEB-fib: FIP model code for concrete structures 2010. In. Ernst & Sohn Berlin, (2013)
Chandrabhan, S., Kumar, G.P.: Biaxial behaviour of concrete and its failure mechanics under quasi-static and dynamic loading: A numerical study. Eng Fract Mech **300**, 109931 (2024)
Chandrappa, A.K., Biligiri, K.P.: Effect of pore structure on fatigue of pervious concrete. Road Materials and Pavement Design **20**(7), 1525-1547 (2019)
Chateau, C., Nguyen, T.T., Bornert, M., Yvonnet, J.: DVC-based image subtraction to detect microcracking in lightweight concrete. Strain **54**(5), e12276 (2018)
Chen, C., Fan, X., Chen, X.: Experimental investigation of concrete fracture behavior with different loading rates based on acoustic emission. Constr. Build. Mater. **237**, 117472 (2020a)
Chen, H., Xu, B., Mo, Y., Zhou, T.: Behavior of meso-scale heterogeneous concrete under uniaxial tensile and compressive loadings. Constr. Build. Mater. **178**, 418-431 (2018)
Chen, H., Xu, B., Wang, J., Zhou, T., Nie, X., Mo, Y.: Parametric analysis on compressive strain rate effect of concrete using mesoscale modeling approach. Constr. Build. Mater. **246**, 118375 (2020b)
Chen, L., Xie, P., Feng, B., Hong, J., Fang, Q.: A modified K&C model for concrete subjected to coupled effect of high temperature and high strain rate. Int. J. Impact Eng. **181**, 104760 (2023a)
Chen, M., Xu, S., Yuan, L., Miao, C., Lu, J., Ma, H., Gao, G., Wang, P.: Influence of stress state on dynamic behaviors of concrete under true triaxial confinements. Int. J. Mech. Sci. **253**, 108399 (2023b)
Chen, P., Liu, J., Cui, X., Si, S.: Mesoscale analysis of concrete under axial compression. Constr. Build. Mater. **337**, 127580 (2022a)
Chen, P., Liu, J., Cui, X., Si, S.J.C., Materials, B.: Mesoscale analysis of concrete under axial compression. Constr Build Mater **337**, 127580 (2022b)
Chen, Q., Zhang, J., Wang, Z., Zhao, T., Wang, Z.: A review of the interfacial transition zones in concrete: Identification, physical characteristics, and mechanical properties. Eng. Fract. Mech., 109979 (2024)
Chen, W., Ravichandran, G.: An experimental technique for imposing dynamic multiaxial-compression with mechanical confinement. Exp. Mech. **36**(2), 155-158 (1996)
Chen, W., Ravichandran, G.: Dynamic compressive failure of a glass ceramic under lateral confinement. J. Mech. Phys. Solids **45**(8), 1303-1328 (1997)
Chen, X., Wu, S.: Influence of water-to-cement ratio and curing period on pore structure of cement mortar. Constr. Build. Mater. **38**, 804-812 (2013)
Chen, Y.-S., Chiu, H.-J., Chan, Y.-W., Chang, Y.-C., Yang, C.-C.: The correlation between air-borne salt and chlorides cumulated on concrete surface in the marine atmosphere zone in North Taiwan. Journal of Marine Science and Technology **21**(1), 4 (2013)
Chen, Z., Hu, Y., Li, Q., Sun, M., Lu, P., Liu, T.: Behavior of concrete in water subjected to dynamic triaxial compression. J. Eng. Mech. **136**(3), 379-389 (2010)
Choy, T.C.: Effective medium theory: principles and applications, vol. 165. Oxford University Press, (2015)
Christensen, R., Swanson, S., Brown, W.: Split-hopkinson-bar tests on rock under confining pressure: Description of apparatus and test results is given. Attention is given to complete measurement of principal strain and resolution of initial stress-strain data. Exp. Mech. **12**(11), 508-513 (1972)
Cole, R., Kinder, J., Yu, W., Ning, C.L., Wang, F., Chao, Y.: Ocean climate monitoring. Frontiers in Marine Science **6**, 503 (2019)

Coleri, E., Harvey, J.T., Yang, K., Boone, J.M.: Investigation of asphalt concrete rutting mechanisms by X-ray computed tomography imaging and micromechanical finite element modeling. Materials and structures **46**, 1027-1043 (2013)
Constantinides, G., Ulm, F.-J.: The effect of two types of CSH on the elasticity of cement-based materials: Results from nanoindentation and micromechanical modeling. Cem. Concr. Res. **34**(1), 67-80 (2004)
Costa, A., Appleton, J.: Chloride penetration into concrete in marine environment—Part I: Main parameters affecting chloride penetration. Materials and Structures **32**(4), 252-259 (1999)
Cui, G., Liu, M., Dai, W., Gan, Y.: Pore-scale modelling of gravity-driven drainage in disordered porous media. International Journal of Multiphase Flow **114**, 19-27 (2019)
Cui, J., Hao, H., Shi, Y.: Numerical study of the influences of pressure confinement on high-speed impact tests of dynamic material properties of concrete. Constr. Build. Mater. **171**, 839-849 (2018)
Cui, J., Hao, H., Shi, Y., Li, X., Du, K.: Experimental study of concrete damage under high hydrostatic pressure. Cem. Concr. Res. **100**, 140-152 (2017)
Cui, W., Yan, W.-s., Song, H.-f., Wu, X.-l.: DEM simulation of SCC flow in L-Box set-up: Influence of coarse aggregate shape on SCC flowability. Cement and Concrete Composites **109**, 103558 (2020)
Cusatis, G.: Strain-rate effects on concrete behavior. Int. J. Impact Eng. **38**(4), 162-170 (2011)
Cusatis, G., Rezakhani, R., Alnaggar, M., Zhou, X., Pelessone, D.: Multiscale computational models for the simulation of concrete materials and structures. In: Proceedings of the EURO-C 2014
Czaderski, C., Martinelli, E., Michels, J., Motavalli, M.: Effect of curing conditions on strength development in an epoxy resin for structural strengthening. Compos. B Eng. **43**(2), 398-410 (2012)
Dastgerdi, A.S., Peterman, R.J., Riding, K., Beck, B.T.: Effect of concrete mixture components, proportioning, and compressive strength on fracture parameters. Constr. Build. Mater. **206**, 179-192 (2019)
Davis, M., Bellemore, D., Kersey, A.: Distributed fiber Bragg grating strain sensing in reinforced concrete structural components. Cem. Concr. Compos. **19**(1), 45-57 (1997)
De Schutter, G., Taerwe, L.: Degree of hydration-based description of mechanical properties of early age concrete. Materials and structures **29**(6), 335-344 (1996)
Delagrave, A., Bigas, J., Ollivier, J., Marchand, J., Pigeon, M.: Influence of the interfacial zone on the chloride diffusivity of mortars. Advanced Cement Based Materials **5**(3-4), 86-92 (1997)
Delagrave, A., Marchand, J., Samson, E.: Prediction of diffusion coefficients in cement-based materials on the basis of migration experiments. Cem. Concr. Res. **26**(12), 1831-1842 (1996)
Denis, A., Attar, A., Breysse, D., Chauvin, J.J.: Effect of coarse aggregate on the workability of sandcrete. Cement and Concrete Research **32**(5), 701-706 (2002)
Dilger, W., Koch, R., Kowalczyk, R.: Ductility of plain and confined concrete under different strain rates. In: Journal Proceedings 1984, vol. 1, pp. 73-81
Dobrescu, M., Vasilescu, M.: Reinforcing bar corrosion for buildings construction. Advanced Materials Research **1114**, 219-223 (2015)
Du, Q., Faber, V., Gunzburger, M.: Centroidal Voronoi tessellations: Applications and algorithms. SIAM review **41**(4), 637-676 (1999)
Du, X., Jin, L., Ma, G.: A meso-scale numerical method for the simulation of chloride diffusivity in concrete. Finite Elem. Anal. Des. **85**, 87-100 (2014)

Duan, Z., Zhu, Z., Su, H., Zhang, F., Mao, Z.: Numerical Analysis of Impact Compression Failure and Dynamic Mechanical Behavior of Lightweight Aggregate Concrete at Low Temperatures. J. Adv. Concr. Technol. **21**(10), 821-836 (2023)
Duffó, G., Morris, W., Raspini, I., Saragovi, C.: A study of steel rebars embedded in concrete during 65 years. Corrosion science **46**(9), 2143-2157 (2004)
El-Hawary, M., Al-Khaiat, H., Fereig, S.: Performance of epoxy-repaired concrete in a marine environment. Cem. Concr. Res. **30**(2), 259-266 (2000)
El-Maaty, A.E.A.: Establishing a balance between mechanical and durability properties of pervious concrete pavement. American Journal of Traffic and Transportation Engineering **1**(2), 13-25 (2016)
El-Reedy, M.A.: Asset integrity management for offshore and onshore structures. Gulf Professional Publishing, (2022)
El Awad, S.: The inference of the mechanical properties of materials at micro and meso-scale via the micro-bending technique. University of Houston (2020)
Eldho, C.A., Nanayakkar, O., Xia, J., Jones, S.: Performance of concrete patch repairs: from a durability point of view. (2016)
Elsener, B., Angst, U.: Corrosion inhibitors for reinforced concrete. In: Science and technology of concrete admixtures. pp. 321-339. Elsevier, (2016)
Erdoğan, S., Martys, N., Ferraris, C., Fowler, D.: Influence of the shape and roughness of inclusions on the rheological properties of a cementitious suspension. Cement and Concrete Composites **30**(5), 393-402 (2008)
Fajardo, G., Escadeillas, G., Arliguie, G.: Electrochemical chloride extraction (ECE) from steel-reinforced concrete specimens contaminated by “artificial” sea-water. Corrosion science **48**(1), 110-125 (2006)
Fan, H., Yu, H., Ma, H.: Dynamic increase factor (DIF) of concrete with SHPB tests: review and systematic analysis. J. Build. Eng. **79**, 107666 (2023)
Fang, J., Jiang, C., Gu, X.-L.: Moisture transports in high-cycle compressive fatigue-damaged concrete. Constr. Build. Mater. **409**, 133994 (2023)
Fantilli, A.P., Jóźwiak-Niedźwiedzka, D.: Supplementary cementitious materials in concrete, part I. In, vol. 14. vol. 9, p. 2291. MDPI, (2021)
Fantinel, P., Borgman, O., Holtzman, R., Goehring, L.: Drying in a microfluidic chip: experiments and simulations. Scientific reports **7**(1), 1-12 (2017)
Ferellec, J.-F., McDowell, G.: A simple method to create complex particle shapes for DEM. Geomechanics and Geoengineering: An International Journal **3**(3), 211-216 (2008)
Ferellec, J.-F., McDowell, G.J.G., Journal, G.A.I.: A simple method to create complex particle shapes for DEM. **3**(3), 211-216 (2008)
Fernlund, J.M.R.: Image analysis method for determining 3-D shape of coarse aggregate. Cement and Concrete Research **35**(8), 1629-1637 (2005)
Gang, X., Yun-pan, L., Yi-biao, S., Ke, X.: Chloride ion transport mechanism in concrete due to wetting and drying cycles. Structural Concrete **16**(2), 289-296 (2015)
Gao, L., Zhou, Y., Jiang, J., Yang, Y., Kong, H.: Mix-mode fracture behavior in asphalt concrete: Asymmetric semi-circular bending testing and random aggregate generation-based modelling. Constr. Build. Mater. **438**, 137225 (2024)
Gao, W., Yu, H., Ma, H., Guo, J., Mei, Q., Da, B., Zeng, X.: Mechanical properties and mesoscopic failure mechanism of concrete under impact compressive loading: Effects of cement and aggregate types. Constr. Build. Mater. **490**, 142448 (2025)
Garboczi, E., Bentz, D.: Computational materials science of cement-based materials. MRS Bulletin **18**(3), 50-54 (1993)

Garboczi, E.J.: Three-dimensional mathematical analysis of particle shape using X-ray tomography and spherical harmonics: Application to aggregates used in concrete. Cem. Concr. Res. **32**(10), 1621-1638 (2002)
Gatuingt, F., Snozzi, L., Molinari, J.-F.: Numerical determination of the tensile response and the dissipated fracture energy of concrete: role of the mesostructure and influence of the loading rate. International Journal for Numerical and Analytical Methods in Geomechanics **37**(18), 3112-3130 (2013)
Ge, L., Chen, J.-F.: Meso-scale fracture analysis of concrete based on phase-field theory and cohesive zone method. Eng. Fail. Anal., 109684 (2025)
Gérard, B., Marchand, J.: Influence of cracking on the diffusion properties of cement-based materials: Part I: Influence of continuous cracks on the steady-state regime. Cem. Concr. Res. **30**(1), 37-43 (2000)
Gerwick Jr, B.C.: Ocean structures of prestressed concrete. PCI Jorunal, 10-23 (1970)
Geubelle, P.H., Baylor, J.S.: Impact-induced delamination of composites: a 2D simulation. Compos. B Eng. **29**(5), 589-602 (1998)
Ghahremani, G., Bagheri, A., Zanganeh, H.: The effect of size and shape of pores on the prediction model of compressive strength of foamed concrete. Constr. Build. Mater. **371**, 130720 (2023)
Ghosh, S., Deng, Z., Kim, G., Goodman, C., Moreno, J., Nunez, R., Foster, M.A., Hurley, R.C.: Quantifying 3D ejecta velocities during high-velocity impact experiments into concrete. Int. J. Impact Eng., 105543 (2025)
Gjørv, O.E.: Durability of concrete structures. Arabian Journal for Science and Engineering **36**(2), 151-172 (2011)
Gong, C., Ding, W., Mosalam, K.M., Günay, S., Soga, K.: Comparison of the structural behavior of reinforced concrete and steel fiber reinforced concrete tunnel segmental joints. Tunn. Undergr. Space Technol. **68**, 38-57 (2017)
Gran, J., Florence, A., Colton, J.: Dynamic triaxial tests of high-strength concrete. J. Eng. Mech. **115**(5), 891-904 (1989)
Guida, G., Viggiani, G.M., Casini, F.: Multi-scale morphological descriptors from the fractal analysis of particle contour. Acta Geotechnica **15**(5), 1067-1080 (2020)
Guo, J., Zhang, J., Ma, H., Yu, H., Wu, Z., Han, W., Liu, T.: Dynamic behavior of a new type of coral aggregate concrete: experimental and numerical investigation. Journal of Materials in Civil Engineering **35**(6), 04023124 (2023a)
Guo, R., Ren, H., Zhang, L., Long, Z., Jiang, X., Wu, X., Wang, H.: Direct dynamic tensile study of concrete materials based on mesoscale model. Int. J. Impact Eng. **143**, 103598 (2020)
Guo, W., Wang, W., Cui, Y., Wang, B., Bao, J., Zhang, P., Lei, D.: Dynamic mechanical behavior and damage properties of SHCC under high strain rate loading. Journal of Materials Research and Technology **26**, 6304-6315 (2023b)
Guo, Y., Ren, M., Li, J., Zhang, T., Zhu, W., Ren, Q., Wei, J., Yu, Q.: Synergetic optimizing particle size distributions of aggregate and cementitious materials: Toward lower chloride diffusivity of concrete. Constr. Build. Mater. **436**, 136979 (2024)
Hafid, H., Ovarlez, G., Toussaint, F., Jezequel, P., Roussel, N.: Effect of particle morphological parameters on sand grains packing properties and rheology of model mortars. Cement and Concrete Research **80**, 44-51 (2016)
Hales, T.C.: The sphere packing problem. Journal of Computational and Applied Mathematics **44**(1), 41-76 (1992)
Han, J., Sun, W., Pan, G., Caihui, W.: Monitoring the evolution of accelerated carbonation of hardened cement pastes by X-ray computed tomography. Journal of materials in civil engineering **25**(3), 347-354 (2013)

Han, X., Wang, B., Feng, J.: Relationship between fractal feature and compressive strength of concrete based on MIP. Constr. Build. Mater. **322**, 126504 (2022)
Hashin, Z., Shtrikman, S.: A variational approach to the theory of the effective magnetic permeability of multiphase materials. Journal of applied Physics **33**(10), 3125-3131 (1962)
Hashin, Z., Shtrikman, S.: A variational approach to the theory of the elastic behaviour of multiphase materials. J. Mech. Phys. Solids **11**(2), 127-140 (1963)
Hassan, A.I., Mhadhbi, M., Saleh, H.: Reinforced Concrete Structures-Innovations in Materials, Design and Analysis: Innovations in Materials, Design and Analysis. BoD–Books on Demand, (2023)
He, D.: Review of Corrosion Evaluation Methods for Steel Reinforcement in Concrete. Corrosion and Materials Degradation **6**(3), 37 (2025)
He, Z.-j., Zhang, J.-x.: Strength characteristics and failure criterion of plain recycled aggregate concrete under triaxial stress states. Constr. Build. Mater. **54**, 354-362 (2014)
Hirao, H., Yamada, K., Takahashi, H., Zibara, H.: Chloride binding of cement estimated by binding isotherms of hydrates. J. Adv. Concr. Technol. **3**(1), 77-84 (2005)
Hoch, B.O.: Modelling of hydrogen diffusion in heterogeneous materials: implications of the grain boundary connectivity. Université de La Rochelle (2015)
Hoek, E., Martin, C.: Fracture initiation and propagation in intact rock–a review. Journal of Rock Mechanics and Geotechnical Engineering **6**(4), 287-300 (2014)
Holtzman, R.: Effects of pore-scale disorder on fluid displacement in partially-wettable porous media. Scientific reports **6**, 36221 (2016)
Hong, S.-H., Choi, J.-S., Yuan, T.-F., Yoon, Y.-S.: A review on concrete creep characteristics and its evaluation on high-strength lightweight concrete. Journal of Materials Research and Technology **22**, 230-251 (2023)
Hong, S., Liu, P., Zhang, J., Kuang, C., Dong, B., Luo, Q., Liu, W.: Interior fracture analysis of rubber-cement composites based on X-ray computed tomography and digital volume correlation. Constr. Build. Mater. **259**, 119833 (2020)
Hornung, U.: Homogenization and porous media, vol. 6. Springer Science & Business Media, (1996)
Hou, D.-W., Zhang, J., Chen, H.-Y., Liu, W.: Development of strength and elastic modulus of concrete under moisture and drying curing conditions. Shuili Xuebao(Journal of Hydraulic Engineering) **43**(2), 198-208 (2012)
Hou, D., Zhang, W., Ge, Z., Wang, P., Wang, X., Zhang, H.: Experimentally validated peridynamic fracture modelling of mortar at the meso-scale. Constr. Build. Mater. **267**, 120939 (2021)
Hsieh, S.-S., Ting, E., Chen, W.: A plastic-fracture model for concrete. Int. J. Solids Struct. **18**(3), 181-197 (1982)
Hu, J., Stroeven, P.: Shape characterization of concrete aggregate. Image analysis and stereology **25**(1), 43-53 (2006)
Hu, J., Zhang, S., Chen, E., Li, W.: A review on corrosion detection and protection of existing reinforced concrete (RC) structures. Constr. Build. Mater. **325**, 126718 (2022)
Hu, Y.J., Du, Y.L.: Effect of pore structure on the chloride permeability of concrete with mineral admixture. Advanced Materials Research **690**, 835-838 (2013)
Huang, Y.-j., Guo, F.-q., Zhang, H., Yang, Z.-j.: An efficient computational framework for generating realistic 3D mesoscale concrete models using micro X-ray computed tomography images and dynamic physics engine. Cem Concr Compos **126**, 104347 (2022)

Huang, Y.-j., Natarajan, S., Zhang, H., Guo, F.-q., Xu, S.-l., Zeng, C., Zheng, Z.-s.: A CT image-driven computational framework for investigating complex 3D fracture in mesoscale concrete. Cem. Concr. Compos. **143**, 105270 (2023)
Huang, Y., Yang, Z., Chen, X., Liu, G.: Monte Carlo simulations of meso-scale dynamic compressive behavior of concrete based on X-ray computed tomography images. Int. J. Impact Eng. **97**, 102-115 (2016)
Huang, Y., Yang, Z., Ren, W., Liu, G., Zhang, C.: 3D meso-scale fracture modelling and validation of concrete based on in-situ X-ray Computed Tomography images using damage plasticity model. Int. J. Solids Struct. **67**, 340-352 (2015)
Hughes, B., Watson, A.: Compressive strength and ultimate strain of concrete under impact loading. Mag. Concr. Res. **30**(105), 189-199 (1978)
Idiart, A.E., López, C.M., Carol, I.: Chemo-mechanical analysis of concrete cracking and degradation due to external sulfate attack: A meso-scale model. Cement and Concrete Composites **33**(3), 411-423 (2011)
Imran, I., Pantazopoulou, S.J.: Experimental study of plain concrete under triaxial stress. ACI Materials Journal **93**(6), 589-601 (1996)
Inderfurth, K.F., Fabrycky, D., Cohen, S.: The 2004 Indian Ocean tsunami: one year report. The Sigur Center Asia Papers, 1-40 (2005)
Ishida, T., Iqbal, P.O.N., Anh, H.T.L.: Modeling of chloride diffusivity coupled with non-linear binding capacity in sound and cracked concrete. Cem. Concr. Res. **39**(10), 913-923 (2009)
Islam, J., Collins, F., Aldridge, L., Gates, W.: Effect of pore characteristics and chloride binding on time-dependent chloride diffusion into cementitious material. (2016)
Ismail, M., Siti Fatimah, A., Muhammad, B., Norhazilan Md, N., Bakhtiar, H.: Embedded sensor for detecting corrosion of reinforcement in concrete. Advanced Materials Research **250**, 1118-1123 (2011)
Jamnam, S., Maho, B., Techaphatthanakon, A., Sonoda, Y., Yoo, D.-Y., Sukontasukkul, P.: Steel fiber reinforced concrete panels subjected to impact projectiles with different caliber sizes and muzzle energies. Case Stud. Constr. Mater. **13**, e00360 (2020)
Jennings, H.M.: A model for the microstructure of calcium silicate hydrate in cement paste. Cem. Concr. Res. **30**(1), 101-116 (2000)
Jiang, S., Shen, L.: Aggregate shape effect on fracture and breakage of cementitious granular materials. Int. J. Mech. Sci. **220**, 107161 (2022)
Jiang, W.-q., Shen, X.-h., Xia, J., Mao, L.-x., Yang, J., Liu, Q.-f.: A numerical study on chloride diffusion in freeze-thaw affected concrete. Constr. Build. Mater. **179**, 553-565 (2018)
Jiao, C., Sun, W., Huan, S., Jiang, G.: Behavior of steel fiber-reinforced high-strength concrete at medium strain rate. Frontiers of Architecture and Civil Engineering in china **3**(2), 131-136 (2009)
Jiao, Y., Torquato, S.: Quantitative characterization of the microstructure and transport properties of biopolymer networks. Physical biology **9**(3), 036009 (2012)
Jie, W., Dassekpo, J.-B.M., Wan, C., Zha, X.: Experimental and numerical modeling of chloride diffusivity in hardened cement concrete considering the aggregate shapes and exposure-duration effects. Results in physics **7**, 1427-1432 (2017)
Jin, L., Liu, K., Zhang, R., Yu, W., Du, X.: Effects of content and size of aggregate on the mechanical responses of concrete at cryogenic temperatures. Eng. Fract. Mech. **273**, 108737 (2022a)
Jin, L., Wan, S., Li, D., Miao, L., Du, X.: Influence of concrete strength and aggregate size on the size effect of shear capacity of RC beam-column joints under monotonic loading: Mesoscale numerical tests. In: Structures 2022b, pp. 671-685. Elsevier

Jin, L., Yu, W., Du, X.: Size effect on static splitting tensile strength of concrete: Experimental and numerical studies. Journal of Materials in Civil Engineering **32**(10), 04020308 (2020a)
Jin, L., Yu, W., Du, X., Yang, W.: Mesoscopic numerical simulation of dynamic size effect on the splitting-tensile strength of concrete. Eng. Fract. Mech. **209**, 317-332 (2019)
Jin, L., Yu, W., Du, X., Yang, W.: Meso-scale simulations of size effect on concrete dynamic splitting tensile strength: Influence of aggregate content and maximum aggregate size. Eng. Fract. Mech. **230**, 106979 (2020b)
Jin, L., Yu, W., Li, D., Du, X.: Numerical and theoretical investigation on the size effect of concrete compressive strength considering the maximum aggregate size. Int J Mech Sci **192**, 106130 (2021)
Jin, Z., Hou, D., Zhao, T.: Electrochemical chloride extraction (ECE) based on the high performance conductive cement-based composite anode. Constr. Build. Mater. **173**, 149-159 (2018)
Jóhannesson, H., Halle, B.: Solvent diffusion in ordered macrofluids: a stochastic simulation study of the obstruction effect. The Journal of chemical physics **104**(17), 6807-6817 (1996)
Kachkouch, F.Z., Noberto, C.C., Babadopulos, L.F.d.A.L., Melo, A.R.S., Machado, A.M.L., Sebaibi, N., Boukhelf, F., El Mendili, Y.: Fatigue behavior of concrete: A literature review on the main relevant parameters. Constr. Build. Mater. **338**, 127510 (2022)
Kantar, E., Yuen, T.Y., Kobya, V., Kuang, J.: Impact dynamics and energy dissipation capacity of fibre-reinforced self-compacting concrete plates. Constr. Build. Mater. **138**, 383-397 (2017)
Khatami, D., Hajilar, S., Shafei, B.: Investigation of oxygen diffusion and corrosion potential in steel-reinforced concrete through a cellular automaton framework. Corrosion Science **187**, 109496 (2021)
Kiesse, T.S., Bonnet, S., Amiri, O., Ventura, A.: Analysis of corrosion risk due to chloride diffusion for concrete structures in marine environment. Marine structures **73**, 102804 (2020)
Kim, J.-K., Moon, Y.-H., Eo, S.-H.: Compressive strength development of concrete with different curing time and temperature. Cem. Concr. Res. **28**(12), 1761-1773 (1998)
Kim, K.-M., Lee, S., Cho, J.-Y.: Effect of maximum coarse aggregate size on dynamic compressive strength of high-strength concrete. Int. J. Impact Eng. **125**, 107-116 (2019)
Kim, S.-M., Al-Rub, R.K.A.: Meso-scale computational modeling of the plastic-damage response of cementitious composites. Cem. Concr. Res. **41**(3), 339-358 (2011)
Klanac, A., Varsta, P.: Design of marine structures with improved safety for environment. Reliability Engineering & System Safety **96**(1), 75-90 (2011)
Korouzhdeh, T., Eskandari-Naddaf, H., Kazemi, R.: The ITZ microstructure, thickness, porosity and its relation with compressive and flexural strength of cement mortar; influence of cement fineness and water/cement ratio. Frontiers of Structural and Civil Engineering **16**(2), 191-201 (2022)
Kotsovos, M.D., Newman, J.B.: Mathematical description of deformational behavior of concrete under generalized stress beyond ultimate strength. Proc. **77**(5) (1980)
Krčmářová, N., Šleichrt, J., Falta, J., Koudelka, P., Kytýř, D., Čítek, D., Fíla, T.: Split Hopkinson bar and flash X-ray characterization of ultra high performance concrete reinforced by steel fibers subjected to dynamic compression. Emergent Mater. **8**(3), 2045-2061 (2025)

Krejsová, J., Doleželová, M., Pernicová, R., Svora, P., Vimmrová, A.: The influence of different aggregates on the behavior and properties of gypsum mortars. Cement and Concrete Composites **92**, 188-197 (2018)
Kumar, R., Bhattacharjee, B.: Porosity, pore size distribution and in situ strength of concrete. Cem. Concr. Res. **33**(1), 155-164 (2003)
Kunawisarut, A., Kawabata, Y., Iwanami, M.: Mechanical behavior of concrete under high water pressure: water penetration as a critical factor for mechanical properties. Cem. Concr. Res. **190**, 107820 (2025)
Kušter Marić, M., Ivanović, A., Fusić, M., Srbić, M., Vlašić, A.: Experimental Investigation of the Explosion Effects on Reinforced Concrete Slabs with Fibers. Buildings **14**(4), 1080 (2024)
Kwan, A.K., Mora, C., Chan, H.: Particle shape analysis of coarse aggregate using digital image processing. Cement and Concrete Research **29**(9), 1403-1410 (1999)
Lai, J., Sun, W.: Dynamic behaviour and visco-elastic damage model of ultra-high performance cementitious composite. Cem. Concr. Res. **39**(11), 1044-1051 (2009)
Laím, L., Caetano, H., Santiago, A.: Review: effects of nanoparticles in cementitious construction materials at ambient and high temperatures. J Build Eng 35: 102008. In. (2020)
Land, G., Stephan, D.: Controlling cement hydration with nanoparticles. Cem. Concr. Compos. **57**, 64-67 (2015)
Landis, E.N., Keane, D.T.: X-ray microtomography. Materials characterization **61**(12), 1305-1316 (2010)
Laubie, H., Monfared, S., Radjai, F., Pellenq, R., Ulm, F.-J.: Disorder-induced stiffness degradation of highly disordered porous materials. Journal of the Mechanics and Physics of Solids **106**, 207-228 (2017a)
Laubie, H., Radjai, F., Pellenq, R., Ulm, F.-J.: Stress transmission and failure in disordered porous media. Phys. Rev. Lett. **119**(7), 075501 (2017b)
Le Thanh, C., Minh, H.-L., Sang-To, T.: A nonlinear concrete damaged plasticity model for simulation reinforced concrete structures using ABAQUS. Fracture and Structural Integrity **16**(59), 232-242 (2022)
Li, D., Li, Z., Lv, C., Zhang, G., Yin, Y.: A predictive model of the effective tensile and compressive strengths of concrete considering porosity and pore size. Constr. Build. Mater. **170**, 520-526 (2018a)
Li, F., Feng, J., Chen, X.: Dynamic fracture of high-strength concrete based on 3D discrete element rate-dependent model. J. Build. Eng. **103**, 112006 (2025a)
Li, K., Li, L.: Crack-altered durability properties and performance of structural concretes. Cem. Concr. Res. **124**, 105811 (2019)
Li, K., Zhang, Y., Wang, S., Zeng, J.: Impact of carbonation on the chloride diffusivity in concrete: experiment, analysis and application. Materials and Structures **51**(6), 164 (2018b)
Li, L.-Y., Xia, J., Lin, S.-S.: A multi-phase model for predicting the effective diffusion coefficient of chlorides in concrete. Construction and Building Materials **26**(1), 295-301 (2012)
Li, M., Hao, H., Cui, J.: Numerical investigation of the failure mechanism of concrete specimens under tri-axial dynamic loads. Eng. Fract. Mech. **266**, 108425 (2022a)
Li, R., Mu, C., Zhang, Y., Ma, L., Wang, F., Li, B., Xie, Q.: Dynamic mechanical performance of SCAC with various CCRL coarse aggregate: Experimental and numerical investigation. Constr. Build. Mater. **461**, 139784 (2025b)
Li, S., Li, Q.: Method of meshing ITZ structure in 3D meso-level finite element analysis for concrete. Finite Elem. Anal. Des. **93**, 96-106 (2015)

Li, W., Luo, Z., Gan, Y., Wang, K., Shah, S.P.: Nanoscratch on mechanical properties of interfacial transition zones (ITZs) in fly ash-based geopolymer composites. Compos. Sci. Technol. **214**, 109001 (2021)
Li, Y., Ma, H., Wen, L., Yuan, J., Zhang, Y., Li, Y., Zhou, H., Chen, J.: Influence of pore size distribution on concrete cracking with different AEA content and curing age using acoustic emission and low-field NMR. J. Build. Eng. **58**, 105059 (2022b)
Li, Z., Li, L.-y., Cheng, S.: Evaluation of modulus of elasticity of concrete containing both natural and recycled concrete aggregates. Journal of Cleaner Production **447**, 141591 (2024)
Liang, Y., Chen, H., Xu, X., Xu, Y., Xiao, A.: A comprehensive framework for 3D mesoscopic modelling of concrete: Innovations in aggregate mixing, placement domain shapes, and aggregate volume fraction adaptability. Constr. Build. Mater. **472**, 140894 (2025)
Liasneuski, H., Hlushkou, D., Khirevich, S., Höltzel, A., Tallarek, U., Torquato, S.: Impact of microstructure on the effective diffusivity in random packings of hard spheres. Journal of Applied Physics **116**(3), 034904 (2014)
Lindvall, A.: Chloride ingress data from field and laboratory exposure–Influence of salinity and temperature. Cem. Concr. Compos. **29**(2), 88-93 (2007)
Liu, C., Xie, D., She, W., Liu, Z., Liu, G., Yang, L., Zhang, Y.: Numerical modelling of elastic modulus and diffusion coefficient of concrete as a three-phase composite material. Constr. Build. Mater. **189**, 1251-1263 (2018)
Liu, C., Zhang, R., Liu, H., He, C., Wang, Y., Wu, Y., Liu, S., Song, L., Zuo, F.: Analysis of the mechanical performance and damage mechanism for 3D printed concrete based on pore structure. Constr. Build. Mater. **314**, 125572 (2022a)
Liu, J., Chen, X., Rong, H., Yu, A., Ming, Y., Li, K.: Effect of interface transition zone and coarse aggregate on microscopic diffusion behavior of chloride ion. Materials **15**(12), 4171 (2022b)
Liu, J., Wenxuan, Y., Xiuli, D., Zhang, S., Dong, L.: Meso-scale modelling of the size effect on dynamic compressive failure of concrete under different strain rates. Int. J. Impact Eng. **125**, 1-12 (2019)
Liu, K., Guo, T., Yang, J., Ma, S.: Static and dynamic fracture behavior of rock-concrete bi-material disc with different interface crack inclinations. Theor. Appl. Fract. Mech. **123**, 103659 (2023)
Liu, L., Shen, D., Chen, H., Xu, W.: Aggregate shape effect on the diffusivity of mortar: a 3D numerical investigation by random packing models of ellipsoidal particles and of convex polyhedral particles. Computers & structures **144**, 40-51 (2014)
Liu, L., Sun, W., Ye, G., Chen, H., Qian, Z.: Estimation of the ionic diffusivity of virtual cement paste by random walk algorithm. Construction and Building Materials **28**(1), 405-413 (2012)
Liu, M., Qiao, P., Sun, L.: Dependence of chloride ion diffusivity on evolution of pore-structures in freeze-thawed shotcrete: Multiscale characterization and modeling. Cem. Concr. Compos. **123**, 104222 (2021)
Liu, Q., Cheng, A., Sun, C., Chen, K., Wang, Y., Li, W.: Effects of aggregate's type and orientation on stress concentration and crack propagation of modeled concrete applied a shear force. J. Build. Eng. **95**, 110340 (2024a)
Liu, Q., Ma, J., Qiao, P., Wu, E., Zhou, G.: Mesoscale modeling of new-to-old concrete interface under combined shear and compressive loads. Eng. Fract. Mech. **307**, 110331 (2024b)
Liu, Q., Wei, D., Gan, Y.: Mesoscale Modelling of Triaxial Concrete Fracture: The Role of Aggregate Shapes. Int. J. Mech. Sci., 110570 (2025)

Lorenzoni, R., Lima, V.N., Figueiredo, T.C.S., Hering, M., Paciornik, S., Curbach, M., Mechtcherine, V., de Andrade Silva, F.: Macro and meso analysis of cement-based materials subjected to triaxial and uniaxial loading using X-ray microtomography and digital volume correlation. Constr. Build. Mater. **323**, 126558 (2022)
Loto, R.T., Cleophas, A.: Corrosion and protection of facilities and infrastructures in telecommunications industry-a review. In: IOP Conference Series: Materials Science and Engineering 2021, vol. 1, p. 012014. IOP Publishing
Lowes, L.N.: Finite element modeling of reinforced-concrete beam-column bridge connections. University of California, Berkeley, (1999)
Lu, X., Hsu, C.-T.T.: Stress-strain relations of high-strength concrete under triaxial compression. J Mater Civ Eng **19**(3), 261-268 (2007)
Lubliner, J., Oliver, J., Oller, S., Onate, E.: A plastic-damage model for concrete. Int. J. Solids Struct. **25**(3), 299-326 (1989)
Luping, T.: Chloride ingress in concrete exposed to marine environment-field data up to 10 years exposure. (2003)
Luping, T.: Engineering expression of the ClinConc model for prediction of free and total chloride ingress in submerged marine concrete. Cem. Concr. Res. **38**(8-9), 1092-1097 (2008)
Luping, T., Gulikers, J.: On the mathematics of time-dependent apparent chloride diffusion coefficient in concrete. Cem. Concr. Res. **37**(4), 589-595 (2007)
Lv, T., Chen, X., Chen, G.: Analysis on the waveform features of the split Hopkinson pressure bar tests of plain concrete specimen. Int. J. Impact Eng. **103**, 107-123 (2017)
Ma, D., Zhang, M., Cui, J.: A review on the deterioration of mechanical and durability performance of marine-concrete under the scouring action. J. Build. Eng. **66**, 105924 (2023)
Ma, H., Xu, W., Li, Y.: Random aggregate model for mesoscopic structures and mechanical analysis of fully-graded concrete. Computers & Structures **177**, 103-113 (2016)
Mačiulaitis, R., Vaičiene, M., Žurauskiene, R.: The effect of concrete composition and aggregates properties on performance of concrete. Journal of civil engineering and management **15**(3), 317-324 (2009)
Mahi, M.S.H., Ridoy, T.A.: Corrosion Mechanisms in Reinforced Concrete: Causes, Effects, and Sustainable Mitigation Strategies. Current Problems in Research **1**(1), 52-66 (2025)
Maleki, M., Rasoolan, I., Khajehdezfuly, A., Jivkov, A.P.: On the effect of ITZ thickness in meso-scale models of concrete. Constr. Build. Mater. **258**, 119639 (2020)
Malvern, L.E., Ross, C.: Dynamic Response of Concrete and Concrete Structures. In: Understanding the Tensile Properties of Concrete. (1986)
Manzur, T., Hasan, M., Baten, B., Torsha, T., Khan, M., Hossain, K.: Significance of service life based concrete mix design in marine environment. In: 7th international conference on engineering mechanics & materials by CSCE, Laval (Greater Montreal), Canada 2019
Markel, V.A.: Maxwell Garnett approximation (advanced topics): tutorial. Journal of the Optical Society of America A **33**(11), 2237-2255 (2016)
Marzec, I., Tejchman, J.: Fracture evolution in concrete compressive fatigue experiments based on X-ray micro-CT images. International Journal of Fatigue **122**, 256-272 (2019)
Mathern, A., von der Haar, C., Marx, S.: Concrete support structures for offshore wind turbines: Current status, challenges, and future trends. Energies **14**(7), 1995 (2021)
Mazars, J., Millard, A.: Dynamic behavior of concrete and seismic engineering. Wiley Online Library, (2009)

Mazloom, M., Ramezanianpour, A., Brooks, J.: Effect of silica fume on mechanical properties of high-strength concrete. Cem. Concr. Compos. **26**(4), 347-357 (2004)
Mazzucco, G., Pomaro, B., Xotta, G., Garbin, E., Majorana, C., De Marchi, N., Concheri, G.: Meso-scale XCT-based modeling of ordinary concrete. Constr. Build. Mater. **286**, 122850 (2021)
Mazzucco, G., Xotta, G., Pomaro, B., Salomoni, V., Faleschini, F.: Elastoplastic-damaged meso-scale modelling of concrete with recycled aggregates. Compos. B Eng. **140**, 145-156 (2018)
Megahed, F., Seleem, M., Badawy, A., Sharaky, I.: The flexural response of RC beams strengthened by EB/NSM techniques using FRP and metal materials: a state-of-the-art review. Innovative Infrastructure Solutions **8**(11), 289 (2023)
Meira, G.R., Andrade, M., Padaratz, I., Alonso, M.C., Borba Jr, J.: Measurements and modelling of marine salt transportation and deposition in a tropical region in Brazil. Atmospheric Environment **40**(29), 5596-5607 (2006)
Meyers, M.A.: Dynamic behavior of materials. John wiley & sons, (1994)
MH, W.I., Hamzah, A., Jamaluddin, N., Mangi, S., Ramadhansyah, P.: Influence of bottom ash as a sand replacement material on durability of self-compacting concrete exposed to seawater. Journal of Engineering Science and Technology **15**(1), 555-571 (2020)
Minh, H.-L., Khatir, S., Wahab, M.A., Cuong-Le, T.: A concrete damage plasticity model for predicting the effects of compressive high-strength concrete under static and dynamic loads. J. Build. Eng. **44**, 103239 (2021)
Mo, Y.-L.: Dynamic behavior of concrete structures, vol. 44. Elsevier, (2013)
Mollon, G., Zhao, J.: Fourier–Voronoi-based generation of realistic samples for discrete modelling of granular materials. Granular matter **14**(5), 621-638 (2012)
Mollon, G., Zhao, J.: 3D generation of realistic granular samples based on random fields theory and Fourier shape descriptors. Comput. Method Appl. Mech. Eng. **279**, 46-65 (2014)
Moon, H.Y., Kim, H.S., Choi, D.S.: Relationship between average pore diameter and chloride diffusivity in various concretes. Constr. Build. Mater. **20**(9), 725-732 (2006)
Mora, C., Kwan, A.: Sphericity, shape factor, and convexity measurement of coarse aggregate for concrete using digital image processing. Cem. Concr. Res. **30**(3), 351-358 (2000)
Morger, F., Kenel, A., Kaufmann, W.: Passive confinement of reinforced concrete members revisited. Structural Concrete **25**(6), 4283-4299 (2024)
Mosig, O., Curbach, M.: The crack propagation velocity as a reason for the strain rate effect of concrete: An analytical model. Civil Engineering Design **2**(4), 123-130 (2020)
Mostafavi, M., Baimpas, N., Tarleton, E., Atwood, R., McDonald, S., Korsunsky, A., Marrow, T.: Three-dimensional crack observation, quantification and simulation in a quasi-brittle material. Acta Materialia **61**(16), 6276-6289 (2013)
Naderi, S., Tu, W., Zhang, M.: Meso-scale modelling of compressive fracture in concrete with irregularly shaped aggregates. Cem Concr Res **140**, 106317 (2021)
Naderi, S., Zhang, M.: Meso-scale modelling of static and dynamic tensile fracture of concrete accounting for real-shape aggregates. Cem. Concr. Compos. **116**, 103889 (2021a)
Naderi, S., Zhang, M.: Meso-scale modelling of static and dynamic tensile fracture of concrete accounting for real-shape aggregates. Cem Concr Compos **116**, 103889 (2021b)
Naderi, S., Zhang, M.: 3D meso-scale modelling of tensile and compressive fracture behaviour of steel fibre reinforced concrete. Composite Structures **291**, 115690 (2022)

Nagrockiene, D., Pundienė, I., Kicaite, A.: The effect of cement type and plasticizer addition on concrete properties. Constr. Build. Mater. **45**, 324-331 (2013)
Naik, T.R., Singh, S., Ye, C.: Fatigue behavior of plain concrete made with or without fly ash. A Progress Report Submitted to EPRI (1993)
Nassar, N.E.A.: Corrosion in marine and offshore steel structures: Classification and overview. International Journal of Advanced Engineering, Sciences and Applications **3**(1), 7-11 (2022)
Nath, P., Sarker, P.: Effect of fly ash on the durability properties of high strength concrete. Procedia Eng. **14**, 1149-1156 (2011)
Neville, A.M.: Properties of concrete, vol. 4. Longman London, (1995)
Newman, J.: Concrete under complex stress. Developments in concrete technology **1**, 151-219 (1979)
Nilsson, L., Sandberg, P., Poulsen, E., Tang, L., Andersen, A., Frederiksen, J.: HETEK—a system for estimation of chloride ingress into concrete, theoretical background (report no. 83). Road Directorate, Denmark, Ministry of Transport (1997)
Ning, Z., Li, Y., Liu, Y., Li, Y., Dong, J., Wang, Q.: A unified meso-scale simulation method for dynamic compressive and tensile properties of hydraulic asphalt concrete based on the viscoelastic damage contact model. Constr. Build. Mater. **484**, 141861 (2025)
Nitka, M., Tejchman, J.: Comparative DEM calculations of fracture process in concrete considering real angular and artificial spherical aggregates. Eng. Fract. Mech. **239**, 107309 (2020)
Okumu, V.: Influence of constituent materials properties on the compressive strength of in situ concrete in Kenya. Open Journal of Civil Engineering (2017)
Ouyang, X., Wu, Z., Shan, B., Chen, Q., Shi, C.: A critical review on compressive behavior and empirical constitutive models of concrete. Constr. Build. Mater. **323**, 126572 (2022)
Özakça, M., Hind, M.K., Ekmekyapar, T.: A review on nonlinear finite element analysis of reinforced concrete beams retrofitted with fiber reinforced polymers. Journal of Advanced Research in Applied Mechanics **22**(1), 13-48 (2016)
Ožbolt, J., Sharma, A., Reinhardt, H.-W.: Dynamic fracture of concrete–compact tension specimen. Int. J. Solids Struct. **48**(10), 1534-1543 (2011)
Pabst, W., Gregorová, E.: The thermal conductivity of alumina–water nanofluids from the viewpoint of micromechanics. Microfluidics and nanofluidics **16**, 19-28 (2014)
Pae, J., Zhang, Y., Poh, L.H., Moon, J.: Three-dimensional transport properties of mortar with a high water-to-cement ratio using X-ray computed tomography. Construction and Building Materials **281**, 122608 (2021)
Pająk, M., Baranowski, P., Janiszewski, J., Kucewicz, M., Mazurkiewicz, Ł., Łaźniewska-Piekarczyk, B.: Experimental testing and 3D meso-scale numerical simulations of SCC subjected to high compression strain rates. Constr. Build. Mater. **302**, 124379 (2021)
Pająk, M., Janiszewski, J.: Dynamic Mechanical Response of Confined and Unconfined Concrete Reinforced with Recycled Steel Fibers. In: International RILEM Conference on Early-age and Long-term Cracking in RC Structures 2025, pp. 98-107. Springer
Pan, G., Song, T., Li, P., Jia, W., Deng, Y.: Review on finite element analysis of meso-structure model of concrete. J. Mater. Sci. **60**(1), 32-62 (2025)
Pan, Z., Fang, X., Chen, A.: Effect of aggregate morphology on physical tortuosity of chloride diffusive path at meso-scale of concrete. Constr. Build. Mater. **323**, 126215 (2022)

Papaelias, M., Marquez, F.P.G., Karyotakis, A.: Non-destructive testing and condition monitoring techniques for renewable energy industrial assets. Butterworth-Heinemann, (2019)
Papanikolaou, V.K., Kappos, A.J.: Confinement-sensitive plasticity constitutive model for concrete in triaxial compression. Int. J. Solids Struct. **44**(21), 7021-7048 (2007)
Patel, R.A., Phung, Q.T., Seetharam, S.C., Perko, J., Jacques, D., Maes, N., De Schutter, G., Ye, G., Van Breugel, K.: Diffusivity of saturated ordinary Portland cement-based materials: A critical review of experimental and analytical modelling approaches. Cement and Concrete Research **90**, 52-72 (2016)
Pellenq, R.J.-M., Kushima, A., Shahsavari, R., Van Vliet, K.J., Buehler, M.J., Yip, S., Ulm, F.-J.: A realistic molecular model of cement hydrates. Proceedings of the National Academy of Sciences **106**(38), 16102-16107 (2009)
Peng, J., Hu, S., Zhang, J., Cai, C., Li, L.-y.: Influence of cracks on chloride diffusivity in concrete: A five-phase mesoscale model approach. Constr. Build. Mater. **197**, 587-596 (2019)
Peng, Q., Wang, L., Lu, Q.: Influence of recycled coarse aggregate replacement percentage on fatigue performance of recycled aggregate concrete. Constr. Build. Mater. **169**, 347-353 (2018)
Petrone, C., Rossetto, T., Baiguera, M., De la Barra Bustamante, C., Ioannou, I.: Fragility functions for a reinforced concrete structure subjected to earthquake and tsunami in sequence. Eng. Struct. **205**, 110120 (2020)
Pijaudier-Cabot, G., Bažant, Z.P.: Nonlocal damage theory. J. Eng. Mech. **113**(10), 1512-1533 (1987)
Poinard, C., Piotrowska, E., Malecot, Y., Daudeville, L., Landis, E.N.: Compression triaxial behavior of concrete: the role of the mesostructure by analysis of X-ray tomographic images. European Journal of Environmental and Civil Engineering **16**(sup1), s115-s136 (2012)
Popovics, S., Ujhelyi, J.: Contribution to the concrete strength versus water-cement ratio relationship. Journal of Materials in Civil Engineering **20**(7), 459-463 (2008)
Pushpakumara, B., Fernando, M.: Deterioration assessment model for splash zone of marine concrete structures. Case Stud. Constr. Mater. **18**, e01731 (2023)
Qin, F., Hua, Z.J.: Three-dimensional numerical modelling of concrete-like materials subjected to dynamic loadings. Advances in protective structures research **1**, 33 (2012)
Qu, F., Li, W., Dong, W., Tam, V.W., Yu, T.: Durability deterioration of concrete under marine environment from material to structure: A critical review. J. Build. Eng. **35**, 102074 (2021)
Rahman, M., Chamberlain, D., Balakhrishna, M., Kipling, J.: Performance of pore-lining impregnants in concrete protection by unidirectional salt-ponding test. Transportation research record **2342**(1), 17-25 (2013)
Ranger, M., Hasholt, M.T., Jensen, O.M.: Chloride ingress parameters derived from migration and diffusion tests for systems with calcined smectitic clay and limestone. Cem. Concr. Res. **194**, 107893 (2025)
Reches, Y.: Nanoparticles as concrete additives: Review and perspectives. Constr. Build. Mater. **175**, 483-495 (2018)
Ren, Q., Pacheco, J., de Brito, J.: Methods for the modelling of concrete mesostructures: a critical review. Constr. Build. Mater. **408**, 133570 (2023)
Ren, X., Yang, W., Zhou, Y., Li, J.: Behavior of high-performance concrete under uniaxial and biaxial loading. ACI materials journal **105**(6), 548 (2008)

Ren, Y., Chen, J., Lu, G.: Mesoscopic simulation of uniaxial compression fracture of concrete via the nonlocal macro–meso-scale consistent damage model. Eng. Fract. Mech. **304**, 110148 (2024)
Richardson, M.G.: Fundamentals of durable reinforced concrete. CRC Press, (2023)
Richart, F.E., Brandtzæg, A., Brown, R.L.: A study of the failure of concrete under combined compressive stresses. University of Illinois. Engineering Experiment Station. Bulletin; no. 185 (1928)
Riyar, R.L., Bhowmik, S.: Fatigue behaviour of plain and reinforced concrete: A systematic review. Theor. Appl. Fract. Mech. **125**, 103867 (2023)
Rocco, C., Elices, M.: Effect of aggregate shape on the mechanical properties of a simple concrete. Eng. Fract. Mech. **76**(2), 286-298 (2009)
Rong, C., Shi, Q., Zhang, T., Zhao, H.: New failure criterion models for concrete under multiaxial stress in compression. Constr. Build. Mater. **161**, 432-441 (2018)
Roobankumar, R., SenthilPandian, M.: Investigating the correlation between ultrasonic pulse velocity and compressive strength in polyurethane foam concrete. Sci. Rep. **15**(1), 23995 (2025)
Röös, J., Uddmyr, A.: Repair of submerged concrete piles with FRP composites. (2017)
Rorschach, H., Chang, D., Hazlewood, C., Nichols, B.: The diffusion of water in striated muscle. Annals of the New York Academy of Sciences **204**(1), 444-452 (1973)
Ross, C.A., Tedesco, J.W., Kuennen, S.T.: Effects of strain rate on concrete strength. ACI Mater. J. **92**(1), 37-47 (1995)
Rozenbaum, O., du Roscoat, S.R.: Representative elementary volume assessment of three-dimensional x-ray microtomography images of heterogeneous materials: Application to limestones. Physical Review E **89**(5), 053304 (2014)
Safiuddin, M., Gonzalez, M., Cao, J., Tighe, S.L.: State-of-the-art report on use of nano-materials in concrete. International Journal of Pavement Engineering **15**(10), 940-949 (2014)
Sai, K.P.P., Rao, B.K., Veerendra, G., Dey, S., Manoj, A.V.P.: A critical examination on service life prediction of rc structures with respect to chloride-ion penetration. Journal of Bio-and Tribo-Corrosion **10**(1), 5 (2024)
Sakai, Y.: Relationship between pore structure and chloride diffusion in cementitious materials. Constr. Build. Mater. **229**, 116868 (2019)
Santhanam, M., Otieno, M.: Deterioration of concrete in the marine environment. Marine concrete structures, 137-149 (2016)
Santos, A.R., do Rosário Veiga, M., Silva, A.S., de Brito, J.: Microstructure as a critical factor of cement mortars' behaviour: The effect of aggregates' properties. Cement and Concrete Composites, 103628 (2020)
Sattar, M., Othman, A., Muzamil, M., Kamaruddin, S., Akhtar, M., Khan, R.: Development of new creep material model for use through computational modelling for stainless-steel. (2024)
Savvas, D., Stefanou, G., Papadrakakis, M.: Determination of RVE size for random composites with local volume fraction variation. Computer Methods in Applied Mechanics and Engineering **305**, 340-358 (2016)
Schlangen, E., Garboczi, E.J.: Fracture simulations of concrete using lattice models: computational aspects. Eng. Fract. Mech. **57**(2-3), 319-332 (1997)
Schlangen, E., Van Mier, J.: Simple lattice model for numerical simulation of fracture of concrete materials and structures. Mater Struct **25**, 534-542 (1992)
Seleem, H.E.-D.H., Rashad, A.M., El-Sabbagh, B.A.: Durability and strength evaluation of high-performance concrete in marine structures. Constr. Build. Mater. **24**(6), 878-884 (2010)

Selyutina, N., Smirnov, I.: Dynamic fractures of concrete made of recycled aggregate or reinforced with fibres. Mech. Mater. **179**, 104613 (2023)
Sfer, D., Carol, I., Gettu, R., Etse, G.: Study of the behavior of concrete under triaxial compression. J. Eng. Mech. **128**(2), 156-163 (2002)
Shafikhani, M., Chidiac, S.: Quantification of concrete chloride diffusion coefficient–A critical review. Cement and Concrete Composites **99**, 225-250 (2019)
Shahrin, R., Bobko, C.P.: Characterizing strength and failure of calcium silicate hydrate aggregates in cement paste under micropillar compression. Journal of Nanomechanics and Micromechanics **7**(4), 06017002 (2017)
Shakib, H., Alemzadeh, H.: The effect of earthquake site-source distance on dynamic response of concrete elevated water tanks. Procedia Eng. **199**, 260-265 (2017)
Shane, J.D., Mason, T.O., Jennings, H.M., Garboczi, E.J., Bentz, D.P.: Effect of the interfacial transition zone on the conductivity of Portland cement mortars. Journal of the American Ceramic Society **83**(5), 1137-1144 (2000)
Shang, H.-s., Cao, W.-q., Wang, B.: Effect of Fast Freeze-Thaw Cycles on Mechanical Properties of Ordinary-Air-Entrained Concrete. The Scientific World Journal **2014**(1), 923032 (2014a)
Shang, H.-s., Yang, S.-t., Niu, X.-y.: Mechanical behavior of different types of concrete under multiaxial tension–compression. Constr. Build. Mater. **73**, 764-770 (2014b)
Shazali, M., Rahman, M., Al-Gadhib, A., Baluch, M.: Transport modeling of chlorides with binding in concrete. Arabian Journal for Science and Engineering **37**, 469-479 (2012)
Shi, D., Chen, X.: Flexural tensile fracture behavior of pervious concrete under static preloading. Journal of Materials in Civil Engineering **30**(11), 06018015 (2018)
Shi, J., Zhao, Y.: Pore structure of concrete under fatigue load in areas with large temperature differences. Structural Concrete **23**(4), 2132-2149 (2022)
Shi, L., Liu, J., Liu, J.: Effect of polymer coating on the properties of surface layer concrete. Procedia Eng. **27**, 291-300 (2012)
Shoukry, S.N., William, G.W., Downie, B., Riad, M.Y.: Effect of moisture and temperature on the mechanical properties of concrete. Constr. Build. Mater. **25**(2), 688-696 (2011)
Silva, R., de Brito, J., Dhir, R.: The influence of the use of recycled aggregates on the compressive strength of concrete: A review. European Journal of Environmental and Civil Engineering **19**(7), 825-849 (2015)
Sinaie, S., Heidarpour, A., Zhao, X.-L., Sanjayan, J.G.: Effect of size on the response of cylindrical concrete samples under cyclic loading. Constr. Build. Mater. **84**, 399-408 (2015)
Singh, C., Gupta, P.K.: Numerical analysis of failure mechanics of concrete under true dynamic triaxial loading using a four-phase meso-model. Constr. Build. Mater. **450**, 138661 (2024)
Skibsted, J., Snellings, R.: Reactivity of supplementary cementitious materials (SCMs) in cement blends. Cem. Concr. Res. **124**, 105799 (2019)
Slowik, V., Saouma, V.E.: Water pressure in propagating concrete cracks. J. Struct. Eng. **126**(2), 235-242 (2000)
Snozzi, L., Caballero, A., Molinari, J.-F.: Influence of the meso-structure in dynamic fracture simulation of concrete under tensile loading. Cem. Concr. Res. **41**(11), 1130-1142 (2011)
Song, G., Zou, N., Wei, Y., Aili, A., Liang, S.: Numerical investigation into the influence of interfacial transition zone on elastic modulus, creep, shrinkage of concrete. Constr. Build. Mater. **447**, 138112 (2024)
Sovják, R., Vogel, F., Beckmann, B.: Triaxial compressive strength of ultra high performance concrete. Acta Polytech (2013)

Stamati, O., Roubin, E., Andò, E., Malecot, Y., Charrier, P.: Fracturing process of micro-concrete under uniaxial and triaxial compression: Insights from in-situ X-ray mechanical tests. Cem. Concr. Res. **149**, 106578 (2021)
Stock, A., Hannantt, D., Williams, R.: The effect of aggregate concentration upon the strength and modulus of elasticity of concrete. Mag. Concr. Res. **31**(109), 225-234 (1979)
Stoyanov, A.J., Fischer, E.C., Überall, H.: Effective medium theory for large particulate size composites. Journal of Applied Physics **89**(8), 4486-4490 (2001)
Su, H., Zhu, Z., Li, T., Xiang, H.: Experimental studies and numerical analysis of the dynamic mechanical properties of concrete at low temperatures. Constr. Build. Mater. **404**, 133221 (2023)
Su, Y., Iyela, P.M., Zhu, J., Chao, X., Kang, S., Long, X.: A Voronoi-based gaussian smoothing algorithm for efficiently generating RVEs of multi-phase composites with graded aggregates and random pores. Materials & Design **244**, 113159 (2024)
Sun, G., Poh, L.: Homogenization of intergranular fracture towards a transient gradient damage model. J. Mech. Phys. Solids **95**, 374-392 (2016)
Sun, G., Zhang, Y., Sun, W., Liu, Z., Wang, C.: Multi-scale prediction of the effective chloride diffusion coefficient of concrete. Constr. Build. Mater. **25**(10), 3820-3831 (2011)
Sun, J., Jin, Z., Chang, H., Zhang, W.: A review of chloride transport in concrete exposed to the marine atmosphere zone environment: Experiments and numerical models. J. Build. Eng. **84**, 108591 (2024a)
Sun, J., Xie, J., Zhou, Y., Zhou, Y.: A 3D three-phase meso-scale model for simulation of chloride diffusion in concrete based on ANSYS. Int. J. Mech. Sci. **219**, 107127 (2022)
Sun, M., Lv, T., Zhang, J.: Upscaling coarse-grained simulation study for hydrated cement paste from mesoscale to microscale. Developments in the Built Environment **17**, 100379 (2024b)
Sun, Q., Williams, B., Loeffler, C., Martin, B., Heard, W., Frew, D., Nie, X.: Comparative study of strength-based damage evolution in ultra-high-performance concrete (UHPC) and conventional concrete (CC) under dynamic loading. Int. J. Impact Eng. **155**, 103893 (2021a)
Sun, R.W., Fanourakis, G.C.: An assessment of factors affecting the elastic modulus of concrete. Structural Concrete **23**(1), 593-603 (2022)
Sun, Y., Edwards, M.G., Chen, B., Li, C.: A state-of-the-art review of crack branching. Eng. Fract. Mech. **257**, 108036 (2021b)
Sundar, V.: Ocean wave mechanics: Applications in marine structures. John Wiley & Sons, (2017)
Tagle, S., Jünemann, R., Vásquez, J., de la Llera, J., Baiguera, M.: Performance of a reinforced concrete wall building subjected to sequential earthquake and tsunami loading. Eng. Struct. **238**, 111995 (2021)
Taheri-Shakib, J., Al-Mayah, A.: 4D evolutions of cracks, voids, and corrosion products in reinforced concrete materials. Sci. Rep. **13**(1), 22455 (2023)
Tahmasebi, P., Sahimi, M., Kohanpur, A.H., Valocchi, A.: Pore-scale simulation of flow of CO2 and brine in reconstructed and actual 3D rock cores. Journal of Petroleum Science and Engineering **155**, 21-33 (2017)
Tai, Y.: Uniaxial compression tests at various loading rates for reactive powder concrete. Theor. Appl. Fract. Mech. **52**(1), 14-21 (2009)
Takahashi, K., Kawabata, Y., Kobayashi, M., Gotoh, S., Nomura, S., Kasaya, T., Iwanami, M.: Action of hydraulic pressure on Portland cement mortars-current understanding

and related progress of the first-ever in-situ deep sea tests at a 3515 m depth. J. Adv. Concr. Technol. **19**(3), 226-239 (2021)
Takeda, T., Sozen, M.A., Nielsen, N.N.: Reinforced concrete response to simulated earthquakes. J. Struct. Eng. **96**(12), 2557-2573 (1970)
Takiya, H., Watanabe, N., Kozaki, T., Sato, S.: Effects of water-to-cement ratio and temperature on diffusion of water in hardened cement pastes. Journal of nuclear science and technology **52**(5), 728-738 (2015)
Tang, L.: Chloride transport in concrete-measurement and prediction. Chalmers University of Technology, Sweden, Doctor Thesis (1996)
Tedesco, J., Ross, C.: Strain-rate-dependent constitutive equations for concrete. J. Press. Vessel. Technol. **120**(4), 398-405 (1998)
Thilakarathna, P.S.M., Baduge, K.K., Mendis, P., Vimonsatit, V., Lee, H.: Mesoscale modelling of concrete–a review of geometry generation, placing algorithms, constitutive relations and applications. Eng. Fract. Mech. **231**, 106974 (2020)
Thirumalaiselvi, A., Anandavalli, N., Rajasankar, J.: Mesoscale studies on the effect of aggregate shape idealisation in concrete. Mag. Concr. Res. **71**(5), 244-259 (2019)
Tian, T., Lu, W., Wang, H.: Dynamic responses and damage mechanisms of low-rise reinforced concrete frame structures subjected to rockfall impacts. J. Asian Archit. Build. Eng. **24**(2), 730-750 (2025)
Tibbetts, C.M., Riding, K.A., Ferraro, C.C.: A critical review of the testing and benefits of permeability-reducing admixtures for use in concrete. Cement **6**, 100016 (2021)
Tong, L.y., Liu, Q.f., Xiong, Q., Meng, Z., Amiri, O., Zhang, M.: Modeling the chloride transport in concrete from microstructure generation to chloride diffusivity prediction. Computer-Aided Civil and Infrastructure Engineering **40**(9), 1129-1149 (2025)
Torquato, S.: Effective electrical conductivity of two-phase disordered composite media. Journal of Applied Physics **58**(10), 3790-3797 (1985)
Torquato, S., Haslach Jr, H.: Random heterogeneous materials: microstructure and macroscopic properties. Appl. Mech. Rev. **55**(4), B62-B63 (2002)
Treu, A., Zimmer, K., Brischke, C., Larnøy, E., Gobakken, L.R., Aloui, F., Cragg, S., Flæte, P.-O., Humar, M., Westin, M.: Durability and protection of timber structures in marine environments in Europe: an overview. BioResources **14**(4) (2019)
Tu, Z., Lu, Y.: Mesoscale modelling of concrete for static and dynamic response analysis Part 1: model development and implementation. Struct. Eng. Mech. **37**(2), 197-213 (2011)
Udumulla, D., Ginigaddara, T., Jayasinghe, T., Mendis, P., Baduge, S.: Effect of graphene oxide nanomaterials on the durability of concrete: a review on mechanisms, provisions, challenges, and future prospects. Materials **17**(10), 2411 (2024)
Ueno, A., Ogawa, Y.: Influence of coarse aggregate shape on optimum fine to total aggregate ratio using a virtual voids-ratio diagram in concrete compaction. Cement and Concrete Composites **106**, 103463 (2020)
Ulm, F.-J., Constantinides, G., Heukamp, F.H.: Is concrete a poromechanics materials?—A multiscale investigation of poroelastic properties. Materials and structures **37**(1), 43-58 (2004)
Uzbas, B., Aydin, A.C.: Microstructural analysis of silica fume concrete with scanning electron microscopy and X-ray diffraction. Engineering, Technology & Applied Science Research **10**(3), 5845-5850 (2020)
Van Eekelen, H.: The random-spheres model for porous materials. Journal of Catalysis **29**(1), 75-82 (1973)
Van Steen, C., Pahlavan, L., Wevers, M., Verstrynge, E.: Localisation and characterisation of corrosion damage in reinforced concrete by means of acoustic emission and X-ray computed tomography. Constr. Build. Mater. **197**, 21-29 (2019)

Vandamme, M., Ulm, F.-J.: Nanogranular origin of concrete creep. Proceedings of the National Academy of Sciences **106**(26), 10552-10557 (2009)
Vandamme, M., Ulm, F.-J.: Nanoindentation investigation of creep properties of calcium silicate hydrates. Cem. Concr. Res. **52**, 38-52 (2013)
Vandamme, M., Ulm, F.: The nanogranular origin of concrete creep: a nanoindentation investigation of microstructure and fundamental properties of calcium-silicate-hydrates, vol. 69. vol. 07(2008)
Verma, S., Mohanty, S., Nayak, S.: A review on protective polymeric coatings for marine applications. Journal of coatings technology and research **16**(2), 307-338 (2019)
Votsis, R.A., Michailides, C., Tantele, E.A., Onoufriou, T.: Review of technologies for monitoring the performance of marine structures. In: ISOPE International Ocean and Polar Engineering Conference 2018, pp. ISOPE-I-18-576. ISOPE
Wadell, H.: Volume, shape, and roundness of rock particles. The Journal of Geology **40**(5), 443-451 (1932a)
Wadell, H.J.T.J.o.G.: Volume, shape, and roundness of rock particles. **40**(5), 443-451 (1932b)
Wan, Y., Zhu, L., Fang, H., Liu, W., Mao, Y.: Experimental testing and numerical simulations of ship impact on axially loaded reinforced concrete piers. Int. J. Impact Eng. **125**, 246-262 (2019)
Wang, B., Song, X., Weng, C., Yan, X., Zhang, Z.: A Hybrid Method Combining Voronoi Diagrams and the Random Walk Algorithm for Generating the Mesostructure of Concrete. Materials **17**(18), 4440 (2024a)
Wang, B., Song, X., Zhang, Z.: Mesoscopic fracture modelling of lightweight aggregate concrete under compression. International Journal of Computational Methods (2025a)
Wang, D., Yang, C., Lin, Y., Lü, L.: An ultrasonic approach for characterising subsurface fractures in concrete. Nondestructive Testing and Evaluation **39**(7), 2002-2014 (2024b)
Wang, H.-L., Dai, J.-G., Sun, X.-Y., Zhang, X.-L.: Characteristics of concrete cracks and their influence on chloride penetration. Constr. Build. Mater. **107**, 216-225 (2016a)
Wang, H., Lu, W., Zhan, W.: Dynamic response and damage mechanism of reinforced concrete beam bridges under rockfall impacts. Sci. Rep. **15**(1), 5090 (2025b)
Wang, J., Jivkov, A.P., Li, Q., Engelberg, D.L.: Experimental and numerical investigation of mortar and ITZ parameters in meso-scale models of concrete. Theor. Appl. Fract. Mech. **109**, 102722 (2020)
Wang, J., Li, X., Jivkov, A.P., Li, Q., Engelberg, D.L.: Interfacial transition zones in concrete meso-scale models–Balancing physical realism and computational efficiency. Constr. Build. Mater. **293**, 123332 (2021)
Wang, J., Yu, X., Fu, Y., Zhou, G.: A 3D meso-scale model and numerical uniaxial compression tests on concrete with the consideration of the friction effect. Materials **17**(5), 1204 (2024c)
Wang, L., Sun, X., Xie, L., Yu, Z., Lian, H., Lian, Y., He, H.: Research on the shear multiaxial performance and meso-mechanical mechanism of concrete. Materials and Structures **58**(3), 1-22 (2025c)
Wang, M.L., Lynch, J.P., Sohn, H.: Sensor technologies for civil infrastructures. (2014)
Wang, Q., Xu, Y.: Macro-meso cracking inversion modelling of three-point bending concrete beam with random aggregates using cohesive zone model. Theor. Appl. Fract. Mech. **133**, 104566 (2024)
Wang, X., Jivkov, A.P.: Combined numerical-statistical analyses of damage and failure of 2D and 3D mesoscale heterogeneous concrete. Math. Probl. Eng. **2015**(1), 702563 (2015)

Wang, X., Liang, Z., Nie, Z., Gong, J.: Stochastic numerical model of stone-based materials with realistic stone-inclusion features. Construction and Building Materials **197**, 830-848 (2019a)
Wang, X., Yang, Z., Jivkov, A.P.: Monte Carlo simulations of mesoscale fracture of concrete with random aggregates and pores: a size effect study. Constr. Build. Mater. **80**, 262-272 (2015a)
Wang, X., Yang, Z.J., Yates, J., Jivkov, A., Zhang, C.: Monte Carlo simulations of mesoscale fracture modelling of concrete with random aggregates and pores. Constr. Build. Mater. **75**, 35-45 (2015b)
Wang, X., Zhang, M., Jivkov, A.P.: Computational technology for analysis of 3D meso-structure effects on damage and failure of concrete. Int. J. Solids Struct. **80**, 310-333 (2016b)
Wang, Y., Ueda, T., Gong, F., Zhang, D.: Meso-scale mechanical deterioration of mortar due to sodium chloride attack. Cem. Concr. Compos. **96**, 163-173 (2019b)
Wang, Y., Wu, J., Ma, D., Yang, S., Yin, Q., Feng, Y.: Effect of aggregate size distribution and confining pressure on mechanical property and microstructure of cemented gangue backfill materials. Advanced Powder Technology **33**(8), 103686 (2022)
Wang, Y., Zhang, W., Wang, J., Huang, R., Lou, G., Luo, S.: Effects of coarse aggregate size on thickness and micro-properties of ITZ and the mechanical properties of concrete. Cem. Concr. Compos. **154**, 105777 (2024d)
Wang, Z., Chauhan, K., Pereira, J.-M., Gan, Y.: Disorder characterization of porous media and its effect on fluid displacement. Physical Review Fluids **4**(3), 034305 (2019c)
Wei, D., Chongpu, Z., Hanaor, D., Yixiang, G.: Contact behaviour of simulated rough spheres generated with spherical harmonics. Int. J. Solids Struct. **193**, 54-68 (2020a)
Wei, D., Hurley, R.C., Poh, L.H., Dias-da-Costa, D., Gan, Y.: The role of particle morphology on concrete fracture behaviour: A meso-scale modelling approach. Cem Concr Res **134**, 106096 (2020b)
Wei, D., Hurley, R.C., Poh, L.H., Dias-da-Costa, D., Gan, Y.J.C., Research, C.: The role of particle morphology on concrete fracture behaviour: A meso-scale modelling approach. **134**, 106096 (2020c)
Wei, D., Wang, J., Nie, J., Zhou, B.: Generation of realistic sand particles with fractal nature using an improved spherical harmonic analysis. Computers and Geotechnics **104**, 1-12 (2018)
Wei, D., Wang, Z., Pereira, J.M., Gan, Y.: Permeability of uniformly graded 3D printed granular media. Geophysical Research Letters **48**(5) (2021)
Wei, D., Zhao, B., Dias-da-Costa, D., Gan, Y.: An FDEM study of particle breakage under rotational point loading. Eng. Fract. Mech. **212**, 221-237 (2019)
Wei, X., Sun, Y., Gong, H., Zhao, Y., Hu, M., Chen, J.: 2D aggregate gradation conversion framework integrated with 3D random aggregate method and machine-learning for asphalt concrete. Journal of Materials in Civil Engineering **36**(5), 04024091 (2024)
Westerholm, M., Lagerblad, B., Silfwerbrand, J., Forssberg, E.: Influence of fine aggregate characteristics on the rheological properties of mortars. Cement and Concrete Composites **30**(4), 274-282 (2008)
Wilson, J.F.: Dynamics of offshore structures. John Wiley & Sons, (2003)
Wilson, K., Jawed, M., Ngala, V.: The selection and use of cathodic protection systems for the repair of reinforced concrete structures. Constr. Build. Mater. **39**, 19-25 (2013)
Winslow, D.N., Cohen, M.D., Bentz, D.P., Snyder, K.A., Garboczi, E.J.: Percolation and pore structure in mortars and concrete. Cem. Concr. Res. **24**(1), 25-37 (1994)
Wu, Y.-C., Xiao, J.: The effect of microscopic cracks on chloride diffusivity of recycled aggregate concrete. Constr. Build. Mater. **170**, 326-346 (2018)

Wu, Y., Wang, T., Duan, J., Song, L.: Mesoscale numerical study of size effect on concrete fracture characteristics based on FDEM. Electronic Journal of Structural Engineering **25**(1), 46-51 (2025)
Wu, Z., She, W., Zhang, J., Tang, J., Cao, Y., Da, B.: 3D mesoscale modelling of steel fiber-reinforced aggregate concrete. Int. J. Mech. Sci. **257**, 108550 (2023a)
Wu, Z., Yu, H., Zhang, J., Ma, H.: Mesoscopic study of the mechanical properties of coral aggregate concrete under complex loads. Composite Structures **308**, 116712 (2023b)
Wu, Z., Zhang, J., Fang, Q., Yu, H., Haiyan, M.: Mesoscopic modelling of concrete material under static and dynamic loadings: A review. Constr Build Mater **278**, 122419 (2021a)
Wu, Z., Zhang, J., Yu, H., Ma, H., Fang, Q.: 3D mesoscopic analysis on the compressive behavior of coral aggregate concrete accounting for coarse aggregate volume and maximum aggregate size. Composite Structures **273**, 114271 (2021b)
Xiao, J., Ying, J., Shen, L.: FEM simulation of chloride diffusion in modeled recycled aggregate concrete. Construction and Building Materials **29**, 12-23 (2012)
Xie, J., Elwi, A., MacGregor, J.: Mechanical properties of three high-strength concretes containing silica fume. ACI Mater. J. **92**(2), 135-145 (1995)
Xie, Y., Guan, K., Zhan, L., Wang, Q.: Mechanical behavior and chloride penetration of precracked reinforced concrete beams with externally bonded CFRP exposed to marine environment. International Journal of Polymer Science **2016**(1), 1790585 (2016)
Xiong, Q., Wang, X., Jivkov, A.P.: A 3D multi-phase meso-scale model for modelling coupling of damage and transport properties in concrete. Cement and Concrete Composites **109**, 103545 (2020a)
Xiong, Q., Wang, X., Jivkov, A.P.: A 3D multi-phase meso-scale model for modelling coupling of damage and transport properties in concrete. Cem Concr Compos **109**, 103545 (2020b)
Xu, G., Ji, C., Xu, Y., Yu, E., Cao, Z., Wu, Q., Lin, P., Wang, J.: Machine learning in coastal bridge hydrodynamics: a state-of-the-art review. Applied Ocean Research **134**, 103511 (2023)
Xu, J., Li, F.: A meso-scale model for analyzing the chloride diffusion of concrete subjected to external stress. Construction and Building Materials **130**, 11-21 (2017)
Xu, J., Peng, C., Wan, L., Wu, Q., She, W.: Effect of crack self-healing on concrete diffusivity: Mesoscale dynamics simulation study. Journal of Materials in Civil Engineering **32**(6), 04020149 (2020)
Xu, Q., Liu, B., Dai, L., Yao, M., Pang, X.: Factors influencing chloride ion diffusion in reinforced concrete structures. Materials **17**(13), 3296 (2024)
Xu, W., Xu, B., Guo, F.: Elastic properties of particle-reinforced composites containing nonspherical particles of high packing density and interphase: DEM–FEM simulation and micromechanical theory. Computer Methods in Applied Mechanics and Engineering **326**, 122-143 (2017)
Yang, C.-C.: On the relationship between pore structure and chloride diffusivity from accelerated chloride migration test in cement-based materials. Cem. Concr. Res. **36**(7), 1304-1311 (2006)
Yang, C., Zhang, J., Guo, W.: Effect of aggregate characteristics on chloride diffusion in concrete based on mesoscale numerical simulation. Constr. Build. Mater. **472**, 140839 (2025)
Yang, H., Zhu, E., Liu, L.: Analysis of the effect of pore structure on the mechanical properties of concrete based on the meso numerical model. Applied Sciences **12**(11), 5428 (2022a)

Yang, L.: Techniques for corrosion monitoring. Woodhead Publishing, (2020)
Yang, L., Li, K., Hu, X., Peng, Z., Liu, Q.-f., Shi, C.: Mesoscopic discrete modeling of compression and fracture behavior of concrete: effects of aggregate size distribution and interface transition zone. Cem. Concr. Compos. **147**, 105411 (2024)
Yang, L.F., Cai, R., Yu, B.: Investigation of computational model for surface chloride concentration of concrete in marine atmosphere zone. Ocean Engineering **138**, 105-111 (2017)
Yang, S., Liu, B., Li, F.: Estimations of the elastic moduli of concrete at different temperatures and humidities by mesomechanics methods. Case Stud. Constr. Mater. **17**, e01254 (2022b)
Yankelevsky, D.Z.: The uniaxial compressive strength of concrete: revisited. Mater Struct **57**(6), 144 (2024)
Yi, Y., Zhu, D., Guo, S., Zhang, Z., Shi, C.: A review on the deterioration and approaches to enhance the durability of concrete in the marine environment. Cem. Concr. Compos. **113**, 103695 (2020)
Yılmaz, O., Molinari, J.-F.: A mesoscale fracture model for concrete. Cem. Concr. Res. **97**, 84-94 (2017)
Yu, H., Sun, W., Yan, L., Ma, H.: Study on prediction of concrete service life I-theoretical model. Guisuanyan Xuebao(Journal of the Chinese Ceramic Society)(China)(China) **30**, 686-690 (2002)
Yu, W., Jin, L., Du, X.: Experiment and meso-scale modelling on combined effects of strain rate and specimen size on uniaxial-compressive failures of concrete. Int. J. Damage Mech. **32**(5), 683-714 (2023)
Yu, Y., Lin, L.: Modeling and predicting chloride diffusion in recycled aggregate concrete. Constr. Build. Mater. **264**, 120620 (2020)
Yu, Z., Ma, J., Ye, G., van Breugel, K., Shen, X.: Effect of fly ash on the pore structure of cement paste under a curing period of 3 years. Constr. Build. Mater. **144**, 493-501 (2017)
Yuan, G., Li, Q.: The use of surface coating in enhancing the mechanical properties and durability of concrete exposed to elevated temperature. Constr. Build. Mater. **95**, 375-383 (2015)
Yuxin, H., Chuansheng, X., Heng, Y., Zuquan, J., Penggang, W., Xiangke, G., Zhuren, W., Yuan, H., Xinyu, Z.: Effect of temperature on epoxy resin deterioration for fibre-reinforced polymer reinforcement in simulated concrete pore solutions. Constr. Build. Mater. **409**, 133701 (2023)
Zaitsev, Y., Wittmann, F.: Simulation of crack propagation and failure of concrete. Matériaux et Construction **14**, 357-365 (1981)
Zhai, C., Herbold, E., Hall, S., Hurley, R.: Particle rotations and energy dissipation during mechanical compression of granular materials. J. Mech. Phys. Solids **129**, 19-38 (2019)
Zhang, B.: Relationship between pore structure and mechanical properties of ordinary concrete under bending fatigue. Cem. Concr. Res. **28**(5), 699-711 (1998)
Zhang, C., Gholipour, G., Mousavi, A.A.: Nonlinear dynamic behavior of simply-supported RC beams subjected to combined impact-blast loading. Eng. Struct. **181**, 124-142 (2019)
Zhang, G., Torquato, S.: Precise algorithm to generate random sequential addition of hard hyperspheres at saturation. Physical Review E—Statistical, Nonlinear, and Soft Matter Physics **88**(5), 053312 (2013)

Zhang, H., Li, H.-N., Li, C., Cao, G.-W.: Experimental and numerical investigations on seismic responses of reinforced concrete structures considering strain rate effect. Constr. Build. Mater. **173**, 672-686 (2018a)
Zhang, H., Xu, C., Zhou, Y., Shu, J., Huang, K.: Hybrid phase-field modeling of mesoscopic failure in concrete combined with Fourier-Voronoi stochastic aggregate distribution modelling approach. Constr. Build. Mater. **394**, 132106 (2023)
Zhang, J.: Application of ultra-high performance concrete in the marine environment. In: E3S Web of Conferences 2025, p. 04008. EDP Sciences
Zhang, J., Bian, F., Zhang, Y., Fang, Z., Fu, C., Guo, J.: Effect of pore structures on gas permeability and chloride diffusivity of concrete. Constr. Build. Mater. **163**, 402-413 (2018b)
Zhang, J., Emelianenko, M., Du, Q.: PERIODIC CENTROIDAL VORONOI TESSELLATIONS. International Journal of Numerical Analysis & Modeling **9**(4) (2012a)
Zhang, J., Li, C., Zhu, C., Zhao, Z.: Analysis of biaxial mechanical properties and failure criterion of self-compacting concrete. Frontiers in Materials **8**, 691342 (2021a)
Zhang, J., Li, W., Yuan, Q., Wang, J., Gao, Y.: Insights on the representative elementary volume of plain cement paste from a micromechanical perspective. J. Build. Eng. **100**, 111741 (2025)
Zhang, J., Wu, J., Zhang, Y., Gao, Y., Wang, J.: Time-varying relationship between pore structures and chloride diffusivity of concrete under the simulated tidal environment. European Journal of Environmental and Civil Engineering **26**(2), 501-518 (2022)
Zhang, L., Xie, H., Feng, J.: Effect of Meso-Structure on Macroscopic Behavior of Concrete: A 3D Numerical Study. Arabian Journal for Science and Engineering, 1-17 (2024a)
Zhang, M.: Multiscale lattice Boltzmann-finite element modelling of transport properties in cement-based materials. (2013a)
Zhang, M.: Multiscale lattice Boltzmann-finite element modelling of transport properties in cement-based materials. VSSD–Student Union, (2013b)
Zhang, M., Wu, H., Li, Q., Huang, F.: Further investigation on the dynamic compressive strength enhancement of concrete-like materials based on split Hopkinson pressure bar tests. Part I: Experiments. Int. J. Impact Eng. **36**(12), 1327-1334 (2009)
Zhang, M., Ye, G., van Breugel, K.: Modeling of ionic diffusivity in non-saturated cement-based materials using lattice Boltzmann method. Cement and Concrete Research **42**(11), 1524-1533 (2012b)
Zhang, M., Ye, G., van Breugel, K.: Multiscale lattice Boltzmann-finite element modelling of chloride diffusivity in cementitious materials. Part I: Algorithms and implementation. Mechanics Research Communications **58**, 53-63 (2014a)
Zhang, M., Ye, G., van Breugel, K.: Multiscale lattice Boltzmann-finite element modelling of chloride diffusivity in cementitious materials. Part II: Simulation results and validation. Mechanics Research Communications **58**, 64-72 (2014b)
Zhang, Q., Wang, F., Ling, Y., Chen, H., Li, Z.: Investigation on numerical simulation of chloride transport in unsaturated concrete. Advances in Materials Science and Engineering **2021**(1), 7548071 (2021b)
Zhang, Q., Xu, Z., Tao, W.: Rate dependent cohesive zone model for fatigue crack growth. Int. J. Mech. Sci. **271**, 109144 (2024b)
Zhang, S., Cao, K., Wang, C., Wang, X., Deng, G., Wei, P.: Influence of the porosity and pore size on the compressive and splitting strengths of cellular concrete with millimeter-size pores. Constr. Build. Mater. **235**, 117508 (2020a)

Zhang, X., Wu, H., Li, J., Pi, A., Huang, F.: Numerical simulation of high-strength concrete under uniaxial/triaxial compression based on meso-scale model. Journal of Physics: Conference Series **1507**(8), 082053 (2020b)
Zhang, X., Yang, Z.-J., Huang, Y.-J., Wang, Z.-Y., Chen, X.-W.: Micro CT image-based simulations of concrete under high strain rate impact using a continuum-discrete coupled model. Int. J. Impact Eng. **149**, 103775 (2021c)
Zhang, Y., Zhang, M.: Transport properties in unsaturated cement-based materials–A review. Constr. Build. Mater. **72**, 367-379 (2014)
Zhang, Z., Song, X., Liu, Y., Wu, D., Song, C.: Three-dimensional mesoscale modelling of concrete composites by using random walking algorithm. Composites Science and Technology **149**, 235-245 (2017)
Zhao, G., Xu, J., Feng, Y., Tang, J., Chen, Y., Xin, S., Jian, X., Li, S., Zhang, S., Xu, J.: A rate-dependent cohesive zone model with the effects of interfacial viscoelasticity and progressive damage. Eng. Fract. Mech. **248**, 107695 (2021)
Zhao, H., Gan, Y., Qu, F., Tang, Z., Peng, S., Chen, Y., Li, W.: Nano-and micro-characterisation on the heterogeneity of ITZs in recycled lump concrete. Cem. Concr. Compos. **161**, 106078 (2025)
Zhao, P., Zsaki, A.M., Nokken, M.R.: Using digital image correlation to evaluate plastic shrinkage cracking in cement-based materials. Constr. Build. Mater. **182**, 108-117 (2018)
Zhao, S., GONG, J., SHUI, J.: Probability Analysis of Durability for Existing Reinforced Concrete Bridge in Chloride Environment [J]. Journal of Highway and Transportation Research and Development **23**(7), 82-86 (2006)
Zheng, B., Li, T., Qi, H., Gao, L., Liu, X., Yuan, L.: 3D meso-scale simulation of chloride ion transportation in cracked concrete considering aggregate morphology. Constr. Build. Mater. **326**, 126632 (2022)
Zheng, J.-J., Zhou, X.-Z., Wu, Y.-F., Jin, X.-Y.: A numerical method for the chloride diffusivity in concrete with aggregate shape effect. Construction and Building Materials **31**, 151-156 (2012)
Zheng, J., Hryciw, R.D.: Traditional soil particle sphericity, roundness and surface roughness by computational geometry. Géotechnique **65**(6), 494-506 (2015)
Zheng, J., Zhang, C., Wu, Y., Sun, L.: Random-walk algorithm for chloride diffusivity of concrete with aggregate shape effect. Journal of Materials in Civil Engineering **28**(12), 04016153 (2016)
Zheng, J., Zhou, X., Wu, Z.: A simple method for predicting the chloride diffusivity of cement paste. Materials and Structures **43**(1), 99-106 (2010)
Zhou, A., Büyüköztürk, O., Lau, D.: Debonding of concrete-epoxy interface under the coupled effect of moisture and sustained load. Cem. Concr. Compos. **80**, 287-297 (2017a)
Zhou, C., Feng, D., Wu, X., Cao, P., Fan, X.: Prediction of concrete coefficient of thermal expansion by effective self-consistent method considering coarse aggregate shape. Journal of Materials in Civil Engineering **30**(12), 04018312 (2018)
Zhou, C., Li, K., Ma, F.: Numerical and statistical analysis of elastic modulus of concrete as a three-phase heterogeneous composite. Computers & Structures **139**, 33-42 (2014)
Zhou, G., Xu, Z.: 3D mesoscale investigation on the compressive fracture of concrete with different aggregate shapes and interface transition zones. Constr. Build. Mater. **393**, 132111 (2023)
Zhou, R., Lu, Y., Wang, W., Cheng, C., Lu, Z.: Mesoscale modelling of the dynamic tensile strength enhancement of concrete in spalling tests using interface elements. Eng. Fract. Mech. **295**, 109808 (2024a)

Zhou, R., Song, Z., Lu, Y.: 3D mesoscale finite element modelling of concrete. Computers and Structures **192**, 96-113 (2017b)
Zhou, W., Feng, P., Yang, J.-Q.: Advances in coral aggregate concrete and its combination with FRP: A state-of-the-art review. Advances in Structural Engineering **24**(6), 1161-1181 (2021a)
Zhou, X.-Z., Ye, W.-W., Zhou, Y.-Z., Zheng, J.-J., Shao, H.-X., Rong, H.: A modified effective medium approach for water permeability coefficient of cement paste. Constr. Build. Mater. **442**, 137607 (2024b)
Zhou, X., Xie, Y., Long, G., Zeng, X., Li, J., Yao, L., Jiang, W., Pan, Z.: DEM analysis of the effect of interface transition zone on dynamic splitting tensile behavior of high-strength concrete based on multi-phase model. Cem. Concr. Res. **149**, 106577 (2021b)
Zhou, X., Xie, Y., Long, G., Zeng, X., Li, N., Ma, G., Wang, F., Yao, L.: Multi-scale modeling of the concrete SHPB test based on DEM-FDM coupling method. Constr. Build. Mater. **356**, 129157 (2022)
Zhou, Y., Gao, J., Sun, Z., Qu, W.: A fundamental study on compressive strength, static and dynamic elastic moduli of young concrete. Constr. Build. Mater. **98**, 137-145 (2015)
Zhu, C., Zhu, E., Wang, B., Li, J., Yao, T., Zhang, Z.: Effect of Porosity and Pore Size on the Axial Compressive Properties of Recycled Aggregate Concrete. Materials **18**(12), 2830 (2025)
Zhu, S., Zhou, Z., Xiong, Y.: Mesoscale fracture analysis of three-point bending concrete beams based on cohesive zone model. Eng. Fract. Mech. **296**, 109828 (2024)